SEISMIC VELOCITIES IN POROUS ROCKS:

DIRECT AND INVERSE PROBLEMS

by

CHENG, CHUEN HON (ARTHUR)

B.Sc., Cornell University (1973)

SUBMITTED IN PARTIAL FULFILLMENT

OF THE REQUIREMENTS FOR THE

DEGREE OF

DOCTOR OF SCIENCE

at the

 MASSACHUSETTS INSTITUTE OF TECHNOLOGY

August 25, 1978

Signature of Author.....
Department of Earth and Planetary Sciences, August 25, 1978.

Certified by.....
Thesis Supervisor

Accepted by.....
Chairman, Departmental Committee on Graduate Students

SEISMIC VELOCITIES IN POROUS ROCKS: DIRECT AND INVERSE PROBLEMS

by

Cheng, Chuen Hon Arthur

Submitted to the Department of Earth and Planetary Sciences on August 25, 1978, in partial fulfillment of the requirements for the degree of Doctor of Science.

ABSTRACT

In this thesis the problem of seismic velocities in porous rocks is studied from the standpoint of both the direct and inverse problems. Laboratory measurements of seismic velocities in rocks as a function of pressure and under different saturation conditions have shown that firstly, the compressional wave velocities of the dry or gas-saturated rock are lower than those of the liquid-saturated rock, while the shear wave velocities usually show the opposite behavior; secondly, all velocities increase with differential (confining minus fluid) pressure, very rapidly at low pressures and leveling off at higher pressures. These effects are equally prominent in both high and low porosity rocks.

In the direct problem, the effects of saturation are modelled by approximating the pore spaces in a rock as a collection of oblate ellipsoidal cracks of different aspect ratios. Several different first order averaging schemes for calculating the effective moduli of a solid matrix with ellipsoidal inclusions are examined and the theory of Kuster and Toksöz is found to give the best results. For higher concentrations and possible effects of crack interactions, an extrapolation of the theory of Kuster and Toksöz resulted in a system of integral equations. An iterative solution of the integral equations is proposed and found to be convergent.

The increases in velocities with pressure are then modelled in terms of the closing of the small aspect ratio cracks with pressure. An extension of the Walsh (1965) crack closing rate is presented. With this and an assumed distribution of ellipsoidal cracks of different aspect ratios (the

pore-aspect ratio spectrum) at zero pressure, the observed velocities in a rock as a function of pressure and saturation are fitted by varying the initial spectrum via a trial and error approach. Theoretical in situ rock properties (seismic velocities, acoustic impedance, Poisson's ratio) under full and partial saturation conditions are then calculated using these rock models. The Poisson's ratio is found to be the best indicator of the relative amounts of gas and fluid in a partial saturation condition.

The questions of the uniqueness and the resolution of the pore-aspect ratio spectrum are addressed by posing the problem as an inverse problem. Three techniques are examined: the linear and linearized iterative inversion with solutions by damped least squares and the linear programming inversion. The linearized iterative inversion, with the linear inversion used to generate the initial model, is found to converge quickly and give the best fit to the data. The relative resolution at each aspect ratio crack is found to be between 0.6 and 0.8 with a damping coefficient of 1. The estimated errors for the fractional porosities of individual aspect ratio cracks vary from very good (about 10%) for the very fine cracks to poor (nearly 100%) for the larger aspect ratio cracks. This is because the changes in the velocities are much more sensitive to the smaller aspect ratio cracks. The inversion is found to be stable to changes in the matrix moduli, the aspect ratios specified and the number of data points. The effects of scaling the coefficient matrix and changing the damping coefficient are also examined.

The pore-aspect ratio spectrum obtained from the inversion of velocity data is found to be predictive. It can predict the velocities of a rock under saturated conditions different from those used in the inversion. The spectra of Berea and Navajo sandstones are found to be very similar to each other, just as their porosities. However, the spectrum of Boise sandstone is found to contain fewer thin cracks than either the Berea or the Navajo sandstone despite its much higher porosity. The pore-aspect ratio spectrum of Westerly granite obtained from the inversion of velocity data is compared with and found to be similar to other estimates of its pore shapes (from SEM photographs by Sprunt and Brace, 1974; and Hadley, 1976; and from Differential Strain Analysis by Feves and Simmons, 1976).

Thesis Supervisor: M. Nafi Toksöz
Title: Professor of Geophysics

ACKNOWLEDGEMENTS

First and foremost, I must thank my advisor, Nafi Toksöz, for suggesting this problem and for his guidance throughout this projest. He also provided the opportunity for me to work on various other projects during my tenure as a graduate student which helps to make my education in solid earth Geophysics more complete and rewarding.

Drs. Guy Kuster and Joe Walsh, whose pioneer works on this subjest have laid the solid foundations upon this work is built, deserve special thankyous. Discussions with them have helped tremedously in the development of this thesis. Professors Ted Madden and Keiiti Aki, here at M.I.T., Drs. Don Thompson, Jim Spencer and Turk Timur at Chevron Oil Field Research, Professor Dave Jackson of UCLA and Professor Jan Korringa at Ohio State have also contributed insights to different aspects of the problem.

As for my fellow students, all of them contributed greatly to the atmosphere of learning here at M.I.T. Among them a few deserve special mention. Dave Johnston was involved in the experimental aspects of this project. The fact that he produced data that fit my theory will always be appreciated, as well as his explanations of experimental errors when they don't fit. George Zandt and I spent five years having our desks next to each other, and between his and my projects, we have spent endless hours in deciding what various matrices mean. Tony Shakal, our phantom officemate,

has occasionally actually showed up and join in the discussion. I don't think any of us care if we never heard another word about the resolution or the information density matrices again. Mike Fehler and I have perfected the office intercom system -- yelling through the wall. Randy Richardson kept me busy by challenging me to dart games -- now you know why it took us so long to write our theses. Steve Taylor, well what can you say about Steve except that he stinks. Actually, Steve taught me how to play hockey (and hooky), I just wish he would pass me the puck once in a while. Neal Goins, our answer to Rick Burleson (actually he is closer to Don Zimmer in physique), watched for the periods in the occurance of moonquakes with me. He would get all excited if they missed one, and I would have to remind him, with apologies to Sheila Newton, that they are not his girlfriends.

On a more personal more, Winnie Wong provided me with moral and spiritual support throughout the last three years. She also help drafted most of the figures and typed most of the tables. To her, I have to say thankyou, although no amounts of oral or written acknowledgements are enough to express my deep appreciations. With her by my side, the chore of thesis writing is definitely eased.

This thesis would not be possible without the encouragement and support of my parents. They have always insisted that I tried my best, hopefully I haven't disappointed them. To them this thesis is dedicated.

Lastly, and certainly the least, I would like to thank my Cheryl Tiegs poster for warming up my heart during the cold nights in my office, and myself for the excellent typing.

This research was supported by a Chevron Fellowship and USGS contract no. 14-08-001-16724.

TABLE OF CONTENTS

PAGE

PAGE

PAGE

CHAPTER 1

INTRODUCTION

The velocities of seismic waves in a porous rock are strongly dependent on the saturation condition and the distribution of pore shapes, the latter being a function of pressure. Laboratory experiments have shown that the compressional wave velocity of a liquid-saturated rock is higher than when the rock is empty or gas-saturated. The difference in the velocities is large (more than 10% for most rocks) at atmospheric pressure but decreases rapidly with increasing pressure (Nur and Simmons, 1969; King, 1966; Toksöz et al., 1976; Gardner et al., 1974; Wyllie et al., 1956, 1958; Elliott and Wiley, 1975). Furthermore, this difference exists for both high porosity sedimentary rocks and low porosity igneous rocks (Nur and Simmons, 1969). The shear wave velocity shows a slightly different behavior. The gas-saturated s-wave velocity is usually higher than that of a liquid-saturated rock. The difference in the velocities is usually much less than that of the p-waves. At low pressures, the two s-wave velocities are very close to each other, in some cases the gas-saturated velocity is actually lower than the liquid-saturated one. At higher pressures, the difference in the velocities is more pronounced. This difference is usually larger in higher porosity rocks and is

negligible in very low porosity rocks (Nur and Simmons, 1969; Toksöz et al., 1976).

There have been many attempts to model the above described velocity behaviors theoretically. There are two different approachs among these studies. The first group is more interested in the effects of saturation alone, i.e., given the elastic properties of the dry or empty rock (known as the frame moduli), what will these properties be when the rock is saturated with different fluids? Gassmann (1951) did the pioneering work in this approach. Other investigators have expanded on Gassmann's work to take care of frequency dependence (Biot, 1956a, b; Geertsma, 1957; Geertsma and Smit, 1961) and heterogeneity and anisotropy (Brown and Korringa, 1975). The central characteristic of this approach remains that the effective properties of the saturated rock are calculated given the porosity of the rock and the moduli of the solid matrix material, the fluid saturant and the "frame" or empty rock. Furthermore, it is implicit that the shear modulus of the rock is not a function of saturation, contrary to experimental evidence. The main drawback of this approach is that the effects of the pore shapes are included only implicitly through the frame moduli.

The second approach is to take the pore shapes into account explicitly. Since the dependence of the seismic velocities on saturation is equally prominent in high and low porosity rocks, the pore shapes must play an important

role. Moreover, the increase in the velocities with pressure can be related to the closing of thin, flat cracks (Walsh, 1965; Toksöz et al., 1976). Eshelby (1957), in a now classic paper, had shown that under an uniform applied strain at infinity, the strain inside an ellipsoidal inclusion imbedded in a solid matrix is also uniform. This result enables the use of ellipsoids to model the pore geometry in a rock. A number of investigators have used the oblate ellipsoids or "penny-shaped" cracks in the calculation of the effective moduli of a rock. The difference between them is in the use of averaging schemes to acheive the effects of crack interactions. Walsh (1969) used a strictly isolated crack approach. Wu (1966) and Budiansky and O'Connell (1976) used a "self-consistent" approximation. Kuster and Toksöz (1974a) used a "representative sphere" approach first suggested by Ament (1953, 1959). Among these schemes, that of Kuster and Toksöz seems to work best over a wide range of porosities and pore shapes.

With the ellipsoidal cracks, we can also model the increase in the seismic velocities with pressure by calculating the rate of closing of the cracks with pressure. This rate is dependent on the aspect ratio (the ratio of crack width to crack length) of the crack. Walsh (1965) calculated this rate for spherical cavities and for very small aspect ratio cracks using the reciprocal theorem. In this thesis we extended this to cover cracks of all aspect ratios using

the results of Eshelby (see also Toksöz et al., 1976).

The problem of calculating the effective moduli has also been investigated using a dynamic approach. Unfortunately, the formal problem of the scattering of elastic waves by an obstacle is solvable only for spherical inclusions. (Kuster, 1972). This has been done to the first order in porosity by Yamakawa (1962) and Mal and Knopoff (1967) and to the second order by Chatterjee et al. (1978). The first order solution coincides with the static results.

The questions that remain to be answered are: (1) How do the pore shapes affect the effects of saturation? (2) Given the observed seismic velocities as a function of pressure and saturation conditions, can we determine the distribution of pore shapes, or the pore-aspect ratio spectrum, in a rock? If we can, how unique is our solution and how good is the resolution? (3) Given this pore-aspect ratio spectrum of a rock, can we predict the behavior of its velocities under different saturation conditions? We address these questions in this thesis.

Besides the above questions, the knowledge of the pore-aspect ratio spectrum of a rock has great implications in other areas of rock physics. First and foremost is in the calculation of the attenuation coefficient, or equivalently, Q. Walsh (1966) calculated the effects of friction due to cracks on Q. With the pore-aspect ratio spectrum and the crack closing rate, this can be generalized to cover

pressure dependence (Johnston et al., 1978). Other effects on attenuation such as fluid flow are also dependent on the aspect ratios and the fractional porosities of the cracks (Mavko and Nur, 1975, 1978; Johnston et al., 1978), so as other properties as electrical resistivity (Madden, 1976; Hashin and Shtrikman, 1962; Greenberg and Brace, 1969; Brace et al., 1965; Brace and Orange, 1968) and permeability (Brace, 1972, 1977; Brace et al., 1968, 1972; Zoback and Byerlee, 1975).

In Chapter 2 of this thesis, we begin by reviewing the existing works of modelling a fluid-filled rock as a two-phase medium. We then compare the different first order theories by applying each to data of both solid and liquid matrix materials with spherical inclusions. An extrapolation of the first order theories is then presented together with an iterative scheme for its solution.

In Chapter 3, the applications of the theories to laboratory measurements of seismic velocities in rocks are presented. We have chosen the theory of Kuster and Toksöz (1974a) for this purpose. Theoretical and observed behaviors of the velocities of rocks under full and partial saturation conditions are examined. The increases in the seismic velocities with pressure are modelled by the closing of small aspect ratio cracks. An extension of Walsh's (1965) work on the rate of closing of cracks is presented. Using this crack closing rate and an initial spectrum of different

aspect ratio cracks, the velocities of the dry and saturated rock are fitted by changing the initial spectrum via a trial and error approach. Theoretical behaviors of the velocities under different conditions of saturation and pressure are then calculated using these rock models.

The question of the uniqueness and resolution of these rock models is addressed in Chapter 4 by posing the problem as an inverse problem. Three techniques are examined: the linear least squares inversion, the linearized iterative inversion and the linear programming inversion. Comparisons are made between these techniques in terms of the fit to the velocity data. Different factors affecting the solution of the inverse problem are discussed and their effects on the solution investigated.

In Chapter 5, the pore-aspect ratio spectra of several rocks are obtained by inverting their velocity data using the linearized iterative inversion. These are compared with each other for possible correlations between the pore-aspect ratio spectrum of a rock with its bulk porosity and/or rock type. Finally, the pore-aspect ratio spectrum of Westerly granite obtained from the inversion of velocity data is compared with other estimates of its pore shapes by scanning electron microscope photographs (Sprunt and Brace, 1974; Hadley, 1976) and by Differential Strain Analysis (Feves and Simmons, 1976). The discussions and conclusions of this thesis are presented in Chapter 6.

CHAPTER 2

FIRST ORDER VELOCITY MODELLINGS OF A TWO-PHASE MEDIUM AND THEIR EXTENSIONS

A porous rock can in general be considered a two-phase medium. By a two-phase medium, we mean one that is composed of two different materials. It can be a solid imbedded in another solid, gas bubbles in liquids or solids suspended in fluids. The material that occupies the major portion of the volume is usually termed the matrix material, and the other material the inclusion material. In rare cases, we will call a material the inclusion if it has a regular geometrical shape (e.g. spherical or spheroidal) even if it has a bigger volume than the surrounding matrix material. In the case of typical rocks, the matrix is a solid and the inclusion is a fluid, usually water, air, brine, oil or natural gas.

The calculations of the velocities of seismic waves in a two-phase medium can be carried out by using either a dynamic or static approach. The dynamic problem is severely limited because of the fact that the vector wave equation is not separable in ellipsoidal coordinates (Morse and Feshbach, 1953; Kuster, 1972). As a result, the problem of scattering of elastic waves off an ellipsoidal inclusion cannot be solved exactly. Born approximations to the integral equation

of scattering result only in the static solution. Further discussions on this topic will be given in a later section of this chapter.

The static problem has been studied in a lot more detail than the dynamic problem. In 1951 Gassmann calculated the effective moduli of a material with a solid matrix and fluid inclusions given the effective moduli of the material with empty inclusions (called the frame or skeleton). There is no assumption about the shape of the inclusion except that it is connected. In 1957 Eshelby showed that under uniform applied strain, the strain in an ellipsoidal inclusion is also uniform. This result made it possible, in subsequent works by others (Walsh, 1965; Wu, 1966; Mal and Knopoff, 1967; Kuster and Toksöz, 1974a, Korringa, 1973; Budiansky and O'Connell, 1976), to calculate the effective properties of a material with ellipsoidal inclusions using different averaging schemes to achieve macrohomogeneity and isotropy.

In this chapter we review the major works on two-phase media, compare some of the existing works and introduce an extrapolation of the first order theories to get a better estimate of the effective moduli of a material with a relatively high concentration of inclusions.

2.1 Static Calculations of the Elastic Moduli:

2.1.1 Gassmann's Equation:

In 1951 Gassmann derived the formula for the bulk modulus of a rock with interconnected fluid-filled pores given the bulk modulus of the same rock with empty pores (frame modulus). This equation can be written in the form

$$K^* = K_A + \frac{K'(1 - K_A/K)^2}{c(1 - K'/K) + (1 - K_A/K)K'/K} \qquad (2\text{-}1)$$

where K^* is the effective bulk modulus, K_A the frame modulus, K the bulk modulus of the solid rock matrix material, K' the bulk modulus of the fluid and c, the porosity of the interconnected pores.

The explicit assumption in Gassmann's equation is microhomogeneity and microisotropy. The implicit assumption, which most authors ignored, is that the system under stress is dependent only on pressure. As a result, Gassmann stated, without proof, that the effective shear modulus of the system does not depend on the fluid inside. This is strictly true only in the case of spherical pores.

The disadvantage of Gassmann's equation is that there is no explicit dependence of the effective bulk modulus on pore shape. The dependence comes implicitly through the frame modulus. This is not a major problem when one tries to predict how the bulk modulus of a rock will vary under different saturation conditions if one knows the bulk modulus

of the dry rock. As a matter of fact Gassmann's equation is still widely used in the petroleum industry for interpretation of seismic reflection data. However, one has to be careful at low pressures because the shear modulus of a dry rock is usually lower than that of a liquid-saturated rock at low pressures and if one takes them to be equal the velocities one obtains will be erroneous. Furthermore, Gassmann's equation offers little insight into the physics of the situation and is not very useful in interpreting the pressure dependence of the elastic moduli and cannot be used to generate rock models for other purposes, e.g. attenuation calculations.

Brown and Korringa (1975) presented an extension of Gassmann's equation to a case where the solid matrix is not homogeneous and isotropic by introducing an extra parameter ($K_\phi = -[\partial V_\phi/\partial P_f]_{P_d}/V_\phi$ in their notation) which is defined as the fractional rate of change in pore volume with fluid pressure at a constant differential pressure. This extension is of relatively limited use because K_ϕ is not readily measurable to a high degree of accuracy and most anisotropy in rocks is introduced by preferred orientation of cracks instead of the anisotropy in the solid matrix (for a treatment of crack induced anisotropy see Appendix D).

2.1.2 Hashin and Shtrikman Bounds:

In an entirely different approach to the problem, Hashin

and Shtrikman (1963; also Hashin, 1962) calculated the upper and lower bounds on the effective moduli of a multiphase material using variational principles. They found the stationary value of an integral (U_p in their paper) which turned out to be the strain energy stored in the material. Their results are for a general n-phase material, each of its phases is homogeneous and isotropic, and the composite itself is homogeneous and isotropic. The bounds for a two-phase material are as follows:

$$K_1 + \frac{c_2}{\frac{1}{K_2-K_1} + \frac{3c_1}{3K_1+4\mu_1}} \leq K^* \leq K_2 + \frac{c_1}{\frac{1}{K_1-K_2} + \frac{3c_2}{3K_2+4\mu_2}} \tag{2-2}$$

and

$$\mu_1 + \frac{c_2}{\frac{1}{\mu_2-\mu_1} + \frac{6(K_1+2\mu_1)c_1}{5\mu_1(3K_1+4\mu_1)}} \leq \mu^* \leq \mu_2 + \frac{c_1}{\frac{1}{\mu_1-\mu_2} + \frac{6(K_2+2\mu_2)c_2}{5\mu_2(3K_2+4\mu_2)}} \tag{2-3}$$

where $K_2 > K_1$ and $\mu_2 > \mu_1$, c_i is the volume fraction of the i^{th} material. The upper bound for K^* is exact in the case of a spherical inclusion of material 1 imbedded in a concentric spherical shell of material 2. The significance of this result will be discussed later in this chapter.

Hashin and Shtrikman bounds are most useful for estimating the moduli of a rock matrix from its components. It is very unfortunate that Hashin and Shtrikman bounds are often confused with Reuss-Voigt-Hill (Hill, 1952) averaging. The latter applies only to aggregates of the SAME material and hence is very limited in its usefulness.

2.1.3 The Formulation of Eshelby:

The most significant result in the static study of the two-phase medium was derived by Eshelby (1957). He found that under uniform strain at infinity, the strain inside an ellipsoidal inclusion (or what he called inhomogeneity) is also uniform. This enables the use of ellipsoidal shapes to characterize the pore spaces of a rock and allows us to model a much wider collection of physical phenomena associated with porous rocks.

By a series of imaginary and imaginative cuttings and deformations, Eshelby succeeded in relating the strain field e^C_{ij} due to an ellipsoidal inclusion to the "stress-free" strain e^T_{ij} in the inclusion by a fourth order tensor S that is independent of position, i.e.,

$$e^C_{ij} = S_{ijkl} e^T_{kl} \tag{2-4}$$

The S_{ijkl}'s are given in Appendix A. Under an applied strain e^A_{ij} at infinity, the stresses inside and outside the inclusion are related by

$$K'(e^C + e^A) = K(e^C + e^A - e^T)$$

and

$$\mu'('e^C_{ij} + 'e^A_{ij}) = \mu('e^C_{ij} + 'e^A_{ij} - 'e^T_{ij}) \qquad (2\text{-}5)$$

where e^C, e^A, e^T are the dilatational parts of the respective strain tensors and $'e^C_{ij}$, $'e^A_{ij}$, $'e^T_{ij}$ are the deviatoric parts. The strain inside the inclusion is given by

$$e_{ij} = e^C_{ij} + e^A_{ij} \qquad (2\text{-}6)$$

Substituting equation (2-4) into (2-5) we can write the strain inside the inclusion in terms of the applied strain as

$$e_{ij} = T_{ijkl}e^A_{kl} \qquad (2\text{-}7)$$

As Eshelby pointed out, since the tensor S_{ijkl} does not couple different shears or dilatations to shear, the solution for the shear components is immediately given by

$$e_{13} = \frac{\mu e^A_{13}}{2(\mu'-\mu)S_{1313} + \mu} \qquad (2\text{-}8)$$

(and similarly for the other shear components). For the dilatation components, we have the following equations

$$(\lambda'-\lambda)S_{mmpq}e^T_{pq} + 2(\mu'-\mu)S_{ijpq}e^T_{pq} + \lambda e^T + 2\mu e^T_{ij}$$

$$= (\lambda-\lambda')e^A + 2(\mu-\mu')e^A_{ij}$$

$$ij = 11,\ 22,\ 33;\ pq = 11,\ 22,\ 33. \qquad (2\text{-}9)$$

The solution of this equation, together with the fact that from eq. (2-5) and (2-6)

$$e = \frac{K}{K - K'}e^T; \quad 'e_{ij} = \frac{\mu}{\mu - \mu'}'e^T_{ij} \tag{2-10}$$

will give us the dilatational components of the tensor T_{ijkl}. If the effective two-pahse material is to be macrohomogeneous and isotropic, Kröner (1958) had shown that the tensor T_{ijkl} reduces to two scalars: T_{iijj} associated with the bulk modulus and $T_{ijij} - \frac{1}{3}T_{iijj}$ associated with the shear modulus. The forms of these are given in Appendix A.

Knowing the strain field in the inclusion, the effective elastic moduli can be obtained by considering the change in the elastic energy of a homogeneous material under traction when an inclusion of different elastic moduli is introduced. This change in energy, also known as the interaction energy, is given by

$$E_{int} = -\frac{1}{2}\int[(K-K')e^A e + 2(\mu-\mu')'e^A_{ij}{}'e_{ij}]dv \tag{2-11}$$

which, in the case of ellipsoids, becomes

$$E_{int} = -\frac{1}{2}V[(K-K')e^A(e^A+e^C) + 2(\mu-\mu')'e^A_{ij}('e^A_{ij}+'e^C_{ij})]$$

$$= -\frac{1}{2}V[Ke^A e^T + 2\mu'e^A_{ij}{}'e^T_{ij}]$$

$$= -\frac{1}{2}Vp^A_{ij}e^T_{ij} \tag{2-12}$$

where p^A_{ij} is the applied stress and V is the volume of the inclusion. If we hold the applied stress constant, then the final energy of the system is given by

$$E^* = E_o - E_{int} \tag{2-13}$$

or

$$\frac{1}{2}s^*_{ijkl}p^A_{ij}p^A_{kl}V_o = \frac{1}{2}s_{ijkl}p^A_{ij}p^A_{kl}V_o - E_{int} \tag{2-14}$$

where s^*_{ijkl} is the compliance tensor of the effective system (matrix + inclusion) and V_o is the total volume of the system. This is equivalent to the Reuss averaging in the case of aggregates.

If, however, we wish to hold the strain constant, then the change in energy is $+E_{int}$, i.e.,

$$\frac{1}{2}C^*_{ijkl}e^A_{ij}e^A_{kl}V_o = \frac{1}{2}C_{ijkl}e^A_{ij}e^A_{kl}V_o + E_{int} \tag{2-15}$$

where C^*_{ijkl} is the stiffness tensor of the effective material. This case corresponds to the Voigt averaging in the case of aggregates.

The above analysis is only valid if the volume (size) of the ellipsoid is small compared to the matrix due to the fact that we have assumed the matrix to be infinitely large.

Since we also have the following relationship between the compliance and stiffness tensors:

$$C_{ijkl}s_{klmn} = \delta_{im}\delta_{jn} \tag{2-16}$$

and $|E_{int}|$ is assumed to be small relative to $|E_o|$, equations

(2-14) and (2-15) give identical results to the first order in the fractional volume of the inclusion. In later sections we will discuss different extrapolations from the first order theory to obtain better estimates of the effective moduli under different models and assumptions.

Equations (2-14) and (2-15) are valid for any two-phase material in general. For most rocks, we usually make the assumption of macrohomogeneity and isotropy. This reduces the effective stiffness tensor C^*_{ijkl} to only two independent components just as the T tensor (Kröner, 1958). As a result the tensor equation (2-14 or 2-15) reduces to two independent linear equations, one each for the effective bulk and shear moduli of the rock. For a rock which is anisotropic, the number of independent constants in the effective stiffness tensor increases to five for hexagonal symmetry and nine for orthorhombic symmetry (Love,1927). The case for hexagonal symmetry caused by an oblate spheroidal crack is discussed in Appendix D.

2.1.4 The Formulation of Walsh:

In a separate but related approach, Walsh (1965) derived the effective compressibility of a two-phase medium with empty pores in terms of the rate of change of its porosity with pressure using the reciprocal theorem (Chree, 1892), i.e.

$$\beta^* = \beta - \frac{dc}{dp}; \qquad \beta = \frac{1}{K} \tag{2-17}$$

In the case of a spherical cavity imbedded in a concentric spherical shell, dc/dp is easily calculated (see, e.g., Timoshenko and Goodier, 1951). The result is given by

$$\beta^* = \beta[1 + \frac{3(1 - \sigma)}{2(1 - 2\sigma)} \cdot \frac{c}{1 - c}] \tag{2-18}$$

This is identical to the Hashin-Shtrikman upper bound (eq. 2-2) if we take $K_2 = K$, $K_1 = 0$, $c_1 = c$ and $c_2 = 1 - c$. The same result was obtained by MacKenzie (1950), while the result given in Eshelby (1957) is only good for small c, i.e., when $1 - c \simeq 1$.

In the other limit, i.e., in the case of zero thickness cracks, Walsh did not calculate dc/dp using Eshelby's results. Instead, he rewrote dc/dp as $pdv_c/V_o pdp$. The numerator is just the increase in strain energy dw_c due to the crack and the expression for it is well known in a number of special cases. Walsh gave the expressions for three cases: the "penny-shaped"(oblate spheroidal with zero thickness) crack, the elliptical crack in plane stress and in plane strain. For the sake of comparison, we give only the result for the penny-shaped crack. It is

$$dw_c = \beta[\frac{16(1 - \sigma^2)a^3}{9(1 - 2\sigma)}]pdp \tag{2-19}$$

where a is the half length of the crack. Substituting into (2-17), we get

$$\beta^* = \beta[1 + \frac{16(1 - \sigma^2)a^3}{9(1 - 2\sigma)V_o}] \tag{2-20}$$

Since the volume of a penny-shaped crack is given by $\frac{4}{3}\pi a^3\alpha$ where α is the aspect ratio (i.e. the ratio of thickness of the crack to its length), we can rewrite (2-20) as

$$\beta^* = \beta[1 + \frac{4c(1 - \sigma^2)}{3\pi\alpha(1 - 2\sigma)}] \qquad (2\text{-}21)$$

The later papers of Walsh concerning the Eshelby S tensor (Walsh, 1968, 1969) will be discussed in conjunction with Wu's (1966) formulation of self-consistent methods.

2.2 Dynamic Calculations of the Elastic Moduli:

2.2.1 Scattering of Elastic Waves by a Spherical Obstacle:

Yamakawa (1962) was one of the first to study the problem of scattering of a general elastic plane wave by a spherical obstacle. The technique involved is actually quite well-known in various branches of physics and applied mathematics. He rewrote the plane wave in terms of spherical Bessel functions, then he solved for the scalar and vector potentials in spherical coordinates. These are also done in terms of spherical Bessel functions. Making use of the radiation condition and the fact that there is no physical singularity at the center, he expressed the scattered and transmitted p- and s-waves in terms of different spherical Bessel functions. The Bessel coefficients of these waves were finally obtained by satisfying the boundary conditions (depending on the obstacle) at the interface between the obstacle and the matrix material.

For wavelengths much longer than the obstacle size, the far-field displacements can be found by retaining only the first few terms of the Bessel expansion (Yamakawa, 1962; Kuster, 1972). For an incident p-wave,

$$u = -\frac{iA}{p^2}(pa)^3 \cdot \frac{e^{i(pr-\omega t)}}{r}\left[Be_o - Be_1\cos\theta - \frac{Be_2}{4}(3\cos 2\theta + 1)\right] \quad (2\text{-}22)$$

$$v = -\frac{iA}{sp}(sa)^3 \cdot \frac{e^{i(sr-\omega t)}}{r}\left[Be_1\sin\theta + \frac{3s}{4p}Be_2\sin\theta\right] \quad (2\text{-}23)$$

where

$$Be_o = \frac{K - K'}{3K' + 4\mu}$$

$$Be_1 = \frac{\rho - \rho'}{3\rho}$$

$$Be_2 = \frac{20}{3}\,\frac{\mu(\mu' - \mu)}{6\mu'(K + 2\mu) + \mu(9K + 8\mu)} \quad (2\text{-}24)$$

p and s are the wave numbers of p- and s-waves respectively, a is the radius of the spherical obstacle, K', μ', ρ' its bulk modulus, shear modulus and density, A is the amplitude of the incoming wave, r and θ are the spherical coordinates and u and v are displacements in the r and θ directions respectively.

In the next section we will discuss different ways to obtain the effective elastic moduli of a two-phase medium with spherical inclusions given the displacements of the scattered waves.

2.2.2 The Model of Mal and Knopoff:

Mal and Knopoff (1967) used an integral equation approach to obtain the scattered field of an inclusion of arbitrary shape. They obtained an expression of the following form:

$$u_k(\underline{x}) = u_k^o(\underline{x}) + \int_{R_1} [\Delta\rho\omega^2 v_i(\underline{\xi}) G_{ki}(\underline{x},\underline{\xi}) - \Delta C_{ijpq} \frac{\partial v_p}{\partial \xi_q} \cdot \frac{\partial G_{ki}}{\partial \xi_j}] d\underline{\xi} \qquad (2\text{-}25)$$

where $u_k(\underline{x})$ is the k^{th} component of the scattered displacement field at the point $\underline{x}$ outside the scatterer due to the incident field $u_k^o(\underline{x})$, $v_i(\underline{\xi})$ is the i^{th} component of the displacement field at a point inside the scatterer, $G_{ki}(\underline{x},\underline{\xi})$ is the i^{th} component of the Green's function at $\underline{x}$ due to a point force acting in the k^{th} direction at a point $\underline{\xi}$ in the infinite matrix, $\Delta\rho$ is the density contrast between the scatterer and matrix, ΔC_{ijpq} is the contrast in the stiffness tensor between the scatterer and the matrix, R_1 is the region occupied by the scatterer and ω is the frequency of the wave.

Equation (2-25) is an exact integral equation. Mal and Knopoff obtained an approximate solution to (2-25) in the case of spherical inclusions by taking the Born approximation, i.e., assuming that the displacement field inside the scatterer is the same as the incident field. They also assumed the strain inside the scatterer to be uniform which is valid only in the long wavelength limit. Assuming an

uniform strain field at infinity, Mal and Knopoff obtained the strain field inside the spherical inclusion that is identical to the static result obtained by Eshelby (1957). Mal and Knopoff also used the Eshelby interaction energy formulation to obatin the effective moduli of the two-phase medium from the strains.

2.2.3 The Model of Kuster and Toksöz:

Kuster and Toksöz (1974a) combined the results of Yamakawa, Mal and Knopoff and the static results of Walsh (1965, 1969) and Eshelby (1957) to obtain the effective elastic moduli of a two-phase medium with ellipsoidal inclusions. They used a method first proposed by Ament (1953, 1959), the essense of which is as follows: the scattered displacement field at infinity from aggregate of inclusions imbedded in a matrix is the same as that from an equivalent sphere of effective material imbedded in the same matrix. A similar statement can be made using a static argument. The above statement can also be put into the following form:

$$\underline{u}^{*}(\underline{x},\underline{x}_o) = \sum_{s=1}^{N} \underline{u}^{s}(\underline{x},\underline{x}_o+\Delta\underline{x}_s) \qquad (2\text{-}26)$$

where $\underline{u}^{*}$ is the scattered field at $\underline{x}$ of the equivalent sphere centered at $\underline{x}_o$, $\underline{u}^{s}$ is the scattered field at $\underline{x}$ of the s^{th} inclusion with radius a_s centered at $\underline{x}_o+\Delta\underline{x}_s$ and N is the number of inclusions.

In the case of spherical inclusions, Kuster and Toksöz made use of the results of Yamakawa (eq. 2-22). Let the radius of the equivalent sphere be a_o and much smaller than the wavelength of the incoming wave. Substituting (2-22) into (2-26) and equating terms of similar angular dependence they obtained the following three equations

$$\frac{K^* - K}{3K^* + 4\mu} = c\frac{K' - K}{3K' + 4\mu} \tag{2-27}$$

$$\rho^* - \rho = c(\rho' - \rho) \tag{2-28}$$

$$\frac{\mu^* - \mu}{6\mu^*(K+2\mu) + \mu(9K+8\mu)} = \frac{c(\mu' - \mu)}{6\mu'(K+2\mu) + \mu(9K+8\mu)} \tag{2-29}$$

where $$c = \sum_{s=1}^{N} \left(\frac{a_s}{a_o}\right)^3$$

is the total fractional volume of the inclusions. One significant result is that (2-27) is identical to (2-2) and (2-18), i.e., the results of the Hashin-Shtrikman upper bound and that of Walsh (1965).

For spheroidal inclusions, since they did not know the scattered displacement fields, Kuster and Toksöz took another approach. They used the integral equation form of the displacement field as presented by Mal and Knopoff (1967). Since the result obtained by Mal and Knopoff for spherical inclusions using the Born approximation to solve the integral equation is identical to the static solution (see previous section), Kuster and Toksöz used the Eshelby static results

in their equation for spheroidal inclusions also. Substituting equation (2-7) into (2-25) and equating it with that scattered from an equivalent sphere (eq. 2-26), Kuster and Toksöz (1974a) obtained the following equations for the effective bulk and shear moduli of a two-phase medium with spheroidal inclusions:

$$\frac{K^* - K}{3K^* + 4\mu} = c\frac{K' - K}{3K' + 4\mu}\cdot\frac{1}{3}T_{iijj} \tag{2-30}$$

$$\frac{\mu^* - \mu}{6\mu^*(K+2\mu) + \mu(9K+8\mu)} = \frac{c(\mu' - \mu)}{25\mu(3K+4\mu)}[T_{ijij} - \frac{1}{3}T_{iijj}] \tag{2-31}$$

Since the left-hand side of eq. (2-26) is the sum of the scattered fields from N different scatterers, there is no requirement that all N of them has to be of the same shape. The only requirement is that the distribution and orientation of ellipsoids of different shapes (aspect ratios) be such that the equivalent sphere is macrohomogeneous and isotropic. Hence if we have M different oblate spheroids each of aspect ratio α_m and fractional volume $c(\alpha_m)$, then (2-30) and (2-31) can be rewritten in the following forms:

$$\frac{K^*-K}{3K^*+4\mu} = \frac{K'-K}{3(3K+4\mu)}\sum_{m=1}^{M} c(\alpha_m)T_{iijj}(\alpha_m) \tag{2-32}$$

$$\frac{\mu^*-\mu}{6\mu^*(K+2\mu)+\mu(9K+8\mu)} = \frac{\mu'-\mu}{25\mu(3K+4\mu)}\sum_{m=1}^{M} c(\alpha_m)[T_{ijij}(\alpha_m) - \frac{1}{3}T_{iijj}(\alpha_m)] \tag{2-33}$$

2.3 "Self-Consistent" Averaging Schemes:

2.3.1 The Formulation of Wu:

The idea behind the so-called "self-consistent" approximation methods has been used in physics and material science for many years (Kröner, 1958; Budiansky, 1965). The idea is that each individual inclusion is not subject to the strain field due to the matrix material but rather that due to the effective material. Wu (1966) applied this concept to Eshelby's interaction energy approach. In calculating the interaction energy, the inclusion is assumed to be imbedded in the effective material, hence in eq. (2-12)

$$E_{int} = -\frac{1}{2}V[(K-K')e^{A}e + 2(\mu-\mu')'e^{A}_{ij}{}'e_{ij}]$$

Wu has taken the strain field to be

$$e^{A} = \frac{p^{A}}{3K^{*}}$$

and $$e_{ij} = T_{ijkl}(K^{*}, \mu^{*}, K', \mu')e^{A}_{kl}.$$

Strictly speaking, in the factors (K-K') and (μ-μ'), K and μ should be taken as K^{*} and μ^{*} also. After the above substitutions, Wu obtained the following implicit equations for the effective bulk and shear moduli of a two-phase material:

$$K^{*} = K[1 + \frac{c}{3}T_{iijj}(\frac{K-K'}{K^{*}})]^{-1}$$

$$\mu^{*} = \mu[1 + \frac{c}{5}(Tijij - \frac{1}{3}T_{iijj})(\frac{\mu-\mu'}{\mu^{*}})]^{-1}$$

Both T_{iijj} and T_{ijij} are now functions of K^* and μ^*. Since these equations are valid only for small c, they can be rewritten into the more familiar form:

$$K^* - K = \frac{cK(K' - K)}{3K^*}T_{iijj} \tag{2-34}$$

$$\mu^* - \mu = \frac{c\mu(\mu' - \mu)}{5\mu^*}[T_{ijij} - \frac{1}{3}T_{iijj}] \tag{2-35}$$

Wu is also credited with obtaining the explicit algebraic forms for the two scalars T_{iijj} and $T_{ijij} - \frac{1}{3}T_{iijj}$.

On a similar note, Walsh (1969) later simplified the scalars T_{ijij} and T_{iijj} in the case of α, the aspect ratio of an oblate spheroidal inclusion, going to zero, keeping only terms up to the first order in α. Both the results of Wu (1966) and of Walsh (1969) are given in Appendix A.

2.3.2 The Model of Budiansky and O'Connell:

In a development that is actually reverting back to the earlier days of research on two-phase media (e.g. Walsh, 1965), Budiansky and O'Connell (1976) calculated the effective moduli of a two-phase material with elliptical cracks (with vanishingly small crack widths and elliptical crack surfaces) using arguments of energy due to crack growth and a self-consistent strain field. The cracks are considered either empty or fluid-filled. The results they obtained are, for dry cracks:

$$\frac{K^*}{K} = 1 - \frac{16}{9}\left(\frac{1 - \sigma^{*2}}{1 - 2\sigma^*}\right)\varepsilon \tag{2-36}$$

$$\frac{\mu^*}{\mu} = 1 - \frac{32}{45}\cdot\frac{(1 - \sigma^*)(5 - \sigma^*)}{(2 - \sigma^*)}\varepsilon \qquad (2\text{-}37)$$

where σ^* is the effective Poisson's ratio of the material and ε is the crack parameter given by:

$$\varepsilon = \frac{2N}{\pi}\left\langle \frac{A^2}{P}\right\rangle . \qquad (2\text{-}38)$$

N is the total number of cracks, A is the crack surface area and P is the perimeter of the crack. $\langle\ \rangle$ is the average over all cracks. In the case of circular cracks, ε reduces to simply $N\langle a^3\rangle$, where a is the radius of the crack. For fluid-filled cracks:

$$\frac{K^*}{K} = 1 - \frac{16(1 - \sigma^{*2})}{9(1 - 2\sigma^*)}D\varepsilon \qquad (2\text{-}39)$$

and

$$\frac{\mu^*}{\mu} = 1 - \frac{32}{45}(1 - \sigma^*)\left[D + \frac{3}{(2 - \sigma^*)}\right]\varepsilon \qquad (2\text{-}40)$$

where

$$D = \left[1 + \frac{4(1 - \sigma^{*2})K}{3\pi(1 - 2\sigma^*)K^*}\omega\right]^{-1} \qquad (2\text{-}41)$$

and

$$\omega = \frac{K'}{\alpha K}$$

The above equations are valid only for very small α's.

2.4 Comparisons of the Formulations:

Before we begin to discuss the extrapolations from the first order theories, it is important for us to fully understand the limitations of each formulation presented in the previous sections. It is also necessary to know what each

one models or attempts to model. In particular, we shall focus our attention on the differences between the so-called "non-interaction" theory of Kuster and Toksöz and the "self-consistent interaction" formulations of Wu and of Budiansky and O'Connell. The earlier theories (Walsh, Hashin-Shtrikman bounds) will be introduced for specific comparisons only.

Let it be said once and for all that to the first order of concentration (porosity) all the formulations dealing with ellipsoidal inclusions give identical results. What is different between the theories is the range of application since the formulations of Wu, Kuster and Toksöz and Budiansky and O'Connell all have terms other than the first order term. Only Walsh's results are strictly first order. By range of application we mean the concentration of inclusion to which we can calculate the effective moduli using a particular formulation before the calculated results differ from the actual value by a specific amount.

For ellipsoidal inclusions, the comparison of ranges of application for different theories is not easily done because of the lack of artificial data, all the parameters of which we can readily control. This type of artificial data exists for spherical inclusions though. Kuster and Toksöz (1974b) measured velocities of spheres suspended in liquids, while Walsh et al. (1965) measured the elastic moduli of glass with spherical pores. We shall base our comparisons on these two sets of data. Since the "self-

consistent interaction" formulation of Budiansky and O'Connell is for thin cracks only, we shall use the "self-consistent interaction" formulation of Wu in the comparison with the results of Kuster and Toksöz and of Walsh et al.

In Wu's formulation, the effective bulk modulus of spheres suspended in a fluid is given by

$$K^* - K = c\frac{K^*}{K'}(K' - K^*) \tag{2-43}$$

where now K' is the bulk modulus of the solid spherical inclusions and K is the bulk modulus of the fluid matrix. Eq. (2-43) can be simplified to give

$$\frac{K^*}{K} = \frac{c - 1 + \sqrt{(1-c)^2 + 4cK/K'}}{2c} \tag{2-44}$$

The negative root of the quadratic equation gives a non-physical result. The formulation of Kuster and Toksöz gives, after simplification,

$$\frac{K^*}{K'} = \frac{K/K'}{1 - c(1 - K/K')} \tag{2-45}$$

The term to the first order in c, as given by Walsh (1969) and Mal and Knopoff (1967), is

$$\frac{K^*}{K'} = \frac{K}{K'}[1 + c(1 - \frac{K}{K'})] \tag{2-46}$$

It should be noted at this point that the results for spherical inclusions derived from the general results of Wu (1966) and Walsh (1969) are not the same as those derived by Walsh (1965) earlier using a different approach (see also

section 2.1.4). For the sake of continuity we shall use the results of the later paper of Walsh here.

Figures (2-1) and (2-2) show the comparison of the different theories to data obtained by Kuster and Toksöz (1974b). In order to have a better comparison between theory and data, we have included the inertial density term, as discussed by Kuster and Toksöz (1974a), for all the models under comparison. This inertial density term is given by:

$$\frac{\rho - \rho^*}{\rho + 2\rho^*} = c\frac{\rho - \rho'}{\rho + 2\rho'} \qquad (2\text{-}47)$$

Figure (2-1) shows a plot of normalized velocity versus concentration for polystyrene particles suspended in water. The points are observed data and the solid lines are different theories: line 1 is for the model of Kuster and Toksöz, line 2 is for the model of Wu and line 3 is for the model of Walsh.

As can be seen from the figure, the results show that Kuster and Toksöz's model fits the data best, with Walsh's model next and the self-consistent model worst. The Kuster and Toksöz model also give slightly "stiffer" results than the data while the other two models give reuslts that are "softer" than the data. This phenomenon is well understood since in the case of spheres, Kuster and Toksöz's result reduces to the Hashin-Shtrikman upper bound. As discussed by Hashin (1962) and MacKenzie (1950), this represents, in the case of spherical inclusions, a very special model of concentric spheres of moduli K, μ and K', μ', with respective

volumes corresponding to their fractional concentrations. Such a configuration can be replaced by the equivalent material with moduli K* and μ* without affecting the boundary conditions, and hence the process can be repeated throughout the rock. As pointed out by Madden (personal communication), the point to remember is that this represnts a definite possible model as opposed to some approximations. On the other hand, the "self-consistent" method assumes that the cracks see a surrounding material that is the effective medium. Hence it is implicit in this assumption that the introduction of the new crack has minimal effect on the final result. This is obviously only true for very small concentrations of cracks. For any appreciable finite amounts of cracks, this formulation is obviously an overestimate of the effect of cracks and will give a "softer" result. This same point was discussed in more detail by Bruner (1976) in a comment about Budiansky and O'Connell's (1976) work. This point will also be discussed in the next section in association with extrapolations of first order theories.

Figure (2-2) shows a similar plot as figure (2-1) for glass spheres suspended in ATB (acetylene tetra-bromide-benzine). Here the result of the "self-consistent" model of Wu coincides with that of Kuster and Toksöz, while the result of Walsh is "softer". This surprising (in view of figure 2-1) result can be undersood from equations (2-44) and (2-45). Since the bulk modulus of the glass is about thirty

times more than that of the ATB, K/K' is very small and can be ignored in the denominator of (2-45). By the same argument, we can take the $(1-c)^2$ term in equation (2-44) outside the radical sign, and expand the square-root in a binomial expansion, since 4cK/K' is much smaller than $(1-c)^2$. Ignoring the higher terms in the binomial expansion, we end up with the same result as equation (2-45).

Physically what is happening is that the contrast in the bulk modulus is so high that we are just compressing the matrix (ATB) without much effect on the inclusion (glass), and the effective compressibility is just the compressibility of the soft component times its fractional volume. It is not true if the soft component is the inclusion for the obvious reason that the frame would then be able to sustain the stress without over-compressing the inclusion. The self-consistent model is at least correct in the case of a soft matrix even though it is way off in the case where the matrix and inclusion are of similar compressibility.

Next we will do our comparison based on data of a solid matrix with spherical pores. Walsh et al. (1965) measured the bulk modulus of glass with empty pores as a function of the porosity. They also plotted a theoretical curve from MacKenzie (1950) on the figure and found that the agreement between theory and data is very good, although the theory is a little "stiffer" at high porosities than the data. Their results are reproduced here in figure (2-3). This

result is due to two facts: firstly it is beacuse the result of MacKenzie is equivalent to the Hashin-Shtrikman upper bound and secondly there might have been minute cracks introduced into the glass matrix. As discussed previously, the model of Kuster and Toksöz reduces to the Hashin-Shtrikman upper bound in this case and hence it is also equal to the MacKenzie result. The "self-consistent" model, however, runs into problems. If we use the Wu formulation and assume a linear relationship between the effective Poisson's ratio and porosity (O'Connell and Budiansky, 1974), the theory predicts that the effective bulk modulus goes to zero at around c = 0.5, depending on the initial Poisson's ratio one assumes (line "OB" in figure 2-3; see also figure 2 of Wu, reproduced in this thesis as figure 2-5).

Hence it is obvious from the comparisons with data that the model of Kuster and Toksöz works better than the "self-consistent" method of Wu when applied to spherical cavities and solid spherical inclusions. We have no hard data to make a similar statement on spheroidal inclusions in general. But based on the understanding of the modelling processes of these two approaches as discussed above, we feel quite certain that the same results will hold in cases with spheroidal inclusions.

2.5 Extrapolation of First Order Theories:

2.5.1 Second Order Scattering Theory:

The most obvious and elegant way to extend the first order theories we have presented earlier in this chapter is to keep everything to second order in c, the porosity. This has been accomplished in a recent paper by Chatterjee et al. (1978) using the scattering approach. Since, as mentioned above, the vector wave equation is only separable in spherical coordinates, Chatterjee et al. obtained second order results for spheres and cylindrical fibers only. Their results are therefore not very useful in geophysical applications. Nevertheless, it provides some insight into the physics and mathematics of the problem. It also provides us with some unexpected results when compared with other first order theories in the case of spherical inclusions.

After keeping terms in displacement fields to the second order in concentration and taking into account of the effect of multiple scattering of the first order scattered displacement fields, Chatterjee et al. (1978) obtained, using the constant strain (Voigt) assumption, the following expressions for the effective moduli of a two-phase material with spherical inclusions:

$$\frac{K^*}{K} = 1 - \frac{3K+4\mu}{3K}P_o c + \frac{3K+4\mu}{3K}(3P_o - I_o)c^2 + O(c^3) \quad (2\text{-}48)$$

and

$$\frac{\mu^*}{\mu} = 1 - \frac{15(3K+4\mu)}{4\mu}P_2 c + \left[\frac{135(K+2\mu)(3K+4\mu)}{8\mu^2}P_2^2 - \frac{15(3K+4\mu)}{4\mu}P_2 I_1\right]c^2 + O(c^3) \tag{2-49}$$

where

$$P_o = \frac{3(K-K')+4(\mu-\mu')}{3(3K'+4\mu)} \tag{2-50}$$

$$P_2 = \frac{4\mu(\mu-\mu')}{3[(3K+4\mu)(3\mu+2\mu')-4\mu(\mu-\mu')]} \tag{2-51}$$

$$I_o = \frac{45}{8}P_o P_2 \tag{2-52}$$

$$I_1 = \frac{9}{8}P_2\left\{P_o + \frac{10}{7}P_2\left[\left(1+\frac{3}{4}\tau^2\right)^2+\frac{25}{4}\left(1-\tau^2\right)^2\right]\right\} \tag{2-53}$$

and

$$\tau^2 = \frac{3K+4\mu}{3\mu} \tag{2-54}$$

There are some questions about the validity of these equations since in one of the three cases evaluated numerically (the case of empty voids imbedded in a Poisson solid, i.e., $K' = \mu' = 0$, $\lambda = \mu$) the results are not consistent with the equations given above. Furthermore, for solid spheres suspended in a fluid matrix, Chatterjee's formulae reduce to

$$\frac{K^*}{K} = 1 - P_o c(1-3c) = 1 - \frac{3(K-K')-4\mu'}{9K'}c(1-3c) \tag{2-55}$$

The factor (1-3c) gives this expression some very unphysical results. It says that $K^* = K$ for $c = \frac{1}{3}$ regardless of the matrix and inclusion properties. The expression also has a maximun (since $K' > K$) at $c = \frac{1}{6}$. In contrast all of the first order theories are monotonically increasing with c (see figures 2-1 and 2-2). This error may be due to the basic mathematical problem of the series not converging uniformly. So it is not automatic that a second order theory will always give one a better answer. Care must be taken in the application of these second order theories to get the desired results.

2.5.2 Integral Equation Formulation:

For spheroidal inclusions, since the formal scattering problem cannot be solved, we have to take another approach. As pointed out by Bruner (1976, see also Gubernatis and Krumhansl, 1975) in his criticism of O'Connell and Budiansky's paper, since the "self-consistent" assumption is valid only for vanishingly small concentrations of cracks, we should let the crack "grow" from zero size to its final size, changing the interaction energy along the way. An alternate but equivalent viewpoint is that we should add in the cracks a little at a time, keeping the effects of the newly introduced cracks as small as possible (Cheng and Toksöz, 1976; Cleary, 1978). In all the theories discussed above, we only distinguish cracks by their aspect ratios and the total

total concentrations of each aspect ratio crack and not how many actual cracks there are. So in practice we could subdivide the cracks at each aspect ratio into an infinite number of cracks, each of infinitesimal concentration, and then introduce them one at a time into the rock matrix. Both this and Bruner's approach will give, for the effective moduli, integral equations with kernels that are the expressions given in the first order "self-consistent" models, i.e.

$$K^* - K = \frac{(K' - K)}{3}\int^{c(\alpha)} T_{iijj}\,dc(\alpha) \qquad (2\text{-}56)$$

and

$$\mu^* - \mu = \frac{(\mu' - \mu)}{5}\int^{c(\alpha)} (T_{ijij} - \tfrac{1}{3}T_{iijj})\,dc(\alpha) \qquad (2\text{-}57)$$

where now both T_{iijj} and T_{ijij} are functions of K^*, μ^*, K', μ' and α. In a mixture of aspect ratios, we can do the sum outside the integral. Similarly, for Kuster and Toksöz's formulation, we can write

$$\frac{K^*-K}{3K^*+4\mu} = \frac{K'-K}{3(3K+4\mu)}\int^{c(\alpha)} T_{iijj}\,dc(\alpha) \qquad (2\text{-}58)$$

and

$$\frac{\mu^*-\mu}{6\mu^*(K+2\mu)+\mu(9K+8\mu)} = \frac{\mu'-\mu}{25(3K+4\mu)}\int^{c(\alpha)} (T_{ijij} - \tfrac{1}{3}T_{iijj})\,dc(\alpha) \qquad (2\text{-}59)$$

The difference between equations (2-56) and (2-58) is, as pointed out by Kuster and Toksöz (1974a), a factor of $(3K^*+4\mu)/(3K+4\mu)$ on the right hand side. It is well justified to include that in the kernel, in which case K and μ will

become K^* and μ^*, and the factor becomes unity, giving us back equation (2-56). So these two formulations give us the same results, as they should physically, and as it will be shown later numerically.

2.5.3 Numerical Solution of the Integral Equation:

Equation (2-56) is a non-linear Volterra equation of the second kind. The standard method of solution is that by successive approximations (Tricomi, 1957; Gubernatis and Krumhansl, 1975), but in our case it presents a problem. In the first step of successive approximation, the equation is that of the first order theory. For large concentrations of empty or air-filled cracks, the solution does not necessarily converge and there is no guarantee of a correct answer. Furthermore, a detailed study of the convergence characteristic of the system is too complicated and beyond the scope of this thesis.

An alternate way of solving the integral equation is by numerical quadrature, the simplest of which is by means of step functions. This is usually used only for Fredholm equations where the integral is over a fixed limit. Since the kernels of our system (eq. 2-56, 2-57) are independent of the limit of integration explicitly and only dependent of the solution, for any given value of concentration we can treat the integration limit as fixed and use this method. By subdividing the interval of integration into N parts, we get,

$$K^*-K = \sum_{n=1}^{N} \frac{(K'-K_{n-1})}{3} \int_{c_{n-1}(\alpha)}^{c_n(\alpha)} T_{iijj}(K',\mu',K^*_{n-1},\mu^*_{n-1},\alpha)\,dc(\alpha) \tag{2-61}$$

where

$$c_n = \frac{nc}{N} \tag{2-62}$$

and K^*_n and μ^*_n are given by equations of the sort

$$K^*_n-K^*_{n-1} = \frac{(K'-K^*_{n-1})}{3} \int_{c_{n-1}(\alpha)}^{c_n(\alpha)} T_{iijj}(K',\mu',K^*_{n-1},\mu^*_{n-1},\alpha)\,dc(\alpha) \tag{2-63}$$

Similar expressions are obtained for μ^* and μ^*_{n-1} with $K^*_o = K$ and $\mu^*_o = \mu$. At each n, if we take N to be large enough, we can approximate the functions T_{iijj} and T_{ijij} as constants, and obtain:

$$K^*-K = \sum_{n=1}^{N} \frac{(K'-K^*_{n-1})}{3} T_{iijj}(K',\mu',K^*_{n-1},\mu^*_{n-1},\alpha)\,\Delta c_n(\alpha) \tag{2-64}$$

and

$$\mu^*-\mu = \sum_{n=1}^{N} \frac{(\mu'-\mu^*_{n-1})}{5} [T_{ijij} - \tfrac{1}{3}T_{iijj}]\,\Delta c_n(\alpha) \tag{2-65}$$

where

$$\Delta c_n(\alpha) = c_n(\alpha) - c_{n-1}(\alpha) \tag{2-66}$$

and

$$K^*_n-K^*_{n-1} = \frac{(K'-K^*_{n-1})}{3} T_{iijj}(K',\mu',K^*_{n-1},\mu^*_{n-1},\alpha)\,\Delta c_n(\alpha) \tag{2-67}$$

with a similar expression for μ^*_n.

In actual numerical applications, more bookkeeping is required. Physically, if we introduce c_1 number of cracks in a rock with matrix moduli K and μ and obtain effective moduli

K_1 and μ_1, and then introduce c_2 number of cracks into the effective rock, taking K_1 and μ_1 as matrix moduli the second time, we do not have a rock with matrix moduli K and μ and $c_1 + c_2$ cracks. This is because when we introduce the c_2 cracks randomly, a fraction, $c_1 \cdot c_2$, of these cracks will occupy the same space already occupied by the c_1 cracks previously introduced, leaving only $c_2(1 - c_1)$ new cracks. In order to compensate for this, we will have to introduce $c_2/(1 - c_1)$ cracks at the second step to achieve the effect of having a total of $c_1 + c_2$ cracks. Again, this is only a matter of bookkeeping.

To show that the above method does in fact converge, we have applied it to a theoretical Boise sandstone model (porosity 25%) at atmospheric pressure. The theoretical p- and s-wave velocities are plotted as a fucntion of N, the number of subdivisions of the interval of integration, for both the Walsh model and that of Kuster and Toksöz. This is shown in figure (2-4). It can be seen that both formulae converge to a common solution as N increases, as they should. The model of Kuster and Toksöz converges much faster and starts out much closer to the final solution than the model of Walsh. This can be explained by the extra factor of $(3K^*+4\mu)/(3K+4\mu)$ discussed earlier. The most important point is that, at least for the model of Kuster and Toksöz, this scheme converges rapidly enough. A value of N = 10 gives us results that are within one percent from the final solution.

2.6 The Effects of Other Spheroidal Shapes:

So far we have concentrated our discussion on the oblate spheroidal inclusions and modelling the cracks and pore spaces in a rock after them. Before we close out this chapter, we would like to examine the other extreme, the prolate spheroidal inclusions or "needle-shaped" cracks. These are tubular structures connecting different pores in a rock and can be modelled as prolate spheroids or "needle-shaped" cracks. In the above discussions of different theories, for those based on the Eshelby theory of ellipsoids, viz. the formulations of Walsh, Wu and Kuster and Toksöz, the results can be easily generalized from oblate to prolate spheroids. The equations given in these formulations do not change. The changes are in the evaluation of some of the terms in T_{iijj} and T_{ijij} given in Appendix A. Specifically, for prolate spheroids ($a \geq b = c$), ϕ and g are given by (Wu, 1966)

$$\phi = \frac{\alpha^2}{(1-\alpha^2)^{3/2}}\left[\frac{1}{\alpha}\left(\frac{1}{\alpha^2} - 1\right)^{1/2} - \cosh^{-1}\left(\frac{1}{\alpha}\right)\right] \qquad (2\text{-}68)$$

$$g = \frac{1}{1-\alpha^2}(2 - 3\phi) \qquad (2\text{-}69)$$

instead of the expressions given in Appendix A.

What is then the effect of empty "needle-shaped" cracks on the effective elastic moduli of a two-phased material compared to the effects of a "penny-shaped" crack and a spherical cavity? Wu calculated the effects of each as a

function of concentration and the relative magnitudes of the Young's moduli of the matrix and inclusions. His results are reproduced here in figures (2-5) and (2-6).

Figure (2-5) shows the effects of the contrast in the Young's moduli between the matrix and inclusions for different shapes. For the disc shape, the aspect ratio α is assumed to be zero, while for the needle shape, α is assumed to be infinity. The Poisson's ratio for the matrix is taken to be 0.2 . It is obvious from the figure that the effects of the needle-shaped crack and spherical cavity are very similar to each other, while the effects of the disc- or penny-shaped crack are much more pronounced. This effect is most dramatic for empty cracks, i.e., for $E_2 = 0$ (or $E_1/E_2 = \infty$).

Figure (2-6) shows the results plotted in another manner. Here the effects of the three crack shapes are plotted on the same graph. The ratio of Young's modulus of the matrix to that of the inclusion is 10, typical of liquid inclusions. Once again, the effective Young's modulus (E_o) of the rock decreases more rapidly as a function of concentration (c_2) for the disc-shaped crack than for the needle-shaped and spherical cracks, with little difference between the latter two.

It is clear from the above discussion that for fluid inclusions in a solid matrix, as in the case of liquid- or gas-saturated rocks, the effects of the tubular type pore spaces are essentially similar to those of spherical pore

spaces and we can include the former into the latter without loss of generality.

FIGURE CAPTIONS

Figure 2-1 : Normalized velocity versus concentration for polystyrene spheres suspended in water. The data (points) are obtained by Kuster and Toksöz (1974b). The solid lines represent different theoretical models: line 1 for the model of Kuster and Toksöz (1974a); line 2 for the "self-consistent" interaction model of Wu (1966) and line 3 for the non-interaction model of Walsh (1969).

Figure 2-2 : Same as figure (2-1) for glass spheres suspended in ATB. The data are from Kuster and Toksöz (1974b).

Figure 2-3 : Bulk modulus versus porosity for spherical cavities in glass. The data (points) are from Walsh et al. (1965). The line marked HS represents the Hashin-Shtrikman (1963) upper bound, which in this case corresponds to the results of MacKenzie (1950) and Kuster and Toksöz (1974a). The line OB represents the "self-consistent" approximations of O'Connell and Budiansky (1974) and Wu (1966).

Figure 2-4 : P- and S-wave velocities of a theoretical sandstone model (25% porosity) versus the number of iterations (integration steps in the numerical solution of the integral equation, sections 2.5.2 and 2.5.3). The lines marked KT represent the results of the extrapolation using the Kuster and Toksöz (1974a) formulation while the lines marked WALSH represent the results using

the Walsh model. The dotted lines represent the numerical limits (same for both models) as the number of iterations increases.

Figure 2-5: (from figure 2 of Wu, 1966) The effects of different ellipsoidal shapes on the effective Young's modulus (E_o) of a rock. The subscripts 0, 1 and 2 represent the effective material, the matrix and the inclusion respectively. It can be observed that the effects of the "needle-shaped" and spherical inclusions are very similar.

Figure 2-6: (from figure 4 of Wu, 1966) Effects of different ellipsoidal shapes on the effective Young's modulus of a solid material. $E_1/E_2 = 10$ is typical of liquid inclusions. ν is the Poissons's ratio (σ in our notation).

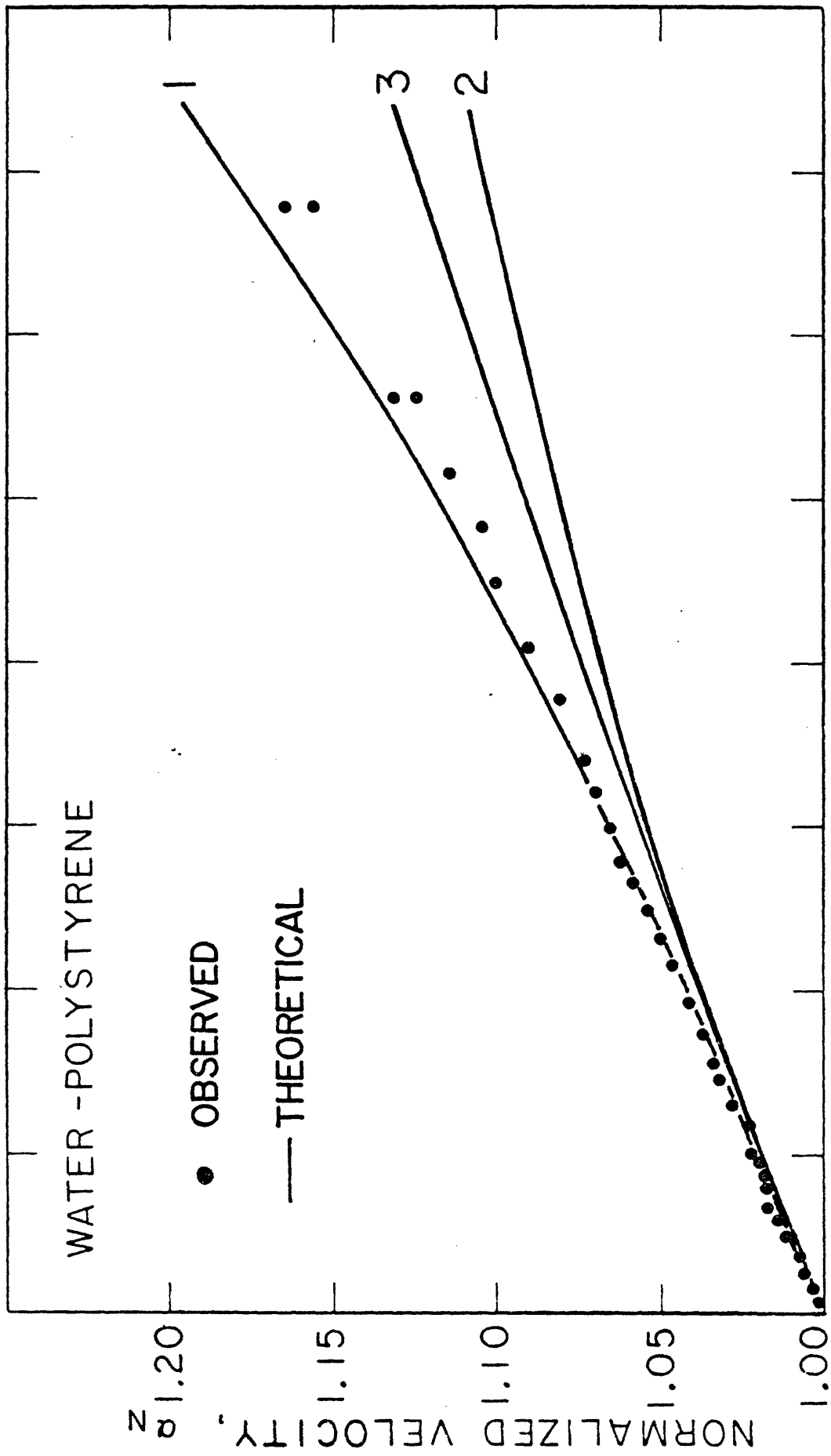
WATER - POLYSTYRENE
OBSERVED
THEORETICAL
1
2
3
NORMALIZED VELOCITY, α_N
1.00
1.05
1.10
1.15
1.20
10
20
30
40
50
60
70
CONCENTRATION (%)

Figure 2-1

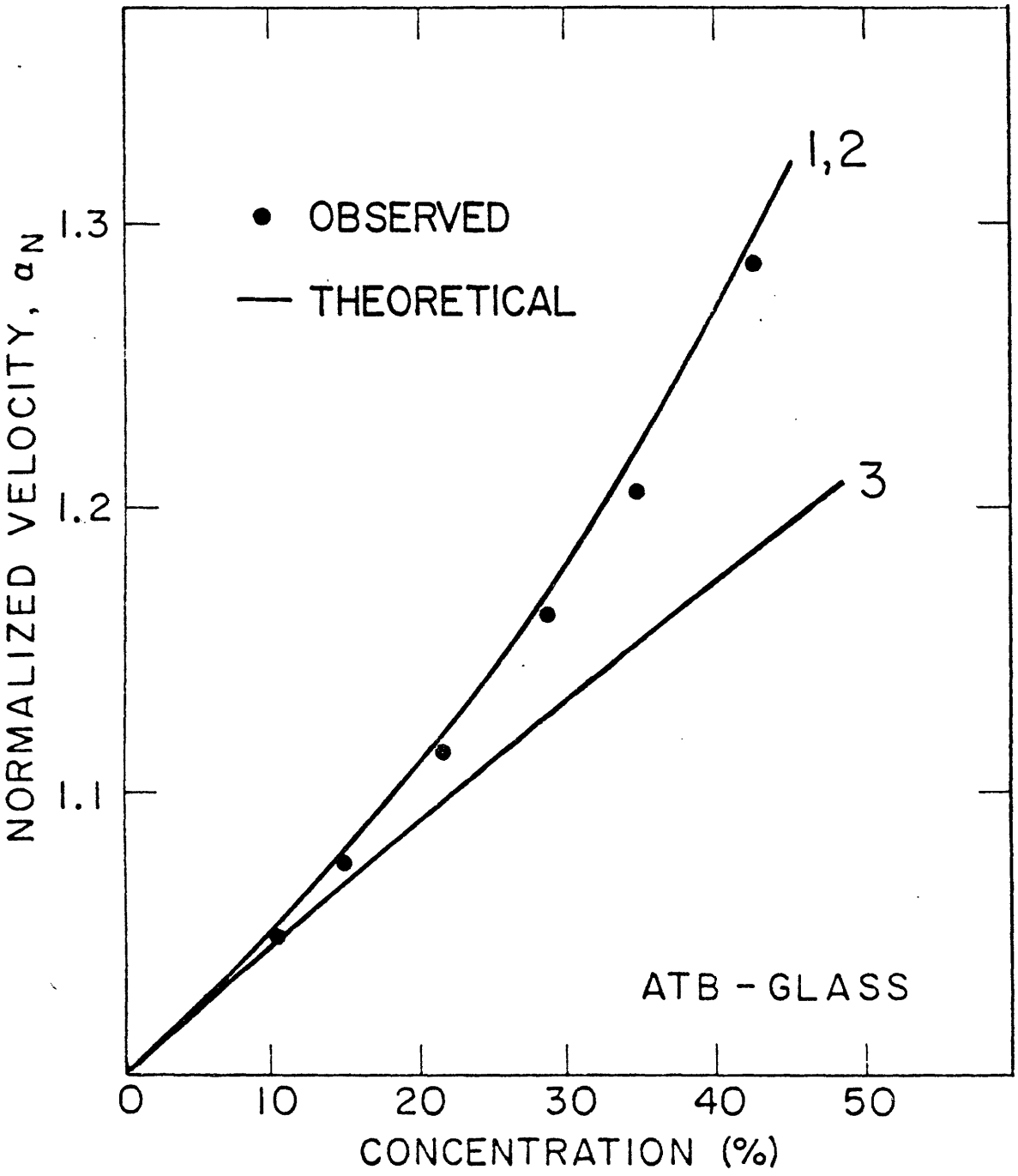
NORMALIZED VELOCITY, a_N
1.3
1.2
1.1
OBSERVED
THEORETICAL
1,2
3
ATB - GLASS
0
10
20
30
40
50
CONCENTRATION (%)

Figure 2-2

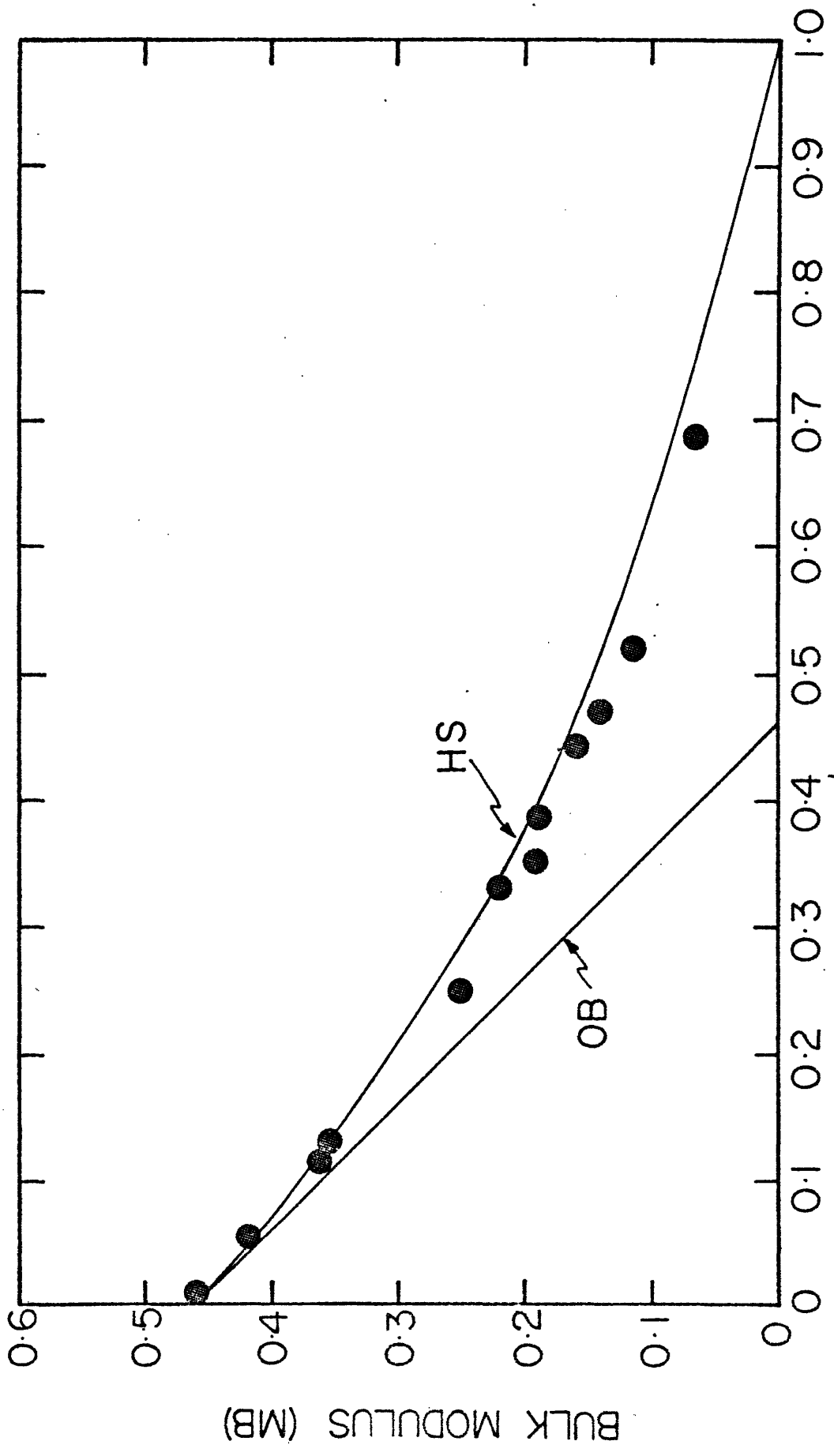
BULK MODULUS (MB)
0·6
0·5
0·4
0·3
0·2
0·1
0
0
0·1
0·2
0·3
0·4
0·5
0·6
0·7
0·8
0·9
1·0
φ POROSITY
HS
OB

Figure 2-3

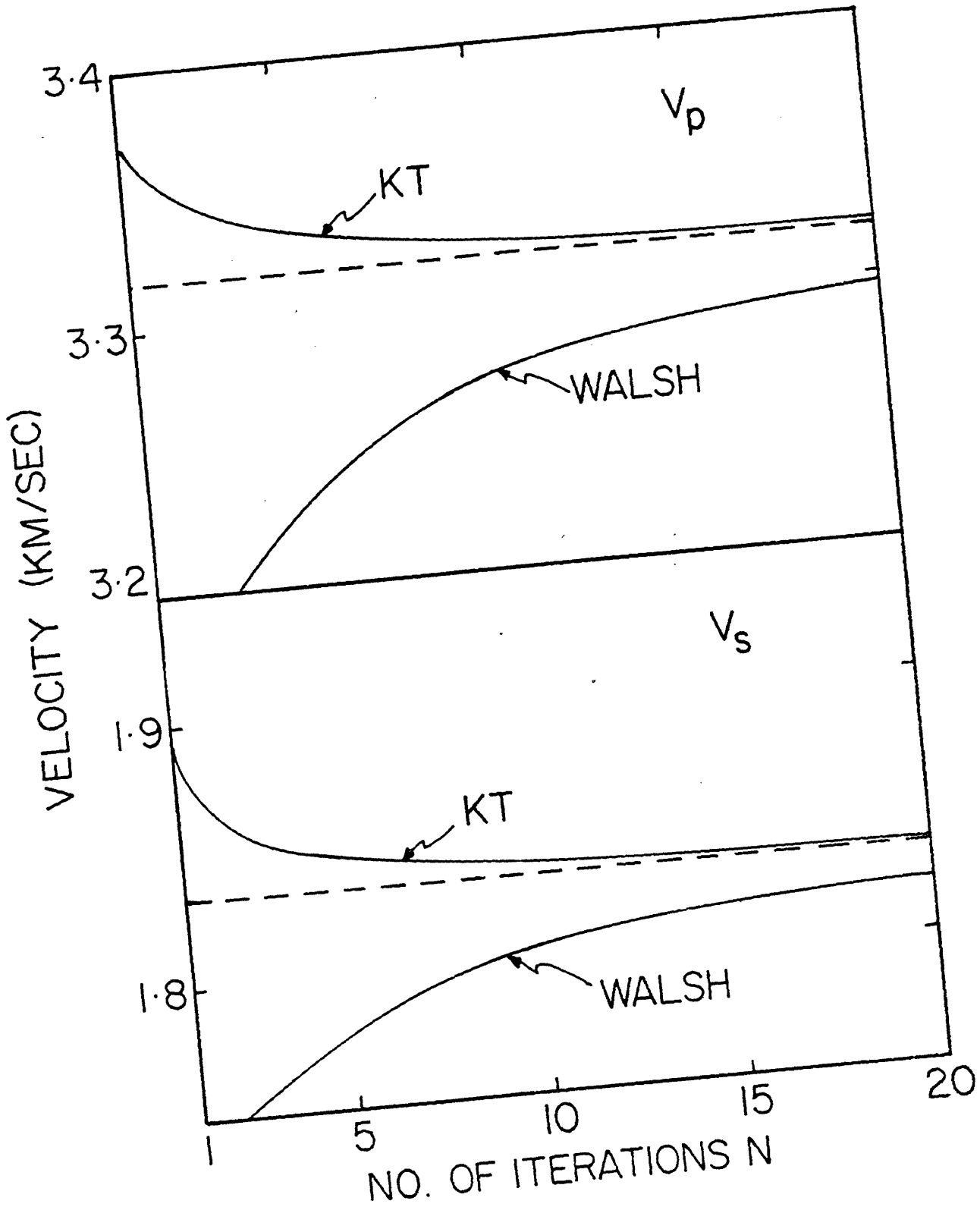
3·4
3·3
3·2
1·9
1·8
VELOCITY (KM/SEC)
V_p
KT
WALSH
V_s
KT
WALSH
1
5
10
15
20
NO. OF ITERATIONS N

Figure 2-4

MATRIX WITH SOFT INCLUSIONS

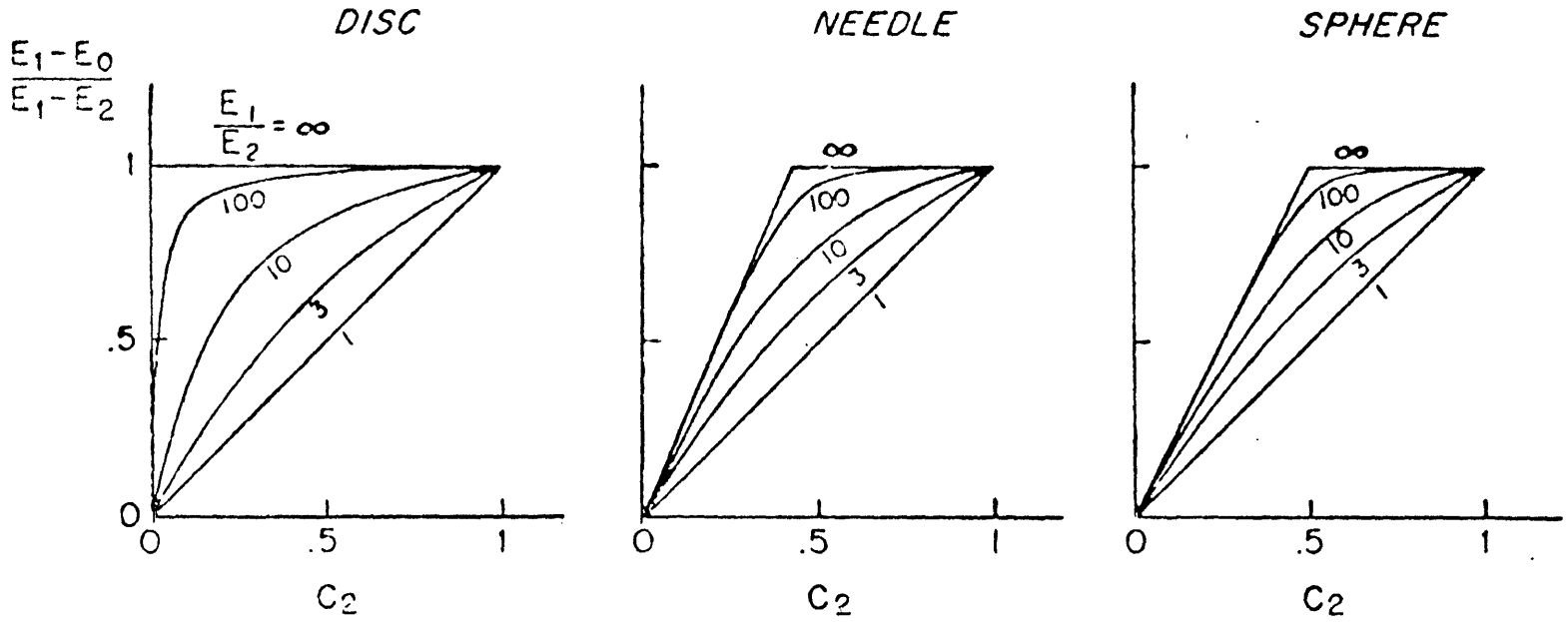

Figure 2-5

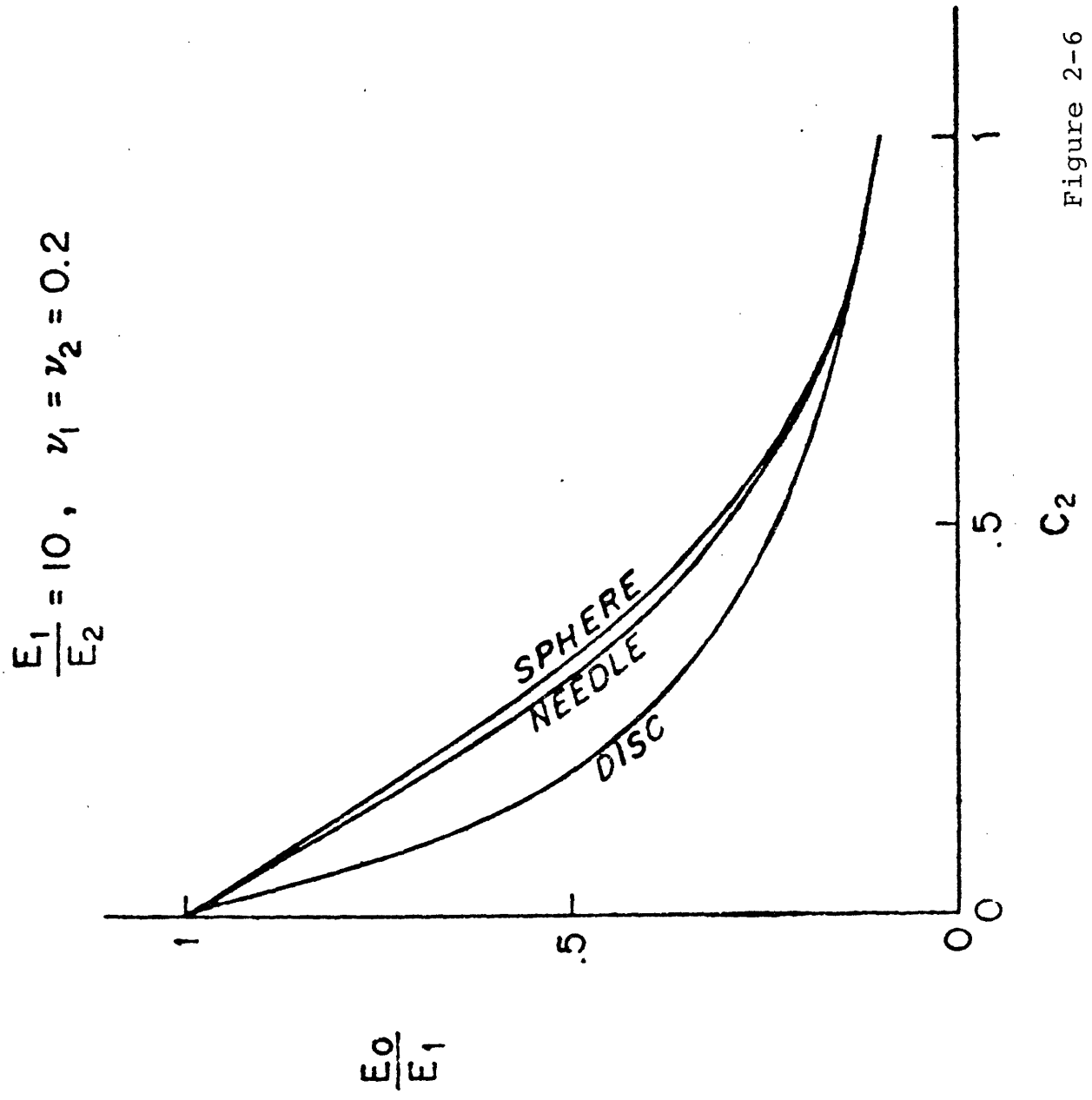
$\frac{E_1}{E_2} = 10$, $\nu_1 = \nu_2 = 0.2$
SPHERE
NEEDLE
DISC
1
.5
0
$\frac{E_0}{E_1}$
0
.5
1
C_2

Figure 2-6

CHAPTER 3

THE PREDICTION OF ROCK PROPERTIES UNDER DIFFERENT CONDITIONS

The ultimate goal of any theory is to be able to explain the observed data and to predict what would happen under different conditions. In the case of a rock system modelled as a two-phase medium, the data takes the form of laboratory measured compressional and shear wave velocities as a function of differential or confining pressure, saturation conditions and temperature. Laboratory measurements in fully or partially saturated rocks show a significant variation of the velocities with the nature of the saturating fluids (Gardner et al., 1974, King, 1966, Wyllie et al., 1956, 1958, Elliott and Wiley, 1975). Even igneous rocks with very low porosities (i.e., less than one percent) demonstrate markedly different behavior when dry and when water-saturated (Nur and Simmons, 1969). Since the relative pore volume and, hence, the fluid content is very small in igneous rocks, the pore shapes must also play an important role in controlling the elastic moduli and seismic velocities. In all cases, the compressional velocities are higher in water-saturated samples than in dry or gas-saturated samples. The shear velocity behavior is less regular and depends upon porosity and saturating fluids. Furthermore, in partially saturated rocks,

small amounts of air or gas mixed with water change compressional velocities significantly.

The questions that arise from these data are: (1) What are the relative effects of pore shapes and of gas-, water- or oil-saturation on velocities? (2) Given the seismic velocities could we determine the pore geometry and saturation state? (3) Given these rock models, what are the seismic velocities under in situ conditions, and how may the saturating fluids be determined from the seismic data?

In this chapter we will try to model the above mentioned behaviors using the theory of Kuster and Toksöz described in the above chapter. We will first examine the effect of saturation on oblate ellipsoidal cracks of different aspect ratios. We will next model the pore spaces and cracks as a collection of oblate spheroids of different aspect ratios. The increases in the seismic velocities can then be explained by the closing of the very fine aspect ratio cracks as the pressure increases. By adjusting the fractional concentrations of the different aspect ratio cracks, we can model the velocity behaviors of different rocks and obtain the pore-aspect ratio spectrum for each. Finally, using these aspect ratio spectra, we can then calculate theoretical seismic velocities under different conditions of saturation and pressure.

3.1 The Effects of Saturation:

One of the most important parameter affecting the seismic

velocities of a rock is the saturating fluid. Since this effect is equally prominent in both high porosity sedimentary rocks and low porosity igneous rocks, it is obvious that the pore shape is as important as porosity in determining how the velocities are affected by different saturation conditions. In general, the p-wave velocities are higher for the dry or gas-saturated rock. The s-wave velocities usually shows the opposite behavior, with exceptions for some rocks at low pressures. In this section we shall first examine the effects of different pore shapes and concentrations on the seismic velocities as a function of full (both liquid and gas) saturation and partial saturation. In the latter case, we shall examine the effects of both miscible and immiscible fluids, and the case of different fluids occupying different pore shapes. Finally, we shall examine some published velocity data of rocks under partial saturation of air and water and try to interpret them using the theory.

3.1.1 Full Saturation:

By full saturation it is meant that the pore spaces in a rock is saturated by one fluid, whether liquid or gas. Figure (3-1) shows the p- and s-wave velocities of a theoretical rock with a solid matrix containing pores of one aspect ratio at a given time, saturated with water or gas. The matrix parameters are K = 0.44 Mb, μ = 0.37 Mb and ρ = 2.7 gm/cc. Inclusion parameters are for water, K = 22 kb and

and ρ = 1 gm/cc; for gas, K = 1.5 bars and $\rho = 10^{-3}$ gm/cc. The velocities are plotted for four different aspect ratio cracks.

The following observations can be made from the figure: For a given concentration, the thinner aspect ratio cracks affect both the p- and s-wave velocities more than the spherical or near spherical pores. For the obvious reason that both liquid and gas do not sustain shear, the saturating fluid has more effect on the p-wave velocities than on the s-wave velocities. The percent depression in the velocities are also higher for p-wave than for s-wave for the same aspect ratio crack under the same saturation condition. One final observation on the theory of Kuster and Toksöz versus than of Gassmann is that the effective shear modulus for a gas-saturated rock is lower than that of a liquid-saturated rock, except for spherical inclusions. This will be looked for in data to resolve the difference between the theories.

3.1.2 Partial Saturation:

A rock may be saturated with a miscible or immiscible mixture of fluids, e.g. oil and gas, brine and gas, oil and brine and steam and water. Before seismic velocities of such rock systems can be calculated, we must know how the mixed fluids are distributed. There are three distinct cases: First, the two fluids are miscible or soluble, such as gas dissolved in oil. In this case the mixed fluid is

homogenous and can be treated as a single fluid with appropriate values for density and bulk modulus.

The second case involves one fluid spread in the other as immiscible inclusions. An example of this is gas bubbles in brine. We can calculate the bulk modulus of this composite using eq. (2-27), which in this case reduces to a simple weighted average of the compressibilities, i.e.,

$$\frac{1}{K^*} = \frac{C}{K'} + \frac{1-C}{K} \qquad (3\text{-}1)$$

Figure (3-2) shows a plot of the effective bulk modulus of a mixture of gas bubbles in brine at different pressures using equation (3-1). It is clear, from figure (3-2), that when a few percent of gas inclusions are introduced into the brine, the bulk modulus of the composite drops rapidly to a value close to that of the gas. The reason can be quite simply understood from equation (3-1). Since the compressibility of gas is about four orders of magnitudes more than that of brine, any amount of gas significantly different from zero will cause the right hand side of equation (3-1) to be dominated by the gas term. This fact is supported by experimental data (Domenico, 1976).

The third case involves each fluid occupying seperate pores. Examples of these are brine occupying the fine (low aspect ratio) pores and cracks while the gas is filling the larger pores, or vice versa. This case can be taken of easily

by the theory of Kuster and Toksöz by doing a seperate sum on the right hand side of equations (2-32) and (2-33) (Toksöz et al., 1976, eq. 8, 9 and 10). Numerical examples of this case will be given in conjunction with the examples on the effects of pressure on partially saturated rocks in the next section.

3.1.3 Laboratory Data on Partial Saturation:

Wyllie et al., (1956) made velocity measurements in sandstones as a function of water and air saturation. Fully water-saturated cores were drained slowly while air was let into the system. Their data for three sandstones with different porosities are shown in figure (3-3). With their procedure, it is most likely that fine cracks remain water-saturated to the very end. This may be especially true for the Cromwell sandstone with sixteen percent porosity and may explain the anomalous decrease in velocity as the water saturation decreases below five percent.

Theoretical models were fitted to the data using equations (2-32) and (2-33) and an air-water mixture. Pore aspect ratio spectra were modelled after those discussed in the next section. It was assumed that Cromwell sandstone has a pore spectrum similar to that of Berea. Others were modelled by multiplying the Boise sandstone spectrum by a factor equal to the ratio of total porosities. Very fine cracks ($\alpha < 10^{-4}$) were not included (essentially remained

water-saturated) in the invasion of air. Matrix moduli were chosen to satisfy velocities at 100 percent water saturation and are given in Table (3-1). The fit of the theoretical curves to the data is very good for all three sandstones, in spite of the fact that the spectra used are actually those of other sandstones. Note that in high porosity (ϕ = 30%) Britton sandstone velocities drop very rapidly when air saturation is only about five percent, while for Cromwell sandstone (ϕ = 16%) the drop in velocity is more gradual.

There are other experimental studies of rocks under partial saturation conditions (Domenico, 1976; Gregory, 1976; Elliott and Wiley, 1975). Figure (3-4) shows a plot of compressional and shear wave velocities as a function of partial saturation of Gulf Coast sand measured by Domenico (1976). By lowering the matrix moduli from those of pure sand to those which fit the full saturation data and by using pores of aspect ratio 1, 0.1 and 0.01, we were able to fit most of the observed data except at extremely low gas concentrations where the observed p-wave velocities stay high instead of dropping as predicted by the theory. Domenico suggested that this fact may be due to the imhomogeneous mixing of gas and brine within the pore spaces. Using our model's capability of separating different pores and pore shapes, we filled a fraction of the spherical (α = 1) pores purely with gas corresponding to the total gas concentration value and the rest of the pore spaces with brine and we were

able to fit these data points also.

3.2 Effects of Pressure:

It has been well established that the increase in the seismic velocities of a rock as a function of increasing pressure is due to the closing of small aspect ratio cracks (Walsh, 1965; Nur and Simmons, 1969; Toksöz et al., 1976). As the pressure increases, the cracks with the smallest aspect ratio will close first, those with larger aspect ratios will remain open, although decreasing in both volume and aspect ratio. In order to model this behavior, we have to calculate the theoretical rate of closing of the ellipsoidal cracks.

Besides the closing of small aspect ratio cracks, the pressure has two other effects on the velocities of a fluid-filled rock. The first is on the compressibility of the rock matrix. This effect does not dominate until all fine cracks are closed (Birch, 1966) and therefore of little interest to us. The second is the change in the compressibility of the fluid saturant with pressure. This is important when a pore fluid pressure exists in addition to the confining hydrostatic pressure. The change in compressibility can be signigicant especially in the case of gas-saturated rocks with high pore pressure. These fluid moduli can be calculated using the appropriate equation of state. For brine, the compressibility and density as a function of pressure and salinity can be obtained from Adams

(1931) and Long and Chierici (1961). For oils, they are classified according to weight by the American Petroleum Institute, and their moduli are given by Standing (1952). For natural gases, the equation of state is given by the Benedict-Webb-Rubin equation (Thomas et al., 1970), and their properties are given by Katz el al., (1959).

3.2.1 Rate of Closing of Ellipsoidal Cracks With Pressure:

Walsh (1965) did the pioneering work on the rate of closing of cracks with pressure. Using an equation obtained by Chree (1892) by means of the reciprocal theorem, Walsh obtained the following relationship between the rate of change of porosity with pressure and the bulk modulus of a rock (eq. 2-17):

$$\frac{dc}{dp} = \frac{1}{K} - \frac{1}{K^*}$$

Using an argument based upon the change in strain energy due to the crack, Walsh calculated the effective bulk modulus of a rock with a penny-shaped crack (eq. 2-21):

$$\frac{1}{K^*} = \frac{1}{K}\left(1 + \frac{4c}{3\pi\alpha}\frac{(1-\sigma^2)}{(1-2\sigma)}\right)$$

Substituting eq. (2-21) into (2-17) gives the desired relationship between the rate of change of the crack volume with pressure and the matrix moduli of the rock:

$$\frac{dc}{dp} = -\frac{4c}{3\pi\alpha K}\frac{(1-\sigma^2)}{(1-2\sigma)} \qquad (3\text{-}2)$$

Since this result is obtained by assuming a penny-shaped crack, it is only valid for a vanishing small aspect ratio. Walsh also dereived a similar expression for the other limit, that of spherical pores. This is obtained by substituting eq.(2-18) into (2-17):

$$\frac{dc}{dp} = -\frac{3}{2}\frac{(1-\sigma)}{(1-2\sigma)}\frac{c}{(1-c)} \qquad (3\text{-}3)$$

To calculate the rate of closing for cracks of all aspect ratios, we could just substitute for K* in eq. (2-17) by any one of the formulae introduced earlier in this chapter. However, it is just as easy and mathematically more consistent to derive it from first principles using the results of Eshelby (1957). Moreover by doing so we will obtain a simpler expression than the more general one involving T_{iijj} and then having to set K' and μ' to zero in that expression. Most of the material discussed here has been published in a paper written jointly by the author and Toksöz and Timur (Toksöz et al., 1976).

Following Eshelby, we can express the dilatational components of the strain field e_{ij} just outside an ellipsoidal cavity in terms of the applied strain field e^A_{ij} as (eq. 2-9)

$$-\lambda S_{mmpq} e_{pq} - 2\mu S_{ijpq} e_{pq} + \lambda e + 2\mu e_{ij}$$
$$= \lambda e^A + 2\mu e^A_{ij}$$

for ij = 11, 22, 33. The summation convention is used, and the pq summation is over 11, 22, 33 only, since $S_{1112} = 0$ and similarly for other S components coupling dilatation and shear. e and e^A are the traces of the respective strain tensors, i.e. the dilatation of the respective strain fields. $S_{\alpha\beta\gamma\delta}$ is a fourth order tensor (see section 2.1.3).

For an applied hydrostatic pressure, $e^A_{11} = e^A_{22} = e^A_{33}$, and we have three simultaneous equations with the same right hand side. For oblate spheroids, the three semi-axes a, b, c of the ellipsoid are related by a = b > c and $\frac{c}{a} = \alpha$, the aspect ratio. With this, the above system is reduced to two coupled equations.

We note that for an applied hydrostatic pressure, P, and effective static bulk modulus K^*_A, the dilatation of the applied strain field is given by

$$e^A = \frac{-P}{K^*_A} \qquad (3\text{-}4)$$

For a cavity of volume c, the dilation of the strain field immediately outside the pore is

$$e = \frac{dc}{c} \qquad (3\text{-}5)$$

where dc is the change in volume of the pore due to the applied stress. Combining (3-4), (3-5) and the solution of the system (2-9), we obtain

$$\frac{dc}{c} = \frac{-p}{K_A^*} \Big/ \left[E_1 - E_2 E_3 / (E_3 + E_4)\right] \qquad (3\text{-}6)$$

where

$$E_1 = \frac{6\mu\, Ia}{2\pi(3K+4\mu)} \qquad (3\text{-}7)$$

$$E_2 = \frac{6\mu}{4\pi(3K+4\mu)}(3Ia - 4\pi) \qquad (3\text{-}8)$$

$$E_3 = \frac{\alpha^2(3 - 9Ia/4\pi)(6K+2\mu)}{2(1-\alpha^2)(3K+4\mu)} + \frac{6\mu\, Ia}{8\pi(3K+4\mu)} \qquad (3\text{-}9)$$

$$E_4 = \frac{1}{2}\left\{\frac{(3 - 9Ia/4\pi)(6K+2\mu)}{2(1-\alpha^2)(3K+4\mu)} - \frac{3\mu(1 - Ia/\pi)}{3K+4\mu}\right\} \qquad (3\text{-}10)$$

and

$$Ia = \frac{2\pi\alpha}{(1-\alpha^2)^{3/2}}\left\{\cos^{-1}\alpha - \alpha(1-\alpha^2)^{1/2}\right\} \qquad (3\text{-}11)$$

It can be shown that (Appendix B) as the aspect ratio goes to zero, our result approaches that of Walsh (3-2) as a limit.

3.2.2 Laboratory Data and the Pore-Aspect Ratio Spectrum:

Seismic compressional and shear wave velocities, measured in the laboratory under controlled conditions as a function of pressure in dry and saturated states, provide the ideal data for testing the applicability of the theory we have chosen to adopt. In this section we will try to model the measured seismic velocities as a function of pressure and saturation conditions of three rocks: a low porosity Troy granite, an intermediate porosity Berea sandstone and a high porosity Boise sandstone.

Before we go into the discussion of laboratory data, we have to define pressure more precisely. In the theory and equations, we used the pressure on the inclusion. If the pore pressure P_f of the fluid is not zero, the pressure on the inclusion is the difference between the confining pressure P_c of the system and the fluid pressure. We call this pressure the differential pressure $P_d = P_c - P_f$. It has been well established from experiments (Wyllie et al., 1958; Nur and Simmons, 1969; Gardner et al., 1974) that the change in seismic velocities with pressure is dependent only on the differential pressure and not on the confining or pore pressure alone.

To fit the measured velocities with theoretical models the following procedure was used. Initial values for matrix moduli (K, μ) and density (ρ) were determined from average mineral composition using formulations of Korringa (1973).

Velocities at very high pressures ($P \geq 3$ kb, if such data exists) were used to check the validity of adopted matrix moduli (Birch, 1966). Values of matrix moduli for the different rocks used are given in Table (3-1). Fluid compressibilities and densities are obtained from literature as discussed in the previous section. Tabulated values of compressibilities and densities for different fluids are given in Table (3-2). A spectrum of pore aspect ratios covering a range of $\alpha = 1$ (spheres) to $\alpha = 10^{-5}$ (very fine cracks) was chosen. Scanning electron microscope photographs (Timur et el., 1971; Sprunt and Brace, 1974; Hadley, 1976) were used as a guide and total porosity as a constraint. Theoretical velocities were calculated as function of pressure by first determining the changes in pore shapes at each pressure using the equation for crack closing rate (eq. 3-6) and then the Kuster and Toksöz equations for effective moduli (eq.2-32) and 2-33). To improve the model, pore aspect ratio spectra were adjusted and calculations were repeated until good fits were obtained to all velocities. Since this is a trial and error process and the judgement of the goodness of the fit is visual, we do not feel it is justified to introduce the numerical extension of the first order theories in our calculations. These will be introduced in the inverse problem.

In the application of the crack closing rate equation to a rock system with a distribution of cracks of different

aspect ratios, we have to be careful in our definition of the different moduli. As pointed by Toksöz et al., (1976), the effective bulk modulus seen by the applied field is actually K_A^*, the effective static bulk modulus or frame bulk modulus. The matrix moduli seen by the crack (used in the definition of the E_i's) are $\hat{K}_A$ and $\hat{\mu}_A$, defined as the effective static matrix moduli of the rock with all the pores except those with aspect ratio α. In the application, we have assumed that these static moduli are independent of fluid content and equal to the effective dynamic moduli of the dry rock. This is an overestimate. In laboratory measurements it was found that at atmospheric pressure the static bulk moduli of most rocks are smaller than the dynamic bulk moduli (Simmons and Brace, 1965; King, 1964). We have taken them to be equal because of the lack of data on the pressure dependence of the static bulk moduli of the rocks considered.

The pressure dependence of seismic velocities in dry and water-saturated Troy granite is shown in figure (3-5): the data are from Nur and Simmons (1969). The ultrasonic measurements were carried out using cylindrical cores. The pore fluid pressure was maintained at P_f = 1 bar for all confining pressures. The rock porosity is ϕ = 0.3 percent for the Troy granite. The behavior of observed velocities is typical of igneous rocks. The velocities increase rapidly at first (especially in the dry rock) as a function

of increasing pressure and then level off to an asymptotic behavior. The compressional velocities are higher when the rock is water-saturated. The shear velocities, however, are almost identical for the dry and water-saturated Troy granite.

Rapid increases of compressional velocities at low pressures are determined primarily by the closing of the very fine cracks. At about 0.5 kb pressure, most low aspect ratio pores close in the Troy granite. The seperation between velocities of the water-saturated and dry rocks at high pressures is controlled by the vugular pores. Shear velocities are less affected by saturation because of the lower sensitivity of the effectice shear modulus to the properties of the saturating fluids. The difference in dry and saturated shear velocities comes mostly through the difference in the effective densities of the rocks.

The fit of theoretical curves to measured compressional and shear velocities is very good. The observed compressional velocities are slightly lower than the theoretical values at intermediate pressures, but the discrepancy is less than the estimated errors in data. Shear velocities are almost the same for the dry and water-saturated cases for the data and the theory. The aspect ratio spectrum of the pores is shown in table (3-3), along with those of the sandstones.

The next set of velocity data to be interpreted is that

measured by King (1966) in Boise sandstone (ϕ = 25 percent) samples while dry and, in turn, saturated with brine and with kerosene (figure 3-6). The experimental procedure was similar to that of Nur and Simmons (1969). Fluid pressure was maintained at one atmosphere, while the confining pressure was increased to about 600 bars. The important aspect of these experiments is that kerosene is one of the saturants. Since kerosene does not interact with rock matrix materials, especially clays, the matrix properties should not be affected by the saturation. As we examine the data for compressional waves, the velocities are highest for brine saturation, intermediate for kerosene, and lowest for the dry rock at all pressures. The shear velocities are highest for the dry rock and lowest for the brine-saturated rock. Theoretical models were computed using the appropriate values for matrix and fluid moduli given in tables (3-1) and (3-2). Pore-aspect ratio spectrum determined from the fit is listed in table (3-3).

To fit the Boise sandstone data, it was necessary to lower the matrix shear modulus by about five percent when the rock is brine-saturated. With constant modulus, the calculated shear velocities of the brine-saturated rock is almost identical to those of the kerosene-saturated rock, as can be expected since the moduli of brine and kerosene are very similar. This is in contradiction to the data which show a considerably lower shear velocity for the brine-

saturated rock than the kerosene-saturated rock. We can explain this decrease in shear velocity by the presence of clay in the matrix. Upon brine-saturation, the shear modulus of the clay will be "softened", leading to the decrease in the matrix shear modulus. The amount of clay in Boise sandstone is estimated to be about fifteen percent (Timur, personal communication). A theoretical model based on the reduction of the shear modulus of clay by one order of magnitude results in a decrease in the matrix shear modulus of about twenty percent. Hence our estimate of five percent decrease is reasonable since not all the clay will be in contact with the brine and the softening effect will be diminished somewhat. This reduction of matrix rigidity reduces the shear velocity while decreasing the compressional velocity only slightly. It is clear that the effect of water on the matrix rigidity must be considered in sandstones, shales or any other rocks containing minerals which would readily interact with water. With this five percent adjustment to the shear modulus, all the theoretical fits to the Boise sandstone in figure (3-6) are very good.

The third and final set of data to be interpreted by the direct trial and error technique is that of Berea sandstone (ϕ = 16.3 percent) plotted in figure (3-7). The data were obtained by Jones et al. (1977) and were also presented by Toksöz et al. (1978) in conjunction with attenuation measurements. The saturants are brine and gas

(mostly methane). The fluid pressure is maintained at a constant ratio of about 0.465 of the confining pressure, so the differential pressure P_d is about 0.535 that of the confining pressure. Other than this the experimental procedure is similar to those used by Nur and Simmons (1969) and King (1966) described earlier. A more detailed description of the experimental system used can also be found in Timur (1977).

As in the case for the Boise sandstone, the Berea sandstone also has a significant percentage of clay in it (nine percent, Jones et al., 1977). In fitting the brine-saturated shear velocities, is was necessary to lower the matrix shear modulus by about four percent. It can be observed from figure (3-7) that the Berea sandstone has much more rapid increases in the velocities as a function of pressure than the Boise sandstone, especially below 250 bars or so of differential pressure. This implies a greater abundance of small aspect ratio cracks and this is verified in the resultant pore-aspect ratio spectrum obtained (table 3-3). The fit to the data is excellent.

We have now shown the ability of the direct theory to fit the velocity data from rocks with a wide range of porosities. The questions remain to be answered are how unique are the pore-aspect ratio spectra obtained and how well can we resolve them. These questions will be answered in a formal manner in Chapter 4.

3.2.3 Prediction of in situ Rock Properties:

With the theoretical formulations and pore-aspect ratio spectra and their proven applicability in the previous section, a complete theoretical modelling of rocks with different porosities, saturation conditions, matrix moduli, overburden and pore fluid pressure is possible. The rocks we have chosen to model are that of Boise and Berea sandstones. The differential pressure is assumed to be about 0.54 of the confining pressure.

The first example we will present is that of Berea sandstone saturated with a mixture of brine and gas. The mixture is assumed to be homogeneous and thus obey equation (3-1) for its effective bulk modulus. The velocities are plotted as a function of differential pressure up to 500 bars and the results are shown in figure (3-8).

Once a small amount of gas is introduced into the system, the compressional velocity decreases rapidly. At gas concentrations about five percent, the compressional velocities could be lower than those of total gas concentration because of the high effective density. This behavior is pressure dependent.

The shear velocity behavior is more regular. The velocities of a rock saturated with the mixture remain close to those of brine-saturated values until gas concentration reaches about 25 percent and then gradually increase toward pure gas-saturated values.

In figure (3-9), we present a different picture of mixed saturation. The two fluids are considered to be occupying selectively different pores. In one case it is assumed that thin pores are filled with brine, while the rest of the pores are filled with gas. In the second example, the gas and brine are reversed. At low pressures, the compressional velocities are strongly controlled by the fluid occupying the fine pores, even though this fluid fills less than one percent of the pore volume. Since fine pores and cracks close at high pressures, this effect disappears and the fluid occupying the vugular pores determines the velocity as the pressure increases. This effect can be significant in the interpretation of partial saturation data as can be seen in Domenico's data (1976) presented in section 3.1.3.

Using the seismic velocity model given in figure (3-8) and the effective densities, reflection coefficients can be calculated for rocks with gas-brine and other interfaces. In figure (3-10), the reflection coefficients for the normally incident compressional waves [$R=(\rho_2 V_2-\rho_1 V_1)/(\rho_2 V_2+\rho_1 V_1)$] are shown for the gas-brine interface and the mixed phase and brine interface as a function of differential pressure and depth for the two sandstone models. The two sets of curves are similar in shape, except that the magnitude of reflection coefficients are higher for the sandstone with the higher porosity.

The general properties of these curves are clear from

the figure. The reflection coefficients decrease rapidly with increasing overburden pressure or the depth of the reflecting interface. The decrease is very rapid at low pressures. At differential pressures above 200 bars (nominal depths of below 2 km), reflection coefficients are generally small and nearly constant. Thus, very large amplitude reflections, "bright spots" and "flat spots", are most likely to be observed from shallower interfaces. The exceptions are those from overpressured formations since the fluid pressures in these would be higher than nominal resulting in a lower differential pressure.

The reflection coefficients for the interface between the mixed gas-brine reservoir and the pure brine reservoir behave more regularly than the corresponding compressional velocities in each reservoir. The curves in figure (3-10) show that the reflection coefficients for ten percent gas and ninety percent brine are about one-half of the values for the 100 percent gas saturation. While the compressional velocities are lower for the mixed saturation (figure 3-8), the effective densities are higher and the resulting reflection coefficients are smaller. At fifty percent gas saturation, the reflection coefficients are nearly the same as those of a 100 percent gas-filled layer.

Combinations of interval velocities and reflection amplitudes may be used to estimate the fractional gas saturation (Toksöz, 1975). In a gas-brine reservoir, very

low interval velocities and relatively small reflections would indicate a relatively small amount (e.g. ≈ 10 percent) of gas, while the low velocities and large reflections will indicate total or high percentages ($\geq$ 50 percent) of gas saturation.

Finally, since compressional and shear wave velocities are affected differently upon gas saturation, their combined characteristics may be used to identify saturating fluids. This is shown in the form of the Poisson's ratio $\{ \sigma = (3K-2\mu)/(6K+2\mu) \}$ in figure (3-11) for gas, brine and mixed saturation for the sandstone model with sixteen percent porosity. Poisson's ratio is high for the brine-saturated, low for the gas-saturated rock. The difference is largest at depths smaller than about 2 km, but it persists to some extent at all depths. Poisson's ratios for mixed saturations fall between the two extremes, in rough correspondence with the relative amounts of gas and brine. Since it is difficult to determine the actual reflection coefficient of a formation (possible attenuation and non-zero incidence angle), a s-wave velocity profile in addition to the p-wave profile would provide us with better estimates of the amount of gas in a formation through its Poisson's ratio.

TABLE 3-1

POROSITIES AND MATRIX PROPERTIES OF ROCKS USED TO CALCULATE THEORETICAL MODELS OF DIFFERENT SATURATION CONDITIONS

Rock	Total Porosity (%)	Bulk Mod (K) (Mb)	Shear Mod (μ) (Mb)
Boise Sandstone [1]	25.0	0.30	0.18
		(saturated)	0.17
Troy Granite [2]	0.33	0.70	0.35
Cromwell Sandstone [3]	16.0	0.29	0.20
Nichols Buff Sandstone [3]	22.0	0.18	0.09
Britton Sandstone [3]	30.0	0.13	0.065
Berea Sandstone [4]	16.3	0.33	0.26
		(saturated)	0.245
Gulf Coast Sand [5]	37.7	0.15	0.038

Matrix Density (g/cm^3) for all rocks = 2.7

Matrix Density (g/cm^3) for Gulf Coast Sand = 2.65

[1] Data of King (1966)

[2] Data of Nur and Simmons (1969)

[3] Data of Wyllie et al. (1956)

[4] Data of Jones et al. (1977)

[5] Data of Domenico (1976)

TABLE 3-2

PROPERTIES OF SATURATING FLUIDS
AT 20°C AND PRESSURES OF 1, 200,
AND 500 BARS USED IN CALCULATIONS

	Density (g/cc)			Bulk Modulus (K') (Kb)		
Fluid	1 b	200 b	500 b	1 b	200 b	500 b
Water	1.00	-	-	23.2	-	-
Brine (3%) (1)	1.03	1.03	1.03	24.4	25.0	26.5
Oil (2)	0.86	0.87	0.88	14.0	15.8	19.0
Kerosene	0.82	-	-	14.0	-	-
Gas (3)	$1x10^{-3}$	0.14	0.27	$1.50x10^{-3}$	0.29	1.06
Air	$1x10^{-3}$	-	-	$1x10^{-3}$	-	-

(1) Data from Adams (1931)

(2) Average crude (32 -38° API gravity, Standing, 1952)

(3) Mostly methane (Thomas et al. 1970)

TABLE 3-3

Pore Spectra [Aspect Ratio (α) of Pores vs Volume Concentration (c)]

at P = 1 Bar Used to Fit Theoretical Curves

(Note that Pore Spectra Changes as a function of Pressure)

Berea Sandstone		Boise Sandstone		Troy Granite	
c	α	c	α	c	α
0.12	1	0.18	1	0.1×10^{-2}	1
0.04	0.1	0.69×10^{-1}	0.1	0.5×10^{-3}	0.1
0.5×10^{-3}	0.1×10^{-1}	0.1×10^{-3}	0.25×10^{-2}	0.15×10^{-2}	0.01
0.1×10^{-3}	0.17×10^{-2}	0.1×10^{-3}	0.2×10^{-2}	0.5×10^{-4}	0.5×10^{-3}
0.1×10^{-3}	0.14×10^{-2}	0.15×10^{-3}	0.15×10^{-2}	0.75×10^{-4}	0.4×10^{-3}
0.2×10^{-3}	0.1×10^{-2}	0.2×10^{-3}	0.1×10^{-2}	0.1×10^{-3}	0.25×10^{-3}
0.15×10^{-3}	0.6×10^{-3}	0.1×10^{-3}	0.5×10^{-3}	0.5×10^{-4}	0.1×10^{-3}
0.75×10^{-4}	0.3×10^{-3}	0.2×10^{-4}	0.1×10^{-3}	0.5×10^{-5}	0.1×10^{-4}
0.3×10^{-4}	0.1×10^{-3}				
0.9×10^{-5}	0.3×10^{-4}				
0.3×10^{-5}	0.1×10^{-4}				

FIGURE CAPTIONS

Figure 3-1: Normalized P- and S-wave velocities versus volume concentration of inclusions of different aspect ratios for water- and gas-saturated inclusions. The matrix parameters are K = 0.44 Mb and μ = 0.37 Mb. Inclusion parameters are given in Table (3-2).

Figure 3-2: Effective bulk moduli (K*) of gas bubbles in brine mixture at different pressures. Note the sharp drop when even only a few volume percent of gas is introduced. The gas is methane. NaCl concentration in brine is 3 percent.

Figure 3-3: Compressional wave velicities versus partial saturation for three different sandstones. The data (points) are from Wyllie et al. (1956). The models used are similar to those of Boise and Berea sandstones. The matrix moduli are given in Table (3-1).

Figure 3-4: Direct theoretical fit to partial saturation data of Gulf Coast Sand (Domenico, 1976). Only ellipsoids of aspect ratios 1, 0.1 and 0.01 are used. A non-homogeneous mixture of air and brine has to be assumed for brine saturation over 90%, with all the gas assumed to stay in spherical pores. The matrix moduli used are given in Table (3-1).

Figure 3-5: Observed and theoretical P- and S-wave velocities in dry and water-saturated Troy granite as a function of

differential (confining minus fluid) pressure. The data (points) are from Nur and Simmons (1969). Fluid pressure is maintained at 1 bar.

Figure 3-6: Same as figure (3-5) for Boise sandstone. The data (points) are from King (1966). The fluid pressure is maintained at 1 bar. The matrix shear modulus is reduced for the brine-saturated case (Table 3-1) to account for the matrix softening because of the effect of water on clay minerals. The pore-aspect ratio spectrum used is given in Table (3-3).

Figure 3-7: Same as figures (3-4) and (3-5) for Berea sandstone (ϕ = 16.3%). The data is from Jones et al. (1977). The fluid pressure is maintained at 0.465 of the confining pressure.

Figure 3-8: Theoretical P- and S-wave velocities versus differential pressure for 16 percent porosity sandstone model saturated with different gas-brine mixtures. Curves designated by "brine" and "gas" indicate that the rock is saturated 100 percent with brine and gas respectively. The percentages next to other curves indicate volume percent of gas in the saturating fluid mixture (i.e. 10 percent means 10 percent gas and 90 percent brine). Note that at high pressures, even 5 percent of gas bubbles in brine pushes the velocity to lower than the velocity of the pure gas-saturated rock.

Figure 3-9: Theoretical P-wave velocities versus differential pressure for a 16 percent porosity sandstone model when brine and gas are occupying different cracks. The fluid that is occupying the small aspect ratio cracks has more influence on the velocities at low pressure, while the other fluid is more dominant at high pressures.

Figure 3-10: Theoretical reflection coefficients for gas-brine and mixed phase-brine interfaces in sandstone models as a function of differential pressure.

Figure 3-11: Poisson's ratios for the rock model in figure (3-8) as a function of differential pressure when the rock is saturated with brine, gas or mixture.

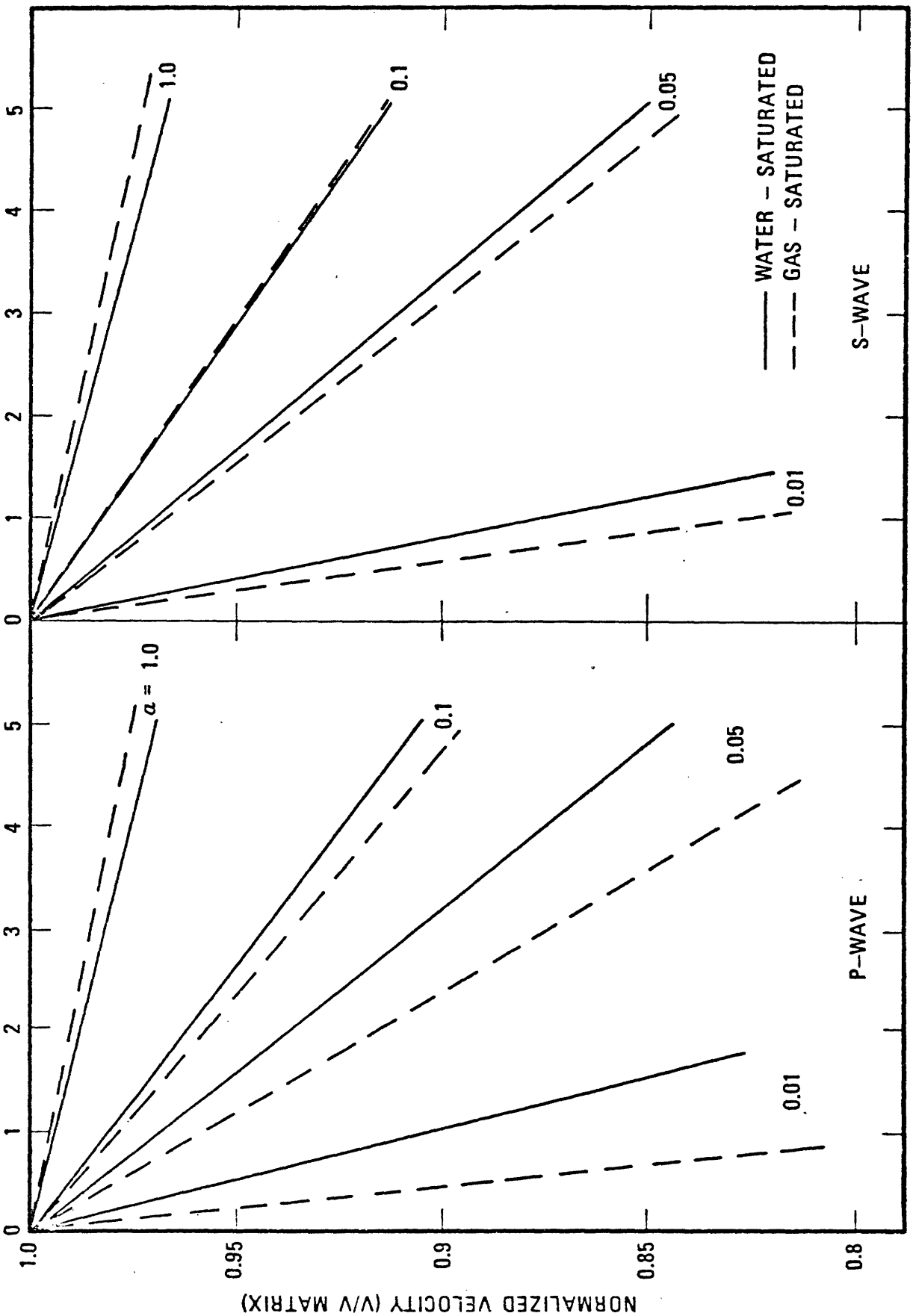
NORMALIZED VELOCITY (V/V MATRIX)
1.0
0.95
0.9
0.85
0.8
0
1
2
3
4
5
P-WAVE
S-WAVE
POROSITY (%)
POROSITY (%)
α = 1.0
0.1
0.05
0.01
1.0
0.1
0.05
0.01
WATER – SATURATED
GAS – SATURATED

Figure 3-1

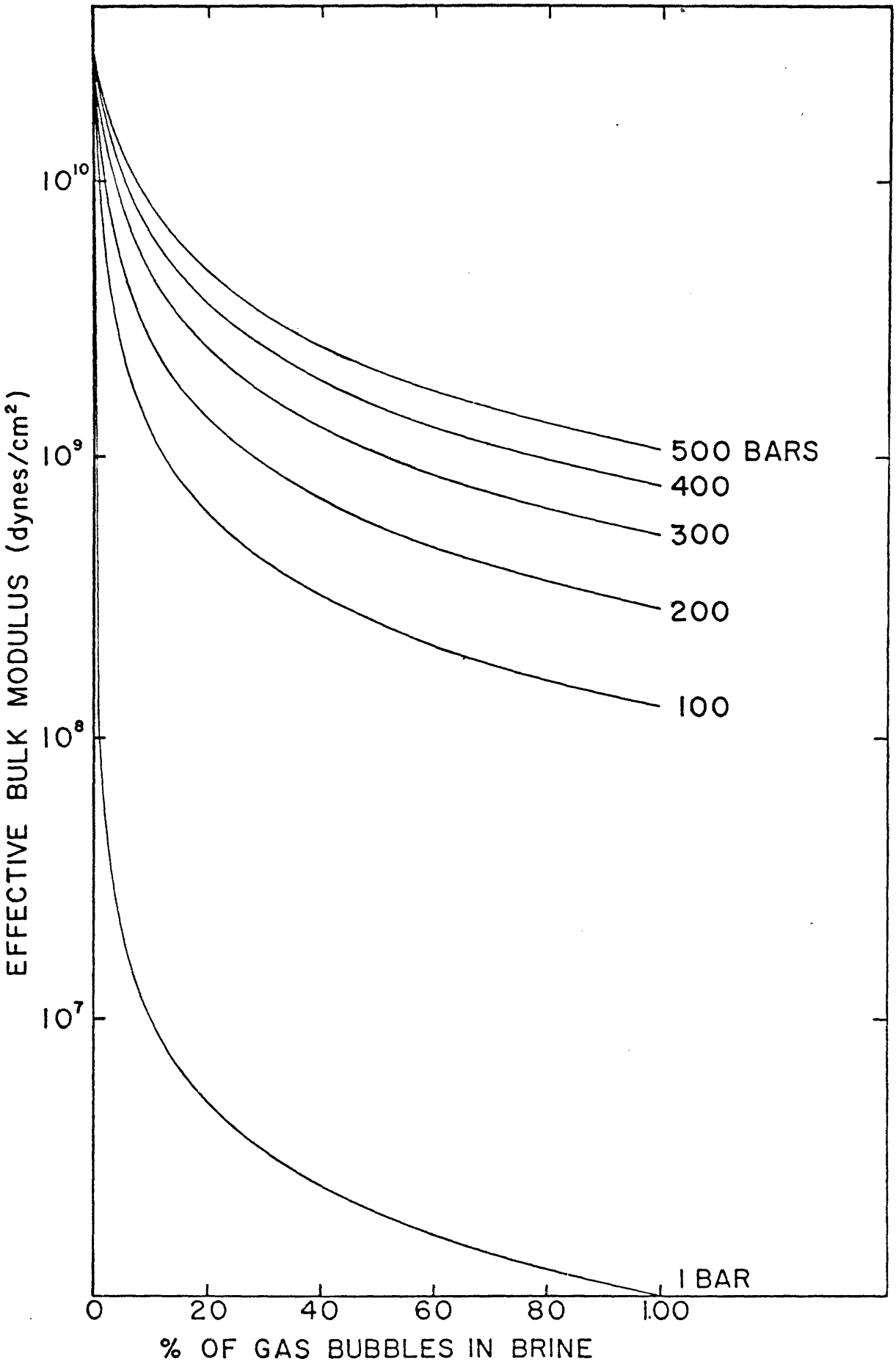
EFFECTIVE BULK MODULUS (dynes/cm²)
10¹⁰
10⁹
10⁸
10⁷
500 BARS
400
300
200
100
1 BAR
0
20
40
60
80
100
% OF GAS BUBBLES IN BRINE

Figure 3-2

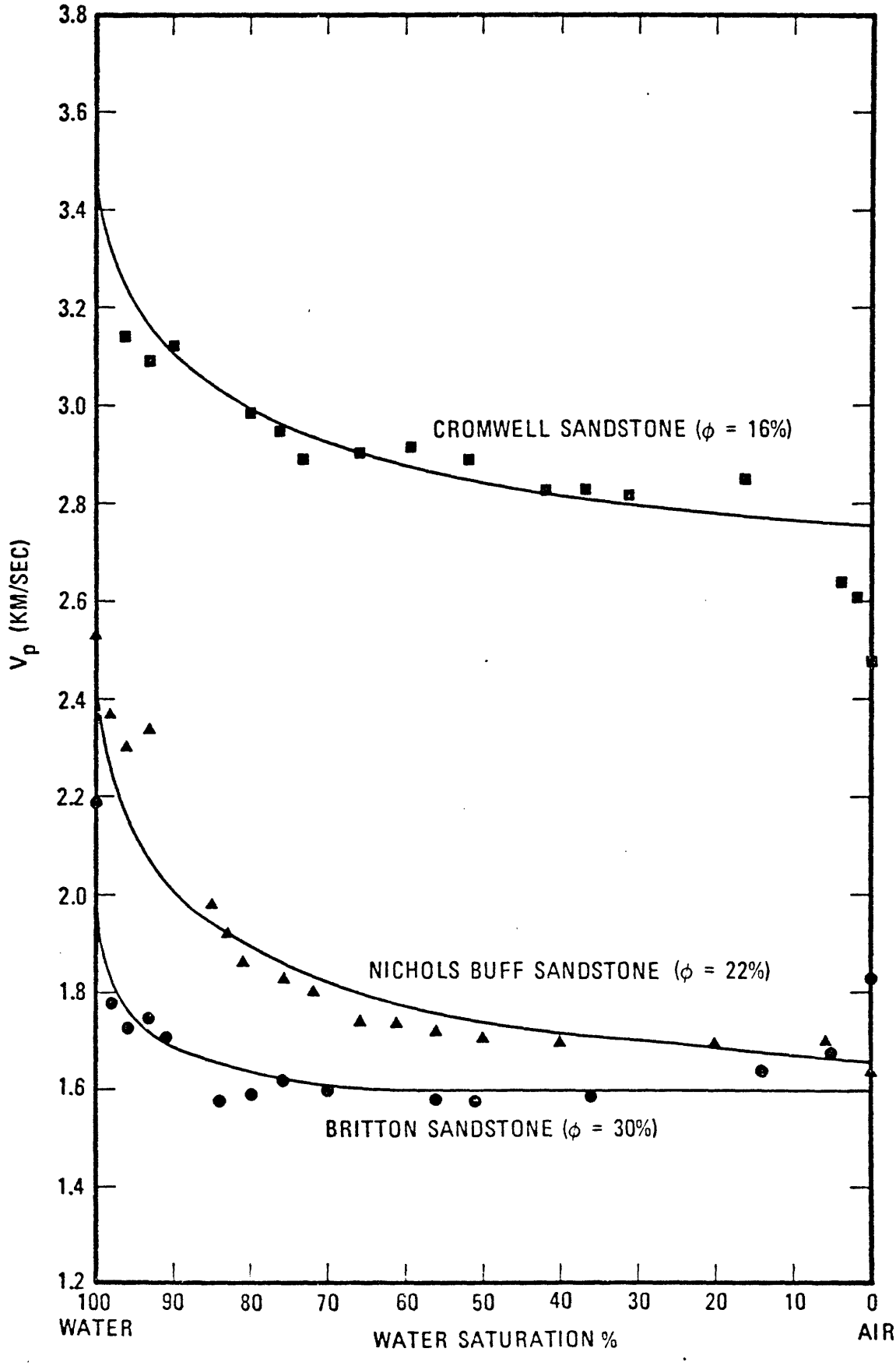
3.8
3.6
3.4
3.2
3.0
2.8
2.6
2.4
2.2
2.0
1.8
1.6
1.4
1.2
V_p (KM/SEC)
CROMWELL SANDSTONE (ϕ = 16%)
NICHOLS BUFF SANDSTONE (ϕ = 22%)
BRITTON SANDSTONE (ϕ = 30%)
100
90
80
70
60
50
40
30
20
10
0
WATER
WATER SATURATION %
AIR

Figure 3-3

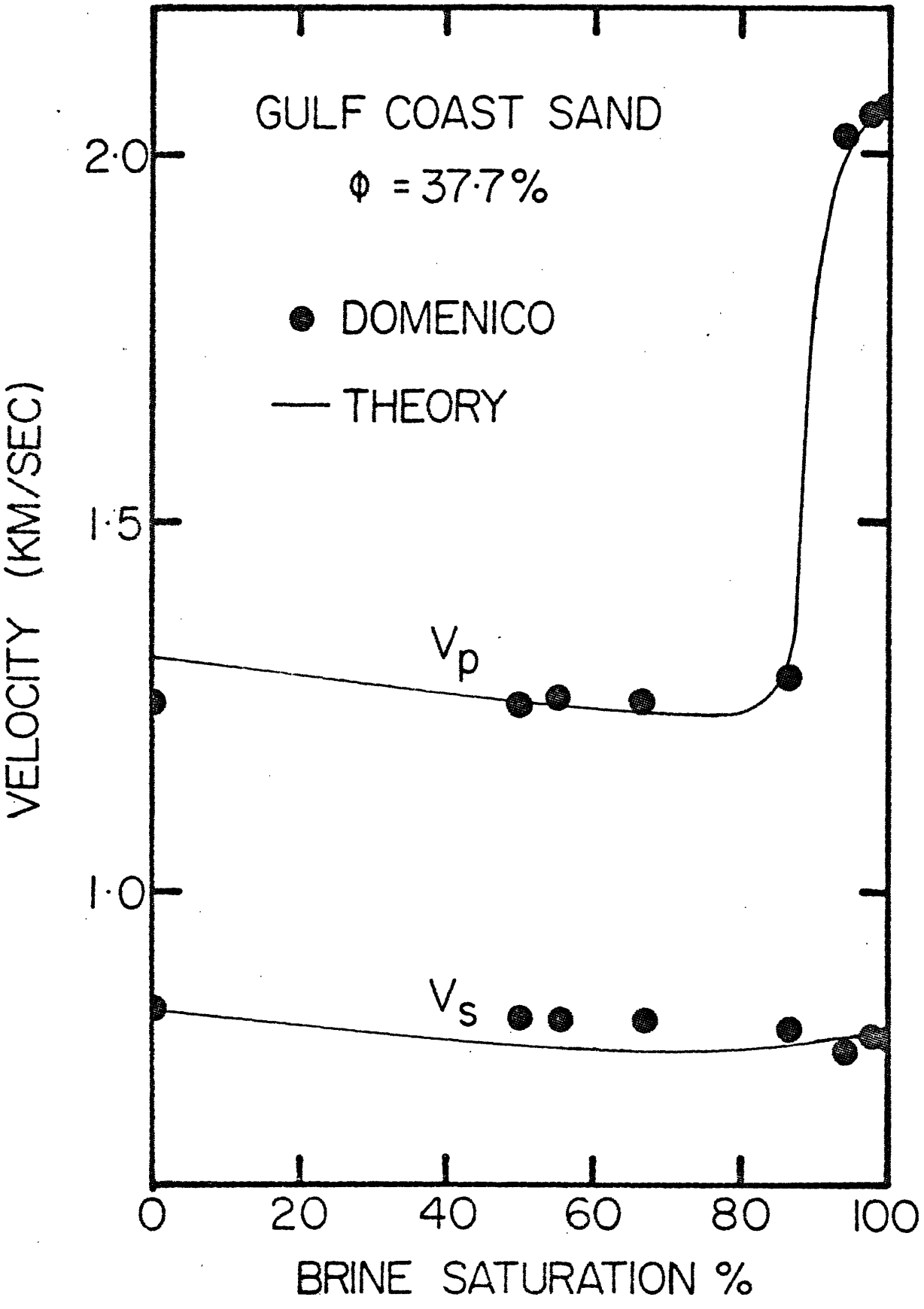
GULF COAST SAND
Φ = 37·7%
DOMENICO
THEORY
V_p
V_s
VELOCITY (KM/SEC)
2·0
1·5
1·0
0
20
40
60
80
100
BRINE SATURATION %

Figure 3-4

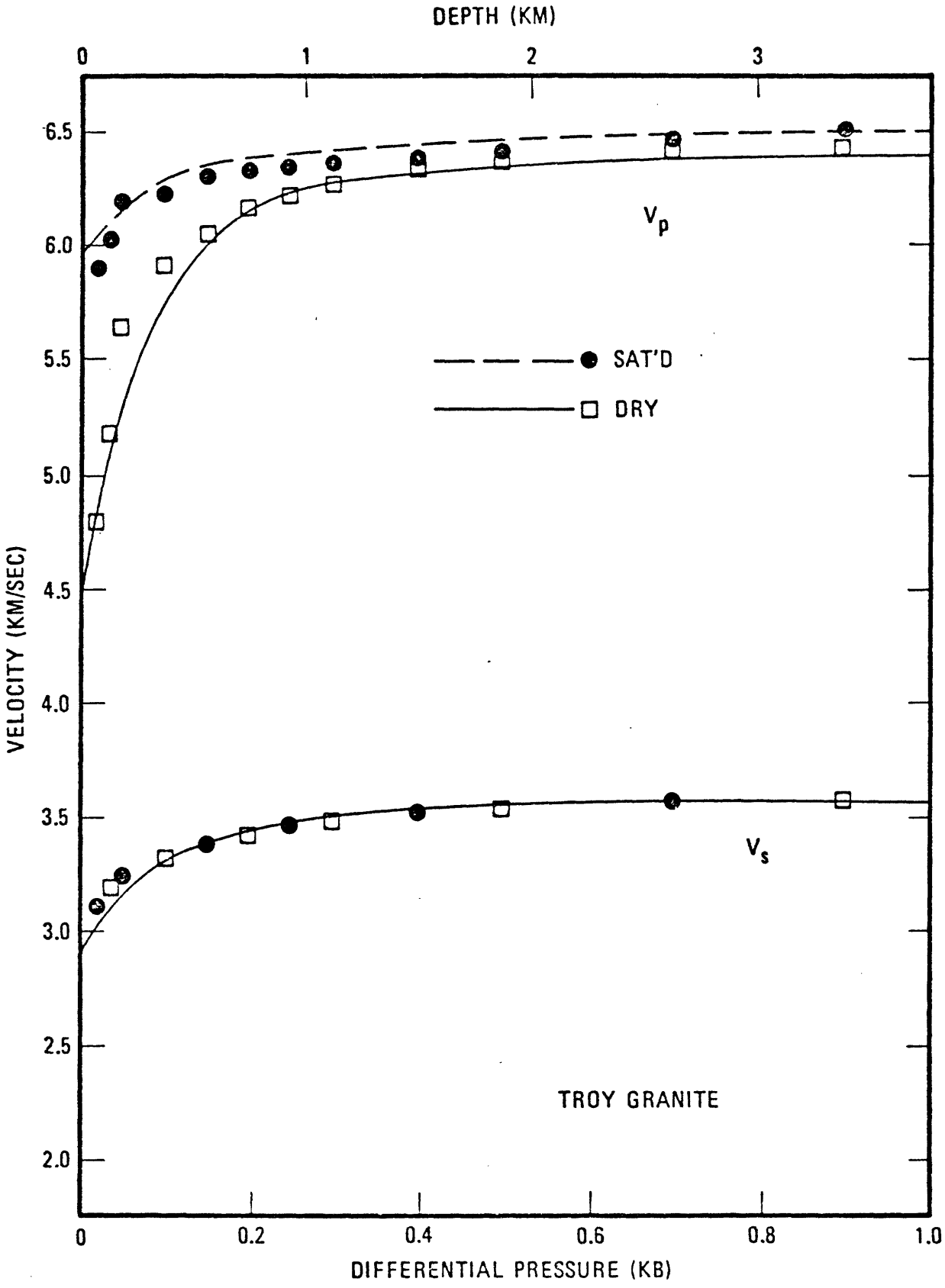
DEPTH (KM)
0
1
2
3
6.5
6.0
5.5
5.0
4.5
4.0
3.5
3.0
2.5
2.0
VELOCITY (KM/SEC)
V_p
SAT'D
DRY
V_s
TROY GRANITE
0
0.2
0.4
0.6
0.8
1.0
DIFFERENTIAL PRESSURE (KB)

Figure 3-5

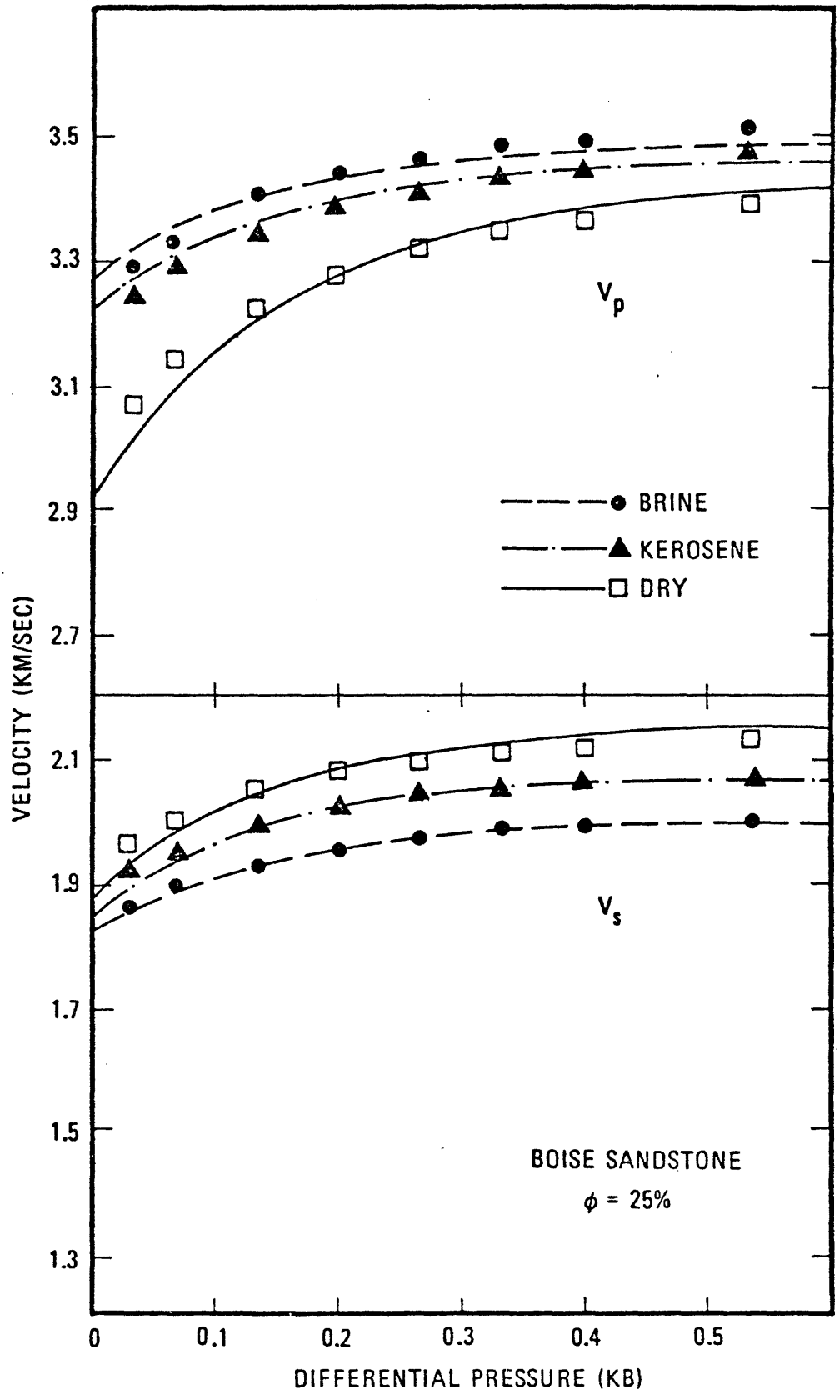
3.5
3.3
3.1
2.9
2.7
2.1
1.9
1.7
1.5
1.3
VELOCITY (KM/SEC)
V_p
BRINE
KEROSENE
DRY
V_s
BOISE SANDSTONE
ϕ = 25%
0
0.1
0.2
0.3
0.4
0.5
DIFFERENTIAL PRESSURE (KB)

Figure 3-6

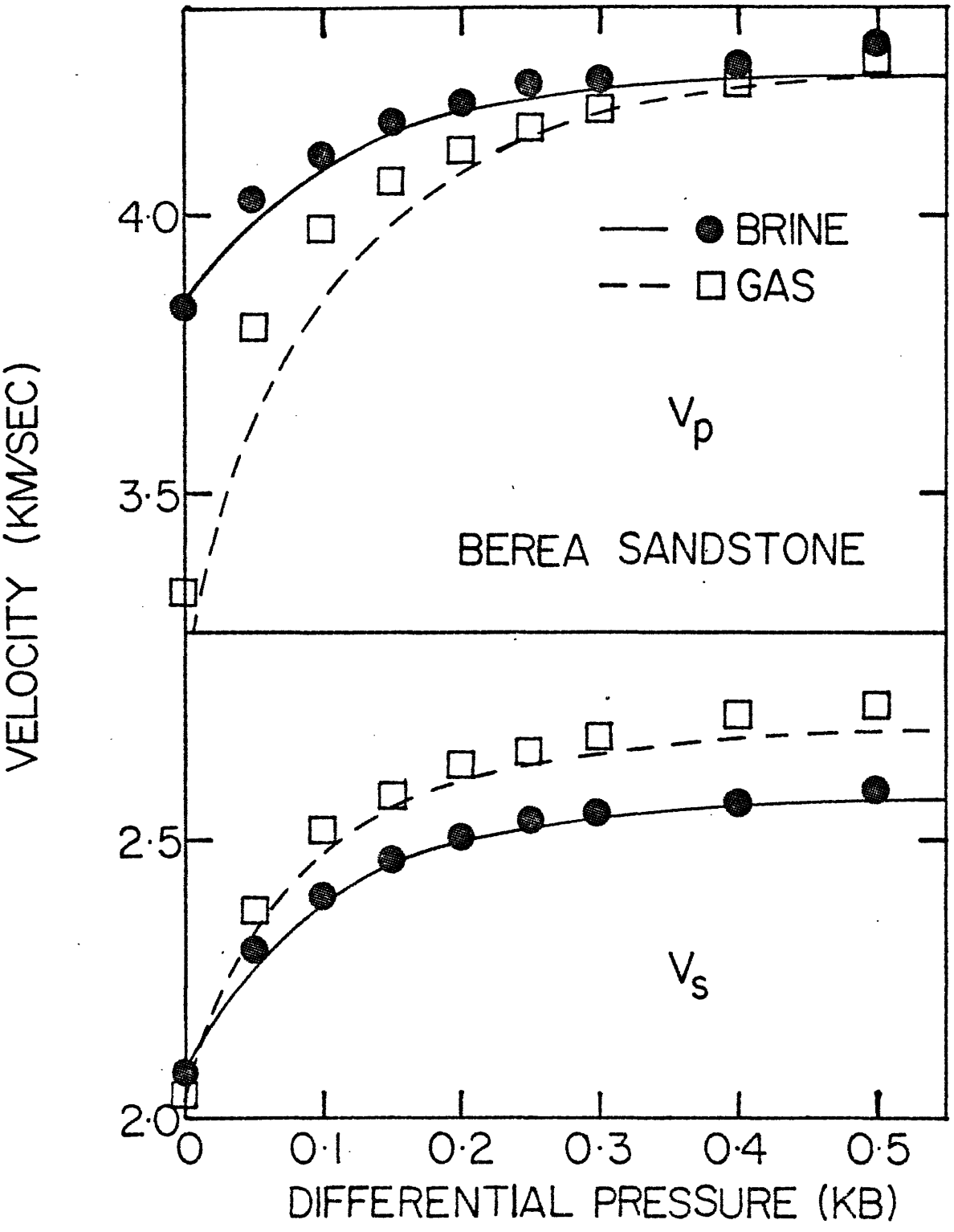
VELOCITY (KM/SEC)
4·0
3·5
2·5
2·0
BRINE
GAS
V_p
BEREA SANDSTONE
V_s
0
0·1
0·2
0·3
0·4
0·5
DIFFERENTIAL PRESSURE (KB)

Figure 3-7

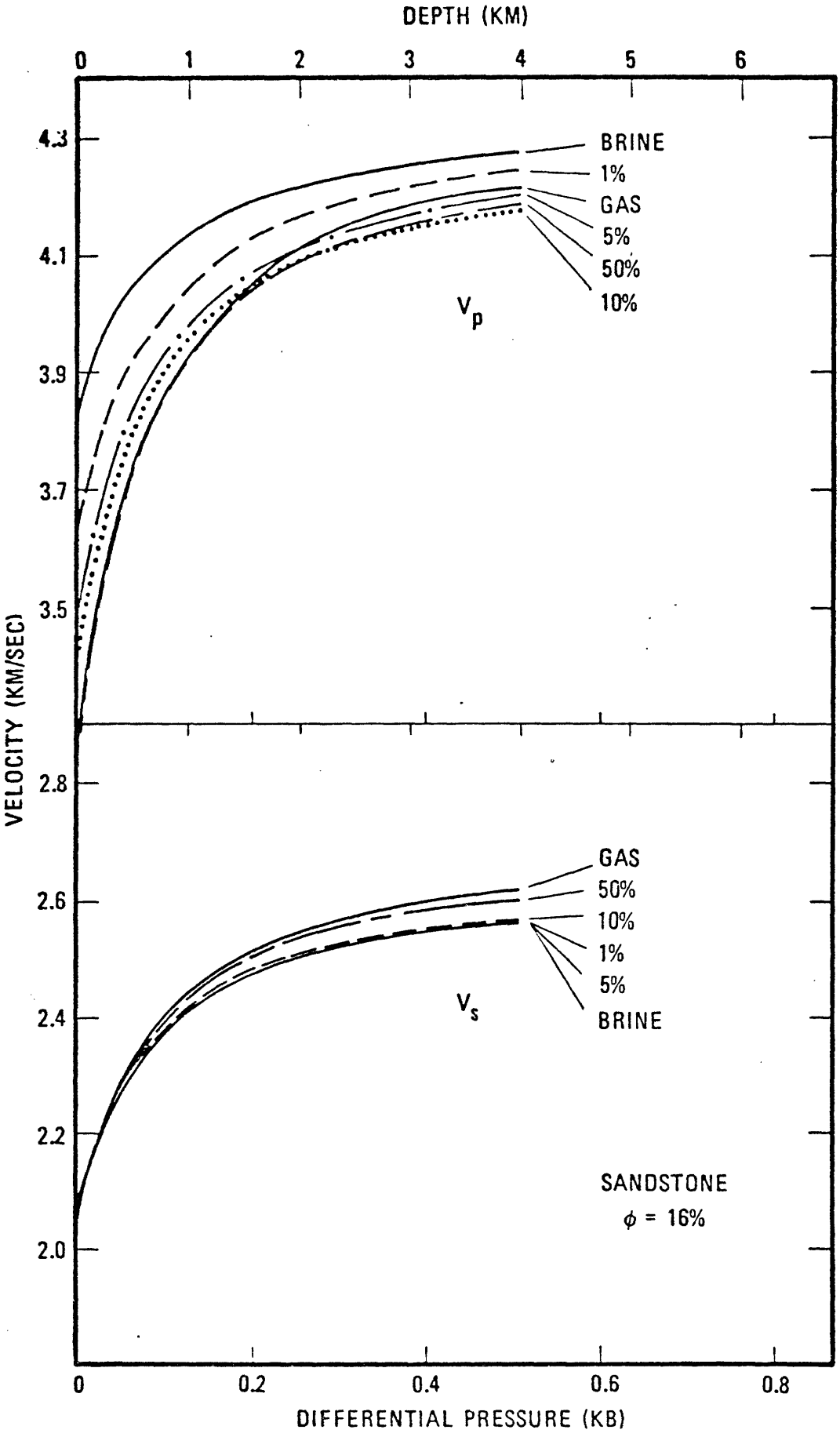
DEPTH (KM)
0
1
2
3
4
5
6
4.3
4.1
3.9
3.7
3.5
BRINE
1%
GAS
5%
50%
10%
V_p
VELOCITY (KM/SEC)
2.8
2.6
2.4
2.2
2.0
GAS
50%
10%
1%
5%
BRINE
V_s
SANDSTONE
ϕ = 16%
0
0.2
0.4
0.6
0.8
DIFFERENTIAL PRESSURE (KB)

Figure 3-8

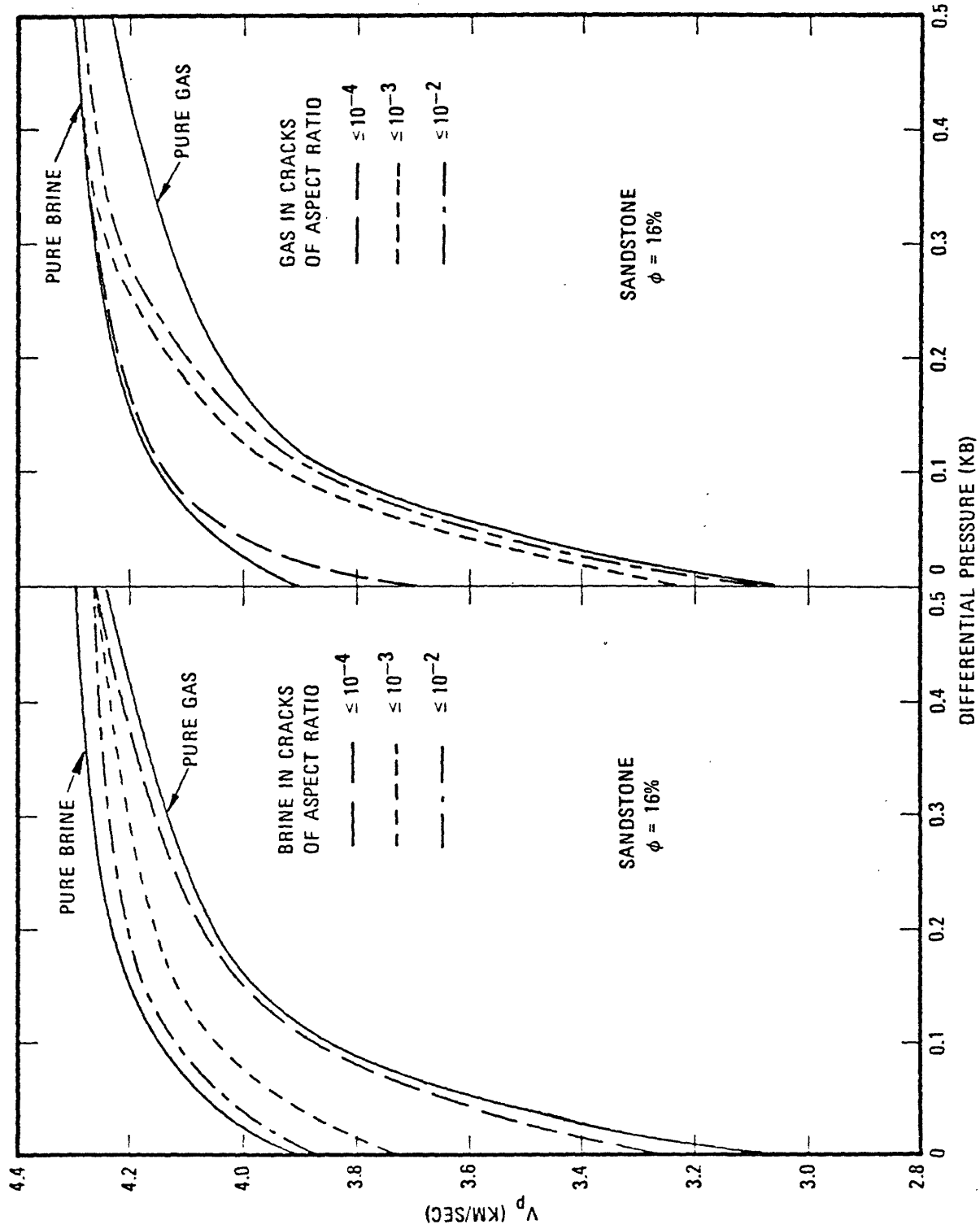
PURE BRINE
PURE GAS
GAS IN CRACKS
OF ASPECT RATIO
≤ 10⁻⁴
≤ 10⁻³
≤ 10⁻²
SANDSTONE
φ = 16%
PURE BRINE
PURE GAS
BRINE IN CRACKS
OF ASPECT RATIO
≤ 10⁻⁴
≤ 10⁻³
≤ 10⁻²
SANDSTONE
φ = 16%
V_p (KM/SEC)
DIFFERENTIAL PRESSURE (KB)
4.4
4.2
4.0
3.8
3.6
3.4
3.2
3.0
2.8
0
0.1
0.2
0.3
0.4
0.5
0
0.1
0.2
0.3
0.4
0.5

Figure 3-9

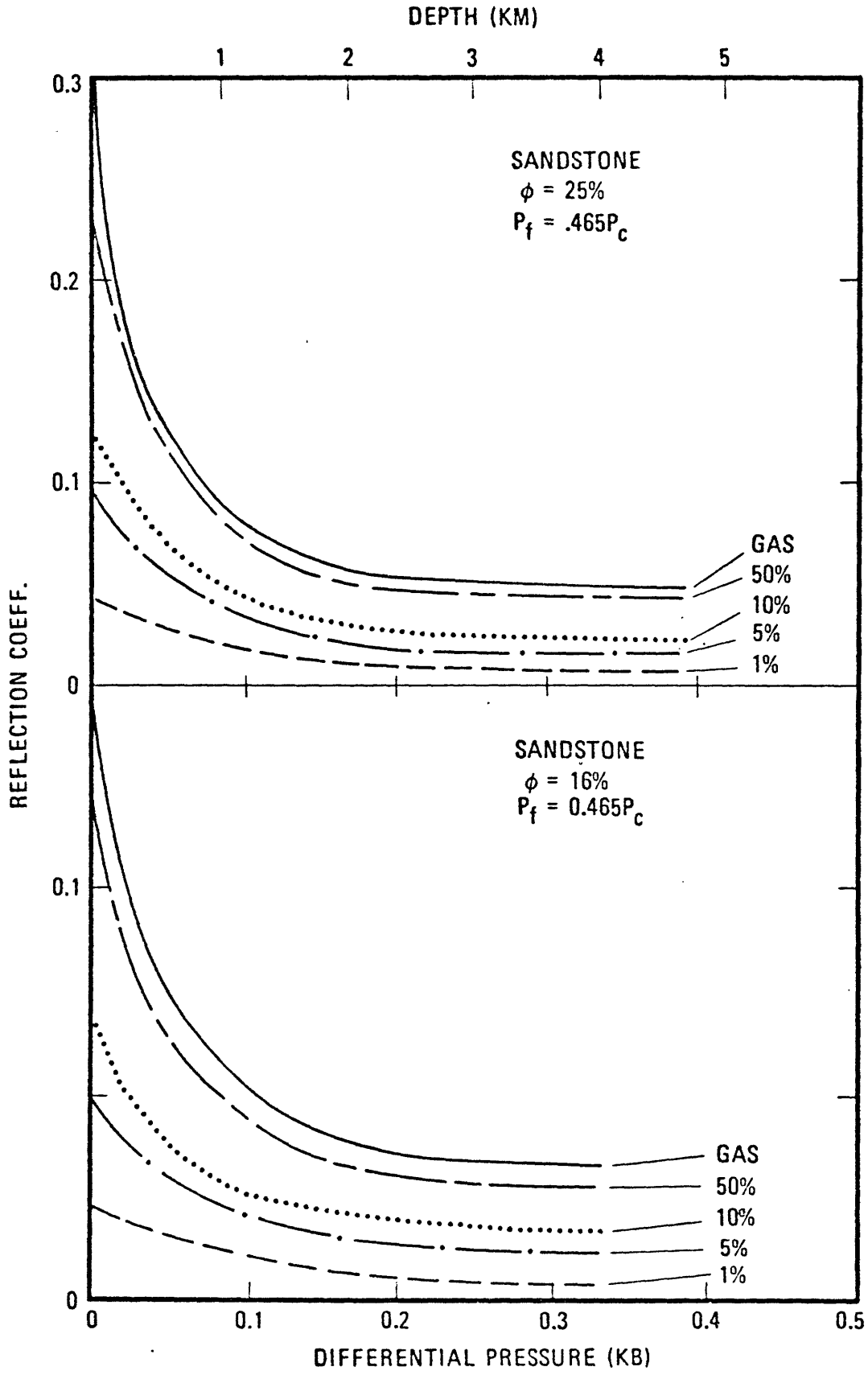
DEPTH (KM)
1
2
3
4
5
0.3
0.2
0.1
0
SANDSTONE
ϕ = 25%
P_f = .465P_c
GAS
50%
10%
5%
1%
SANDSTONE
ϕ = 16%
P_f = 0.465P_c
0.1
0
GAS
50%
10%
5%
1%
REFLECTION COEFF.
0
0.1
0.2
0.3
0.4
0.5
DIFFERENTIAL PRESSURE (KB)

Figure 3-10

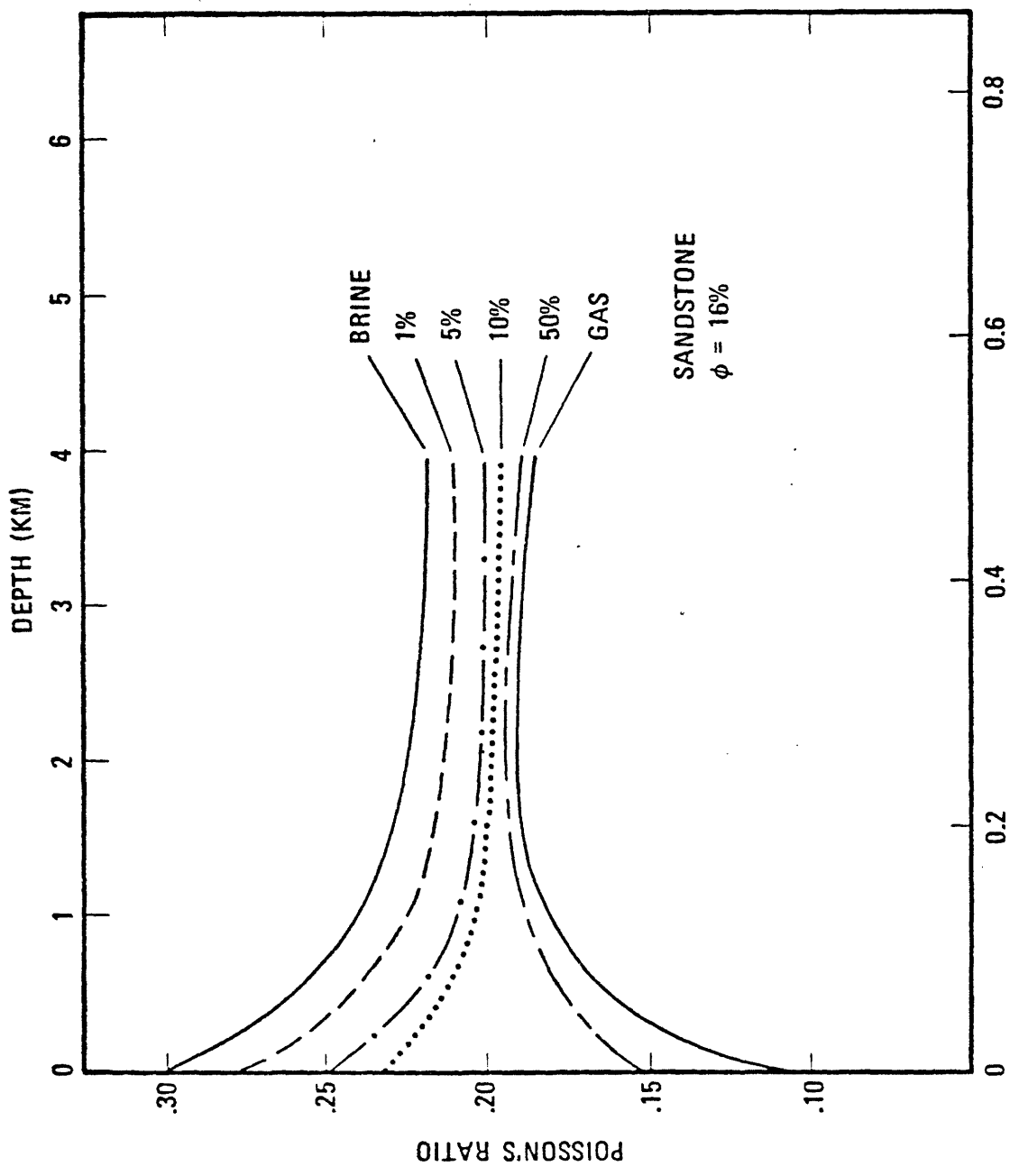
DEPTH (KM)
0
1
2
3
4
5
6
POISSON'S RATIO
.30
.25
.20
.15
.10
DIFFERENTIAL PRESSURE (KB)
0
0.2
0.4
0.6
0.8
BRINE
1%
5%
10%
50%
GAS
SANDSTONE
ϕ = 16%

Figure 3-11

CHAPTER 4

INVERSION OF VELOCITY DATA TO OBTAIN THE PORE-ASPECT RATIO SPECTRUM OF A ROCK -- THEORY

Up to this point we have been discussing the theoretical modelling of a two-phase material from the stand point of a direct problem, i.e. given the crack-aspect ratio spectrum and the elastic moduli of the matrix and inclusion material, we can calculate the effective moduli of the composite material. The fits to the data given in the previous chapter are calculated by a trial and error process. We would like to find out the uniqueness of the crack-aspect ratio spectrum we obtained from such a fit and the resolution between the individual aspect ratios. To be able to do this we will formulate the problem as an inverse problem. In this chapter we will introduce three different formulations of the inverse problem; namely the linear inversion, the linearized iterative inversion and the linear programming inversion. We will discuss their differences theoretically and when actually applied to inverting laboratory measurements. We will also discuss the resolution and uniqueness of the solution in the context of each inversion scheme. The application of the theory to laboratory data will be presented in the next chapter.

4.1 The Linear Inversion:

4.1.1 Formulation:

The simplest and most direct of the three inversion methods is the linear inversion. We are given the laboratory measured compressional and shear wave velocities of a rock at different pressures (P_n, n = 1,...,N) and under one or more saturation conditions (dry, wet, oil-, kerosene-, brine- or gas-saturated). We are also given the total porosity of the rock, the bulk moduli and densities of the saturating fluids. We can estimate the density, bulk and shear moduli of the rock matrix form its composition using Hashin-Shtrikman bounds (Toksöz et al., 1976, Korringa and Thompson, 1977) or from high pressure data (Simmons and Brace, 1965; Walsh, 1965). We would like to find the crack (pore) concentration versus aspect ratio spectrum of the rock at zero pressure.

The first step in formulating the inverse problem is to specify the aspect ratios of the cracks and pores (α_m, m = 1,...,M at zero pressure) at which we want to resolve the concentrations. Then we make use of the set of linear relationships of effective moduli with concentrations obtained by Kuster and Toksöz (1974a). At each pressure P_n, eq. (2-32) and (2-33) can be written as

$$\frac{K_n^*-K}{3K_n^*+4\mu} = \frac{K'-K}{3(3K+4\mu)} \sum_{m=1}^{M} c_n(\alpha_{mn}) T_{iijj}(\alpha_{mn}) \qquad (4-1)$$

and $$\frac{\mu_n^*-\mu}{6\mu_n^*(K+2\mu)+\mu(9K+8\mu)}$$

$$= \frac{\mu'-\mu}{25\mu(3K+4\mu)} \sum_{m=1}^{M} c_n(\alpha_{mn}) [T_{ijij}(\alpha_{mn}) - \frac{1}{3}T_{iijj}(\alpha_{mn})] \tag{4-2}$$

where K_n^* and μ_n^* are the effective bulk and shear moduli of the rock at pressure P_n, $c_n(\alpha_{mn})$ is the concentration of the crack with aspect ratio α_m at P_n and μ' is zero for fluid saturants.

The concentration of a crack of aspect ratio α_m at a pressure of P_n is related to its concentration at zero pressure by

$$c_n(\alpha_{mn}) = c(\alpha_{mn})[1 + \frac{dc}{c}(\alpha_m, P_n)] \tag{4-3}$$

where dc/c, the fractional change in volume of a crack with aspect ratio α_m under a pressure of P_n, is given by eq.(3-6). Similarly, since $c(\alpha) = \frac{4}{3}\pi\alpha\, a^3$ for an oblate spheroidal crack with aspect ratio α and semi-major axis a, the change in the aspect ratio of a crack with pressure is given by

$$\frac{d\alpha}{\alpha} = \frac{dc(\alpha)}{c(\alpha)}, \tag{4-4}$$

neglecting the change, if any, in the semi-major axis a, and we have

$$\alpha_{mn} = \alpha_m[1 + \frac{dc(\alpha_m, P_n)}{c(\alpha_m)}] \tag{4-5}$$

This result means that the ratio $c(\alpha)/\alpha$ for a given crack is a constant as a function of pressure, as long as the crack stays open. When dc/c is less than -1, then we will consider the crack closed and drop that aspect ratio from the spectrum for that and higher pressures.

To put the equations into a form of simultaneous linear equations Ax=b, we rewrite (4-1) and (4-2) as follows:

$$\frac{K_n^*-K}{K'-K}\cdot\frac{3K_n^*+4\mu}{3K+4\mu}$$

$$= \sum_{m=1}^{M} \alpha_m \left[1 + \frac{dc}{c}(\alpha_{mn}, P_n)\right] \frac{1}{3} T_{iijj}(\alpha_{mn}) \frac{c(\alpha_m)}{\alpha_m} \qquad (4\text{-}6)$$

and

$$\frac{\mu_n^*-\mu}{\mu'-\mu}\cdot\frac{25\mu(3K+4\mu)}{6\mu_n^*(K+2\mu)+\mu(9K+8\mu)} \qquad (4\text{-}7)$$

$$= \sum_{m=1}^{M} \alpha_m \left[1 + \frac{dc}{c}(\alpha_{mn}, P_n)\right] \left[T_{ijij}(\alpha_{mn}) - \frac{1}{3} T_{iijj}(\alpha_{mn})\right] \frac{c(\alpha_m)}{\alpha_m}$$

Equations (4-6) and (4-7) are of the form y=Ax. The data vector y is identified with the left-hand-sides of (4-6) and (4-7) instead of just K_n^* and μ_n^* in order to preserve the linearity of the system. The parameter (or model) vector x is identified with $c(\alpha_m)/\alpha_m$ instead of just $c(\alpha_m)$. Both are done to maintain the scale of the problem for easier numerical solution. The data vector y as constructed now has a magnitude of about unity, independent of the system chosen. The model vector x now ranges from less than one to about 0.1, whereas if we had chosen $c(\alpha_m)$, its value would

range from 0.1 to 10^{-5} or less, and the condition number for the matrix A would be much worse. The coefficient matrix A is identified with the rest of the right-hand-side of (4-6) and (4-7).

If we have observations from L saturation conditions, then the dimension of the data vector y will be 2LN. The dimension of the model vector x is only M-1 because we have the constraint that the sum of the concentrations at each aspect ratio must add up to the porosity of the rock ϕ , a known quantity. We can satisfy this constraint by taking

$$c(\alpha=1) = \phi - \sum_{m=2}^{M} c(\alpha_m) \qquad (4\text{-}8)$$

The coefficient matrix A is thus of the order 2LN by M-1.

4.1.2 Solution and Resolution:

The linear simultaneous equations formulated for inversion in the preceeding section is only a first order approximation to the rock system, as discussed in chapter 2. Besides that fact, there are other approximations introduced when we apply this system to data. As discussed in Chapter Four and in Toksöz et al. (1976), the expression for dc/c (α_m, P_n) (eq. 3-6) is a function of K_A^*, the static bulk modulus of the rock, and $\hat{K}_A$, $\hat{\mu}_A$, the static bulk and shear moduli of the rock with cracks of aspect ratio α_m left out. Since we do not know the values for these moduli we have taken them to be the same as the effective dynamic moduli of

of the dry or gas-saturated rock; and in the cases in which we have only liquid-saturated data, to be that of the effective dynamic moduli of the rock. The error we make by this assumption is of second order, and is consistent with the order of approximation in the system.

As a general rule of thumb, we take M, the number of aspect ratios, to be roughly equal to N, the number of pressure increments. Since A is a 2LN by M-1 matrix, the system y=Ax is an overdetermined system of linear equations. We can solve this system by constructing the stochastic or damped least squares inverse A_s^{-1}, given by (Franklin, 1970)

$$A_s^{-1} = (A^T A + \varepsilon^2 I)^{-1} A^T \qquad (4\text{-}9)$$

where ε is an adjustable parameter relating to the smallest eigenvalue of $A^T A$ one allows in the solution. The solution $x_s = A_s^{-1} y$ is related to the least squares solution $\bar{x}$ through the resolution matrix R, given by

$$R = (A^T A + \varepsilon^2 I)^{-1} A^T A = A_s^{-1} A \qquad (4\text{-}10)$$

R gives us the information of how uniquely we can resolve the individual parameters in x. If we take $\varepsilon = 0$ and if $A^T A$ is non-singular, then R = I, the identity matrix, and we get the least squares solution and it is unique. If R is not the identity matrix, then the off-diagonal elements in R gives us information about the interdependence of the parameters in x. There is a trade off between the resolution

of our solution and the variance in the results. By increasing ε , it is possible to get a reasonable bound on the variance in the solution, but we will have to sacrifice the resolution in the process. Decreasing ε will increase the resolution but will also increase the variance. The calculation of the variance of the solution through the covariance matrix is discussed in Appendix C.

4.2 The Linearized Iterative Inversion:

4.2.1 Formulation:

The linear inversion described above is based on the first order theory of Kuster and Toksöz (1974a). In this section we would like to introduce a linearized iterative inversion based on the integral equation extension to the first order theory discussed in section 2.5 of this thesis.

The idea behind a linearized iterative inversion is as follows: If we have a nonlinear relationship between model and data, i.e., $y = A(x)$, then expanding in a Taylor series around an inital guess model x_o, we have, ignoring terms of second and higher orders in Δx,

$$y(x_o+\Delta x)=y(x_o) + \frac{\partial A}{\partial x}\Big|_{x_o} \Delta x$$

or
$$\Delta y = \frac{\partial A}{\partial x}\Big|_{x_o} \Delta x \qquad (4\text{-}11)$$

where
$$\Delta y = y(x_o+\Delta x) - y(x_o)$$

If we take $y(x_o + \Delta x)$ to be the observed data, then Δx will be the difference between the actual model and the initial guess model. Hence (4-11) gives a linear relationship between Δy, the difference in the observed and predicted data, and Δx. Using an initial guess model x_o, we can calculate Δy, and by inverting eq.(4-11), obtain Δx, the change in the model necessary to fit the data. Since this is accurate to only first order in Δx, the answer we get will not, in general, give us the exact solution. We improve our solution by modifying x_o by Δx, and repeat the whole process until the changes in the model are reasonably small.

We shall apply this method to the integral equation extension of the first order theory, given by eq.(2-56) and (2-57)

$$K^*-K = \frac{(K'-K)}{3}\int^{c(\alpha)} T_{iijj}\,dc(\alpha)$$

and

$$\mu^*-\mu = \frac{(\mu'-\mu)}{5}\int^{c(\alpha)} [T_{ijij} - \frac{1}{3}T_{iijj}]\,dc(\alpha)$$

Assuming an initial model of $c_o(\alpha)$ and expanding in an increment of $\Delta c(\alpha)$, we have

$$\frac{K^*-K_o}{K'-K_o} = \frac{T_{iijj}}{3}\Delta c(\alpha) \qquad (4\text{-}12)$$

and

$$\frac{\mu^*-\mu_o}{\mu'-\mu_o} = \frac{1}{5}[T_{ijij} - \frac{1}{3}T_{iijj}]\Delta c(\alpha) \qquad (4\text{-}13)$$

where K_o and μ_o are the effective bulk and shear moduli of the rock calculated with initial model $c_o(\alpha)$, T_{iijj} and

T_{ijij} are evaluated at K_o and μ_o, and K* and μ* are the observed effective bulk and shear moduli of the rock. The matrix moduli K and μ comes in only implicitly through T_{iijj} and T_{ijij}.

We can do a similar expansion with Kuster and Toksöz's formulation (eq. 2-58 and 2-59) This will result in identical right-hand-sides as that of eq.(4-12) and (4-13) but with a more complicated left-hand-side. As pointed out in section 2.5.2, the two formulations give the same results, the only difference being the rate of convergence. Since we are dealing with Δc, the changes in the concentration, rather than c, the concentration itself, this difference is insignificant and we can use the simpler expression without significant losses in the rate of convergence.

The effect of pressure can be taken into account in the same way as in the case for linear inversion, so is the effect of more than one aspect ratio. At a pressure of P_n and for a group of aspect ratios α_m, m = 1,...M, we have, analogous to (4-6) and (4-7),

$$\frac{K_n^*-K_{on}}{K'-K_{on}} = \sum_{m=1}^{M} \frac{\alpha_m}{3}[1+\frac{dc}{c_o}(\alpha_{mn},P_n)]T_{iijj}(\alpha_{mn})\frac{dc(\alpha_m)}{\alpha_m} \quad (4\text{-}14)$$

and

$$5(\frac{\mu_n^*-\mu_{on}}{\mu'-\mu_{on}}) = \sum_{m=1}^{M} \alpha_m[1+\frac{dc}{c_o}(\alpha_{mn},P_n)].$$

$$[T_{ijij}(\alpha_{mn}) - \frac{1}{3}T_{iijj}(\alpha_{mn})]\frac{dc(\alpha_m)}{\alpha_m} \quad (4\text{-}15)$$

The constraint on the porosity has a different form. The sum of concentrations being equal to a constant, the porosity, implies that the sum of the changes in the concentrations must be equal to zero, i.e.

$$\Delta c(\alpha=1) = -\sum_{m=2}^{M} \Delta c(\alpha_m) \qquad (4\text{-}16)$$

For N pressure points and L saturation conditions, the coefficient matrix $\partial A / \partial x$ remains of the order 2LN by M-1, the same as in the linear case.

4.2.2 Solution and Resolution:

One of the chief sources of error introduced by the linear inversion is in the calculation of dc/c (see section 4.1.2). In the case of the linearized iterative inversion, we are able to correct some of these errors. We still have no information on the static moduli of the rock. However, since we have an initial trial model, we can calculate the dynamic moduli of the dry rock, i.e. we can calculate, from our initial model, the dynamic bulk modulus of the dry rock K_d^*, as well as $\hat{K}_d$ and $\hat{\mu}_d$, the dynamic bulk and shear moduli of the dry rock with cracks of aspect ratio α_m left out. This is an overestimate since in laboratory measurements it was found that for most rocks, K_A^* is less than K_d^* at atmospheric pressure, with the difference decreasing as the confining pressure increases (Simmons and Brace, 1965; King, 1964). The errors made by this approximation will still be

less than that made by the linear inversion, and are at least consistent with those in the direct problem (Toksöz et al., 1976).

The solution of the linearized system (4-14) and (4-15) together with the constraint (4-16) can be obtained in a similar way as that of the linear inversion, namely by means of the damped least squares inverse. In this case, however, we have to be more careful in the interpretation of the resolution and covariance matrices, since we are dealing with changes in the model and data instead of the actual model and data themselves. A more detailed discussion is given in Appendix C, and we shall not go into the subject here. Finally, the solution of the linear inversion can be used as the initial model for the linearized iterative inversion.

4.3 The Linear Programming Inversion:

4.3.1 Formulation:

The third and final inversion we are going to discuss is the linear programming method. The idea behind linear programming is to maximize or minimize a given linear objective function subject to a given set of constraints. The variables are keep positive at all times. This method has been widely used in economics and industrial engineering for a long time and has only recently been applied to geophysical problems (Johnson, 1972; Lee and Solomon, 1975).

In the case of two-phase materials we are discussing here, the linear programming problem is posed as follows: we start out with the linear system defined in section 4.1, i.e. $y = Ax$. We then define a solution model vector x_u and an error vector e_u satisfying the constraint

$$Ax_u + e_u = y \tag{4-17}$$

together with the linear objective function that the sum of the components of the error vector e_u be a minimum, i.e.

$$\sum_{i=1}^{2LN} e_{ui} = \text{minimum} \tag{4-18}$$

Since y is basically a vector containing the difference between the effective and matrix moduli (see eq. 4-6 and 4-7), and since one of the constraints of a linear program is that the solution is positive, this solution corresponds to the upper bound in the resultant effective moduli.

Similarly, we can define a lower bound solution x_l and a lower bound error vector e_l by

$$Ax_l - e_l = y \tag{4-19}$$

together with the objective function

$$\sum_{i=1}^{2LN} e_{li} = \text{minimum} \tag{4-20}$$

Finally, we can define an average solution

$$\bar{x} = \frac{1}{2}(x_u + x_l) \tag{4-21}$$

with the corresponding error vector $\bar{e}$

$$\bar{e} = |A\bar{x} - y| \tag{4-22}$$

It should be noted that we are minimizing the error and not the squares of the error in the linear programming inversion. The motivation of using a linear program in the present problem is that physically the model vector we are inverting for consists of fractional concentrations of cracks of different aspect ratios and are always positive. This point is not automatically guaranteed in the least squares inversion.

4.3.2 Solution and Resolution:

The solution of a linear program is done by the revised simplex method, the mathematical intricacies of which we will not go into in this thesis (for a detailed discussion see Dantzig, 1963; Luenberger, 1973 and Strang, 1976). Briefly, the way we have set up our linear program, each linear equation in x and e represent a M dimensional hyperplane in a 2LN+M-1 dimensional space. These constraints, together with the constraints that the solution be positive define a 2LN+M-1 dimensional space in which all solutions satisfying these constraints lie. This set of solutions is a convex set, i.e., all points on a line joining two possible solutions are themselves possible solutions. The revised simplex method is a method to find the minimum (or maximum) in the objective

function among this set of possible solutions.

In our application to the two-phase materials, we used a prepackaged IBM subroutine (DOSP from subroutine library -- mathematics) in order to avoid unnecessary programming errors. This program automatically reinverts the matrix after a prescribed number of operations in order to preserve the accuracy of the solution.

The question of resolution and variance of the solution is addressed in a completely different form from the least-squares inversion. For our linear program, the question in the variance in the solution is easily answered. The variance in the average model $\bar{x}$, called $\Delta\bar{x}$, is given by

$$\Delta\bar{x} = \frac{1}{2}|x_u - x_l| \tag{4-23}$$

This is obviously justified since the upper and lower solution provides an envelope to the data. As a matter of fact, we shall find out in the next chapter that the variance so defined are in gereral larger than that defined through the covariance matrix in the least squares inversion.

The question of resolution is again different from that of the least squares inversion. The linear programming inversion does not couple different components of the solution vector, hence the resolution is always perfect. A poorly resolved component of the model vector usually results in that component being set to zero in the solution. Furthmore, if a particular constraint is incompatible with the rest,

then the program will automatically reject the system and a different model vector has to be selected. There are other ways of setting up a linear program (see Lee and Solomon, 1975). If one has a priori knowledge of the variance in the data, then the scheme of Lee and Solomon would be more appropriate than the one we used. Their technique involves finding the upper and lower bound of the solution such that the error vector is less than the variance in the data. This technique will generate more incompatible constraints than our method since the solution space is reduced.

4.4 Comparisons of Different Inversion Techniques:

The most direct comparison between different theories is their respective fits to data. To obtain the fit to data we first calculate the pore-aspect ratio spectrum of a rock by one of the three inversion schemes. We then substitute the spectrum back into the direct problem. We can measure how good the fit is by the estimate of variance in the data (see Appendix C). We shall base our comparison on three different rocks: a high (25%) porosity sandstone (Boise), a medium (16.3%) porosity sandstone (Berea) and a low (0.9%) porosity granite (Westerly). The data we use are ultrasonic measurements of seismic velocities under a confining hydrostatic pressure and, in some cases, an internal fluid pressure. The Boise and Berea sandstone data have been presented in Chapter 3 in conjunction with the

direct problem. The Westerly granite is similar to the Troy granite and the velocity data was obtained by Nur and Simmons (1969). For the Boise sandstone and Westerly granite, the fluid pressures are maintained at one atmosphere, while for the Berea sandstone the fluid pressure is kept at 0.465 of that of the confining pressure. We have chosen, for the linear and linearized iterative inversions, a damping coefficient $\varepsilon = 1$. For the linearized iterative inversion, we have taken the results of the linear inversion as our starting model, and the number of iterations is chosen to be five, unless a local error of less than five percent is acheived first. The effects of these choices will be discussed in section 4.6.

4.4.1 Inversion Procedure:

Before carrying out the actual inversion, we have to set up the coefficient matrices properly. We do not have actual measurements of the matrix moduli of any rock. We can estimate K and μ by the following procedure: we assume at the highest pressure point the observed K^* and μ^* are due to K and μ with all the porosity in the spherical pores. From previously calculated values (e.g. figure 3-1 in this thesis and figure 2 in Kuster and Toksöz, 1974a) we can estimate K and μ. This estimate will be revised as we proceed with the inversion to keep the calculated K^* and μ^* at high pressures in agreement with the observed K^* and μ^*.

The second point we have to consider is the choice of aspect ratios for the spectrum. This choice is obviously limited by both the pressure range and the pressure increments of the data. Furthermore, the rate of closing of the cracks is dependent on the dynamic bulk modulus of the dry rock K_d^* (see Chapter 3), and the rate is different from one rock to another. As a result, the critical aspect ratio that closes at a particular pressure is different for different rocks and we have to adjust accordingly. Ideally, for the best resolution, we would like to have one aspect ratio crack for each pressure point. This way the pore aspect ratio spectrum will decrease by one aspect ratio at each pressure point and will have very good resolution for that aspect ratio crack. As a rule of thumb, we can estimate the largest aspect ratio that will close at the highest pressure point by substituting K_d^* for K in eq. (3-2). We can then divide the aspect ratio spectrum into the same number of aspect ratios as there are pressure points. Each aspect ratio will then be roughly scaled with respect to the highest one in the same ratio as the pressure points. We add in vugular pores (α = 1, 0.1 and in some cases 0.01) to account for the porosity and the lower dry p-wave velocity at high pressures. Again we will have to adjust the aspect ratio spectrum as we proceed with the inversion in order to obtain the optimal results.

4.4.2 Inversion Results:

Figures (4-1) and (4-2) show the fits of the three inversion methods to the Berea sandstone. The data was obtained by Jones et al. (1977). In figure (4-1) we have plotted the results of the linear inversion and the linearized iterative inversion. In figure (4-2) we have plotted the results of the linear programming inversion. We can observe in figure (4-1) that both the linear and the linearized iterative inversions fit the data rather well. They both fit the brine-saturated p-wave velocities and both s-wave velocities. They predict a lower p-wave velocity for the gas-saturated rock at low pressures ($P_d \leq 200$ bars) than that observed. The differences between the observed and inversion velocities are, as expected, slightly more the the linear inversion than for the linearized iterative inversion. This is confirmed by the variances in the solutions. The results of the two schemes are so similar, however, that one does not have a significant improvement over the other. The pore-aspect ratio spectra and variances are given in Table (4-1) together with the spectra of the Boise sandstone and the Westerly granite.

Figure (4-2) shows the results of the linear programming inversion. The shaded areas represent the ranges of possible solutions defined by the upper and lower bound solutions. The solid lines within the shaded areas represent the average solutions. It is obvious from the figure that the average

solutions do not fit the observed data as well as the two previous inversion schemes. Furthermore, the upper and lower bounds are too far apart, especially in the case of p-wave velocities of the gas-saturated rock, to be of much significance. This is because the upper and lower bound approach we used is very sensitive to any error in the data. There are other formulations that can minimize the effects of a bad data point (Lee and Solomon, 1975, 1978) but those will reduce the resolution of some of the aspect ratios rather arbitrarily.

The next set of data used in the comparison is that of the Westerly granite data obtained by Nur and Simmons (1969). Figure (4-3) shows the results of the linear and linearized iterative inversions. The results are very similar to those of the Berea sandstone. There are no significant differences between the results of the linear and linearized iterative inversions for V_p-wet, V_s-wet and V_s-dry. The iterative scheme does give a better fit to the observed data for V_p-dry than the linear inversion. The linearized iterative inversion predicts higher p-wave velocities for the water-saturated rock at low pressures than those observed and the linear inversion predicts lower p-wave velocities for the dry rock at low pressures than those observed. As we will discover, this phenomenum exists for most rocks we performed the inversion schemes on. Possible explanations will be discussed later.

Figure (4-4) shows the results of the linear programming inversion. As in the case of Berea sandstone, the range of solution defined by the upper and lower bounds are quite large, especially for the p-wave velocities of the dry rock. The average solutions for V_p-wet, V_s-dry and V_s-wet are reasonably close to the observations but that of V_p-dry is quite far off. The reason for this behavior can again be traced to the errors in the data, particularly low pressure data.

The third and final set of data used in the comparison is that of Boise sandstone measured by King (1966). King measured the velocities of the rock under three saturation conditions: dry, kerosene-saturated and brine-saturated. Here we inverted the dry and kerosene-saturated data only. Figure (4-5) shows the results from the linear and linearized iterative inversions.

Once more, as in the previous two cases, the linear inversion fits the p- and s-wave velocities of the kerosene-saturated rock but it predicts lower p- and s-wave velocities for the dry rock. The differences between the observed and predicted velocities are much more than those in the previous cases. The linearized iterative inversion, however, fits the observed V_p-dry much better, and does a reasonably good job of fitting the s-wave velocities of both the kerosene-saturated and dry rock. Again the observed p-wave velocities of the kerosene-saturated rock are higher than predicted at low pressures. The linear programming inversion gives

totally erroneous results and they are not plotted.

It is evident from the above observations that the linearized iterative inversion consistently give the best results, as expected. The linear inversion does a good job in most cases but is off in some cases. It does provide a good starting model for the linearized iterative inversion. The linear programming inversion, as it was set up, runs a poor third. We have therefore taken the linearized iterative inversion to be our approach in the later sections in the determination of the pore-aspect ratio spectra of different rocks.

4.5 Resolution:

After we have decided on the inversion method, we would like to examine the resolution of the method. In order to do this, we focus mostly on one rock, the Berea sandstone. Besides the usual approach of examining the resolution matrix, we will discuss the resolution in terms of how the solution vary with changes in the matrix moduli, the aspect ratios used, the number of aspect ratios used and the number of data points used.

4.5.1 The Resolution Matrix:

The resolution matrix gives us the resolution between the different components of the model vector in our solution. In our present case this represents the relative resolution

between the changes in the fractional concentration at each aspect ratio we have chosen in our initial model. In the linear inversion, it is the relative resolution between the concentrations of each aspect ratio. Without the damping factor ε, the resolution matrix will be the identity matrix, unless the rank of the coefficient matrix A is less than the dimension of the model vector. For the linear inversion, and thus the initial model of the linearized iterative inversion, the rank of the coefficient matrix is usually equal to the dimension of the model vector, i.e., the number of aspect ratios we used. For the linearized iterative inversion, however, this is not necessarily the case. Small changes in the velocities at high pressures will result in relatively large changes in the concentrations of the larger aspect ratio cracks that are closing at these pressures. In other words, the concentrations of these large aspect ratio cracks are more sensitive to the errors in the velocities. Hence we cannot always get good constraints on the relative changes in the concentrations of large aspect ratio cracks without a damping factor. We will discuss this further in the section on the effects of ε on the variance of the solution.

The resolution matrix for the Berea sandstone from the linear inversion is given in Table (4-2). The damping factor ε is taken to be one. The diagonal elements of the resolution matrix are between 0.5 and 0.8, indicating relatively good

resolution between the aspect ratios. These kind of numbers are typical of the results of the linear inversion. The resolution matrix of the fifth iteration of the linearized iterative inversion is also shown in Table (4-2). It is similar to that of the linear inversion, with the diagonal elements between 0.6 and 0.8. Hence the iterative inversion also seems to be rather well resolved.

4.5.2 The Matrix Moduli:

We have mentioned in the introduction to section 4.4 that we have to adjust the matrix moduli as we do the inversion for optimal results. This is because we do not have direct measurements of the matrix moduli. We would like to examine the dependence of the inversion results on the matrix moduli chosen. In figure (4-6) we have plotted the results of the linearized iterative inversions for Boise sandstone with different matrix moduli (K = 0.31 Mb, μ = 0.19 Mb in one case and K = 0.3 Mb, μ = 0.19 Mb in the other). There are no drastic changes between the two results. The predicted velocities are a little higher for the results of the model with a higher matrix bulk modulus, as can be expected. The two pore-aspect ratio spectra are given in Table (4-3). We can see that the concentrations of the smaller aspect ratio cracks are very similar in the two cases, but those of the larger aspect ratio cracks are not. Specifically, we have higher concentration at α = 0.1 for the case with the higher

matrix modulus than the other case. The other combinations of K and μ we have tried are K = 0.31 Mb, μ = 0.18 Mb and K = 0.3 Mb and μ = 0.18 Mb, among other combinations. In both cases the inversion becomes slightly unstable and resulted in negative concentrations in one or more of the aspect ratios. These instabilities disappear as we increase the damping factor ε. A further discussion on the effects of ε is given in section 4.6.2.

Thus the results seem to indicate that there is a limited range of the matrix moduli we can use in our inversion schemes. In practice it takes no more than a few tries before one finds an optimal combination of K and μ.

As to inversions dealing with data that are water- or brine-saturated, the discussion in section 3.2.2 concerning the effects of clay in some sandstones has to be taken into account. Because of the interaction between water and clay, we will have to lower the matrix shear modulus of a water- or brine-saturated sandstone by 4-5 percent from the value used for the dry rock in order to get consistent results. The values we present in Table (4-1) for the Berea sandstone reflect this change. This procedure is also carried out for all water- or brine-saturated sandstone data (Berea, Boise and Navajo) we discuss in later sections.

4.5.3 The Choice of Aspect Ratios:

As in the case of matrix moduli, there is no one

deterministic way of specifying the aspect ratios and how many of them to be included in the model vector. We have discussed the general guidelines in section 4.4. In this section we would like to examine the effects of changes in the aspect ratios we specified in the model vector.

To a certain extent, we could only resolve the parameter concentration divided by the aspect ratio (c/α) at each data point. This is analogous to the problem of inverting for the structure of the earth using group and phase velocities of surface waves (Lee and Solomon, 1975; Solomon, 1972). In that case one can only determine the velocity structure if one specifies the layer thickness. It is not possible to resolve both the velocity structure and layer thickness simultaneously. In our case we cannot resolve both c and α simultaneously but we can determine $c(\alpha)$ given the aspect ratios.

In order to examine the sensitivity of our inversion to the changes in the aspect ratios specified in the model, we have inverted the Berea sandstone data using different aspect ratios but keeping the matrix moduli and the damping constant. The pore-aspect ratio spectra obtained are presented in Table (4-4a).

The model C1 is the one we have presented in the previous section. C2 is a model with a slightly higher value for each aspect ratio (except those of the vugular pores). C3 is a model with lower values for the crack aspect ratios. C4 is a variation of C3 to cover all 10^{-4} increments of aspect

ratios from 2×10^{-4} to 1.9×10^{-3} not covered by C1, C2 and C3. The results are quite similar. In fact, if we plotted the resultant velocities on the same figure, we would have a tough time distinguishing the different models. On the average least squares sense, C1 still gives the best fit, as shown by the estimate of the variance σ_y^2. Model C2 is the next best with models C3 and C4 similar to each other but with larger variances than the other two. The differences in σ_y^2 between the four models are only about thirty percent.

The pore-aspect ratio spectra tell a similar story. The concentrations at the vugular pores (α = 1, 0.1 and 0.01) are almost identical for all four models, as can be expected. The concentrations at the small aspect ratios, however, show much larger variations from model to model. This is especially true for the models C3 and C4 when compared with models C1 and C2. Models C3 and C4 are very similar to each other, although C4 has an extra aspect ratio crack ($\alpha = 1.9 \times 10^{-3}$) specified.

Comparing models C1 and C2 we found that the concentrations at $\alpha = 1.7 \times 10^{-3}$ and 1.8×10^{-3} are very similar. Model C2 has slightly more small aspect ratio cracks ($\alpha < 10^{-3}$) and slightly less large aspect ratio cracks ($2 \times 10^{-3} > \alpha \geq 10^{-3}$) than model C1. The total crack concentrations ($\alpha < 10^{-2}$) are very similar (0.68×10^{-3} for C1 and 0.69×10^{-3} for C2).

If we look at the spectra in terms of c/α, the similarity between models C1 and C2 are just as evident (Table 4-4b).

The small aspect ratio cracks differ in c/α by about ten percent, while the c/α of the larger cracks differ slightly more. In both cases the differences between the two models are within the estimates of the variances of the solutions, i.e., their error estimates overlap.

The comparison between models C3 and C4 is similar to that between models C1 and C2. In this case model C4 has more of the larger aspect ratio cracks ($2 \times 10^{-3} > \alpha \geq 10^{-3}$) and less of the smaller aspect ratio cracks ($\alpha < 10^{-3}$) than model C3. The extra non-vugular aspect ratio crack introduced at $\alpha = 1.9 \times 10^{-3}$ for C4 has a minimal effect since it has only a concentration of 1.679×10^{-5} and a c/α ratio of 0.0088. All it does is to increase the total crack concentration slightly. The c/α versus aspect ratio spectra are very similar between C3 anc C4, as are the estimates of variances.

Lastly we want to compare models C1 and C3. Of the five aspect ratios used in each of the crack spectra, concentrations of the thicker three (1.7, 1.4 and 1×10^{-3} for C1; 1.6, 1.3 and 0.9×10^{-3} for C3) aspect ratio cracks are very similar to each other. For the two smallest aspect ratio cracks, the situation is a little different. The sums of the concentrations of these two aspect ratio cracks are similar for the two models (0.244×10^{-3} for C1 and 0.25×10^{-3} for C3). The concentrations of the individual aspect ratio cracks, however, are different. It seems that the division of the aspect ratios are such that the concentration of the 0.5×10^{-3}

aspect ratio crack of model C3 includes the concentration of the 0.6×10^{-3} aspect ratio crack of model C1 plus about half of the concentration of the 0.3×10^{-3} aspect ratio crack, leaving the other half of the concentration to the 0.2×10^{-3} aspect ratio crack of model C3. This phenomenon is also present in the c/α versus α spectrum (see Table 4-4b).

It is thus evident from the above discussions that changing the aspect ratios specified in the spectrum does not significantly change the resulting concentration versus aspect ratio spectrum or the fit to the data, as long as we spread out the aspect ratios evenly and in accordance to the pressure increments. This, together with the relatively good resolution matrices we obtained from our damped least squares inversions, indicates our system is well resolved and the results are meaningful.

4.5.4 The Number of Data Points:

The third factor that can affect the resolution of our solution is the number of data points. As we have discussed earlier, the aspect ratio spectrum specified is roughly proportional to the pressures at which the data were taken. Thus, in order to get the best coverage of aspect ratios over the whole spectrum, sometimes it is necessary to interpolate between the actual data points or to drop one or more pressure points from the data set so that we do not have a situation where there is an overabundance of data within one pressure

range and a lack of data within another.

As for the experimental accuracy of the data, Johnston (personal communications) pointed out that in general it is more accurate for the higher pressure data than for the low pressure data owing to the fact the coupling between the sample and the transducers is better at higher confining pressures. Johnston estimated that the errors in the velocity measurements are roughly three percent above 200 bars but increase at low pressures and could be as high as ten percent at zero confining pressure. These are the upper limits on the errors, and by no means represent the average errors, especially in the low pressure range. However, an error of about five percent at zero pressure is not unreasonable. This is particularly true for older data (e.g. those of Nur and Simmons, 1969 and King, 1966). In some cases, if one calculates the bulk moduli of the water-saturated rock from the p- and s-wave velocities, one would find that they decrease instead of increase with pressure in the low pressure region. There is no elastic theory that would explain this behavior and this can be traced to the errors in the measurements of the p- and s-wave velocities.

It would be, therefore, instructive to find out the effects of the zero pressure data point on the results of the inversion. Figure (4-7) shows the results of the linear and linearized iterative inversions for Westerly granite with zero pressure data included. The results are almost identical

to the results plotted in figure (4-3), which do not include the zero pressure data. The spectra, excluding the smallest aspect ratio (included for the extra data point), are very similar to each other. The differences between them are within the estimates of the variances in the solutions. These spectra are given in Table (4-5).

We have also examined the effects of including higher pressure data. This has an even less effect on the fit to the data. The concentrations of the smaller aspect ratio cracks (corresponding to the lower pressure data) are virtually unchanged, as expected. There is a little readjustment of the concentrations of the higher aspect ratio cracks, but the changes are within the estimated variances in the solution.

4.5.5 Scaling:

One of the most important keys to obtaining good resolution is scaling. We have discussed this point briefly earlier in this chapter when we were setting up the problem. We have scaled the model vector by inverting for c/α instead of just c. We have also scaled the data vector in a less obvious way. For the shear components, instead of just $(\mu^*-\mu_o)/(\mu'-\mu_o)$, we have moved the factor of five from the right hand side of eq. (4-13) to the left hand side of eq. (4-15). A similar scaling was done in the linear inversion (eq. 4-7). This is done to keep the components of the coefficient matrix at roughly the same order. The result of this is that the

diagonal elements of the resolution matrix (see Table 4-2) varies over a narrow range of 0.6 to 0.8.

What will the result be if we have not done this scaling? First the range of the eigenvalues of the matrix A^TA would be large, giving poor resolution. Table (4-6) shows the resolution matrix of the fifth iteration of the linearized iterative inversion without scaling. We have left the factor of five in the right hand side of eq. (4-13) where it is, i.e., eq. (4-15) becomes

$$\frac{\mu_n^*-\mu_{on}}{\mu'-\mu_{on}} = \frac{1}{5}\sum_{m=1}^{M}\alpha_m[1 + \frac{dc}{c_o}(\alpha_{mn},P_n)]$$

$$[T_{ijij}(\alpha_{mn}) - \frac{1}{3}T_{iijj}(\alpha_{mn})]\frac{dc(\alpha_m)}{\alpha_m} \qquad (4\text{-}24)$$

It is obvious from Table (4-6) that the resolution suffers greatly without the scaling. Most of the diagonal elements of the resolution matrix are around 0.2 to 0.3 with the smallest aspect ratio crack having a relative resolution of less than 0.1. This kind of resolution is less than ideal.

A second effect of scaling is that it puts proper emphasis on the fits to various data. Figure (4-8) shows the results of the inversions of Berea sandstone data with and without scaling. The results of the scaled inversion fit three sets of data: brine-saturated V_p, V_s and gas-saturated V_p, perfectly. On the other hand, the results of the unscaled inversion fit only the gas-saturated V_p data perfectly. Since the gas-saturated V_p data is probably the worst of the four

data sets because of possible moisture contamination of the fine cracks (Johnston, 1978), it is obvious that the scaled inversion results are much more dependable. Another telltale fact is that the scaled inversion results fit both s-wave velocities perfectly whereas the unscaled results do not. Since the effective shear modulus of a rock is less sensitive to the possible contamination of the fine cracks, we can conclude that the scaled inversion results are probably more realistic.

4.6 Variance:

One of the main reasons for adopting the damped least squares inversion is that we can get an optimal trade off between the resolution and variance in the solution by adjusting the damping factor ε. In this section we will examine this trade off as a function of the damping factor. We will also examine the convergence of the linearized iterative inversion by calculating the variance in the data as a function of the number of iterations.

4.6.1 The Covariance Matrix:

The covariance matrix relates the covariances in the solution to the covariances in the data. In geophysical problems, we have always assumed that the variances in the data are independent of and equal to each other. We have made the same assumption here. This is actually not totally

justifiable since we are not measuring the bulk modulus directly but obtaining it from measured V_p and V_s. Hence the variance of the observed bulk modulus is actually more than that of the shear modulus, assuming the same variances in the observed V_p and V_s. On the other hand, since all we are interested in finding are the variances in the resultant concentrations at each aspect ratio and not worrying too much about the covariances between the components of the solution vector, the assumption of a simple and independent variance in the data is adequate.

Table (4-7) shows the covariance matrix of the linear inversion of the Berea sandstone data. The diagonal elements ranges from 0.1 to 0.2. The off-diagonal elements are small compared to the diagonal elements and are all less than half of their values. This implies that the correlation between any two components of the solution vector is not too significant. The covariances between the different components of the solution are therefore ignored.

4.6.2 Damping:

The effects of introducing a damping factor ε into the least squares solution are two fold: to get a better trade off between the resolution and the variance of the solution and to stablize the linearized iterative inversion in some cases. In this section we will examine the effects of the trade off both theoretically and when applied to laboratory

measured velocity data. We will also discuss the effects of damping on the stability of the iterations.

The least squares generalized inverse can be written as (Aki and Richards, 1978; Golub and Kahan, 1965; Wiggins, 1972; Lanczos, 1961):

$$A_g^{-1} = V \Lambda^{-1} U^T \tag{4-25}$$

where Λ is a diagonal matrix whose elements λ_i are the singular values of A, i.e., they are the non-negative square roots of the eigenvalues of A^TA (or AA^T in the case of an underdetermined system). U and V are matrices of eigenvectors satisfying the following relationships:

$$AA^TU = \Lambda^2 U \tag{4-26}$$

and

$$A^TAv = \Lambda^2 V \tag{4-27}$$

The orthonormal condition of the eigenvectors gives us the following:

$$U^TU = V^TV = I \tag{4-28}$$

If the number of non-zero eigenvalues of A^TA is $p < n$, the number of columns of A, then the least squares inverse becomes

$$A_g^{-1} = V_p \Lambda_p^{-1} U_p^T \tag{4-29}$$

where U_p, Λ_p and V_p are of dimensions m x p, p x p and n x p

respectively.

The damped least squares inverse is given by:

$$A_s^{-1} = (A^TA + \varepsilon^2 I)^{-1}A^T \tag{4-30}$$

In terms of U_p, Λ_p and V_p, this can be written as

$$A_s^{-1} = V_p \frac{\Lambda_p}{\Lambda_p^2 + \varepsilon^2} U_p^T \tag{4-31}$$

since the eigenvalues of $(A^TA + \varepsilon^2 I)$ are $\lambda_p^2 + \varepsilon^2$.

The covariance matrix of the solution can be expressed as

$$\langle \Delta x \cdot \Delta x^T \rangle = \sigma_y^2 (A^TA + \varepsilon^2 I)^{-1} A^TA (A^TA + \varepsilon^2 I)^{-1}$$

$$= \sigma_y^2 V_p \frac{\Lambda_p^2}{(\Lambda_p^2 + \varepsilon^2)^2} V_p^T \tag{4-32}$$

Similarly the resolution matrix R is given by

$$R = A_s^{-1}A = (A^TA + \varepsilon^2 I)^{-1}A^TA$$

$$= V_p \frac{\Lambda_p^2}{\Lambda_p^2 + \varepsilon^2} V_p^T \tag{4-33}$$

It is thus clear from eq. (4-32) and (4-33) that the introduction of the damping factor ε reduces both the resolution and the covariance in the solution. The estimate of variance in the data, σ_y^2, will of course increase as ε increases since $|y - Ax|^2$ is minimum for x being the least

squares solution.

Table (4-8) shows the resultant pore-aspect ratio spectra of the linear inversion of Berea sandstone data without damping and with the damping coefficient $\varepsilon = 1$. The resolution matrix for the later case is given previously in Table (4-2). The resolution matrix for the undamped case is of course the identity matrix.

As expected, the estimated variance for the data σ_y^2 is slightly larger for the damped than for the undamped case. The variances in the damped solution, however, are down by about a factor of two from the undamped case. The greatest decrease comes in the concentrations of the larger aspect ratio cracks ($\alpha = 1.7 \times 10^{-3}$, 10^{-2}, etc.). Although these results are for the linear inversion, we can expect similar behavior for the linearized iterative inversion, based on the resolution matrices (see Table 4-2).

The second point we should observe in this comparison is the appearance of a negative concentration at $\alpha = 10^{-2}$ for the undamped case. This is because the inversion scheme does not require that the solution remains positive. However, if we add in a damping factor, this peculiar phenomenon disappears. This is true in a number of cases we have tried and is related to the errors in the solution. If one restricts the errors in the solution by damping, the solution will be constrained to be positive.

One final word about the damping factor ε. The magni-

tudes of the elements of the coefficient matrix A is about unity. Since the number of columns of A is about ten, the diagonal elements of A^TA is of the order of ten also. The damping factor of one is thus about ten percent of the magnitudes of the diagonal elements of A^TA.

4.6.3 The Number of Iterations:

Finally, we would like to examine the convergence characteristic of the linearized iterative inversion. We will approach this question by looking at both the changes in the pore-aspect ratio spectrum and in the estimated variances in the data as a function of the number of iterations.

Table (4-9) shows the resultant pore-aspect ratio spectra and the estimated variances in the data as a function of the number of iterations for the linearized iterative inverion of the Berea sandstone data. As we can see from the table, there are significant changes both in the pore-aspect ratio spectrum and in the estiamted variance in the data in the first one or two iteration steps. By the fifth iteration, however, the solution has stablized to the point that most of these changes are no longer significant. The only concentrations that are changing by any significant amounts (more than one percent or so) are those of cracks of aspect ratios $\alpha = 0.1$ and 0.01. The concentration at the $\alpha = 0.01$ crack is not very well resolved and the error in

the solution is estimated to be roughly the same as the concentration (see Table 4-1). At any rate, since these cracks do no close at the pressure range we are interested in, the only effect they have is that of compensating the matrix moduli to fit the data at the highest pressure. Thus it is expected that the resolution at these aspect ratio cracks will not be as good as the smaller aspect ratio cracks. The lesser resolution, however, will not affect the more important characteristics of the solution at lower pressures and is therefore inconsequential to our results. It can therefore be concluded that the solutions of the linearized iterative inversion is stable and five iterations are adequate to get a final meaningful result.

TABLE 4-1a

Pore-Aspect Ratio Spectra for Berea Sandstone

$K = 0.32$ Mb $\quad \mu_d = 0.255$ Mb $\quad \mu_w = 0.245$ Mb

porosity = 16.3% $\quad \varepsilon = 1$

	Linear Inversion	Iterative Inversion
α	$c(\alpha)$	$c(\alpha)$
1	0.1454 ± 0.00472	0.1399 ± 0.00422
0.1	$(0.1601 \pm 0.0416) \times 10^{-1}$	$(0.2207 \pm 0.0367) \times 10^{-1}$
0.01	$(0.8803 \pm 0.3402) \times 10^{-3}$	$(0.3725 \pm 0.3447) \times 10^{-3}$
0.17×10^{-2}	$(0.2038 \pm 0.0695) \times 10^{-3}$	$(0.1402 \pm 0.0702) \times 10^{-3}$
0.14×10^{-2}	$(0.1217 \pm 0.0623) \times 10^{-3}$	$(0.1363 \pm 0.0567) \times 10^{-3}$
0.1×10^{-2}	$(0.1403 \pm 0.0413) \times 10^{-3}$	$(0.1572 \pm 0.0391) \times 10^{-3}$
0.6×10^{-3}	$(0.1466 \pm 0.0243) \times 10^{-3}$	$(0.1315 \pm 0.0246) \times 10^{-3}$
0.3×10^{-3}	$(0.9453 \pm 0.1422) \times 10^{-4}$	$(0.1126 \pm 0.0135) \times 10^{-3}$
σ_y^2	0.01322	0.00938
		after 5 iterations

TABLE 4 -1b

Pore-Aspect Ratio Spectra for Westerly granite

K = 0.59 Mb μ = 0.32 Mb ε = 1 porosity = 0.9%

	Linear Inversion	Iterative Inversion
α	$c(\alpha)$	$c(\alpha)$
1	$(0.7293 \pm 0.0724) \times 10^{-2}$	$(0.7011 \pm 0.0675) \times 10^{-2}$
0.01	$(0.1207 \pm 0.0475) \times 10^{-2}$	$(0.1514 \pm 0.0436) \times 10^{-2}$
0.17×10^{-2}	$(0.1495 \pm 0.0934) \times 10^{-3}$	$(0.9255 \pm 0.9036) \times 10^{-4}$
0.12×10^{-2}	$(0.7027 \pm 0.6644) \times 10^{-4}$	$(0.5973 \pm 0.6560) \times 10^{-4}$
0.85×10^{-3}	$(0.1005 \pm 0.0471) \times 10^{-3}$	$(0.1536 \pm 0.0445) \times 10^{-3}$
0.55×10^{-3}	$(0.1180 \pm 0.0290) \times 10^{-3}$	$(0.1063 \pm 0.0264) \times 10^{-3}$
0.25 x 10-3	$(0.6170 \pm 0.1267) \times 10^{-4}$	$(0.6248 \pm 0.1271) \times 10^{-4}$
σ_y^2	0.01809	0.01716
		after 5 iterations

TABLE 4-1c

Pore-Aspect Ratio Spectra for Boise Sandstone

$K = 0.31$ Mb $\mu = 0.19$ Mb $\varepsilon = 1$ porosity = 25%

	Linear Inversion	Iterative Inversion
α	$c(\alpha)$	$c(\alpha)$
1	0.2024 ± 0.0092	0.1877 ± 0.0025
0.1	$(0.4611 \pm 0.0808) \times 10^{-1}$	$(0.6176 \pm 0.0222) \times 10^{-1}$
0.35×10^{-2}	$(0.8740 \pm 0.2877) \times 10^{-3}$	$(0.3655 \pm 0.7566) \times 10^{-4}$
0.28×10^{-2}	$(0.2568 \pm 0.2398) \times 10^{-3}$	$(0.6050 \pm 0.6612) \times 10^{-4}$
0.21×10^{-2}	$(0.1262 \pm 1.7810) \times 10^{-4}$	$(0.6377 \pm 0.4942) \times 10^{-4}$
0.17×10^{-2}	$(0.1162 \pm 0.1441) \times 10^{-3}$	$(0.1362 \pm 0.0395) \times 10^{-3}$
0.13×10^{-2}	$(0.9976 \pm 1.0830) \times 10^{-4}$	$(0.1096 \pm 0.0299) \times 10^{-3}$
0.9×10^{-3}	$(0.1078 \pm 0.0741) \times 10^{-3}$	$(0.8516 \pm 0.2145) \times 10^{-4}$
0.5×10^{-3}	$(0.4875 \pm 0.4647) \times 10^{-4}$	$(0.6171 \pm 0.1296) \times 10^{-4}$
σ_y^2	0.02566	0.00311 after 5 iterations

TABLE 4-2

Resolution Matrices of the Berea Sandstone

Linear Inversion

0.6307	0.2590	0.0499	0.0019	0.0007	-0.0084	-0.0019
0.2590	0.5040	0.2641	0.0603	-0.0209	-0.0092	-0.0045
0.0499	0.2641	0.4915	0.1328	0.0475	0.0157	0.0041
0.0019	0.0603	0.1328	0.6630	0.1255	0.0155	0.0013
0.0007	-0.0209	0.0475	0.1255	0.7506	0.0881	0.0082
-0.0084	-0.0092	0.0157	0.0155	0.0881	0.7794	0.0948
-0.0019	-0.0045	0.0041	0.0013	0.0082	0.0948	0.6709

Iterative Inversion (5 iterations)

0.6032	0.3087	0.0227	-0.0010	-0.0059	-0.0040	-0.0023
0.3087	0.6160	0.1173	0.0276	0.0003	-0.0030	-0.0015
0.0227	0.1173	0.6559	0.1692	0.0295	0.0067	0.0020
-0.0010	0.0276	0.1692	0.6894	0.0988	0.0133	0.0024
-0.0059	0.0003	0.0295	0.0988	0.7584	0.0975	0.0182
-0.0040	-0.0030	0.0067	0.0133	0.0975	0.6988	0.1484
-0.0023	-0.0015	0.0020	0.0024	0.0182	0.1484	0.6052

TABLE 4-3

Pore-Aspect Ratio Spectra of Boise Sandstone

Linearized Iterative Inversion (5 iterations)

porosity = 25% $\varepsilon = 1$

	K = 0.31 Mb μ = 0.19 Mb	K = 0.3 Mb μ = 0.19 mb
α	$c(\alpha)$	$c(\alpha)$
1	0.1877 ± 0.0025	0.1928 ± 0.0028
0.1	$(0.6176 \pm 0.0222) \times 10^{-1}$	$(0.5655 \pm 0.0245) \times 10^{-1}$
0.35×10^{-2}	$(0.3655 \pm 0.7566) \times 10^{-4}$	$(0.1668 \pm 0.0832) \times 10^{-3}$
0.28×10^{-2}	$(0.6050 \pm 0.6612) \times 10^{-4}$	$(0.5513 \pm 0.7286) \times 10^{-4}$
0.21×10^{-2}	$(0.6377 \pm 0.4942) \times 10^{-4}$	$(0.6337 \pm 0.5443) \times 10^{-4}$
0.17×10^{-2}	$(0.1362 \pm 0.0395) \times 10^{-3}$	$(0.1380 \pm 0.0435) \times 10^{-3}$
0.13×10^{-2}	$(0.1096 \pm 0.0299) \times 10^{-3}$	$(0.1075 \pm 0.0330) \times 10^{-3}$
0.9×10^{-3}	$(0.8516 \pm 0.2145) \times 10^{-4}$	$(0.8517 \pm 0.2363) \times 10^{-4}$
0.5×10^{-3}	$(0.6171 \pm 0.1296) \times 10^{-4}$	$(0.6198 \pm 0.1428) \times 10^{-4}$
σ_y^2	0.00311	0.00377

TABLE 4-4a

Pore-Aspect Ratio Spectra for Berea Sandstone

K = 0.32 Mb μ_d = 0.255 Mb μ_w = o.245 Mb
Porosity = 16.3% ε = 1 5 iterations

α	C1	C2	C3	C4
1	0.1399	0.1399	0.1400	0.1399
0.1	0.02207	0.02204	0.02200	0.02207
0.01	0.3127×10^{-3}	0.3807×10^{-3}	0.3993×10^{-3}	0.3758×10^{-3}
0.19×10^{-2}				0.1676×10^{-4}
0.18×10^{-2}		0.1464×10^{-3}		
0.17×10^{-2}	0.1402×10^{-3}			
0.16×10^{-2}			0.1285×10^{-3}	0.1797×10^{-3}
0.15×10^{-2}		0.1001×10^{-3}		
0.14×10^{-2}	$0.1363\times^{10-3}$			
0.13×10^{-2}			0.1276×10^{-3}	
0.12×10^{-2}				0.1434×10^{-3}
0.11×10^{-2}		0.1013×10^{-3}		
0.1×10^{-2}	0.1572×10^{-3}			
0.9×10^{-3}			0.1440×10^{-3}	
0.8×10^{-3}				0.1119×10^{-3}
0.7×10^{-3}		0.1732×10^{-3}		
0.6×10^{-3}	0.1315×10^{-3}			
0.5×10^{-3}			0.2045×10^{-3}	0.1835×10^{-3}
0.4×10^{-3}		0.1656×10^{-3}		
0.3×10^{-3}	0.1126×10^{-3}			
0.2×10^{-3}			0.4543×10^{-4}	0.4511×10^{-4}
σ_y^2	0.00938	= 0.01162	0.01656	0.01764
α <0.01	0.6778×10^{-3}	0.6866×10^{-3}	0.6500×10^{-3}	0.6804×10^{-3}

TABLE 4-4b

Pore-Aspect Ratio Spectra for Berea Sandstone

α	$C1/\alpha$	$C2/\alpha$	$C3/\alpha$	$C4/\alpha$
1	0.1399	0.1399	0.1400	0.1399
0.1	0.2207	0.2204	0.2200	0.2207
0.01	0.03725	0.03807	0.03993	0.03758
0.19×10^{-2}				0.0088
0.18×10^{-2}		0.0813		
0.17×10^{-2}	0.0825			
0.16×10^{-2}			0.0803	0.1123
0.15×10^{-2}		0.0667		
0.14×10^{-2}	0.0974			
0.13×10^{-2}			0.0982	
0.12×10^{-2}				0.1195
0.11×10^{-2}		0.0921		
0.1×10^{-2}	0.1572			
0.9×10^{-3}			0.1600	
0.8×10^{-3}				0.1399
0.7×10^{-3}		0.2474		
0.6×10^{-3}	0.2192			
0.5×10^{-3}			0.4090	0.3670
0.4×10^{-3}		0.4140		
0.3×10^{-3}	0.3753			
0.2×10^{-3}			0.2272	0.2256
total c/α	1.3295	1.2999	1.3746	1.3713
for $\alpha < 0.01$	0.9316	0.9015	0.9747	0.9731

TABLE 4-5

Pore-Aspect Ratio Spectra for Westerly granite

$K = 0.59$ Mb $\mu = 0.32$ Mb $\varepsilon = 1$ porosity = 0.9%

Linearized Iterative Inversion (5 iterations)

α	Without zero pressure data $c(\alpha)$	With zero pressure data $c(\alpha)$
1	$(0.7011 \pm 0.0675) \times 10^{-2}$	$(0.6929 \pm 0.699) \times 10^{-2}$
0.01	$(0.1514 \pm 0.0436) \times 10^{-2}$	$(0.1558 \pm 0.0447) \times 10^{-2}$
0.17×10^{-2}	$(0.9255 \pm 0.9036) \times 10^{-4}$	$(0.8440 \pm 0.9255) \times 10^{-4}$
0.12×10^{-2}	$(0.5973 \pm 0.6560) \times 10^{-4}$	$(0.6689 \pm 0.6770) \times 10^{-4}$
0.85×10^{-3}	$(0.1536 \pm 0.0445) \times 10^{-3}$	$(0.1513 \pm 0.0461) \times 10^{-3}$
0.55×10^{-3}	$(0.1063 \pm 0.0264) \times 10^{-3}$	$(0.1050 \pm 0.0272) \times 10^{-3}$
0.25×10^{-3}	$(0.6248 \pm 0.1271) \times 10^{-4}$	$(0.6569 \pm 0.1269) \times 10^{-4}$
0.1×10^{-3}		$(0.4025 \pm 0.0588) \times 10^{-4}$
σ_y^2	0.01716	0.01817

TABLE 4-6

Resolution Matrix for Berea Sandstone

No Scaling Applied

Linearized Iterative Inversion (5 iterations)

0.5903	0.2945	0.0486	0.0247	0.0011	-0.0033	-0.0031
0.2945	0.4562	0.1677	0.1077	0.0472	0.0078	0.0002
0.0486	0.1677	0.2739	0.2143	0.1561	0.0599	0.0195
0.0247	0.1007	0.2143	0.2524	0.1931	0.0780	0.0266
0.0011	0.0472	0.1561	0.1931	0.2479	0.1099	0.0414
-0.0033	0.0078	0.0599	0.0780	0.1099	0.1948	0.0825
-0.0031	0.0002	0.0195	0.0266	0.0414	0.0825	0.0946

TABLE 4 -7

Covariance Matrix for Berea Sandstone

Linear Inversion

0.1633	-0.0482	-0.0746	-0.0228	-0.0033	0.0051	0.0023
-0.0482	0.1090	-0.0186	-0.0429	-0.0142	0.0020	0.0011
-0.0746	-0.0186	0.1575	-0.0428	-0.0241	-0.0080	-0.0014
-0.0028	-0.0429	-0.0428	0.1862	-0.0583	-0.0196	-0.0032
-0.0033	-0.0142	-0.0241	-0.0583	0.1609	-0.0504	-0.0123
0.0051	0.0020	-0.0080	-0.0196	-0.0504	0.1546	-0.0436
0.0023	0.0011	-0.0014	-0.0032	-0.0123	-0.0423	0.2117

TABLE 4-8

Pore-Aspect Ratio Spectra for Berea Sandstone

Linear Inversion

$K = 0.32$ Mb $\mu_d = 0.255$ Mb $\mu_w = 0.245$ Mb

porosity = 16.3%

	$\varepsilon = 0$	$\varepsilon = 1$
α	$c(\alpha)$	$c(\alpha)$
1	0.1359 ± 0.01346	0.1454 ± 0.00472
0.1	$(0.2698 \pm 0.1121) \times 10^{-1}$	$(0.1601 \pm 0.0416) \times 10^{-1}$
0.01	$(-0.6971 \pm 1.7420) \times 10^{-3}$	$(0.8803 \pm 0.3402) \times 10^{-3}$
0.17×10^{-2}	$(0.3624 \pm 0.2637) \times 10^{-3}$	$(0.2038 \pm 0.0695) \times 10^{-3}$
0.14×10^{-2}	$(0.8863 \pm 1.1960) \times 10^{-4}$	$(0.1217 \pm 0.0623) \times 10^{-3}$
0.1×10^{-2}	$(0.1273 \pm 0.0682) \times 10^{-3}$	$(0.1403 \pm 0.0413) \times 10^{-3}$
0.6×10^{-3}	$(0.1458 \pm 0.0365) \times 10^{-3}$	$(0.1466 \pm 0.0243) \times 10^{-3}$
0.3×10^{-3}	$(0.1298 \pm 0.0230) \times 10^{-3}$	$(0.9453 \pm 0.1422) \times 10^{-4}$
σ_y^2	0.01141	0.01332

TABLE 4-9

Pore-Aspect Ratio Spectra for Berea Sandstone

$K = 0.32$ Mb $\mu_d = 0.255$ Mb $\mu_w = 0.245$ Mb $\varepsilon = 1$ porosity = 16.3%

Iteration:	zeroth	first	second	third	fourth	fifth
α	$c(\alpha)$	$c(\alpha)$	$c(\alpha)$	$c(\alpha)$	$c(\alpha)$	$c(\alpha)$
1	0.1454	0.1433	0.1417	0.1408	0.1402	0.1399
0.1	0.01601	0.01840	0.02006	0.02104	0.02166	0.02207
0.01	0.8803×10^{-3}	0.6671×10^{-3}	0.5530×10^{-3}	0.4692×10^{-3}	0.4117×10^{-3}	0.3725×10^{-3}
0.17×10^{-2}	0.2038×10^{-3}	0.1571×10^{-3}	0.1449×10^{-3}	0.1409×10^{-3}	0.1400×10^{-3}	0.1402×10^{-3}
0.14×10^{-2}	0.1217×10^{-3}	0.1235×10^{-3}	0.1303×10^{-3}	0.1339×10^{-3}	0.1356×10^{-3}	0.1363×10^{-3}
0.10×10^{-2}	0.1403×10^{-3}	0.1524×10^{-3}	0.1558×10^{-3}	0.1568×10^{-3}	0.1571×10^{-3}	0.1572×10^{-3}
0.6×10^{-3}	0.1466×10^{-3}	0.1407×10^{-3}	0.1355×10^{-3}	0.1330×10^{-3}	0.1319×10^{-3}	0.1315×10^{-3}
0.3×10^{-3}	0.9453×10^{-4}	0.1059×10^{-3}	0.1100×10^{-3}	0.1116×10^{-3}	0.1123×10^{-3}	0.1126×10^{-3}
σ_y^2	0.01061	0.00965	0.00949	0.00943	0.00940	0.00938

FIGURE CAPTIONS

Figure 4-1: Results of linear (dashed line) and linearized iterative inversion (solid line) for Berea sandstone. The data (points) are from Jones et al. (1977). Fluid pressure is 0.465 times confining pressure. Matrix parameters and the resultant pore-aspect ratio spectra are given in Table (4-1)

Figure 4-2: Results of the linear programming inversion for the Berea sandstone data. The shaded areas represent the ranges defined by the upper and lower bound solutions.

Figure 4-3: Same as figure (4-1) for Westerly granite. The data are from Nur and Simmons (1969). The fluid pressure is maintained at one atmosphere.

Figure 4-4: Same as figure (4-2) for Westerly granite.

Figure 4-5: Same as figure (4-1) for Boise sandstone. The data are from King (1966). The fluid is maintained at atmospheric pressure.

Figure 4-6: Inversion results for the Boise sandstone using different matrix bulk moduli. Matrix shear modulus is 0.19 Mb.

Figure 4-7: Results of the linearized iterative inversion for Westerly granite with the data at zero differential pressure included.

Figure 4-8: Inversion results for the Berea sandstone with different scalings in the coefficient matrix (sec. 4.5.5).

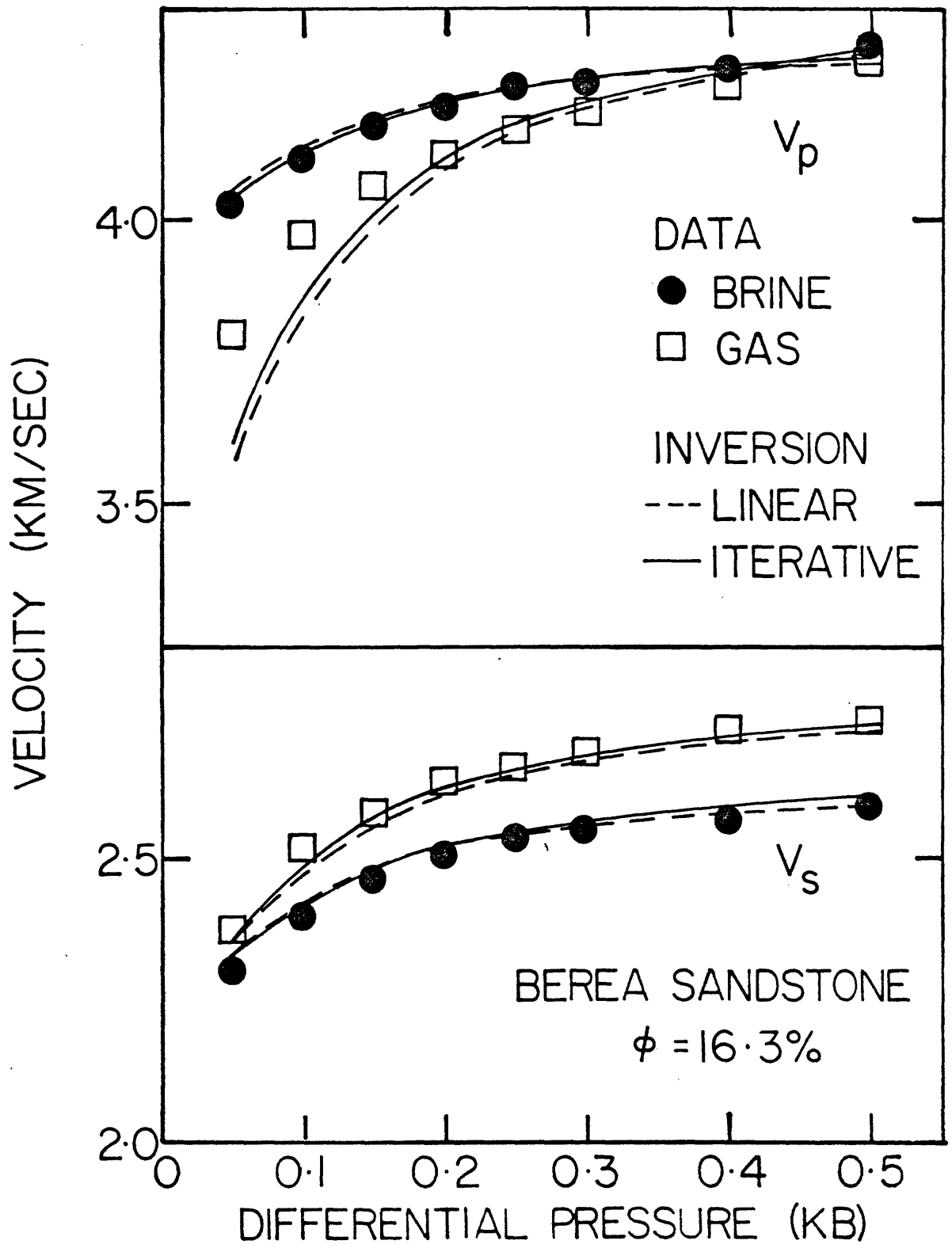
VELOCITY (KM/SEC)
4·0
3·5
2·5
2·0
V_p
DATA
BRINE
GAS
INVERSION
---LINEAR
—ITERATIVE
V_s
BEREA SANDSTONE
ϕ = 16·3%
0
0·1
0·2
0·3
0·4
0·5
DIFFERENTIAL PRESSURE (KB)

Figure 4-1

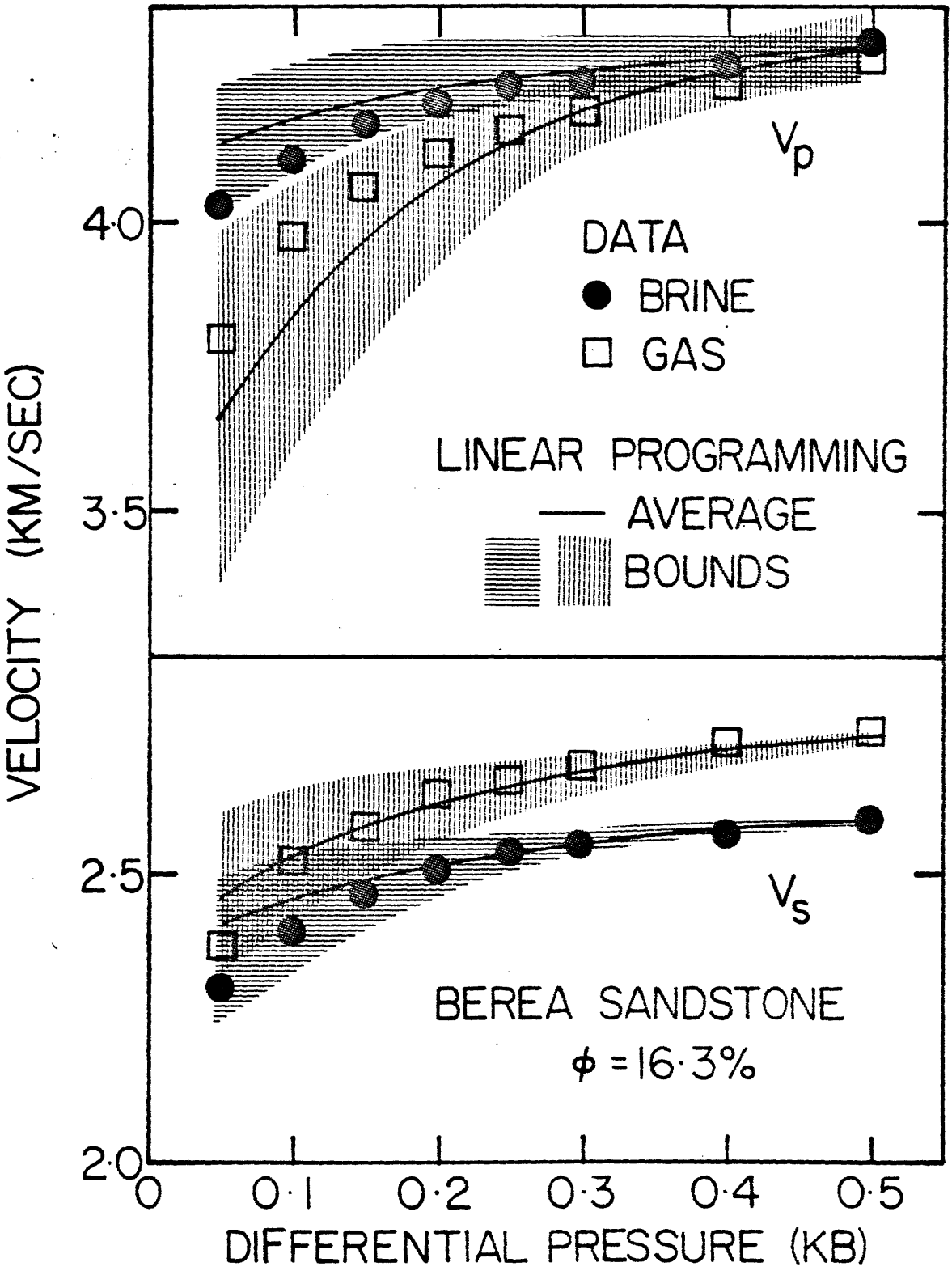
VELOCITY (KM/SEC)
4·0
3·5
2·5
2·0
0
0·1
0·2
0·3
0·4
0·5
DIFFERENTIAL PRESSURE (KB)
V_p
DATA
BRINE
GAS
LINEAR PROGRAMMING
AVERAGE
BOUNDS
V_s
BEREA SANDSTONE
ϕ = 16·3%

Figure 4-2

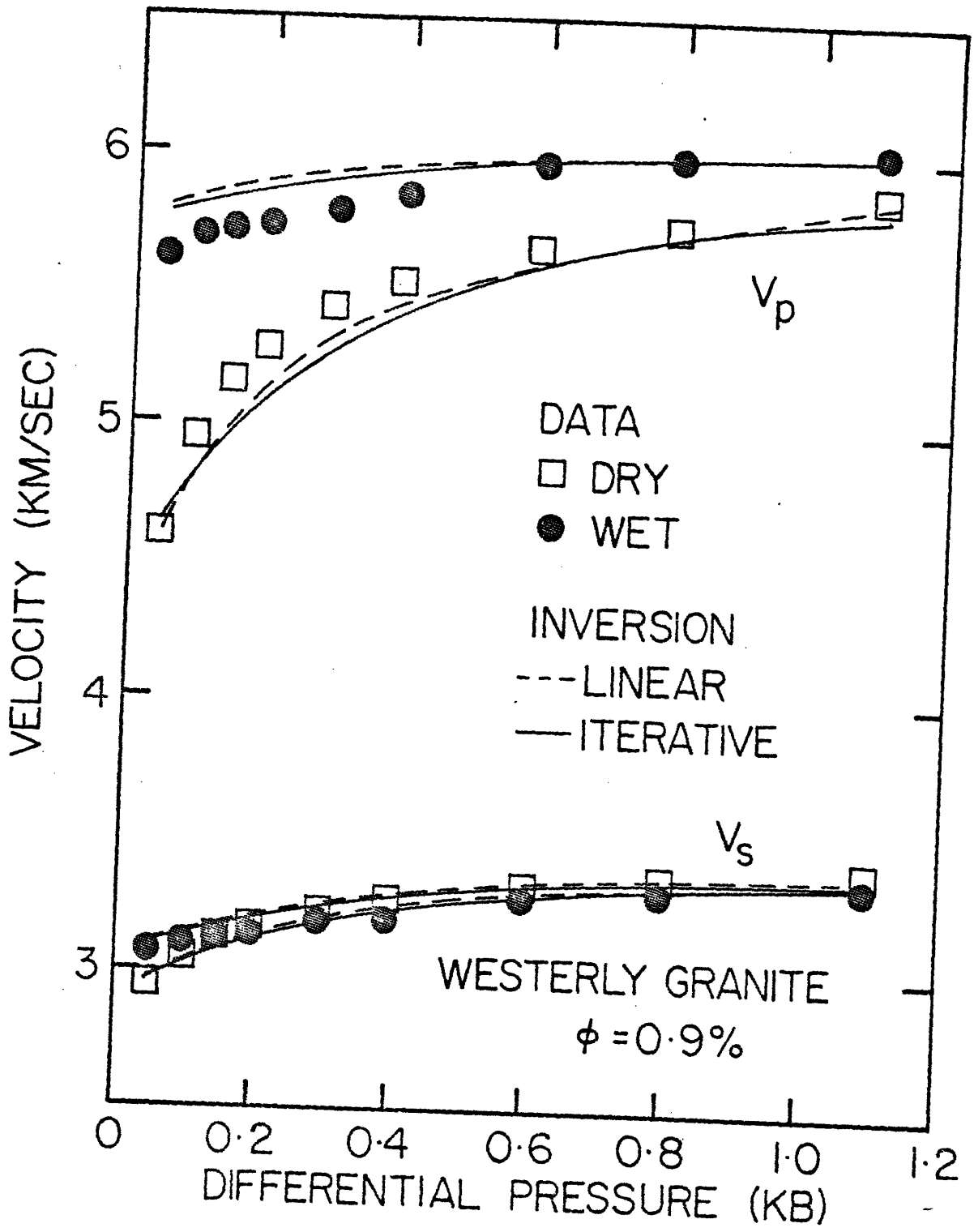
VELOCITY (KM/SEC)
6
5
4
3
V_p
DATA
DRY
WET
INVERSION
---LINEAR
—ITERATIVE
V_S
WESTERLY GRANITE
ϕ = 0·9%
0
0·2
0·4
0·6
0·8
1·0
1·2
DIFFERENTIAL PRESSURE (KB)

Figure 4-3

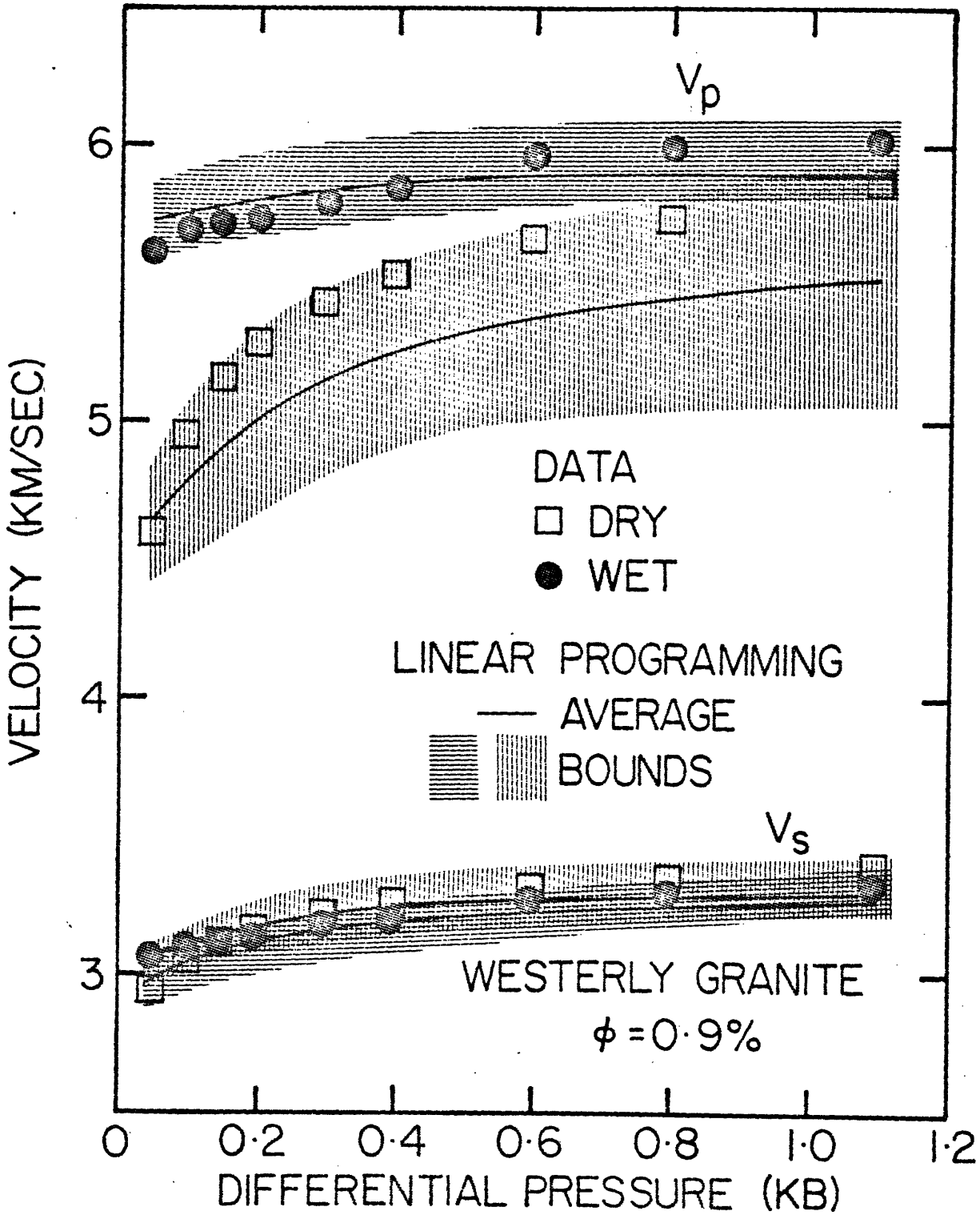
V_p
6
5
4
3
VELOCITY (KM/SEC)
DATA
DRY
WET
LINEAR PROGRAMMING
AVERAGE
BOUNDS
V_S
WESTERLY GRANITE
ϕ = 0·9%
0
0·2
0·4
0·6
0·8
1·0
1·2
DIFFERENTIAL PRESSURE (KB)

Figure 4-4

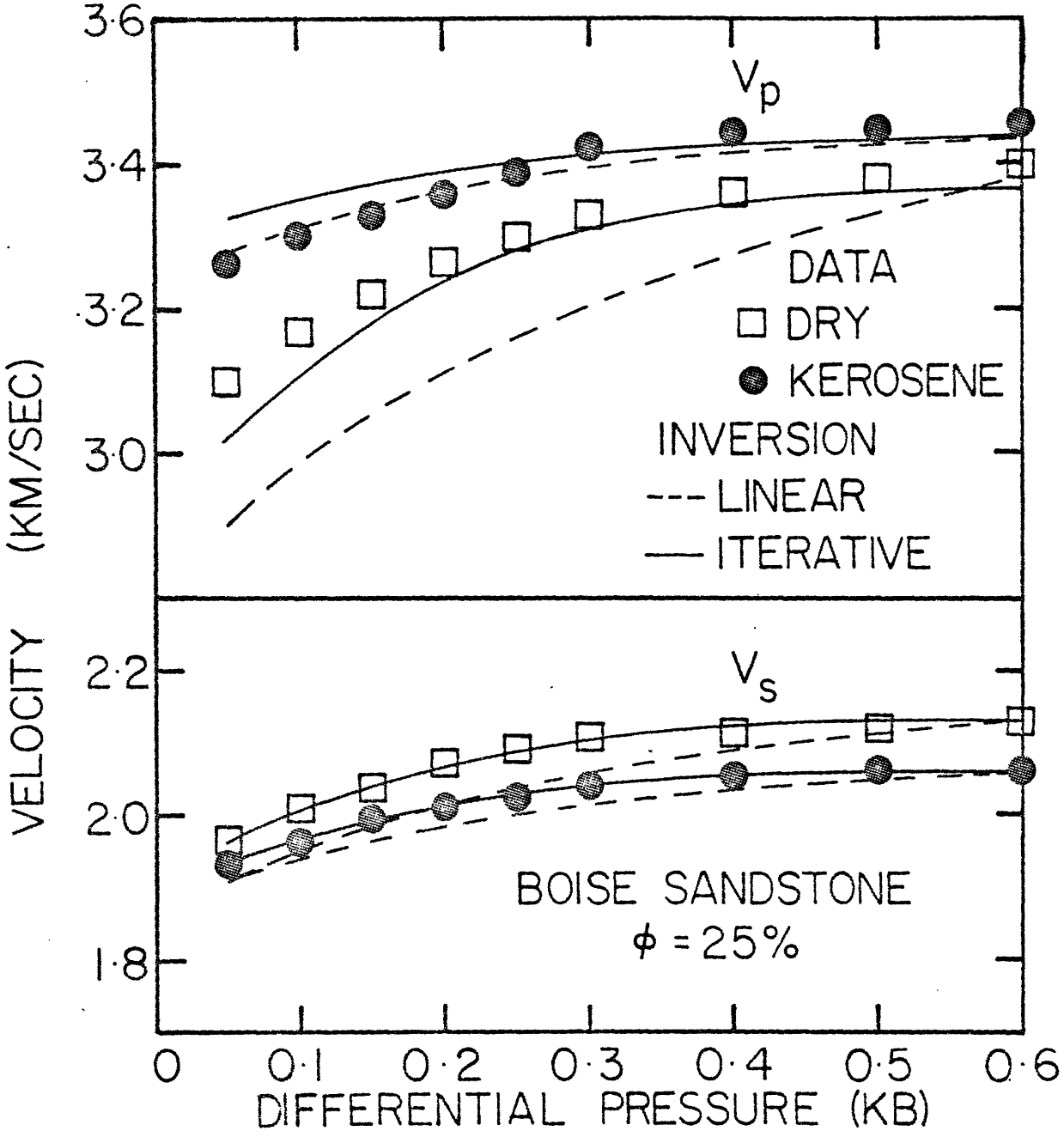
3·6
3·4
3·2
3·0
V_p
DATA
DRY
KEROSENE
INVERSION
--- LINEAR
— ITERATIVE
VELOCITY (KM/SEC)
2·2
2·0
1·8
V_s
BOISE SANDSTONE
ϕ = 25%
0
0·1
0·2
0·3
0·4
0·5
0·6
DIFFERENTIAL PRESSURE (KB)

Figure 4-5

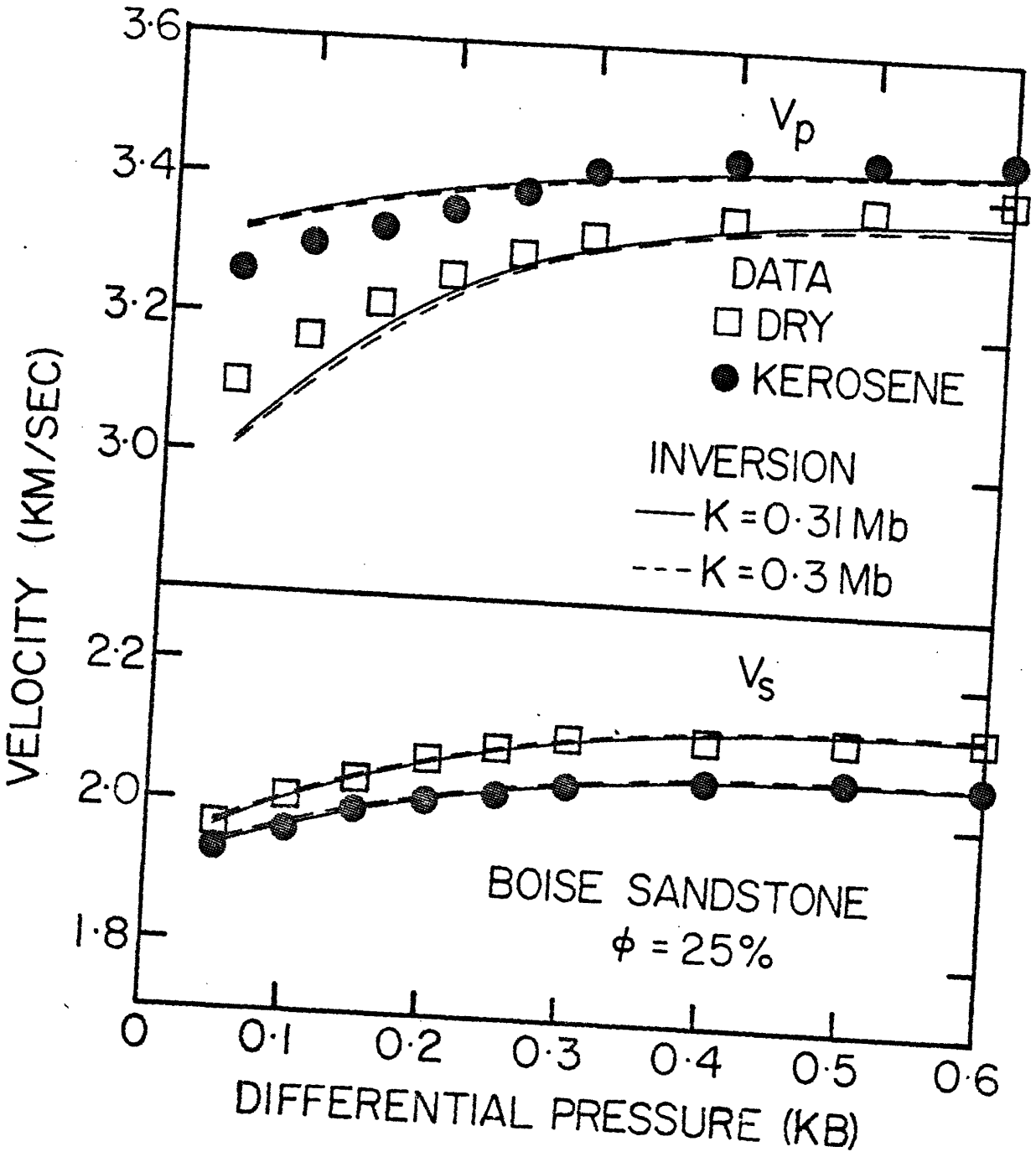
3·6
3·4
3·2
3·0
2·2
2·0
1·8
VELOCITY (KM/SEC)
V_p
DATA
□ DRY
● KEROSENE
INVERSION
—— K = 0·31 Mb
--- K = 0·3 Mb
V_s
BOISE SANDSTONE
ϕ = 25%
0
0·1
0·2
0·3
0·4
0·5
0·6
DIFFERENTIAL PRESSURE (KB)

Figure 4-6

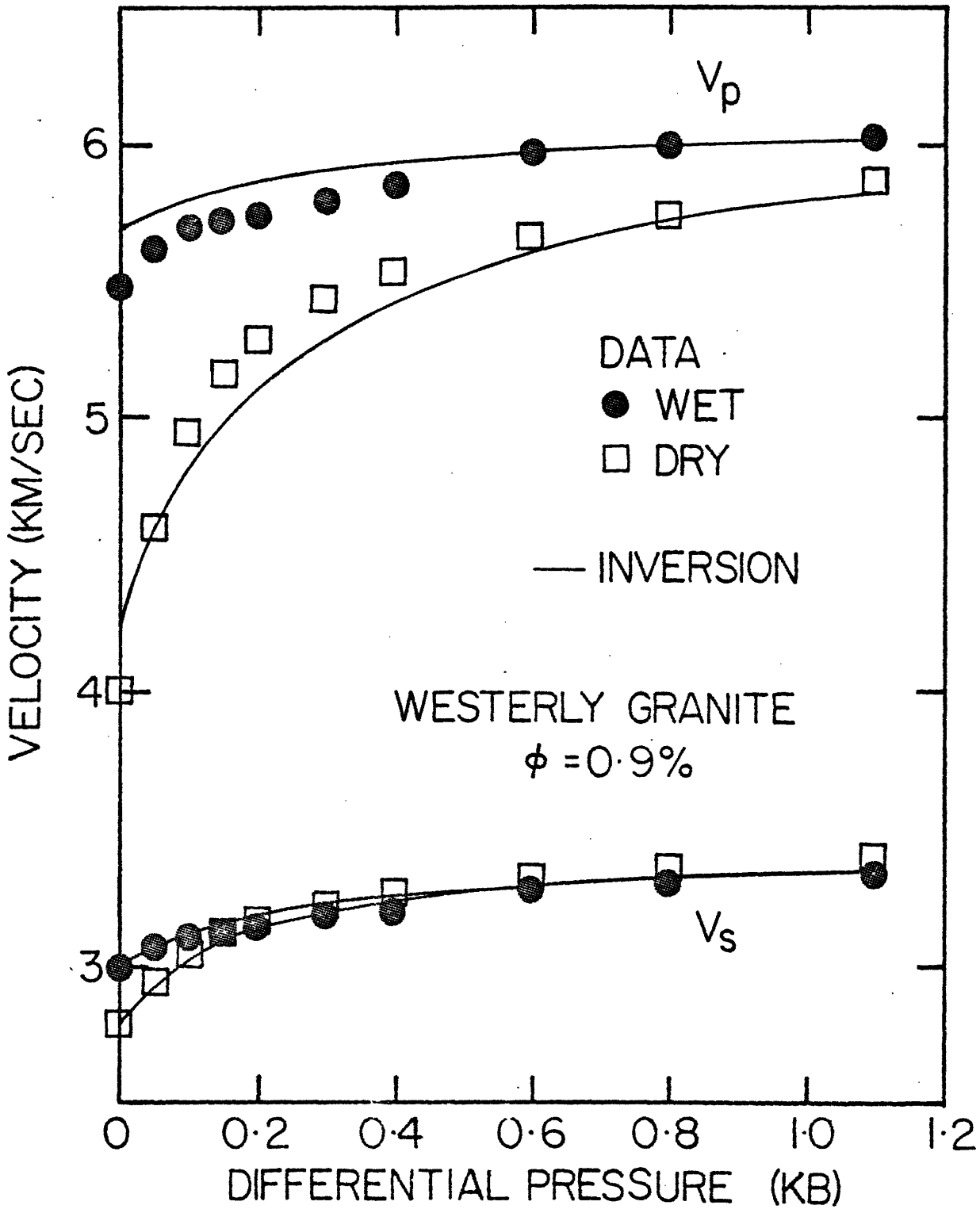
V_p
6
5
4
3
VELOCITY (KM/SEC)
DATA
WET
DRY
INVERSION
WESTERLY GRANITE
ϕ = 0·9%
V_s
0
0·2
0·4
0·6
0·8
1·0
1·2
DIFFERENTIAL PRESSURE (KB)

Figure 4-7

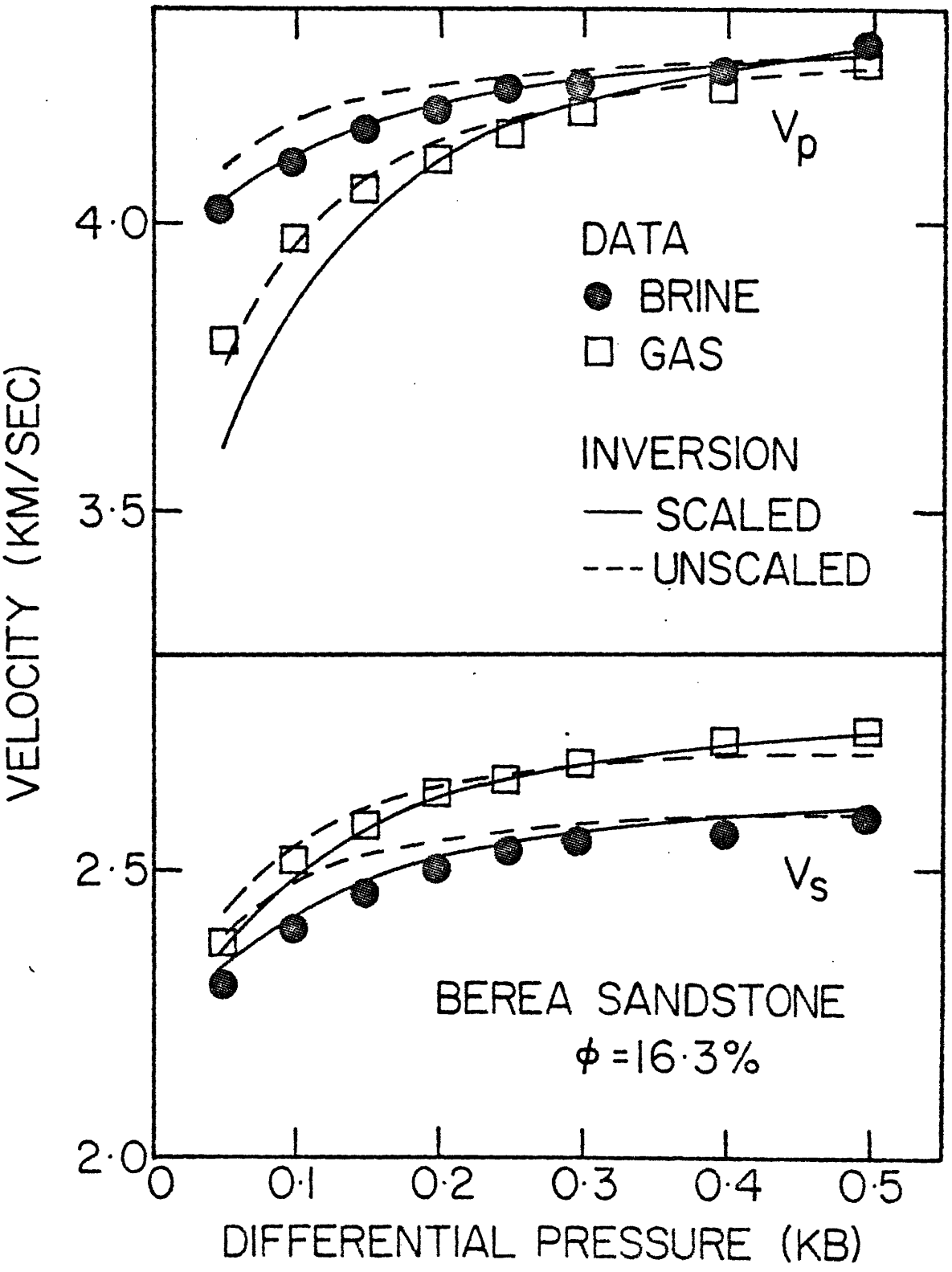
VELOCITY (KM/SEC)
4·0
3·5
2·5
2·0
0
0·1
0·2
0·3
0·4
0·5
DIFFERENTIAL PRESSURE (KB)
V_p
DATA
BRINE
GAS
INVERSION
SCALED
UNSCALED
V_s
BEREA SANDSTONE
ϕ = 16·3%

Figure 4-8

CAHPTER 5

PORE-ASPECT RATIO SPECTRA OF ROCKS FROM VELOCITY DATA

In this chapter we apply the linearized iterative inversion scheme to find the pore-aspect ratio spectra of a number of rocks whose seismic velocities had been measured by different authors and reported in the literature. We start with medium to high porosity sandstones, then medium porosity limestones and finally a low porosity marble. A detail discussion on the composition of most of these rocks can be found in Johnston (1978) and Jones et al., (1977) and will not be repeated here. The pore-aspect ratio spectra of these rocks obtained by the inversion are given in Table (5-1) together with those of the three rocks discussed in the previous chapter, viz., Berea sandstone, Boise sandstone and Westerly granite. The matrix bulk and shear moduli are also given, together with estimated standard deviation in the data. In all cases, unless otherwise stated, the damping factor ε is taken to be one and the number of iterations taken for the linearized iterative inversion is five.

In the second part of this chapter, we compare the pore-aspect ratio spectra of these rocks and see what, if any conclusions we can draw about the pore-aspect ratio spectrum of any specific rock in terms of its porosity and/or rock

type. We also address the question of the predictive power of the inversion. By that we mean that if we obtain a pore-aspect ratio spectrum of a rock by inverting velocity obtained under one saturation condition (say brine-saturated), how well can we use the result to predict the velocities of the rock under a different saturation condition (say gas-saturated)? This question is of utmost importance in petroleum as well as geothermal exploration.

Finally, we would like to compare the pore-aspect ratio spectrum of the Westerly granite obtained from our inversion of velocity data with those estimated by direct observations of scanning electron microscope (SEM) photographs (Sprunt and Brace, 1974; Hadley, 1976) and by Differential Strain Analysis (DSA, Feves and Simmons,1976). This will give us an estimate of how good the oblate spheroidal crack model is compared to the actual pore spaces in a rock.

5.1 Pore-Aspect Ratio Spectra of Several Rocks:

5.1.1 Navajo Sandstone:

Navajo sandstone is a relatvely clean medium porosity sandstone similar to the Berea sandstone we have discussed earlier. The porosity is 16.41% for this sample. The velocity data are obtained by Johnston (1978). The data set include p- and s-wave velocities of the dry and water-saturated rock as a function of pressure. The fluid pressure of the water-saturated sample was maintained at about 0.465 of

the confining pressure. Details of the experiments can be found in Johnston (1978).

The behaviors of the seismic velocities as a function of pressure are very similar to those of the Berea sandstone. This is not surprising at all since they have very similar porosities and, to a certain extent, composition. All four velocities rise moderately as the differential pressure increases and levels off above 400 bars or so (Fig. 5-1). In contrast, in the Berea sandstone (Fig. 4-1), the increases in velocities with pressure are a little more rapid and level off faster. The difference, however, is not a major one.

Figure (5-1) shows the fit of the results of the linearized iterative inversion to the data. The agreement between theory and data is very good indeed. The only error seems to be in the p-wave velocities of the water-saturated rock. The theory predicts slightly higher velocities at low pressures and slightly lower velocities at high pressures than the data. The difference is small and well within the possible errors of the velocity measurements. In fitting these data, it is necessary to lower the matrix shear modulus of the water-saturated rock by about four percent of the value used for the dry rock.

5.1.2 An 18.8% Porosity Berea Sandstone:

The second rock we are going to investigate is a Berea sandstone with a slightly higher porosity than the sample

presented previously. The data are from Jones et al., (1977). Here we have only the brine-saturated p- and s-wave velocity data. The fluid pressure is maintained at 0.465 of the confining pressure. This experimental condition is also true for the next three rock samples we are going to discuss.

For the inversion, we have taken the matrix moduli from the inversions of the 16.3% porosity Berea sandstone in the previous sections. The results are plotted in figure (5-2). As one can see, the fit is very good. A local error of less than five percent in the moduli is achieved after only one iteration. This is to be expected since we were able to fit the p- and s-wave velocities of the brine-saturated 16.3% porosity Berea sandstone very well also (see figure 6-1). A comparison of the pore-aspect ratio spectra of the two different porosity Berea snadstones will be given in a later section.

5.1.3 Spergen Limestone:

Spergen limestone is a medium porosity, very pure limestone. It is also the rock with which the main buildings of M.I.T. are built. The data are from Jones et al., (1977).

Although the porosity of the Spergen limestone is high, the behavior of the velocities with pressure is more like that of the Westerly granite than the sandstones we have investigated. Both p- and s-wave velocities increase rapidly at very low pressures but level off quickly above 100 bars of

differential pressure. It can thus be expected that the Spergen limestone will have fewer thin cracks than the sandstones.

Figure (5-3) shows the results of the inversion as compared with the data. The fit is excellent, except for slightly higher predicted p-wave velocities at very low pressure. The fit is so good that the local error is less than five percent in two iterations.

5.1.4 Florida Dolostone:

The Florida dolostone is a very pure dolostone of 14.5% porosity. The data are obtained by Jones et al., (1977) under the same conditions as the Berea sandstone and Spergen limestone.

The behavior of the s-wave velocities, as can be seen from Figure (5-4), is quite normal and expected. The p-wave velocities, however, show a decrease in the very low pressure range before increasing normally. This phenomena can be traced to the errors in the velocity measurements, as discussed in Johnston (1978) and in section 4.5.4.

Although the porosity of the Florida dolostone is very similar to that of the Spergen limestone, the behavior of the velocities with pressure is very different. Both the p- and s-wave velocities increase slowly and more or less linearly over the whole pressure range (up to 600 bars), with no hint of leveling off. This suggests the presence of a moderate

number of cracks quite evenly distributed between aspect ratios from 10^{-4} to 10^{-3}. This is confirmed by the inversion.

The results of the linearized iterative inversion are plotted with the data on figure (5-4). The results fit the observed data so well that the local error is less than five percent with no iterations. The results here, however, is after five iterations, with the local error tolerence lowered to three percent.

5.1.5 Yule Marble:

Yule marble is a very low porosity calcite, with a porosity of only 0.4 percent. The data are, as for the three previous rocks, obtained by Jones et al., (1977). The p- and s-wave velocities of the brine-saturated rock are plotted in figure (5-5).

The behaviors of the p- and s-wave velocities of the brine-saturated rock are very similar to those of the Westerly granite (figure 4-2). Although it is of extremely low porosity, the increases in velocities with pressure are more gradual than the high porosity Spergen limestone, indicating a higher concentration of cracks. This is confirmed in the resultant pore-aspect ratio spectrum (table 5-1).

The inversion results are plotted in figure (5-5) together with the data. The fit is excellent, needing only two iterations of the inversion to acheive a local error of three percent. The only significant difference between the

observed data and theory is in the p-wave velocities of the three lowest pressure points. However, if one examine the data closely, we will discover that the bulk moduli of these points actually decrease with pressure. So the misfit is due to either errors in the measurements or some non-elastic behavior.

Briefly in summary, the linearized iterative inversion obviously does a very good job of fitting the observed data. This also gives us more confidence about the direct theory used. The almost perfect fits for the brine-saturated data of Jones et al. are a little deceiving though. As seen in figure 2 of Kuster and Toksöz (1974a), the bulk moduli of the water- or brine-saturated rock is not highly dependent on the concentrations of the small aspect ratio cracks. Thus we actually have only the shear moduli to fit. On the other hand, the 16.3% porosity Berea sandstone data of Jones et al. and Navajo sandstone data of Johnston are more conclusive in proving the validity of the theory since both dry and water-saturated data were used. The larger differences between theory and the Boise sandstone data and the Westerly granite data may be due to the fact that these were obtained in an era when both the experimental equipments and techniques were less sophisticated than those used by Jones et al. and Johnston almost a decade later. Thus the errors in the measurements are likely to be larger. All in all, both the direct theory and the

inverse theory perform most satisfactorily.

5.2 Physical Significances of the Pore-Aspect Ratio Spectrum:

Finally, we would like to discuss the physical significances and practical applications of this theoretical exercise. It is not nearly enough to know that our model fits the observed data. The pore-aspect ratio spectra we obtained are based on a model which characterizes the pore spaces in a rock as a collection of oblate spheroids with discrete aspect ratios. In this section we would like to examine the relationships between the fractional concentrations of these spheroids and the actual amount of cracks in a rock as measured by direct scanning electron microscope (SEM) photographs and other indirect techniques. On the other hand, from a purely philosophical standpoint, it is enough to see whether the model can stand on its own merits. It is thus equally important to test the predictive power of the model. This is done by taking the pore-aspect ratio spectrum from the inversion of the data of a rock under one saturation condition and try to predict the velocities of the rock measured under another saturation condition by applying the spectrum in the direct problem. It is also of scientific interest to see if we can characterize the pore-aspect ratio spectrum of a rock by either its rock type or its porosity or both. If we are successful, we would be able to estimate the velocities and perhaps attenuation coeff-

icients of any given rock under in situ conditions.

5.2.1 The Predictive Power of the Pore-Aspect Ratio Spectrum:

In this section we examine the predictive power of the pore-aspect ratio spectrum by taking the results of the inversion of velocity data of a rock under one or more saturation conditions and put it through the direct problem and see if it can predict the velocities of the rock under a different saturation condition. We examine two rocks, the Boise sandstone and the Navajo sandstone.

The Boise sandstone was studied by King (1966). He measured its velocities as a function of pressure under three different saturation conditions: dry, kerosene- and brine-saturated. In an earlier chapter of this thesis, we have inverted the dry and kerosene-saturated data (table 5-1 and figure 4-5). Here we would like to take the results of that inversion and put it in the direct problem to try to predict the brine-saturated data. Because of the interaction of water with clay (see Chapter 3 and section 4.5.2), we have lowered the matrix shear modulus from the value of 0.19 Mb used for the dry and kerosene-saturated rock to 0.18 Mb. The results of the direct calculations are plotted in figure (5-6) together with King's data.

As in the case of the inverse problem (figure 4-5), the results fit the shear velocities extremely well. Just as the inversion results for the kerosene-saturated rock, the direct

results for the brine-saturated rock shows higher p-wave velocities at low pressures than observed. This can be attributed to the inherent experimental errors at those pressures.

Next we tried the prediction for the Navajo sandstone. The data is from Johnston (1978) (see also figure 5-1 and table 5-1). Here we did two seperate predictions: we took in turn the dry and the water-saturated velocity data and inverted them seperately. The resultant spectra (given in table 5-2) were put back through the direct problem and the velocities for the other saturation condition were obtained and compared with the observed data. In figure (5-7) we have plotted the inversion results for the dry rock and the predicted results of the water-saturated rock together with the data. In figure (5-8) the results of the other combination were plotted.

Comparing figures (5-7) and (5-8) with each other and with figure (5-1), the results of inverting both data sets simultaneously, we are hard pressed to distinguish one from the other. The only way to tell which has a better fit is by the estimated variances in the data σ_y^2. By this method we can say that the simultaneous inversion gives the best fit, the water-saturated data next and the dry data the worst. The pore-aspect ratio spectra for the three inversions are also very similar, as can be expected, with the differences between them within the estimated errors.

From the above exercises it seems that we are indeed able to predict the behavior of the seismic velocities of a rock under a given saturation condition if we have knowledge of its pore-aspect ratio spectrum by inverting the velocity data under a different saturation condition.

5.2.2 Characterization of the Pore-Aspect Ratio Spectrum According to Rock Type and Porosity:

One of the points of interest concerning the pore-aspect ratio spectra of rocks is to see if there exists a consistent pattern as to the distribution of pore shapes between rocks of similar types or similar porosity. It is also instructive to examine the spectra to see if the concentrations (amounts) of cracks in rocks of the same type are proportional to their respective bulk porosities. To this end we shall do a qualitative comparison between the spectra of the rocks we have investigated. These spectra are given in table (5-1).

Taken as a whole, the first point one notices is that, except for the very low porosity Westerly granite and Yule marble, almost all of the bulk porosity of a rock is in the vugular or near-vugular pores, i.e., spheroids of aspect ratios α = 1, 0.1, and 0.01. These are the pores that remain open up until the fracturing of the rock under hydrostatic pressure. The second point to notice is that the amount of cracks in a rock and their distribution is NOT related to its bulk porosity. The most obvious is the comparison of the

spectra of the Spergen limestone and the Florida dolostone. Their bulk porosities are almost identical whereas their crack concentrations differ by a factor of two or three or more. These two rocks are the rule rather than the exception.

Within each broad classification of rock types, the situation is a little different. We have examined four sandstones, two of which are the same rock with a fifteen percent difference in their respective porosities (Berea sandstone, 16.3% and 18.8% porosity). In addition to the two Berea sandstones, we have the Navajo sandstone, the porosity of which (16.41%) is almost exactly the same as one of the Berea samples, and a Boise sandstone of 25% porosity.

The first point to look for is to see if there is any consistency between the crack spectrum of the two Berea samples. Table (5-3) shows the comparison of the two pore-aspect ratio spectra. It should be noted that the results for the 18.8% porosity sample are obtained from inverting the brine-saturated velocity data only. Comparing the two spectra and ignoring cracks of $\alpha = 10^{-4}$ which we cannot resolve for the 16.3% porosity sample, we found that the fractional concentrations for the different aspect ratio cracks ($\alpha < 10^{-2}$) are consistently higher for the higher porosity sample. Furthermore, for a given aspect ratio crack, the ratio of the concentrations of the higher to the lower porosity sample is roughly the same or more than the ratio of the bulk porosities. Even in the cases of cracks of aspect ratio $\alpha = 10^{-3}$ and

6×10^{-4}, where this ratio is significantly greater than the ratio of the bulk porosities, the difference is not great enough to significantly alter the results.

Next we shall compare the spectra of the two sandstone samples with similar bulk porosities, the Navajo and the lower porosity Berea sandstone. Their spectra are plotted as histograms in figure (5-9). Here the similarities are striking. Given the inherent errors in both the theory and the velocity measurements, one cannot justifiably distinguish the spectra of the two rocks. By adjusting the matrix moduli, one can very well use either spectrum to fit the observed velocities of either rock without much difference in the results.

The comparison of the pore-aspect ratio spectra of the Boise sandstone and the other three samples shows a different story. In figure (5-10) we have plotted the pore-aspect ratio spectra of the Boise sandstone together with the Navajo and the higher porosity Berea sandstones. The spectra are normalized by the bulk porosities of the rocks with the Navajo sandstone as a reference. We can see that the Boise sandstone, in spite of its higher bulk porosity (25%), has a lower concentration of small aspect ratio cracks than either the Berea or the Navajo sandstones. The concentration of these cracks are in no way proportional to the bulk porosity of the rock when compared to the other sandstones. Thus it is obvious that even within a rock group like the sandstones

the amount of cracks are not in direct proportion to the bulk porosity of a sample.

What then is the common denominator that makes the Navajo and Berea sandstones so similar to each other in the pore-aspect ratio spectra but different from the Boise sandstone? One of the many possible explanations lies in the average grain size and the type of contact of the grains of these rocks. Johnston (1978) gave a discription of these parameters. For both the Navajo and Berea sandstones, the average grain sizes are about 0.1 mm to 0.15 mm, with planar contacts in the Navajo sandstone and points and concavo-convex contacts in the Berea sandstone. The Boise sandstone, however, has a much larger average grain size of about 0.25 mm and the contacts are points and short planes. It is thus obvious that we would have more vugular or equidimensional pores in the Boise sandstone and more thin cracks in the Navajo and Berea sandstones. This is a very qualitative argument but is at least consistent with the pore-aspect ratio spectra obtained from the inversion of velocity data of these rock.

5.2.3 The Pore-Aspect Ratio Spectrum as Compared to Other Estimates of Pore Spaces:

There have been extremely few estimates of the pore-aspect ratio spectrum of a rock. The few that have been done are only on igneous rocks, principally granites. There exist

in the literature two principal methods of estimating the pore spaces in a rock, the first is by direct observations from scanning electron micrographs and counting the amount or pore spaces manually and the second is by Differential Strain Analysis. Both these techniques have been applied to Westerly granite, the former by Hadley (1976) and Sprunt and Brace (1974) and the latter by Feves and Simmons (1976). In this section we shall compare the resultant pore-aspect ratio spectrum of our inversion of the Westerly granite velocity data with the results from the above two methods.

Hadley (1976) studied the pore spaces in the Westerly granite using the SEM photographs. She calculated the fractional concentrations of each aspect ratio crack using two different assumptions: the area average approximation and the volume average approximation. Briefly the area average approximation assumes that the fractional concentrations of the different aspect ratio cracks are proportional to the areas represented in the SEM photographs. The volume average approximation assumes all cracks are penny-shaped and their respective volumes are calculated as if their crack lengths in the third dimension are the same as they are in the SEM photograph. The exact details are given in Hadley (1976). The results for the area average approximation are much more accurate than the volume average approximation as indicated by both the estimated crack porosities and the fit to the seismic velocities (Hadley, 1976).

Figure (5-11) shows the comparison between the crack spectrum of Hadley (1976) and the one we have obtained (see table 5-1) through the inversion of velocity data. The ordinate is plotted as the percent porosity, i.e., the porosities of the cracks of $\alpha < 10^{-2}$ normalized to the total porosity of cracks of $\alpha < 10^{-2}$. We can see the correspondence of the concentration of cracks around $\alpha = 10^{-3}$ between the two estimates. There are more fine cracks of aspect ratios around 10^{-4} in our estimate than Hadley's. This may be because of the limited resolution power of the SEM technique and many cracks of aspect ratios less than 10^{-3} are missed (Hadley, 1976). Other than that, the correspondence is remarkable.

Sprunt and Brace (1974) measured the frequency distribution of cavity aspect ratio in Westerly granite using a technique similar to that used by Hadley. The range of aspect ratios they measured is from very fine cracks (aspect ratio = 10^{-4}) all the way up to equidimensional pores (aspect ratio = 1). Their results are reproduced here in figure (5-12). In comparison with our inversion results (see table 5-1), there are a few interesting features we can observe. The first point is that the pore porosity of 0.7% estimated by Birch (1960) corresponds almost identically with the fractional porosity we obtained at $\alpha = 1$. The second point to observe is that there seems to be a peak in the number of cracks at $\alpha = 10^{-3}$ (not including the pores with $\alpha = 1$ and

0.1). This agrees well qualitatively with Hadley's observations and our inversion results.

Since the results of Sprunt and Brace are presented as the number of cavities versus aspect ratio, we will have to make some assumptions to convert their results to porosity versus aspect ratio. An obvious (but not necessarily valid) assumption is that the crack lengths stay constant. If we do this then the roughly constant number of cavities (see figure 5-12) between $\alpha = 10^{-3}$ and 10^{-2} cracks will imply that the fractional porosity of the $\alpha = 10^{-2}$ cracks will be an order of magnitude more than the $\alpha = 10^{-3}$ cracks (this is because the porosity of an oblate spheroidal crack is proportional to the cube of the crack length and to the first order in α). This indeed is observed in our inversion results (table 5-1). However, if the same argument is applied to cracks of aspect ratio 10^{-4} also, the predicted porosity using Sprunt and Brace's result is an order of magnitude less than that obtained by the inversion of velocity data. This could be explained by the fact that most of the $\alpha = 10^{-2}$ and 10^{-3} cracks have crack lengths of about 100 μm (Sprunt and Brace, 1974), but if we use that value for $\alpha = 10^{-4}$ cracks, their crack widths would be 0.01 μm, less than the resolution (0.02 μm) of the technique. Assuming a crack width of 0.02 μm for these $\alpha = 10^{-4}$ cracks, we would have to use a value of 200 μm for the crack lengths, and with the cubic dependence of porosity on the crack length, the predicted porosity would

then agree well with that obtained by inversion.

In a series of papers, starting with Simmons et al. (1974) and through others (Siegfried and Simmons, 1978; Feves and Simmons, 1976; Feves et al., 1978), a new analysis of strain data has been proposed. It involves the measuring of the strains of a rock as a function of pressure and subtracting from them the simultaneously measured strains of a fused silica sample. The resultant data are differentiated twice to obtain the fractional porosity of the crack that closes at a given pressure. Details are given in Simmons et al. (1974) and are not repeated here. Quantitatively one cannot take the numerical values of the concentrations of cracks that close at a given pressue too literally because of the errors that may be involved in taking derivatives of data. The inherent errors in the measurements are magnified by the numerical differentiation process, especially if the data points are taken at small pressure intervals, as in the case here. However, the qualitative features of the results may be revealing. For the Westerly granite, Feves and Simmons (1976) found that the majority of the cracks closes at around 200 to 300 bars. This corresponds to an aspect ratio of around 0.5×10^{-3} to 0.75×10^{-3}, using the Walsh formulation with the effective bulk modulus of the dry rock instead of the matrix moduli. This also corresponds well with our estimates (figure 5-11).

So, as far as the Westerly granite is concerned, the

pore-aspect ratio spectrum from the inversion of velocity data seems to correspond well with other estimates, within reasonable constraints on both experimental and theoretical errors. It is a pity that we do not have more independent constraints on the other rock samples, especially the sandstones. However, given what we have seen with the good fits to the measured velocities, we can be reasonably sure that the pore-aspect ratio spectra obtained through the inversion technique do represent the actual distributions of pore spaces in the rock samples.

TABLE 5-1

Pore-Aspect Ratio Spectra of Rocks obtained by the Inversion of Velocity Data

Navajo Sandstone		Berea Sandstone	
ϕ = 16.41% ε = 1 K = 0.34 Mb		ϕ = 18.8% ε = 1 K = 0.32 Mb	
μ_d = 0.26 Mb μ_w = 0.25 Mb		μ = 0.245 Mb	
Dry and Brine-saturated Data		Brine-saturated Data	
Local error tolerance = 5%		Local error tolerance = 5%	
Number of iterations = 5		Number of iterations = 5	
α	$c(\alpha)$	α	$c(\alpha)$
1	0.1416 ± 0.0023	1	0.1704 ± 0.0029
0.1	$(0.2112 \pm 0.1728) \times 10^{-1}$	0.1	$(0.1410 \pm 0.0251) \times 10^{-1}$
0.01	$(0.2390 \pm 0.1728) \times 10^{-3}$	0.01	$(0.2497 \pm 0.0238) \times 10^{-2}$
0.35×10^{-2}	$(0.1424 \pm 0.0678) \times 10^{-3}$	0.17×10^{-2}	$(0.1766 \pm 0.0490) \times 10^{-3}$
0.28×10^{-2}	$(0.1981 \pm 0.0537) \times 10^{-3}$	0.14×10^{-2}	$(0.1872 \pm 0.0392) \times 10^{-3}$
0.21×10^{-2}	$(0.1496 \pm 0.0397) \times 10^{-3}$	0.1×10^{-2}	$(0.2616 \pm 0.0284) \times 10^{-3}$
0.16×10^{-2}	$(0.1830 \pm 0.0301) \times 10^{-3}$	0.6×10^{-3}	$(0.2174 \pm 0.0172) \times 10^{-3}$
0.12×10^{-2}	$(0.1364 \pm 0.0240) \times 10^{-3}$	0.3×10^{-3}	$(0.1278 \pm 0.0088) \times 10^{-3}$
0.9×10^{-3}	$(0.6540 \pm 0.1220) \times 10^{-4}$	0.1×10^{-3}	$(0.4833 \pm 0.0308) \times 10^{-4}$
0.6×10^{-3}	$(0.1116 \pm 0.0074) \times 10^{-3}$		
0.3×10^{-3}	$(0.1111 \pm 0.0066) \times 10^{-3}$		
$\sigma_y^2 = 0.00215$		$\sigma_y^2 = 0.00438$	

TABLE 5-1 (cont.)

Yule Marble

ϕ = 0.4% ε = 1 K = 0.84 Mb

μ = 0.30 Mb

Brine-saturated Data

Local error tolerance = 3%

Number of iterations = 2

α	$c(\alpha)$
1	$(0.1675 \pm 0.1579) \times 10^{-2}$
0.1	$(0.2123 \pm 0.1538) \times 10^{-2}$
0.75×10^{-3}	$(0.5442 \pm 0.1374) \times 10^{-4}$
0.6×10^{-3}	$(0.3517 \pm 0.1044) \times 10^{-4}$
0.4×10^{-3}	$(0.3454 \pm 0.0715) \times 10^{-4}$
0.3×10^{-3}	$(0.3623 \pm 0.0538) \times 10^{-4}$
0.15×10^{-3}	$(0.2897 \pm 0.0287) \times 10^{-4}$
0.5×10^{-4}	$(0.1307 \pm 0.0103) \times 10^{-4}$

$\sigma_y^2 = 0.00184$

Westerly Granite

ϕ = 0.9% ε = 1 K = 0.59 Mb

μ = 0.32 Mb

Dry and water-saturated Data

Local error tolerance = 5%

Number of iterations = 5

α	$c(\alpha)$
1	$(0.6929 \pm 0.6990) \times 10^{-2}$
0.01	$(0.1558 \pm 0.0447) \times 10^{-2}$
0.17×10^{-2}	$(0.8440 \pm 0.9255) \times 10^{-4}$
0.12×10^{-2}	$(0.6689 \pm 0.6770) \times 10^{-4}$
0.85×10^{-3}	$(0.1513 \pm 0.0461) \times 10^{-3}$
0.55×10^{-3}	$(0.1050 \pm 0.0272) \times 10^{-3}$
0.25×10^{-3}	$(0.6569 \pm 0.1269) \times 10^{-4}$
0.1×10^{-3}	$(0.4025 \pm 0.0588) \times 10^{-4}$

$\sigma_y^2 = 0.01817$

TABLE 5-1 (cont.)

Berea Sandstone

ϕ = 16.3% ε = 1 K = 0.32 Mb

μ_d = 0.255 Mb μ_w = 0.245 Mb

Gas and Brine-saturated Data

Local error tolerance = 5%

Number of iterations = 5

α	$c(\alpha)$
1	0.1399 ± 0.00422
0.1	$(0.2207 \pm 0.0367) \times 10^{-1}$
0.01	$(0.3725 \pm 0.3447) \times 10^{-3}$
0.17×10^{-2}	$(0.1402 \pm 0.0702) \times 10^{-3}$
0.14×10^{-2}	$(0.1363 \pm 0.0567) \times 10^{-3}$
0.1×10^{-2}	$(0.1572 \pm 0.0391) \times 10^{-3}$
0.6×10^{-3}	$(0.1315 \pm 0.0246) \times 10^{-3}$
0.3×10^{-3}	$(0.1126 \pm 0.0135) \times 10^{-3}$

$\sigma_y^2 = 0.00938$

Boise Sandstone

ϕ = 25% ε = 1 K = 0.31 Mb

μ = 0.19 Mb

Dry and Kerosene-saturated Data

Local error tolerance = 5%

Number of iterations = 5

α	$c(\alpha)$
1	0.1877 ± 0.0025
0.1	$(0.6176 \pm 0.0222) \times 10^{-1}$
0.35×10^{-2}	$(0.3655 \pm 0.7566) \times 10^{-4}$
0.28×10^{-2}	$(0.6050 \pm 0.6612) \times 10^{-4}$
0.21×10^{-2}	$(0.6377 \pm 0.4942) \times 10^{-4}$
0.17×10^{-2}	$(0.1362 \pm 0.0395) \times 10^{-3}$
0.13×10^{-2}	$(0.1096 \pm 0.0299) \times 10^{-3}$
0.9×10^{-3}	$(0.8516 \pm 0.2145) \times 10^{-4}$
0.5×10^{-3}	$(0.6171 \pm 0.1296) \times 10^{-4}$

$\sigma_y^2 = 0.00311$

TABLE 5-1 (cont.)

Spergen Limestone

ϕ = 14% ε = 1 K = 0.63 Mb

μ = 0.235 Mb

Brine-saturated Data

Local error tolerance = 5%

Number of iterations = 2

α	$c(\alpha)$
1	$(0.9593 \pm 0.0120) \times 10^{-1}$
0.1	$(0.4395 \pm 0.0115) \times 10^{-1}$
0.15×10^{-2}	$(0.2476 \pm 0.1743) \times 10^{-4}$
0.11×10^{-2}	$(0.2040 \pm 0.1252) \times 10^{-4}$
0.8×10^{-3}	$(0.1221 \pm 0.0933) \times 10^{-4}$
0.6×10^{-3}	$(0.1637 \pm 0.0706) \times 10^{-4}$
0.3×10^{-3}	$(0.1681 \pm 0.0355) \times 10^{-4}$
0.12×10^{-3}	$(0.1214 \pm 0.0182) \times 10^{-4}$
0.5×10^{-4}	$(0.8356 \pm 0.0639) \times 10^{-5}$

$\sigma_y^2 = 0.00076$

Florida Dolostone

ϕ = 14.5% ε = 1 K = 0.95 Mb

μ = 0.37 Mb

Brine-saturated Data

Local error tolerance = 3%

Number of iterations = 5

α	$c(\alpha)$
1	0.1162 ± 0.0011
0.1	$(0.2862 \pm 0.0109) \times 10^{-1}$
0.9×10^{-3}	$(0.3219 \pm 0.0700) \times 10^{-4}$
0.75×10^{-3}	$(0.2953 \pm 0.0585) \times 10^{-4}$
0.6×10^{-3}	$(0.5275 \pm 0.0731) \times 10^{-4}$
0.4×10^{-3}	$(0.4950 \pm 0.0492) \times 10^{-4}$
0.2×10^{-3}	$(0.1558 \pm 0.0247) \times 10^{-4}$
0.1×10^{-3}	$(0.7581 \pm 0.1265) \times 10^{-5}$
0.5×10^{-4}	$(0.2853 \pm 0.0665) \times 10^{-5}$

$\sigma_y^2 = 0.00082$

TABLE 5-2

Pore-Aspect Ratio Spectra for Navajo Sandstone

Linearized Iterative Inversion (5 Iterations)

K = 0.34 Mb $\quad \mu_d$ = 0.26 Mb $\quad \mu_w$ = 0.25 Mb

porosity = 16.41% $\quad \varepsilon = 1$

	Dry Data	Water-saturated Data
α	$c(\alpha)$	$c(\alpha)$
1	0.1454 ± 0.0020	0.1449 ± 0.0027
0.1	$(0.1706 \pm 0.0149) \times 10^{-1}$	$(0.1753 \pm 0.0217) \times 10^{-1}$
0.01	$(0.6197 \pm 0.1636) \times 10^{-3}$	$(0.5268 \pm 0.2011) \times 10^{-3}$
0.35×10^{-2}	$(0.1399 \pm 0.0952) \times 10^{-3}$	$(0.1314 \pm 0.0780) \times 10^{-3}$
0.28×10^{-2}	$(0.1766 \pm 0.0748) \times 10^{-3}$	$(0.2377 \pm 0.0625) \times 10^{-3}$
0.21×10^{-2}	$(0.1391 \pm 0.0566) \times 10^{-3}$	$(0.1714 \pm 0.0488) \times 10^{-3}$
0.16×10^{-2}	$(0.1792 \pm 0.0428) \times 10^{-3}$	$(0.1907 \pm 0.0376) \times 10^{-3}$
0.12×10^{-2}	$(0.1417 \pm 0.0332) \times 10^{-3}$	$(0.1218 \pm 0.0275) \times 10^{-3}$
0.9×10^{-3}	$(0.7431 \pm 0.1760) \times 10^{-4}$	$(0.8995 \pm 0.1423) \times 10^{-4}$
0.6×10^{-3}	$(0.1100 \pm 0.0102) \times 10^{-4}$	$(0.9470 \pm 0.0948) \times 10^{-4}$
0.3×10^{-3}	$(0.1089 \pm 0.0090) \times 10^{-4}$	$(0.1080 \pm 0.0074) \times 10^{-3}$
σ_y^2	0.00395	0.00279

TABLE 5-3

Pore-Aspect Ratio Spectra for Berea Sandstone

$K = 0.32$ Mb $\mu_d = 0.255$ Mb $\mu_w = 0.245$ Mb $\varepsilon = 1$

$= 16.3\%$* $= 18.5\%$**

α	$c(\alpha)$	$c(\alpha)$	c_{18}/c_{16}
1	0.1399	0.1704	
0.1	0.02207	0.01410	1.15
0.01	0.3725×10^{-3}	0.2492×10^{-2}	
0.17×10^{-2}	0.1402×10^{-3}	0.1766×10^{-3}	1.26
0.14×10^{-2}	0.1363×10^{-3}	0.1872×10^{-3}	1.37
0.1×10^{-2}	0.1572×10^{-3}	0.2616×10^{-3}	1.66
0.6×10^{-3}	0.1315×10^{-3}	0.2174×10^{-3}	1.65
0.3×10^{-3}	0.1126×10^{-3}	0.1278×10^{-3}	1.13
0.1×10^{-3}		0.4833×10^{-4}	
σ_y^2	0.00938	0.00438	

* Five iterations

** Brine-saturated data only. Convergence to 5% local error in moduli after first iteration.

FIGURE CAPTIONS

Figure 5-1: Results of the linearized iterative inversion for Navajo sandstone. The data are from Johnston (1978). The fluid pressure of the water-saturated rock is maintained at 0.465 times that of the confining pressure.

Figure 5-2: Results of the linearized iterative inversion for a high porosity Berea sandstone. The data are from Jones et al. (1977). Fluid pressure is 0.465 times confining pressure.

Figure 5-3: Same as figure (5-2) for Spergen limestone.

Figure 5-4: Same as figure (5-2) for Florida dolostone.

Figure 5-5: Same as figure (5-2) for Yule Marble.

Figure 5-6: Predicted brine-saturated velocities for the Boise sandstone using the pore-aspect ratio spectrum obtained by inverting dry and kerosene-saturated data. (see figure 4-5 and Table 4-1). The matrix shear modulus is lowered to 0.18 Mb.

Figure 5-7: Inversion results for the dry and predicted results for the wet Navajo sandstone (see figure 5-1 for simultaneous inversion of both data sets).

Figure 5-8: Same as figure (5-7) but in this case the inversion is with the wet data and the prediction is for the dry data.

Figure 5-9: Comparisons of the pore-aspect ratio spectra of Navajo and Berea sandstones. The porosities are 16.4%

and 16.3% respectively. Notice the similarity between the two spectra.

Figure 5-10: Pore-aspect ratio spectra of three sandstones: Navajo (ϕ = 16.4%), Berea (ϕ = 18,8%, different from the one shown in figure 5-9) and Boise (ϕ = 25%). The spectra are normalized by their porosities with respect to the Navajo sandstone. Notice that the Boise has a lot less small aspect ratio cracks than the other two.

Figure 5-11: Comparison between pore-aspect ratio spectra obtained by Hadley (1976) using SEM photographs and by the inversion of velocity data (figure 4-7). The porosity is normalized to the total porosity of cracks of aspect ratio less than 10^{-2}. Hadley's resolution of cracks of aspect ratio less than 10^{-3} is limited because of the technique used.

Figure 5-12: The number of cracks versus aspect ratio for Westerly granite (from Sprunt and Brace, 1974).

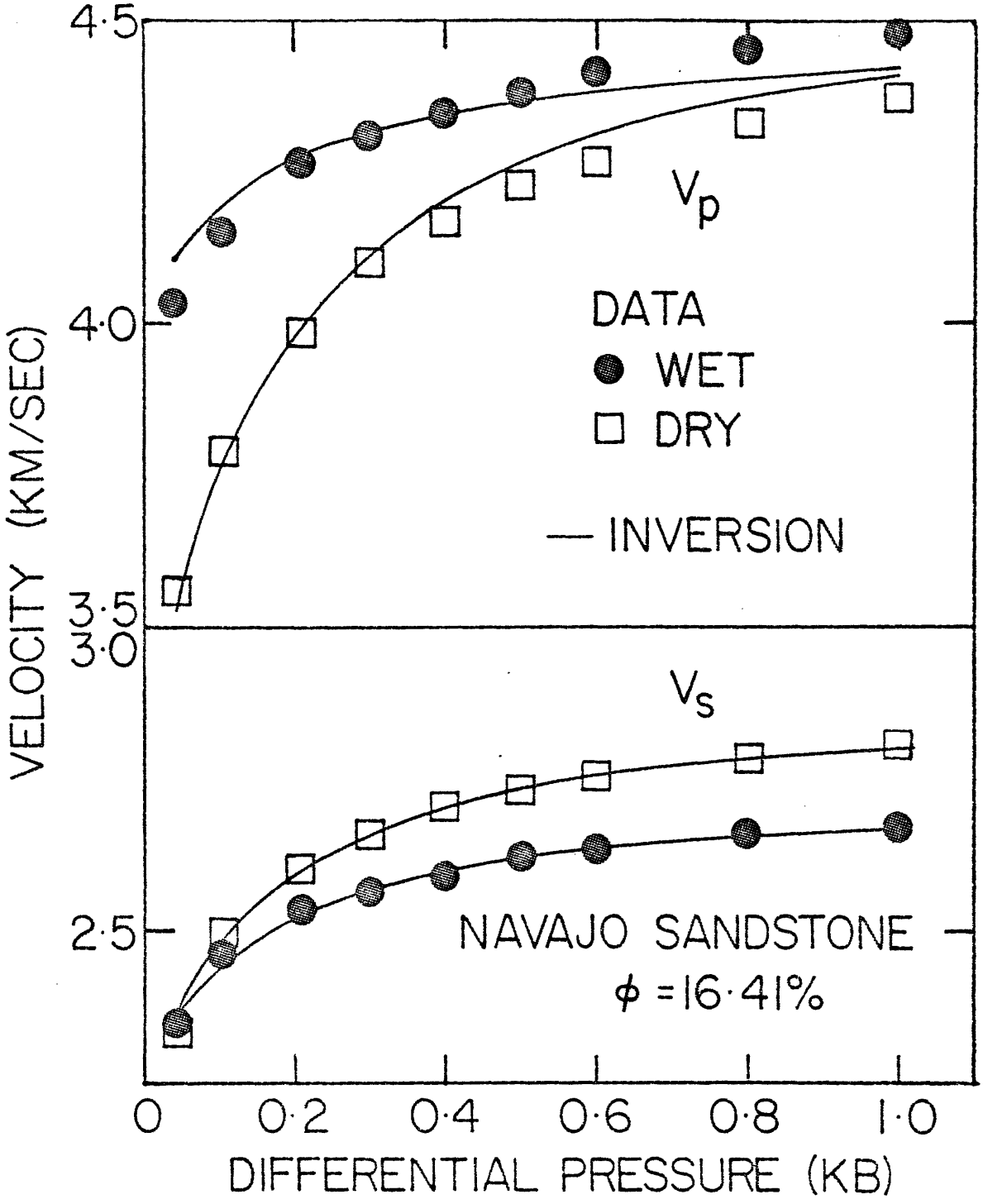
4·5
4·0
3·5
3·0
2·5
VELOCITY (KM/SEC)
V_p
DATA
WET
DRY
— INVERSION
V_s
NAVAJO SANDSTONE
ϕ = 16·41%
0
0·2
0·4
0·6
0·8
1·0
DIFFERENTIAL PRESSURE (KB)

Figure 5-1

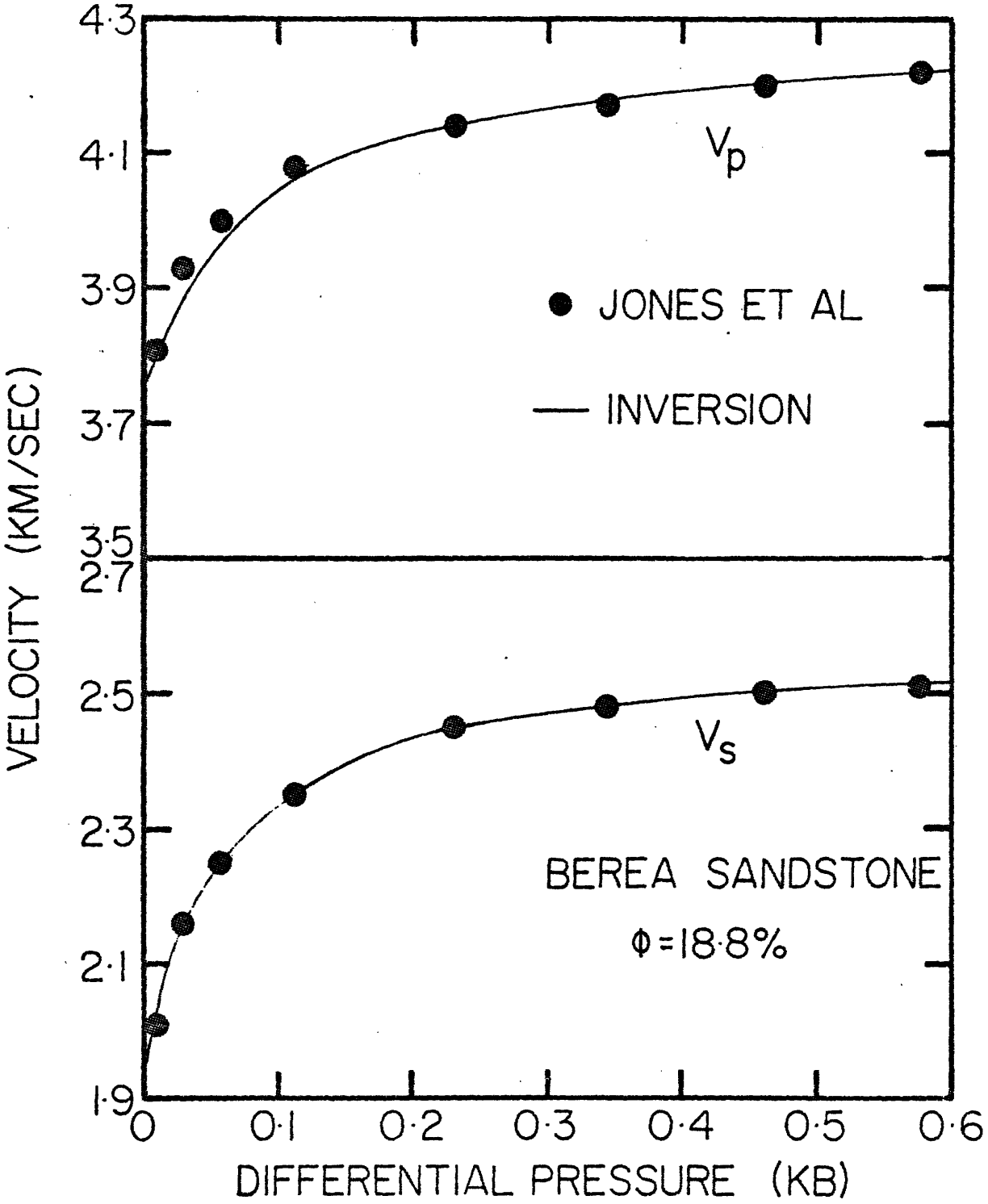
4·3
4·1
3·9
3·7
3·5
2·7
2·5
2·3
2·1
1·9
VELOCITY (KM/SEC)
Vp
JONES ET AL
INVERSION
Vs
BEREA SANDSTONE
Φ=18·8%
0
0·1
0·2
0·3
0·4
0·5
0·6
DIFFERENTIAL PRESSURE (KB)

Figure 5-2

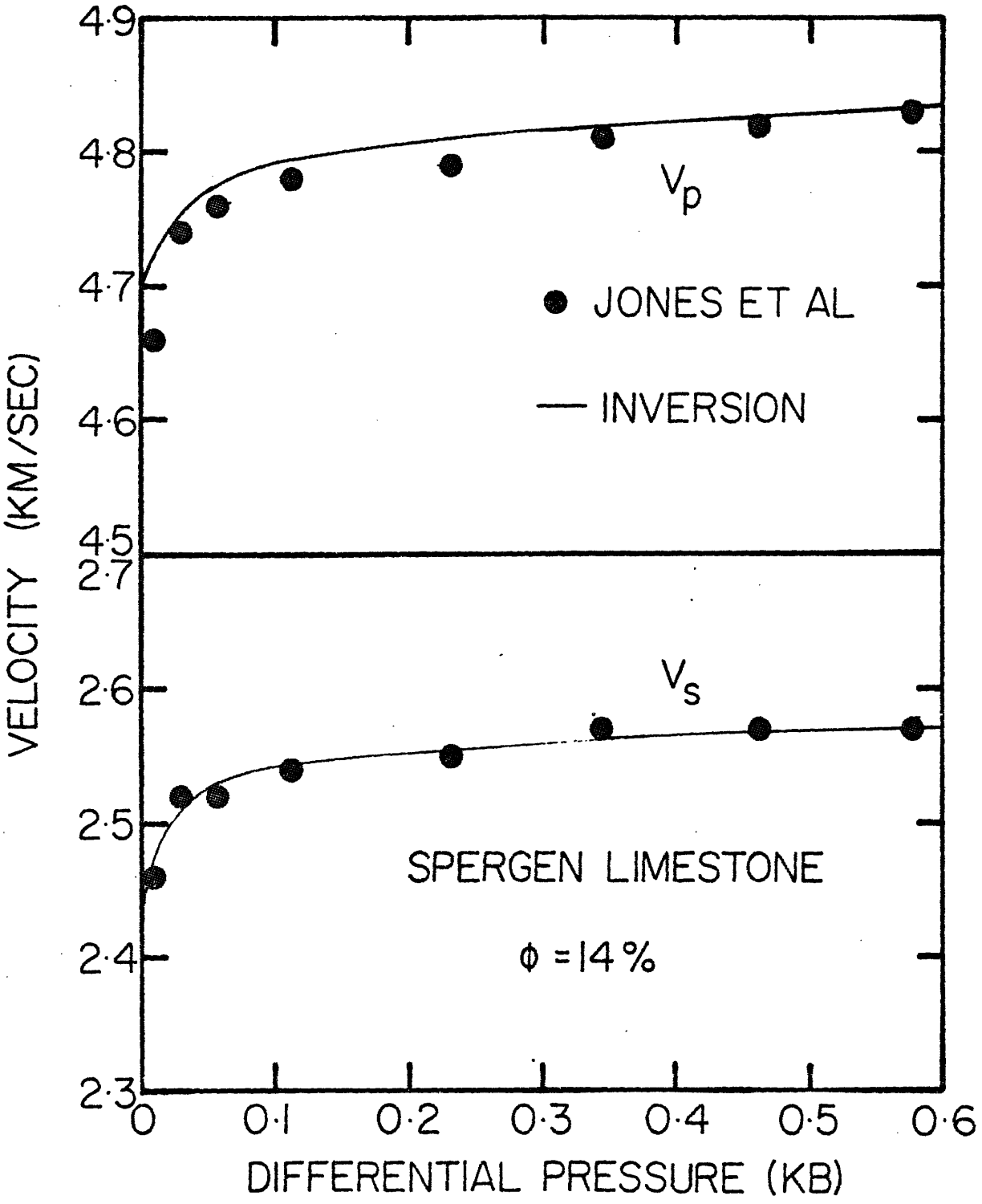
4·9
4·8
4·7
4·6
4·5
V_p
JONES ET AL
INVERSION
2·7
2·6
2·5
2·4
2·3
V_s
SPERGEN LIMESTONE
ϕ = 14 %
VELOCITY (KM/SEC)
0
0·1
0·2
0·3
0·4
0·5
0·6
DIFFERENTIAL PRESSURE (KB)

Figure 5-3

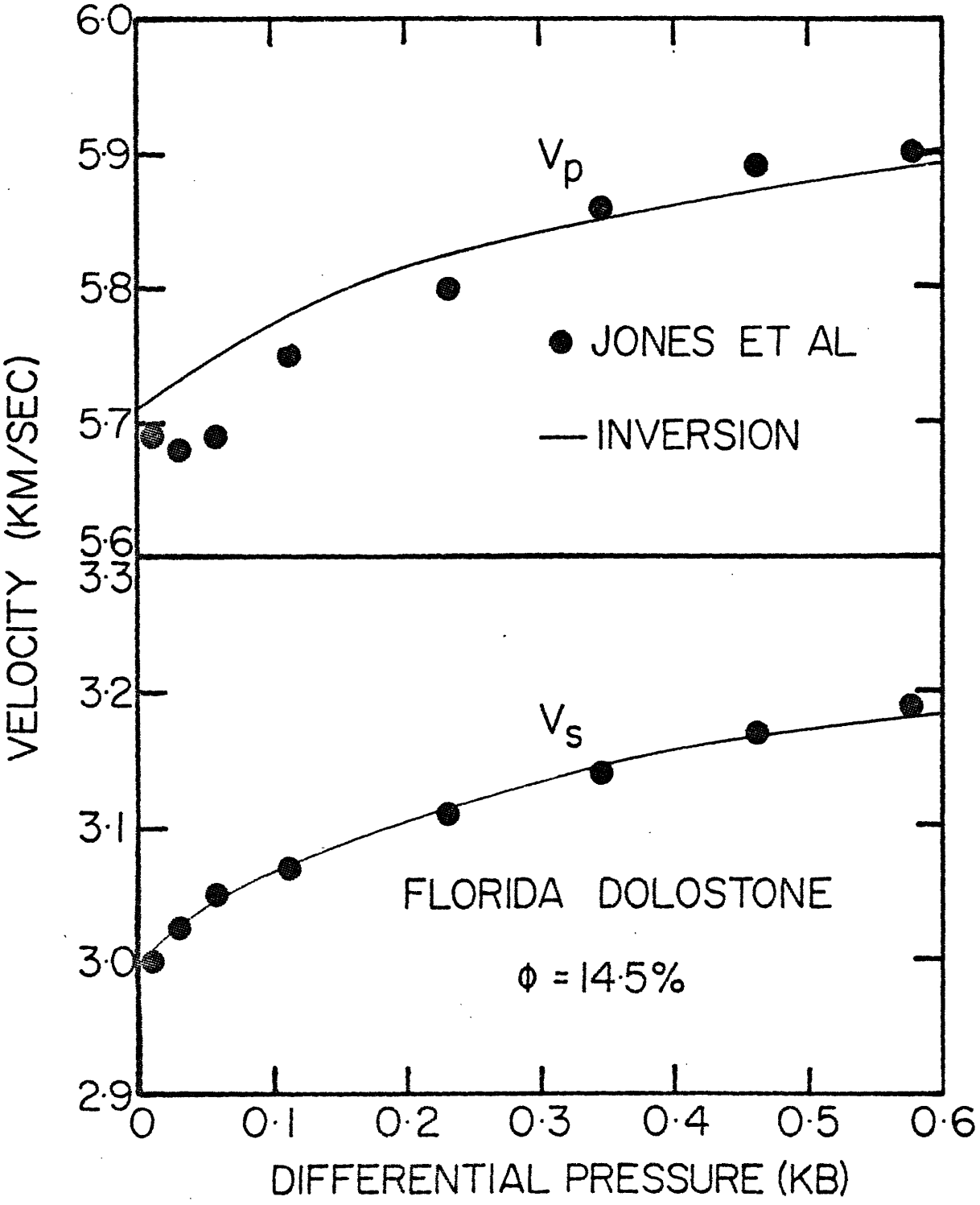
6·0
5·9
5·8
5·7
5·6
V_p
JONES ET AL
INVERSION
3·3
3·2
3·1
3·0
2·9
V_s
FLORIDA DOLOSTONE
ϕ = 14·5%
VELOCITY (KM/SEC)
0
0·1
0·2
0·3
0·4
0·5
0·6
DIFFERENTIAL PRESSURE (KB)

Figure 5-4

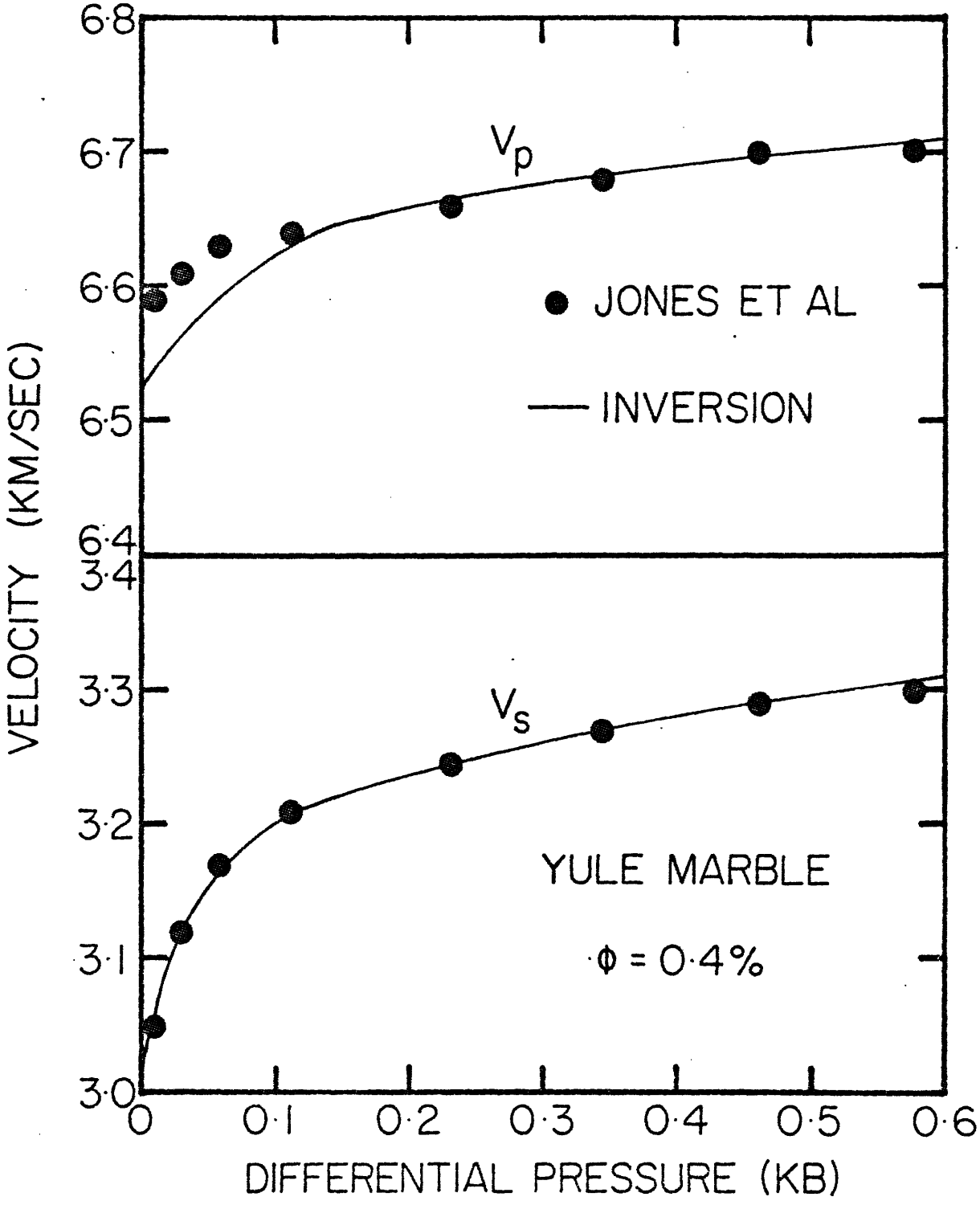
6·8
6·7
6·6
6·5
6·4
3·4
3·3
3·2
3·1
3·0
VELOCITY (KM/SEC)
V_p
JONES ET AL
INVERSION
V_s
YULE MARBLE
ϕ = 0·4%
0
0·1
0·2
0·3
0·4
0·5
0·6
DIFFERENTIAL PRESSURE (KB)

Figure 5-5

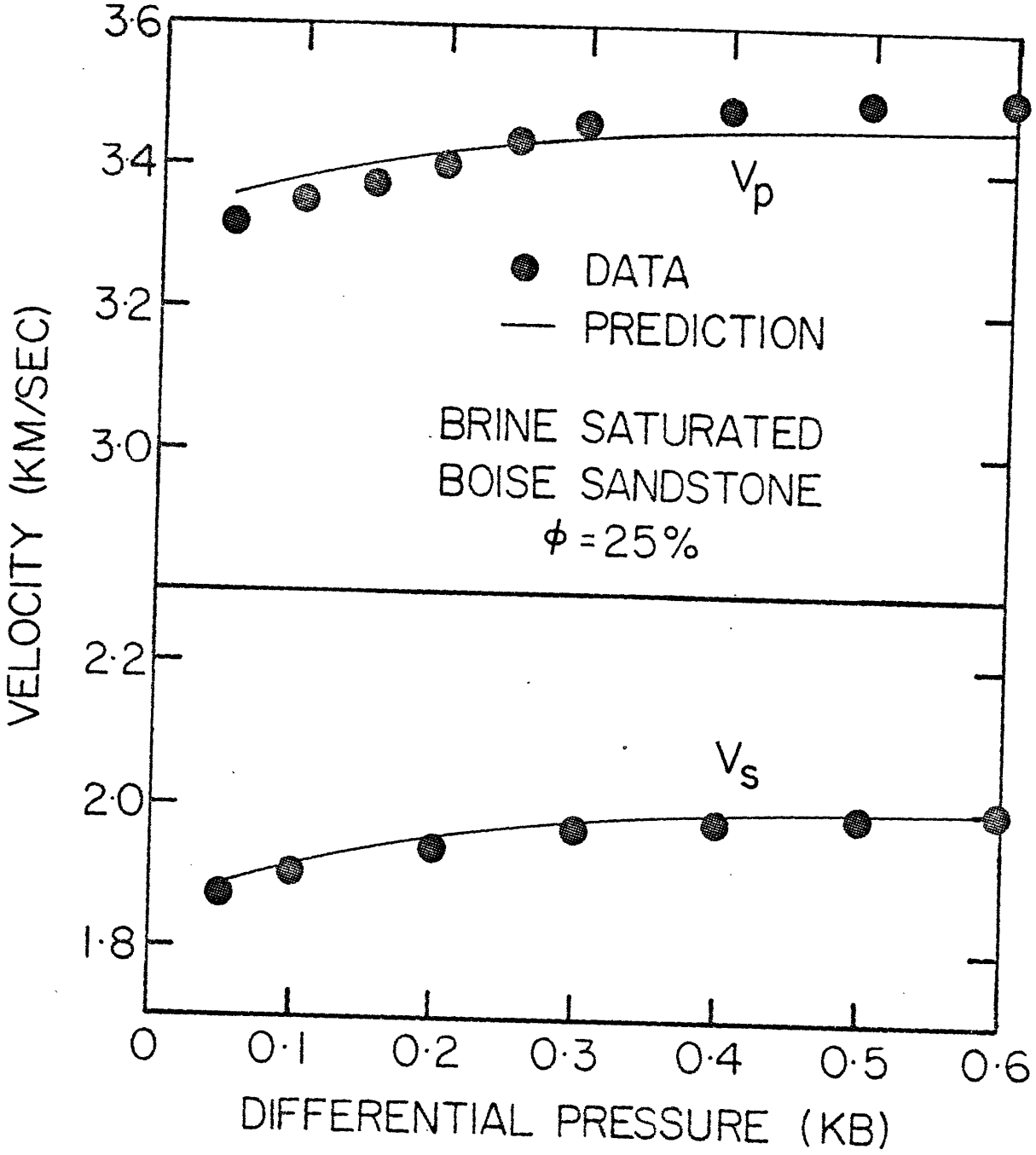
3·6
3·4
3·2
3·0
2·2
2·0
1·8
VELOCITY (KM/SEC)
V_p
DATA
PREDICTION
BRINE SATURATED
BOISE SANDSTONE
ϕ = 25%
V_s
0
0·1
0·2
0·3
0·4
0·5
0·6
DIFFERENTIAL PRESSURE (KB)

Figure 5-6

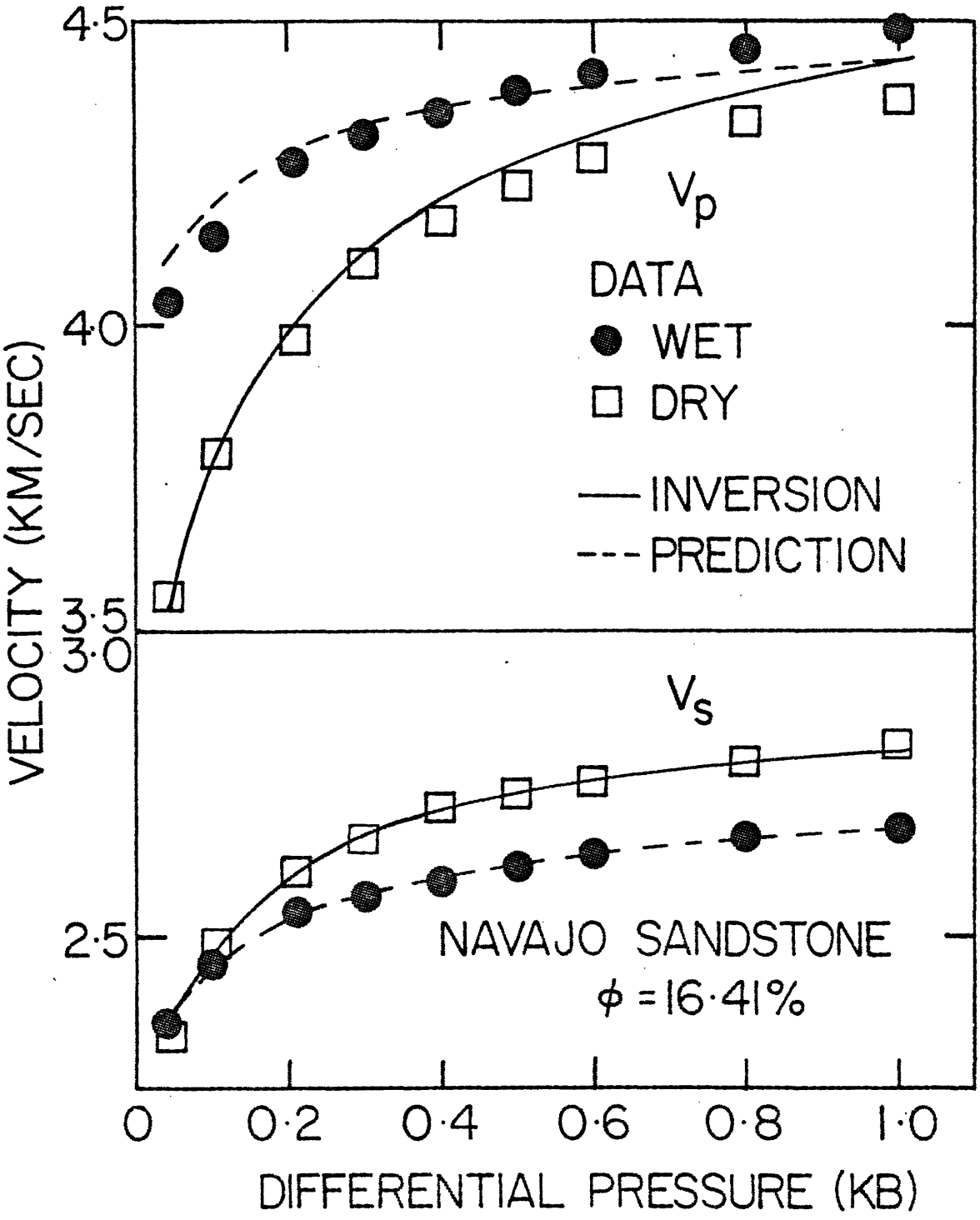
4·5
4·0
3·5
3·0
VELOCITY (KM/SEC)
V_p
DATA
WET
DRY
INVERSION
PREDICTION
V_s
NAVAJO SANDSTONE
ϕ = 16·41%
2·5
0
0·2
0·4
0·6
0·8
1·0
DIFFERENTIAL PRESSURE (KB)

Figure 5-7

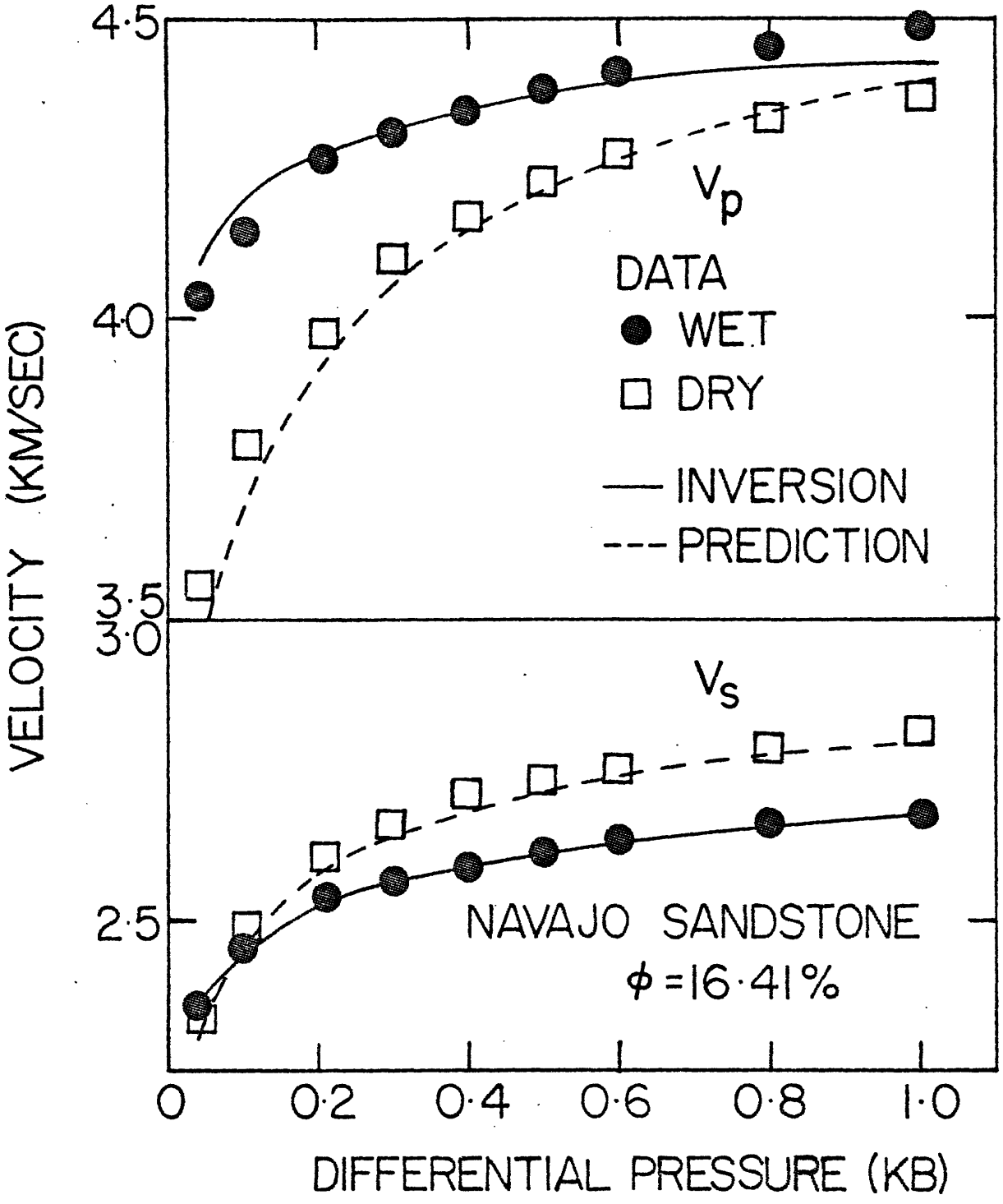
4·5
4·0
3·5
3·0
2·5
VELOCITY (KM/SEC)
V_p
DATA
WET
DRY
INVERSION
PREDICTION
V_s
NAVAJO SANDSTONE
ϕ = 16·41%
0
0·2
0·4
0·6
0·8
1·0
DIFFERENTIAL PRESSURE (KB)

Figure 5-8

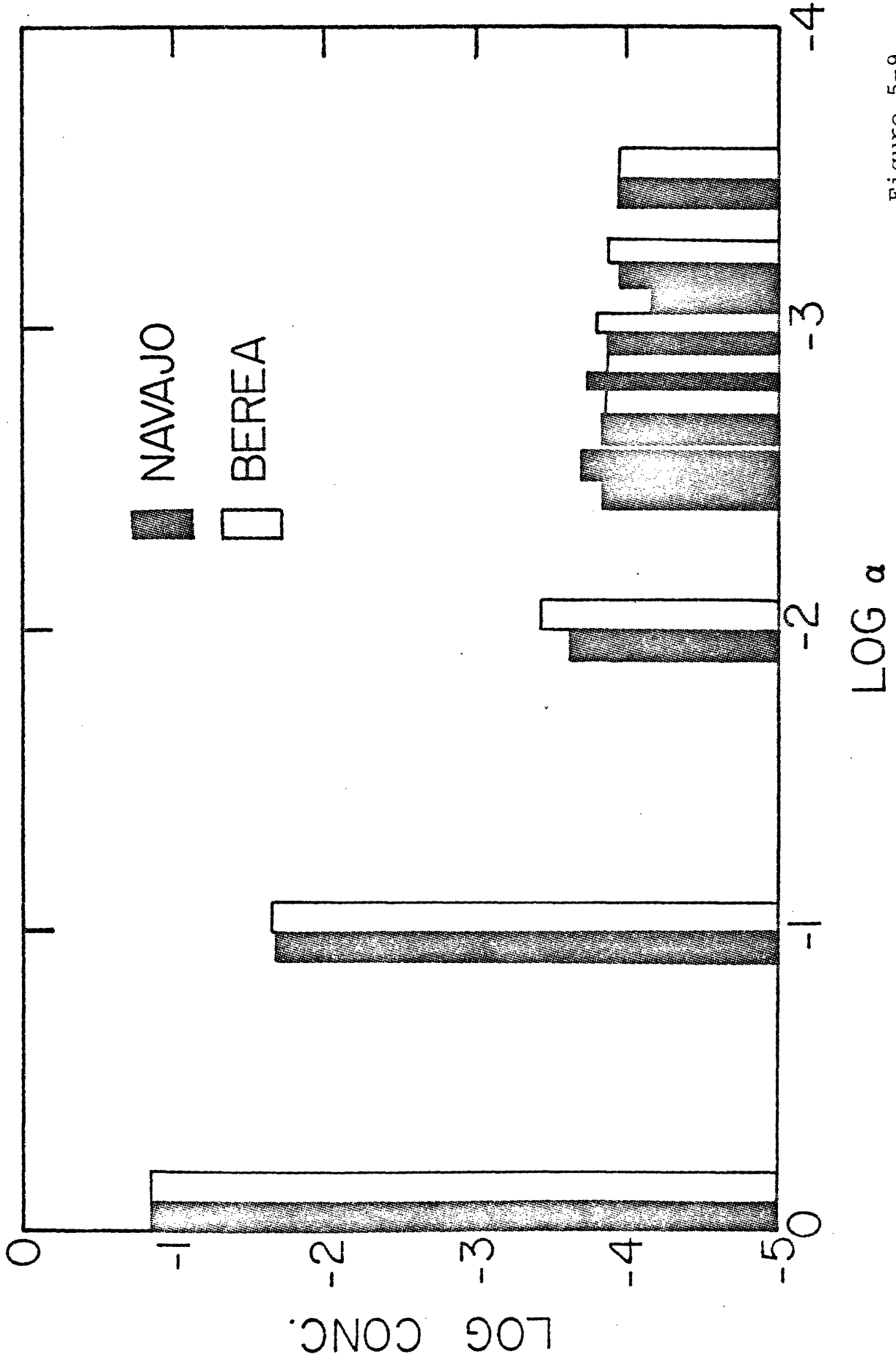

Figure 5-9

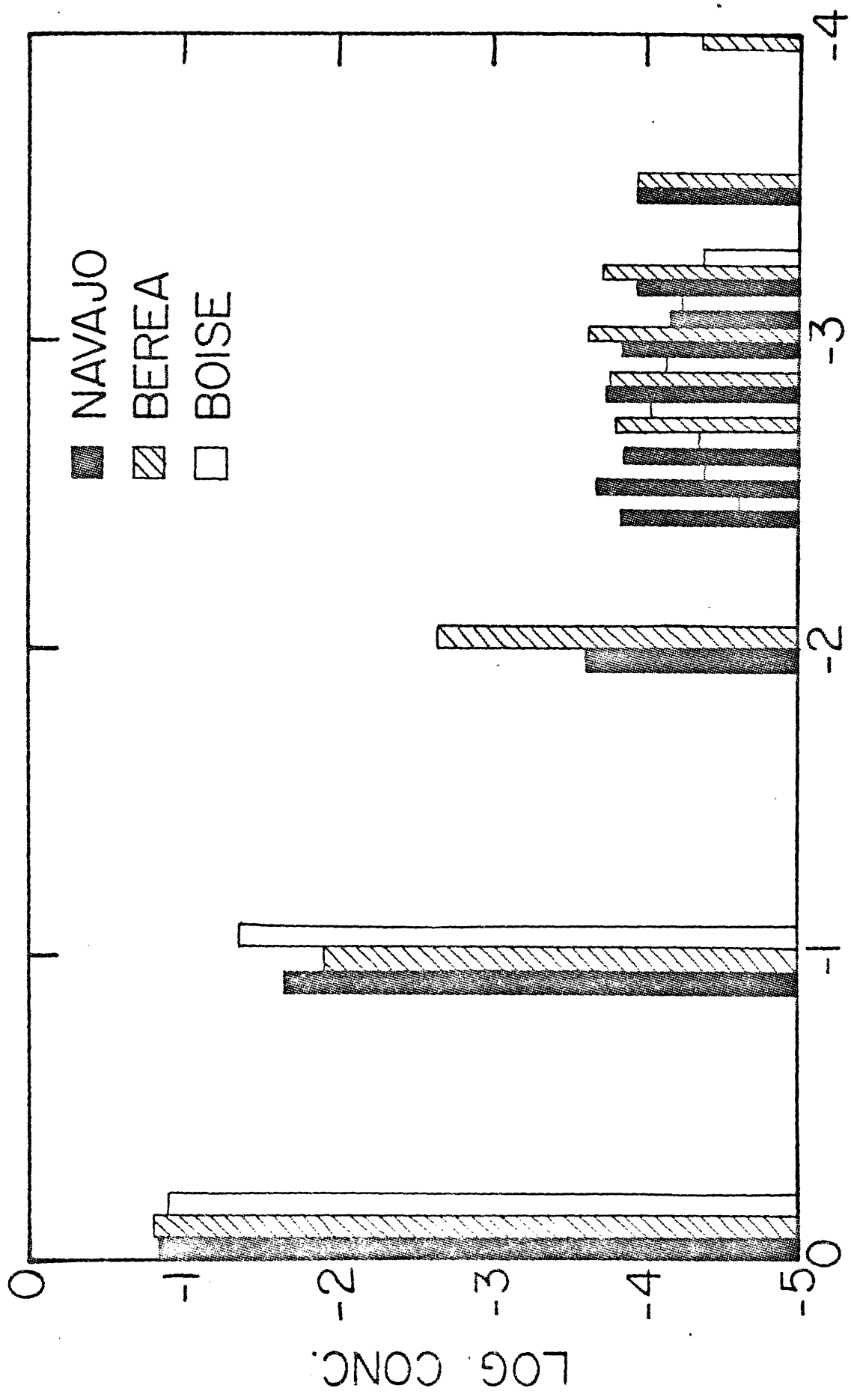

Figure 5-10

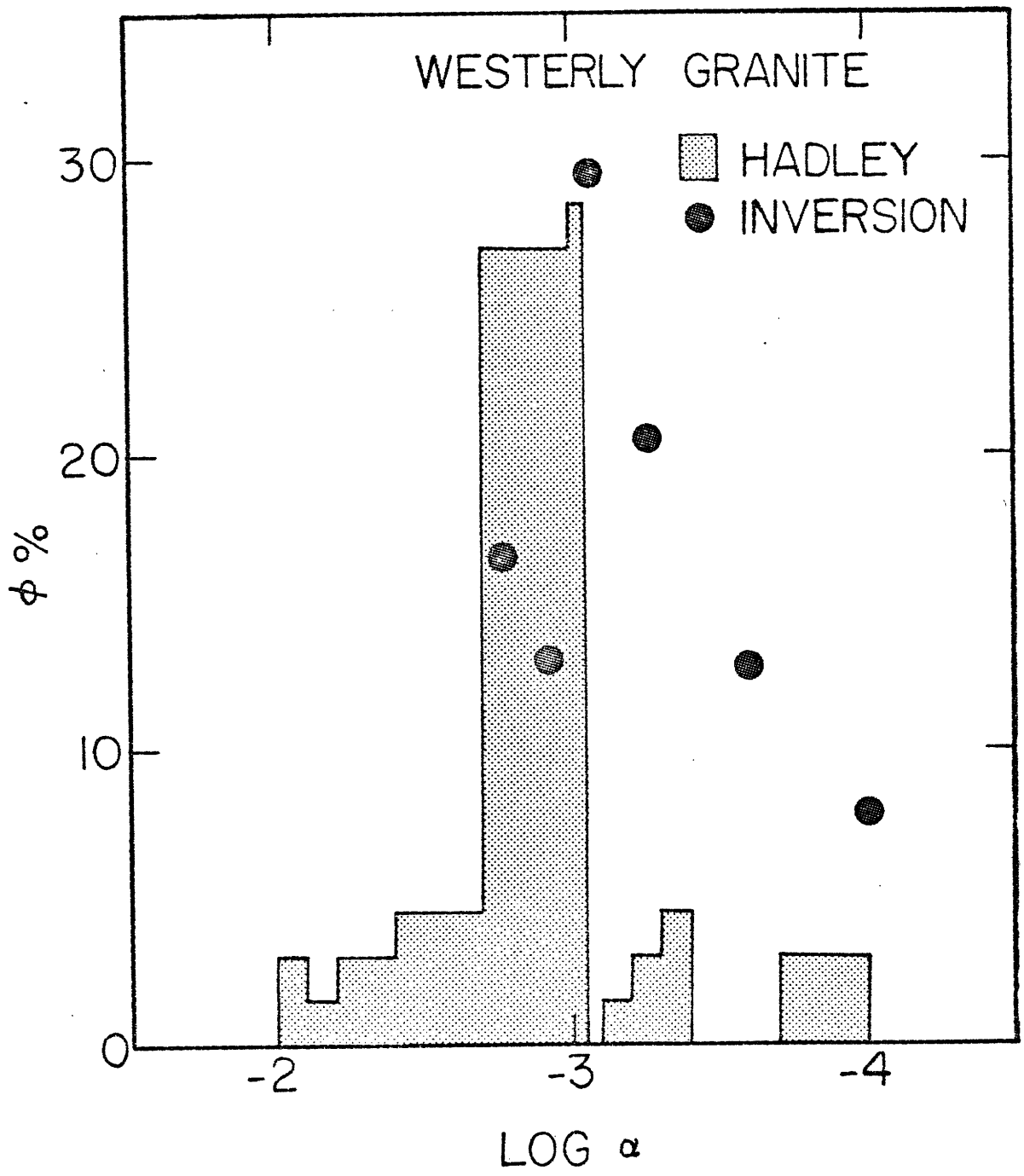

Figure 5-11

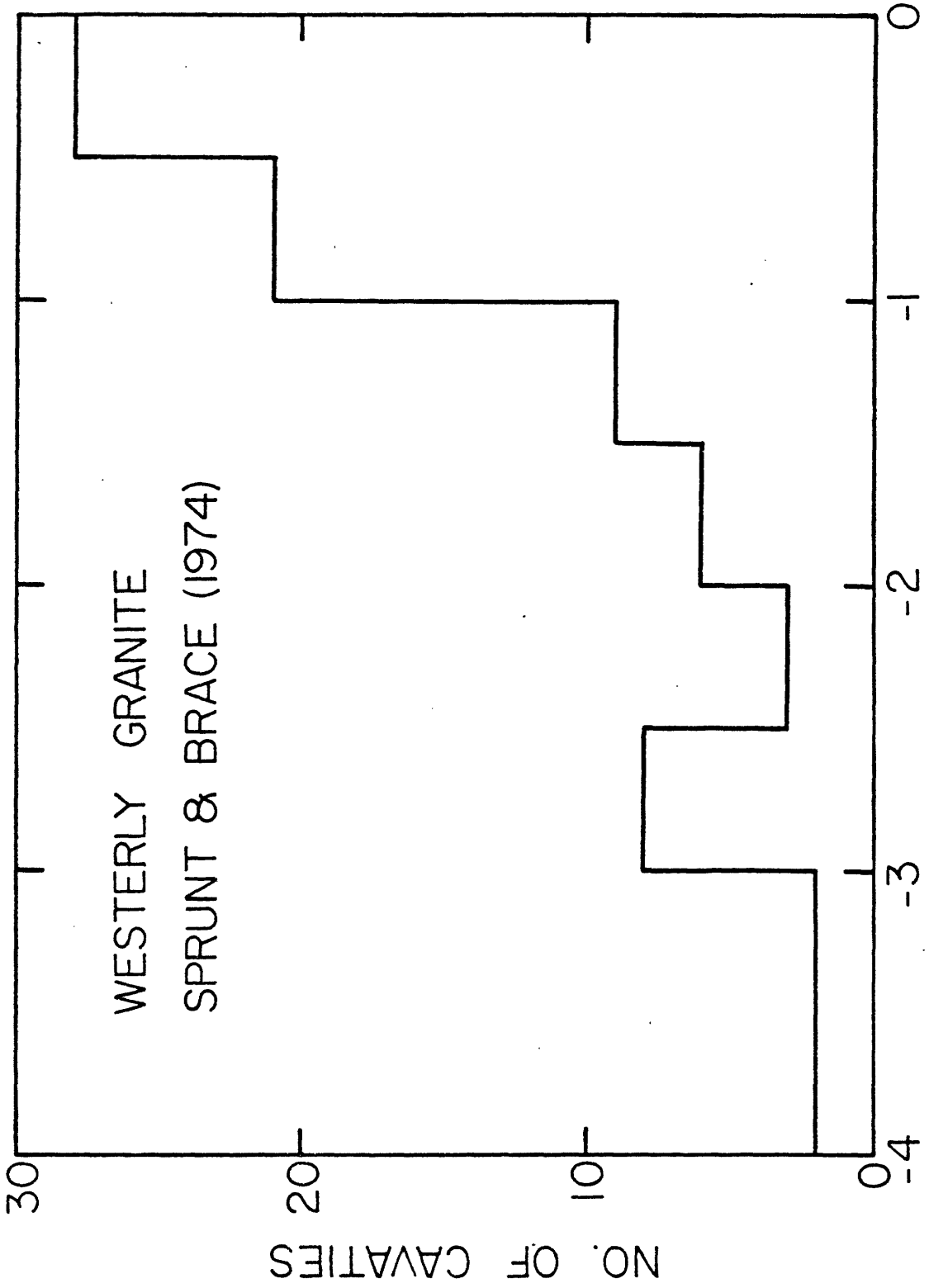
WESTERLY GRANITE
SPRUNT & BRACE (1974)
NO. OF CAVATIES
30
20
10
0
0
-1
-2
-3
-4
LOG ASPECT RATIO

Figure 5-12

CHAPTER 6

DISCUSSIONS AND CONCLUSIONS

In this thesis the problem of seismic velocities in porous rocks was studied from the standpoint of both the direct and inverse problems. In the direct problem, the existing works of first order modelling of cracks in rocks as oblate spheroidal, or "penny-shaped", cracks were reviewed. We compared the different theories with data where the inclusions are spherical shaped. An extension of the first order theories using an iterative approach was then proposed.

In applications to laboratory data of seismic velocities of different rocks under different conditions of pressure and saturation, we found that in general, the p-wave velocities of the dry rock are lower than those of the wet or liquid-saturated rock, while the shear wave velocities usually show the opposite behavior. Furthermore, all velocities increase with differential pressure (confining minus fluid pressure), very rapidly at low pressures and leveling off at higher pressures. These behaviors can be explained by the closing of very small aspect ratio cracks with pressure. Walsh (1965) calculated the rate of closing of very small aspect ratio cracks with pressure using the reciprocal theorem. In this thesis it is extended to cover cracks of all aspect ratios. With this and by using a spectrum of cracks of different

aspect ratios, the velocity data were fitted using a trial and error technique. From the fit to data we obtained for each rock the distribution of fractional porosities with aspect ratios, or the pore-aspect ratio spectrum. Using these rock models, we can then predict the velocities under different full and partial saturation conditions as well as their behaviors under pressure.

In the inverse problem, the question of resolution and uniqueness of the modelling of a rock by its pore-aspect ratio spectrum was addressed. Three techniques were examined: the linear, the linearized iterative and the linear programming inversions The linearized iterative inversion was found to give the best results. Using the damped least squares technique, we were able to get a good trade off between the resolution and the variance of the solution. Our inversion was applied to rocks with a wide range of porosities and was able to fit all the observed velocities very well. Finally, the pore-aspect ratio spectrum of Westerly granite from our inversion of velocity data was found to agree reasonably well with direct observations of pore spaces using SEM photographs and with indirect observation using Differential Strain Analysis.

Before we discuss the conclusions of this thesis and the implications of our work, we would like to point out some of the approximations made and the limitations of our models. In the direct problem, the major and the most obvious appro-

ximation is the use of oblate ellipsoids to characterize the pore spaces in a rock. As can be observed directly from SEM photographs, the pore spaces in a rock are hardly ellipsoidal in shape, although most grain boundary cracks are definitely planar. The question arises naturally of how good an approximation to the actual pore spaces is the ellipsoidal cracks? There is really no definite answer and we can only make an educated guess. The best estimate is that it really does not make too much difference in calculating the effective moduli at a fixed pressure. As far as pressure dependence is concerned, it could be a different story. The tip of an ellipsoidal crack is more resistent to pressure than that of a Hertzian type contact. As a result, the rate of closing of an ellipsoidal crack with pressure is necessarily slower than that of a contact. Furthermore, there is the on-going uncertainty of the difference between the dynamic and static moduli of a rock and the correct values to use in the expression for crack closing, especially in the pressure range we are interested in. This remains to be resolved by more experimental work.

As for the tubular or cylindrical type cavities that connect different pore spaces, they are modelled as prolate spheroidal, or "needle-shaped" cracks. However, their effects on the elastic moduli are found to be very similar to spherical cavities of the same volume. They are therefore included as such in our calculations with loss of generality.

Another question about the moduli of a rock is that of its matrix moduli. Hashin-Shtrikman bounds using individual mineral moduli do not seem to be too satisfactory. They seem to be higher than the values we used in the fit to data. This could be because the shape and orientation of individual grains are not very well defined and could play a much more important role than is accounted for the Hashin-Shtrikman bounds. This could also be resolved by experiments. Theoretically one could measure the matrix bulk modulus by measuring the compressibility of a rock as a function of the confining pressure while keeping the differential pressure zero. It would be interesting to compare the results with both the Hashin-Shtrikman bounds and the values we used in the fit to the velocity data.

On a brighter note, we have found strong support for Bruner's approach to the self-consistent method. Given the approximation of isolated ellipsoids, the exact way of taking into account of the effects of other inclusions is by the integral formulation, or equivalently, letting the cracks "grow" from zero to their final size. In practice, this is achieved by adding in a fraction of the cracks at a time, then calculate the "intermediate" moduli, and add in some more cracks. The method of successive approximation suggested by Gubernatis and Krumhansl (1975) works only for low porosity rocks since for high porosity rocks the first step in the approximation may be so far from the actual solution that it

may have trouble converging back to the actual solution.

Finally, there is the question of the effects of aqueous solutions on the clay in the rock matrix. There is no question about the fact that water saturation depresses the observed shear wave velocities of a rock beyond those predicted by theory, as compared with oil or kerosene saturation. However, the four to five percent decrease in the matrix shear modulus we used is purely as a convenient value that seems to fit the data. How real it is remains open to question.

As for the inverse problem, the major question, in addition to those inherent in the direct problem, concerns the accuracy of the data. Dry samples are never completely dry, like lunar rock samples, and in liquid-saturated samples some of the real fine cracks may not be fully saturated. These are actually minor effects compared to the often less than ideal coupling between the transducers and the sample at low confining pressures. These errors often lead to a fictitous decrease with pressure in the bulk modulus of the liquid-saturated rock at low pressures, thereby affecting the results of the inversion. Furthermore, in rocks with low permeability, in experiments done with fluid pressure there may be a problem of a possible pressure gradient within the rock system owing to the fact that it takes a while for the fluid pressure to reach equilibrium. Johnston (personal communication) pointed out that this condition may exist in his Navajo sandstone data. The result is that the effective differential pressure

is higher than one expects. This might explain the slight difference between the p-wave velocities observed and the inversion results for the water-saturated rock.

One final point about the experimental data is that in order to have a good coverage of the different aspect ratio cracks in the spectrum, it is best that the data points are evenly distributed throughout the pressure range. This is not always the case. As a result, sometimes we might have to interpolate between data points that are too far apart in pressures or drop some data points that are too close together.

With the above mentioned approximations and limitations in mind, we now proceed with the conclusions of this thesis. For the direct problem, we reviewed and compared several different averaging schemes based on the approximation of pore spaces as ellipsoids. It was found that for spherical inclusion shapes, whether they be solids suspended in fluids or empty pores in a solid matrix, comparisons with data show that the Kuster and Toksöz (1974a) scheme works best. The self-consistent averaging schemes of Wu (1966) and Budiansky and O'Connell (1976) do not fit the data at all well in the majority of cases we have look at. The second order scattering theory of Chatterjee et al (1978) fails also because of the non-uniform convergence of the series.

For the oblate ellipsoidal inclusions (aspect ratios close to zero), the picture is less clear because of the lack

of experimental data. However, a similar behavior can be expected because of the fact that the self-consistent methods, as formulated by Wu and Budiansky and O'Connell, overestimate the effects of the cracks (see also Bruner, 1976). We proposed to elimate this overestimate by using an iterative process in conjunction with the self-consistent formulation by adding in a few cracks at a time. This actually amounts to a numerical integration of the exact integral equation formulation of the problem. The iterative technique was found to be convergent and give the same results whether used in conjunction with the Kuster and Toksöz averaging scheme or the Walsh scheme.

We extended Walsh's results for the rate of closing of a penny-shaped crack (aspect ratio approaching zero) with pressure to cracks of all aspect ratios between zero and one using Eshelby's theory. By combining this with the theory of Kuster and Toksöz and by using a spectrum of different aspect ratio cracks, the increases in seismic velocities of a rock with pressure can be modelled. Using a trial and error process, we fitted the measured seismic velocities of several rocks as a function of pressure and under different saturation conditions and obtained the pore-aspect ratio spectra for each. It can therefore be concluded that the modelling of the velocity increases with pressure by the closing of cracks is a viable and realistic approach.

The behavior of rocks under partial saturation conditions

were examined using these rock models. It was found that for a fully liquid-saturated rock, the introduction of a few percent of gas greatly reduces the p-wave velocities, consistent with experimental observations. Furthermore, in a mixed saturation condition, if one of the phases, either liquid or gas, occupies the fine cracks while the other occupies the equidimensional pores, then the resultant velocities will be chiefly determined by the former phase. This fact has to be kept in mind when interpreting experimental data.

As a result of the large reduction in p-wave velocity, the reflection coefficient of a system with relatively low gas concentration will in many cases be comparable to those of one with much higher gas concentration. Since the shear wave velocities are less affected, the Poisson's ratio gives a better estimate of the relative amounts of gas and liquid in such a system than just velocity or reflection coefficient alone. These results affect the interpretation of seismic reflection studies, especially in the exploration for natural gas and geothermal systems.

Because the fine cracks are the major factors in the above observations, those effects decrease with increasing pressure and therefore depth in the earth. However, since the crack closing rate is a function of differential pressure, i.e., the overburden or confining pressure minus the fluid pressure, these effects can persist to great depths

if the fluid pressure remains high. This fact has to be taken into account in both natural gas and geothermal explorations since overpressured formations are likely for these formations.

Finally, the question of uniqueness and resolution of the pore-aspect ratio spectrum of a rock obtained from velocity data was addressed by formulating the technique as an inverse problem. The linearized iterative inversion based on the integral formulation of the direct problem and solved by means of the damped least squares technique was found to give us the best results in terms of the fit to the velocity data. The linear inversion based on the formulations of Kuster and Toksöz gives very good fits for most rocks and is ideal as a starting model for the linearized iterative inversion. In both cases the resolution and variance are reasonably good with the damping coefficient set to one.

The linear inversion problem was also solved using a linear programming technique. The rationale behind this approach was that the fractional porosity would be limited to positive values, whereas in a least squares solution such constraints did not exist. However, the upper and lower bound solutions as posed are too far apart to be practical. This can be traced to the errors in the measurements. Furthermore, numerical experiments with the three techniques did not reveal any practical advantages of the linear programming approach over the damped least squares solution.

We had, therefore, discarded the linear programming approach as a useful solution technique of the inverse problem.

We inverted the velocity data of several different rocks as a function of pressure and for different saturation conditions. The results show that, except for very low porosity (less than one percent) rocks, almost all of the bulk porosity of a rock is contained in the vugular or equidimensional pores. The crack (aspect ratio less than 10^{-2}) spectrum of a rock, however, bears no resemblence to its bulk porosity in general. This is true even within a reasonably small subdivision of rock types like sandstones. The Boise sandstone has a higher bulk porosity than the Berea and the Navajo sandstones, but its crack concentrations are lower than either of them. However, for different samples of the Berea sandstone with different porosities, the pore-aspect ratio spectra are roughly scaled to the individual bulk porosities. This is also true for the spectra of the Navajo and Berea sandstones which are similar in composition, grain size and contact type. The last two factors seem promising in providing us with insights and estimates of the amount of cracks in a rock.

Finally, the pore-aspect ratio spectrum of Westerly granite obtained from the inversion of velocity data was compared to both direct observations of pore spaces using SEM photographs and indirect estimates using the Differential Strain Analysis. It agrees well with direct SEM photographic

observations of both Hadley (1976) and Sprunt and Brace (1974). The peak in the crack spectrum between aspect ratios 5×10^{-4} and 10^{-3} also agrees well with the result of the Differential Strain Analysis (Feves and Simmons, 1976).

In conclusion, the major contributions of this thesis can be summarized as follows:

(1) We have presented a new method of determining the pore-aspect ratio spectrum of a rock by the inversion of its seismic velocities measured as a function of differential pressure. This spectrum, although based on an oblate spheroidal crack model, was shown to agree well with direct observations of pore spaces in a rock.

(2) The pore-aspect ratio spectrum thus determined, when applied in the direct problem, was shown to be able to predict velocities measured under saturation conditions different from those used in the inversion.

(3) Theoretical studies with such rock models showed that in addition to the p-wave velocities, the s-wave velocities provide us with critical information about the properties of the saturating fluids. In particular, the Poisson's ratio of a partially saturated rock formation gives us a better estimate of the relative concentrations of the gas and liquid phases in the saturant than either the interval p-wave velocity or reflection coefficient of that formation alone.

(4) The determination of the pore-aspect ratio spectrum of a rock has wide implications in rock physics. Attenuation

measurements, permeability studies and electrical conductivity models are all dependent on the amount of cracks that exists in a rock. The predictive power of the pore-aspect ratio spectrum together with the importance of s-waves are of significant importance in the interpretation of seismic reflection profiles in petroleum, geothermal and mineral explorations.

REFERENCES

Adams, L. H,. 1931, Equilibrium in binary systems under pressure: I - An experimental and Thermodynamic inverstigation of the system, NaCl-H_2O, at 20°C, Am. Chem. Soc. J., v.53, pt.3, p. 2769-3785.

Aki, K., 1975, Unpublished class notes.

Aki, K. and P. Richards, 1978, Methods of Quantitative Seismology, Freeman.

Ament, W. S., 1953, Sound propagation in gross mixtures, J. Acoust. Soc. Am.,v.25, p.638-641.

Ament, W. S., 1959, Wave propagation in suspensions, U.S. Naval Res. Lab. Report 5307.

Anderson, D. L., B. Minster and D. Cole, 1974, The effect of oriented cracks on seismic velocities, J. Geophys. Res., v.79, p.4011-4016.

Biot, M. A., 1956a, Theory of propagation of elastic waves in a fluid-saturated porous solid: I. low frequency range, J. Acoust. Soc. Am., v.28, p.168-178.

Biot, M. A., 1956b, Theory of Propagation ofelastic waves in a fluid-saturated porous solid: II. higher frequency range, J. Acoust. Soc. Am., v.28, p.179-191.

Birch, F., 1960, The velocity of compressional waves in rocks to 10 kb, I, J. Geophys. Res.,v.65, p.1083-1102.

Birch, F., 1966, Compressibility, elastic constants; in Handbook of Physical Constants, S. P. Clark, ed; Geol. Soc. Am. Mem. 97, p.97-173.

Brace, W. F., 1972, Pore pressure in geophysics, Geophys. Mono. No.16, Flow and Fracture of Rocks, p.265-274, John Wiley and Sons, New York.

Brace, W. F., 1977, Permeability from resistivity and pore shapes, J. Geophys. Res., v.82, p.3343.

Brace, W. F. and A. S. Orange, 1968, Electrical resistivity changes in saturated rocks during fracture and frictional sliding, J. Geophys. Res., v.73, p.1433-1445.

Brace, W. F., A. S. Orange and T. R. Madden, 1965, The effect of pressure on the electricl resistivity of water-saturated crystalline rocks, J. Geophys. Res., v.70, p.5569-5678.

Brace, W. F., E. Silver., K. Hadley and C. Geotze, 1972, Cracks and pores: a closer look, Science, v.178, p. 162-169.

Brace, W. F., J. B. Walsh and W. T. Frangos, 1968, Permeability of granite under high pressure, J. Geophys. Res., v.73 p.2225-2236.

Brown, R. J. S. and J. Korringa, 1975, On the dependence of the elastic properties of a porous rock on the compressibility of the pore fluid, Geophysics, v.40, p.608-616.

Bruner, W. M., 1976, Comments on "Seismic velocities in dry and saturated cracked solids" by Richard J. O'Connell and Bernard Budiansky, J. Geophys. Res., v.81, p.2573-2576.

Budiansky, B., 1965, On the elastic moduli of some heterogeneous materials, J. Mech. Phys. Soilds, v.13, p.223.

Budiansky, B. and R. J. O'Connell, 1976, Elastic moduli of dry and saturated cracked solids, Int. J. Solids Structures, v.12, p.81-97.

Chatterjee, D. K., A. K. Mal and L. Knopoff, 1978, Elastic Moduli of two-component systems, J. Geophys. Res., v.83, p.1785-1792.

Cheng, C. H. and M. N. Toksöz, 1976, Seismic velocities in porous rocks -- direct and inverse problem (abstract), presented at the 46th annual meeting, Society of Exploration Geophysicist, Houston, Texas, Oct. 24-28, 1976.

Chree, C., 1892, Changes in the dimensions of elastic solids due to given systems of forces, Trans. Camb. Phil. Soc., v.15, p.313-337.

Cleary, M. P., 1978, Elastic and dynamic response regimes of fluid-impregnated solids with diverse microstructures, Int. J. Solids Structures, in press.

Dantzig, G., 1963, Linear Programming and Extensions, Princeton Univ. Press, Princeton, N.J.

Domenico, S. N., 1976, Effect of brine-gas mixture on velocity in an unconsolidated sand reservoir, Geophysics, v.41, p.882-894.

Draper, N. and H. Smith, 1966, Applied Regression Analysis, John Wiley and Sons, N.Y., 407p.

Eshelby, J. D., 1957, The determination of the elastic field of an ellipsoidal inclusion, and related problems, Proc. Roy. Soc. London, Ser.A, v.241, p.376-396.

Elliott, S. E. and B. F. Wiley, 1975, Compressional velocities of partially saturated unconsolidated sands, Geophysics, v.40, p.949-954.

Feves, M. and G. Simmons, 1976, Effects of stress on cracks in Westerly granite, Bull. Seismol. Soc. Am., v.66, p.1755-1765.

Feves, M., G. Simmons and R. W. Siegfried, 1978, Microcracks in crustal igneous rocks: physical properties, in The Earth's Crust: Its Nature and Physical Properties, Geophys. Monogr. Ser. 20, in press.

Franklin, J. N., 1970, Well-posed stochastic extensions of ill-posed linear problems, J. Math. Anal. Appl., v.31, p.628-716.

Gardner, G. H. F., L. W. Gardner and A. R. Gregory, 1974, Formation velocity and density -- the diagnostic basics for stratigraphic traps, Geophysics, v.39, p.770-780.

Gassmann, F., 1951, Uber die Elastizitat Poroser Medien, Vierteljahrsschr. Naturforsch. Ges. Zurich, v.96, p.1-21.

Geertsma, J., 1975, The effect of fluid pressure decline on volumetric changes of porous rocks, Trans. AIME, v.210, p.331-340.

Geertsma, J. and D. C. Smit, 1961, Some aspects of elastic wave propagation in fluid-saturated porous solids, Geophysics, v.26, p.169-181.

Golub, G. and W. Kahan, 1965, Calculating the singular values and pseudo-inverse of a matrix, J. SIAM Num. Anal. Ser.B, v.2, p.205-224.

Greenberg, R. S. and W. F. Brace, 1969, Archie's law for rocks modelled by simple networks, J. Geophys. Res., v.74, p.2099-2102.

Gregory, A. R., 1976, Fluid saturation effects on dynamic elastic properties of sedimentary rocks, Geophysics, v.41, p.895-921.

Gubernatis, J. E. and J. A. Krumhansl, 1975, Macroscopic engineering properties of polycrystalline materials: elastic properties, J. Appl. Phys., v.46, p.1875-1883.

Hadley, K., 1976, Comparison of calculated and observed crack densities and seismic velocities in Westerly granite, J. Geophys. Res., v.81, p.3484-3494.

Hashin, Z., 1962, The elastic moduli of Hetergeneous materials, J. Appl. Mech.,v.29E, p.143-150.

Hashin, Z. and S. Shtrikman, 1962, A variational approach to the theory of the effective magnetic permeability of multi-phase materials, J. Appl. Phys., v.33, p.3125-3131.

Hashin, Z. and S. Shtrikman, 1963, A variational approach to the theory of the elastic behavior of multi-phase materials, J. Mech. Phys. Solids, v.11, p.127-140.

Hill, R., 1952, The elastic behaviour of a crystalline aggregate, Proc. Phys. Soc. (Lon.), v.65, p.349-354.

Johnson, C. E., 1972, Regionalized earth models from linear programming methods, M.S. Thesis, M.I.T., Cambridge, Ma.

Johnston, D. H., 1978, Ph.D. Thesis, M.I.T., Cambridge, Ma.

Johnston, D. H., M. N. Toksöz and A. Timur, 1978, Attenuation of seismic waves in dry and saturated rocks: II. Mechanisms, submitted to Geophysics.

Jones, S. B., D. D. Thompson and A. Timur, 1977, A unified investigation of elastic wave propagation in crustal rocks, submitted for publication.

Katz, D. L., D. Cornell, R. Kobayaski, F. H. Poettmann, J. A. Vary, J. R. Elenbaas and C. F. Weinang, 1959, Handbook of Natural Gas Engineering, McGraw Hill, 802p.

King, M. S., 1964, Wave velocities and dynamic elastic moduli of sedimentary rocks, Ph.D. Thesis, U. of Calif., Berkeley.

King, M. S., 1966, Wave velocities in rocks as a function of changes in overburden pressure and pore fluid saturants, Geophysics, v.31, p.50-73.

Kennedy, G. C. and Holser, W. T., 1966, Pressure-volume-temperature and phase relations of water and carbon dioxide, Handbook of Physical Constants, S. P. Clark, ed., Geol. Soc. Am. Mem. 97, p.371-383.

Korringa, J., 1973, Theory of elastic constants of Heterogeneous media. J. Math. Phys., v.14, p.509-513.

Korringa, J. and D. D. Thompson, 1977, Comment on the self-consistent imbedding approximation in the theory of elasticity of porous media, J. Geophys. Res., v.82, p.933-934.

Kröner, E., 1958, Berechnung der elastischen konstanten des vielkristalls aus den konstanten der einkristalls, Z. Phys., v.151, p.504.

Kuster, G. T., 1972, Seismic wave propagation in two-phase media and its application to the earth's interior, Ph.D. Thesis, M.I.T., Cambridge, Ma.

Kuster, G. T. and M. N. Toksöz, 1974a, Velocity and attenuation of seismic waves in two-phase media: part I -- Theoretical formulations, Geophysics, v.39, p.587-606.

Kuster, G. T. and M. N. Toksöz, 1974b, Velocity and attenuation of seismic waves in two-phase media: part II -- Experimental results, Geophysics, v.39, p.607-618.

Lanczos, C., 1961, Linear Differential Operators, Ch.3, Van Nostrand.

Lee, W. B. and S. C. Solomon, 1975, Inversion schemes for surface wave attenuation and Q in the crust and the mantle, Geophys. J. Roy. Astron. Soc., v.43, p.47-71.

Lee, W. B. and S. C. Solomon, 1978, Simultaneous inversion of surface wave phase velocity and attenuation: Love waves in western North America, J. Geophys. Res., v.83, p.3389-3400.

Love, A. E. H., 1947, A Treatise on the Mathematical Theory of Elasticity, Cambridge Univ. Press, 643p.

Luenberger, D. G., 1973, Introduction to Linear and Nonlinear Programming, Addison-Wesley, Reading, Ma.

MacKenzie, J. K., 1950, The elastic constants of a solid containing spherical holes, Proc. Phys. Soc. Lon. Ser.B, v.63, p.2-11.

Madden, T. R., 1976, Random networks and mixing laws, Geophysics, v.41, p.1104-1125.

Mal, A. K. and L. Knopoff, 1967, Elastic wave velocities in two-component systems, J. Inst. Math. Appl., v.3, p.376-387.

Mavko, G. and A. Nur, 1975, Melt squirt in the aesthenosphere, J. Geophys. Res., v.80, p.1444-1448.

Mavko, G. and A. Nur, 1978, Wave attenuation in partially saturated rocks, Geophysics, in press.

Morse, P. M. and H. Feshbach, 1953, Methods of Theoretical Physics, McGraw Hill, New York.

Nur, A. M., 1969, Effects of stress and fluid inclusions on wave propagation in rocks, Ph.D. Thesis, M.I.T., Cambridge, Ma.

Nur, A., 1971, Effects of stress on velocity anisotropy in rocks with cracks, J. Geophys. Res.,v.76, p.2022-2034.

Nur, A. M. and G. Simmons, 1969, The effect of saturation on velocity in low porosity rocks, Earth Plan. Sci. Letters, v.7, p.183-193.

O'Connell, R. J. and B. Budiansky, 1974, Seismic velocities in dry and saturated crack solids, J. Geophys. Res., v.79, p.5412-5426.

Potsma, G. W., 1955, Wave propagation in a stratified medium, Geophysics, v.20, p.780-806.

Rudzki, M. P., 1911, Parametrische darstellung der elastischen wellen in anisotropen medien, Bull. Acad. Cracovie, p.503.

Siegfried, R. and G. Simmons, 1978, Characterization of oriented cracks with differential strain analysis, J. Geophys. Res., v.83, p.1269-1278.

Simmons, G. and W. F. Brace, 1965, Comparison of static and dynamic measurements of compressibility of rocks, J. Geophys. Res., v.70, p.5649-5656.

Simmons, G., R. Siegfried and M. Feves, 1974, Differential strain analysis: a new method for examining cracks in rocks, J. Geophys. Res., v.79, p.4383-4385.

Solomon, S. C., 1972, Seismic wave attenuation and partial melting in the upper mantle of North America, J. Geophys. Res., v.77, p.1483-1502.

Sprunt, E. S. and W. F. Brace, 1974, Direct observations of microcavities in crystalline rocks, Int. J. Rock Mech. Min. Sci. and Geomech. Abst., v.11, p.139-150.

Standing, M. B., 1952, Volumetric and phase behavior of oil field hydrocarbon systems, Reinhold, N.Y., 122p.

Stoneley, R., 1949, The seismological implications of aelotropy in continental structures, Mon. Notic. Roy. Astron. Soc., Geophys. Suppl., v.5, p.343-353.

Strang, G., 1976, Linear Algebra and Its Applications, Academic Press, N.Y.

Thomas, L. K., R. W. Hankinson adn K. A. Phillips, 1970, Determination of acoustic velocities for natural gas, J. Petr. Tech., v.22, p.889-895.

Timoshenko, S. P. and J. N. Goodier, 1951, Theory of Elasticity, McGraw Hill, N.Y., 567p.

Timur, A., 1977, Temperature dependence of compressional and shear wave velocities in rocks, Geophysics, v.42, p.950-956.

Timur, A., W. B. Hempkins and R. M. Weinbrandt, 1971, Scanning electron microscope study of pore systems in rocks, J. Geophys. Res., v.76, p.4932-4948.

Toksöz, M. N., 1975, Using rock physics to search for petroleum, Tech. Rev.,v.77, p.29-33.

Toksöz, M. N., C. H. Cheng and A. Timur, 1976, Velocities of seismic waves in porous rocks, Geophysics, v.41, p.621-645.

Toksöz, M. N., D. H. Johnston and A. Timur, 1978, Attenuation of seismic waves in dry and saturated rocks: I. Laboratory measurements, submitted to Geophysics.

Tricomi, F. G., 1957, Integral Equations, Interscience, New York, N.Y.

Walsh, J. B., 1965, The effect of cracks on the compressibility of rock, J. Geophys. Res., v.70, p.381-389.

Walsh, J. B., 1966, Seismic wave attenuation in rock due to friction, J. Geophys. Res., v.71, p.2591-2599.

Walsh, J. B., 1968, Attenuation in partially melted material, J. Geophys. Res., v.73, p.2209.

Walsh, J. B., 1969, New analysis of attenuation in partially melted rocks, J. Geophys. Res., v.74, p.4333-4337.

Walsh, J. B., W. F. Brace and A. W. England, 1965, Effect of porosity on compressibility of glass, J. Am. Ceramic Soc., v.48, p.605-608.

Wiggins, R. A., 1972, The general linear inversion of body wave observations, Rev. Geophys. Space Phys., v.10, p.251-285.

Wu, T. T., 1966, The effect of inclusion shape on the elastic moduli of a two-phase material, Int. J. Solids Structures, v.2, p.1-8.

Wyllie, M. R. J., A. R. Gregory and L. W. Gardner, 1956, Elastic wave velocities in heterogeneous and porous media, Geophysics, v.21, p.41-70.

Wyllie, M. R. J., A. R. Gregory and G. H. F. Gardner, 1958, An experimental investigation of factors affecting elastic wave velocities in porous media, Geophysics, v.23, p.459-493.

Yamakawa, N., 1962, Scattering and attenuation of elastic waves, Geophys. Mag. (Tokyo), v.31, p.63-103.

Zoback, M. D. and J. D. Byerlee, 1975, The effect of micro-crack dilatancy on the permeability of Westerly granite, J. Geophys. Res., v.80, p.752.

APPENDIX A

The Eshelby S tensor, relating e^c_{ij}, the strain field due to an ellipsoidal inclusion, to e^T_{ij}, the "stress-free" strain in the inclusion, i.e.,

$$e^c_{ij} = S_{ijkl} e^T_{kl},$$

is given by (Eshelby, 1957):

$$S_{1111} = Qa^2 I_{aa} + RI_a \tag{A-1}$$

$$S_{1122} = Qb^2 I_{ab} - RI_a \tag{A-2}$$

$$S_{1212} = \frac{Q}{2}(a^2 + b^2) I_{ab} + \frac{R}{2}(I_a + I_b) \tag{A-3}$$

where

$$Q = \frac{3}{8\pi(1-\sigma)}, \qquad R = \frac{1-2\sigma}{8\pi(1-\sigma)}$$

and other cyclic combinations. The components of S that couple dilatational components to shear components (e.g. S_{1112}), or couple different shear components (e.g. S_{1213}) are zero. a, b and c are the semi-axes of the ellipsoid. We also have the following relationships:

$$I_a + I_b + I_c = 4\pi \tag{A-4}$$

$$I_{aa} + I_{ab} + I_{ac} = 4\pi/3a^2 \tag{A-5}$$

$$a^2 I_{aa} + b^2 I_{ab} + c^2 I_{ac} = I_a \tag{A-6}$$

$$I_{ab} = (I_b - I_a)/3(a^2 - b^2) \tag{A-7}$$

and other similar cyclic combinations. For an oblate ellipsoid, $a = b > c$,

$$I_a = I_b = \frac{2\pi\alpha}{(1-\alpha^2)^{3/2}}[\cos^{-1}\alpha - \alpha(1-\alpha^2)^{1/2}] \tag{A-8}$$

where $\alpha = c/a$ is the aspect ratio and $I_{aa} = 3I_{ab}$.

For the two scalars T_{iijj} and T_{ijij}, Wu (1966) gave the following expressions:

$$T_{iijj} = \frac{3F_1}{F_2} \tag{A-9}$$

$$T_{ijij} - \frac{1}{3}T_{iijj} = \frac{2}{F_3} + \frac{1}{F_4} + \frac{F_4F_5 + F_6F_7 - F_8F_9}{F_2F_4} \tag{A-10}$$

where

$$F_1 = 1 + A[\tfrac{3}{2}(g + \phi) - R(\tfrac{3}{2}g + \tfrac{5}{2}\phi - \tfrac{4}{3})]$$

$$F_2 = 1 + A[1 + \tfrac{3}{2}(g + \phi) - \tfrac{R}{2}(3g + 5\phi)] + B(3 - 4R) + \tfrac{A}{2}(A + 3B)(3 - 4R)[g + \phi - R(g - \phi + 2\phi^2)]$$

$$F_3 = 1 + \frac{A}{2}[R(2 - \phi) + \frac{(1 + \alpha^2)}{2\alpha}g(R - 1)]$$

$$F_4 = 1 + \frac{A}{4}[3\phi + g - R(g - \phi)]$$

$$F_5 = A[R(g + \phi - \frac{4}{3}) - g] + B\phi(3 - 4R)$$

$$F_6 = 1 + A[1 + g - R(g + \phi)] + B(1 - \phi)(3 - 4R)$$

$$F_7 = 2 + \frac{A}{4}[9\phi + 3g - R(5\phi + 3g)] + B\phi(3 - 4R)$$

$$F_8 = A[1 - 2R + \frac{g}{2}(R - 1) + \frac{\phi}{2}(5R - 3)] + B(1 - \phi)(3 - 4R)$$

$$F_9 = A[g(R - 1) - R\phi] + B\phi(3 - 4R)$$

$$A = \frac{\mu'}{\mu} - 1$$

$$B = \frac{1}{3}(\frac{K'}{K} - \frac{\mu'}{\mu})$$

$$R = \frac{3\mu}{3K + 4\mu}$$

and for oblate spheroids,

$$\phi = \frac{\alpha}{(1 - \alpha^2)^{3/2}}[\cos^{-1}\alpha - \alpha(1 - \alpha^2)^{1/2}]$$

$$g = \frac{\alpha^2}{1 - \alpha^2}(3\phi - 2).$$

In the case of $\alpha \to 0$, Walsh (1969) gave the following:

$$T_{iijj} = \frac{3(3K+4\mu')}{3K'+4\mu'+3\pi\alpha\mu(3K+\mu)/(3K+4\mu)} \qquad \text{(A-11)}$$

APPENDIX B

In this appendix we will derive the rate of closing of an ellipsoidal crack. Following Eshelby (1957) we can express the strain field ε_{ij} just outside an ellipsoidal cavity in terms of the applied strain field ε^A_{ij} as

$$-\lambda S_{mmpq}\varepsilon_{pq} - 2\mu S_{ijpq}\varepsilon_{pq} + \lambda\varepsilon + 2\mu\varepsilon_{ij} = \lambda\varepsilon^A + 2\mu\varepsilon^A_{ij}$$

$$ij = 11, 22, 33 \qquad \text{(B1)}$$

and

$$\varepsilon_{13} = \frac{\varepsilon^A_{13}}{1 - 2S_{1313}} \quad \text{and other shear components} \qquad \text{(B2)}$$

where the summation convention is used and the pq summation is over 11, 22, 33 only since $S_{1112} = 0$ and so on. ε and ε^A are the traces of the respective strain tensors, i.e. the dilatation of the respective strain fields, and $S_{\alpha\beta\gamma\delta}$ is a fourth order tensor given by Eshelby (1957).

For an applied hydrostatic pressure, the right hand side of (B2) vanishes, and all we have left is (B1). This is a system of three simultaneous equations which has the same right hand side since now $\varepsilon^A_{11} = \varepsilon^A_{22} = \varepsilon^A_{33}$. In particular, we would like to consider oblete spheroids only where the three semi-axes a, b, c of the ellipsoid are related by $a = b > c$. Then (B1) is reduced to two coupled equations

which we can solve.

We note that for an applied hydrostatic pressure P, and an effective bulk modulus K*, the dilatation of the applied strain field is given by

$$\varepsilon^A = -\frac{P}{K^*} \tag{B3}$$

and also for a crack of volume c, the dilatation of the strain field immediately outside the crack is just

$$\varepsilon = \frac{dc}{c} \tag{B4}$$

where dc is the change in volume of the crack due to the applied strain.

Combining all these, and the solution of the system (B1) we get

$$\frac{dc}{c} = -\frac{P}{K^*}/(F_1 - F_2F_3/(F_3 + F_4)) \tag{B5}$$

where

$$F_1 = \frac{6\mu Ia}{2\pi(3K+4\mu)} \tag{B6}$$

$$F_2 = \frac{6\mu}{4\pi(3K+4\mu)}(3Ia-4\pi) \tag{B7}$$

$$F_3 = \frac{\alpha^2(3-9Ia/4\pi)(6K+2\mu)}{2(1-\alpha^2)(3K+4\mu)} + \frac{6\mu Ia}{8\pi(3K+4\mu)} \tag{B8}$$

$$F_4 = \frac{1}{2}\{\frac{(3-9Ia/4\pi)(6K+2\mu)}{2(1-\alpha^2)(3K+4\mu)} - \frac{3(1-Ia/\pi)}{(3K+4\mu)}\} \tag{B9}$$

where

$$Ia = \frac{2\pi\alpha}{(1-\alpha^2)^{3/2}}\{\cos^{-1}\alpha - \alpha(1-\alpha^2)^{1/2}\} \tag{B10}$$

and $\alpha = c/a$ is the aspect ratio.

Or, in terms of Poisson's ratio σ,

$$F_1 = \frac{Ia(1-2\sigma)}{2\pi(1-\sigma)} \tag{B11}$$

$$F_2 = \frac{(1-2\sigma)}{4\pi(1-\sigma)}(3Ia-4\pi) \tag{B12}$$

$$F_3 = \frac{\alpha^2(3-9Ia/4\pi)}{2(1-\alpha^2)(1-\sigma)} + \frac{Ia(1-2\sigma)}{8\pi(1-\sigma)} \tag{B13}$$

and

$$F_4 = \frac{1}{2}\{\frac{(3-9Ia/4\pi)}{2(1-\alpha^2)(1-\sigma)} - \frac{1-2\sigma}{2(1-\sigma)}(1-Ia/\pi)\} \tag{B14}$$

In this form, we can see that for penny-shaped cracks, i.e. as $\alpha \to 0$, keeping terms of order α,

$$Ia \to \pi^2\alpha + O(\alpha^2) \tag{B15}$$

$$F_2 \to \frac{1-2\sigma}{1-\sigma} + O(\alpha) \tag{B16}$$

$$F_3 \to \frac{Ia(1-2\sigma)}{8\pi(1-\sigma)} + O(\alpha^2) \tag{B17}$$

$$F_3+F_4 \to \frac{1}{2}\{\frac{3}{2(1-\sigma)} - \frac{1-2\sigma}{2(1-\sigma)}\} + O(\alpha)$$

$$= \frac{1+\sigma}{2(1-\sigma)} + O(\alpha) \tag{B18}$$

so

$$\frac{F_2F_3}{F_3+F_4} \to -\frac{Ia(1-2\sigma)^2}{4\pi(1-\sigma^2)} + O(\alpha^2) \tag{B19}$$

and

$$F_1 - F_2F_3/(F_3+F_4)$$

$$\to \frac{Ia(1-2\sigma)}{2\pi(1-\sigma)}\{1 + \frac{1-2\sigma}{2(1+\sigma)}\}$$

$$= \frac{3\pi\alpha(1-2\sigma)}{4(1-\sigma^2)} \tag{B20}$$

or

$$\frac{dc}{c} \to -\frac{P}{K^*}\{\frac{4(1-\sigma^2)}{3\pi\alpha(1-2\sigma)}\} \tag{B21}$$

which is the result derived for penny-shaped cracks by Walsh (1965).

At the other limit, i.e. at $\alpha = 1$, for spherical cavities, Eshelby (1957) gives the result as

$$\varepsilon = \frac{4\mu+3K}{4\mu}\varepsilon^A \tag{B22}$$

or

$$\frac{dc}{c} = -\frac{P}{K^*}\left(\frac{4\mu+3K}{4\mu}\right) \tag{B23}$$

Looking at our expression, the terms that have singularities in them at $\alpha = 1$ are Ia, F_3 and F_4. Now

$$Ia = \frac{2\pi\alpha}{(1-\alpha^2)^{3/2}}\{\cos^{-1}\alpha - \alpha(1-\alpha^2)^{1/2}\}$$

which is of indeterminent form at $\alpha = 1$. Applying l'Hospital's rule,

$$\lim_{\alpha\to 1} Ia = 2\pi\left\{\frac{\cos^{-1}\alpha - 3\alpha(1-\alpha^2)^{1/2}}{-3\alpha(1-\alpha^2)^{1/2}}\right\}$$

$$= 2\pi\left\{1 - \frac{\cos^{-1}\alpha}{3\alpha(1-\alpha^2)^{1/2}}\right\}$$

which is still indeterminent at $\alpha = 1$. Apply l'Hospital's rule again to the indeterminent term, we get

$$\lim_{\alpha\to 1} \frac{\cos^{-1}\alpha}{\alpha(1-\alpha^2)^{1/2}} = \frac{-(1-\alpha^2)^{-1/2}}{(1-\alpha^2)^{1/2} - \alpha^2(1-\alpha^2)^{-1/2}}$$

$$= -1$$

so

$$\lim_{\alpha\to 1} Ia = \frac{4\pi}{3} \tag{B24}$$

Next we look at F_3 and F_4,

$$\lim_{\alpha\to 1} F_3 = 2F_4$$

so $$\lim_{\alpha \to 1} \frac{F_3}{F_3+F_4} = \frac{2}{3} \tag{B25}$$

and $$\lim_{\alpha \to 1} F_2 = \frac{(1-2\sigma)}{4\pi(1-\sigma)}\{3\frac{4\pi}{3} - 4\pi\} = 0 \tag{B26}$$

and $$\lim_{\alpha \to 1} F_1 = \frac{4\pi/3}{2\pi}(\frac{6\mu}{3K+4\mu}) = \frac{4\mu}{3K+4\mu} \tag{B27}$$

so $$\lim_{\alpha \to 1} \frac{dc}{c} = -\frac{P}{F_1 K^*}$$

$$= -\frac{P}{K^*}(\frac{3K+4\mu}{4\mu}) \tag{B28}$$

same as that obtained by Eshelby (1957).

APPENDIX C

LEAST SQUARES AND DAMPED LEAST SQUARES INVERSION

C.1 Least Squares Inversion:

For an overdetermined linear system of equations $y = Ax$, the least squares solution is given by

$$x_s = A_s^{-1} y = (A^T A)^{-1} A^T y \qquad \text{(C-1)}$$

assuming that the matrix $A^T A$ is non-singular. Following the notation of Wiggins (1972), we can define the resolution matrix R by substituting the original equation for y in the solution, i.e.

$$x_s = A_s^{-1} y = A_s^{-1} Ax = Rx \qquad \text{(C-2)}$$

So the resolution matrix R is given by

$$R = A_s^{-1} A = (A^T A)^{-1} A^T A = I \qquad \text{(C-3)}$$

As seen in eq. (C-2), R relates that least squares solution of the model vector x_s to the actual model vector x. So in this case of least squares solution, the model is perfectly resolved. Alternatively, we can solve for the calculated data vector y_s in terms of the observed data vector y,

$$y_s = Ax_s = A(A^T A)^{-1} A^T y = Dy \qquad \text{(C-4)}$$

The matrix D is called the information density matrix

by Wiggins (1972). It relates the calculated data to the observed data. It is in fact a resolution matrix in the data space and tells us which components of the data vector are related and which components are independent from each other.

One of the most important question in any inversion scheme is the estimate of the variance in the solution. The error Δx in the solution due to an error of Δy in the data can be written as

$$\Delta x = A_s^{-1} \Delta y \tag{C-5}$$

So their covariance matrices are related by

$$< \Delta x \cdot \Delta x^T > = A_s^{-1} < \Delta y \cdot \Delta y^T > (A_s^{-1})^T \tag{C-6}$$

Assumming that all the components of the data vector are statistically independent and share the same variance σ_y^2, we can write

$$\begin{aligned} < \Delta x \cdot \Delta x^T > &= \sigma_y^2 A_s^{-1} (A_s^{-1})^T \\ &= \sigma_y^2 (A^T A)^{-1} A^T A (A^T A)^{-1} \\ &= \sigma_y^2 (A^T A)^{-1} \end{aligned} \tag{C-7}$$

If we do not have a *priori* knowledge of the variance in the data, we can estimate it by (Draper and Smith, 1966)

$$\sigma_y^2 = \frac{|y_s - y|^2}{f} \tag{C-8}$$

where f is the number of degrees of freedom in A. In an overdetermined system, f is equal to the number of rows of A minus the number of columns of A.

C.2 Damped Least Squares Inversion:

In most cases of geophysical interest, the components of the model vector may not be independent of each other. When this happens, the matrix A^TA is singular or near singular, i.e., it has zero or near zero eigenvalues. In such cases a direct inversion of A^TA is either not possible or results in a covariance matrix with large elements on the diagonal, thus giving large variances in the solution. In order to avoid such problems, we can either do a complete singular value decomposition of the system and cut off the smaller eigenvalues (Wiggins, 1972; Golub and Kahan, 1965; Lanczos, 1961; Aki, 1975) or in an approach that is similar, make the matrix A^TA non-singular by adding a constant to all eigenvalues through the stochastic or damped least squares inverse (Franklin, 1970). The damped least squares inverse is given by

$$A_d^{-1} = (A^TA + \varepsilon^2 I)^{-1}A^T \qquad \text{(C-9)}$$

Following derivations for the least squares inverse, the resolution matrix is given by

$$R = (A^TA + \varepsilon^2 I)^{-1}A^TA \qquad \text{(C-10)}$$

Note that the resolution matrix is no longer the identity matrix (for $\varepsilon \neq 0$). The off-diagonal element R_{ij} gives the relative resolution between the i^{th} and j^{th} components of the model vector. Similarly, the information density matrix is given by

$$D = A(A^TA + \varepsilon^2 I)^{-1}A^T \qquad \text{(C-11)}$$

and finally, the covariance matrix is given by

$$< \Delta x \cdot \Delta x^T > = \sigma_y^2 (A^TA + \varepsilon^2 I)^{-1} A^T A (A^TA + \varepsilon^2 I)^{-1} \qquad \text{(C-12)}$$

C.3 Resolution and Variance of Linearized Iterative Inversion:

For a linearized system of equations obtained from the non-linear system $y = F(x)$

$$\Delta y = \frac{\partial F}{\partial x}\Delta x = A\Delta x \qquad \text{(C-13)}$$

and we have a relation between the changes in the model and data instead of between the model and data themselves. All of our equations discussed above hold, but we will have to be a little more careful in interpreting their meanings. The resolution and information density matrices now give us the relative resolution between the components in the changes in the model and data respectively. However, the covariance matrix has the same meaning physically, since our linearized equations do couple the changes in the model and data. The only change in the estimation of the variance

in the solution lies in the estimation of the variance in data σ_y^2. If our initial model x_o creates an initial estimate of the data $y_o = F(x_o)$, then the estimate of the variance in data is given by

$$\sigma_y^2 = \frac{|y - F(x_o + \Delta x)|^2}{f} \qquad \text{(C-14)}$$

APPENDIX D

ANISOTROPY

In quite a number of rocks some of the cracks have a preferred direction of orientation due to bedding or in situ tectonic stresses. The amount of anisotropy varies with each rock at each location. Usually the velocity difference between the fastest axis of propagation and the slowest is less than 10%. Furthermore, the preferred orientation of the cracks is such that there usually is axial symmetry. Under these circumstances, the velocity anisotropy in these rocks can be modelled by introducing preferentially oriented oblate spheroidal cracks into the rock matrix. In this appendix, we review the previous works, which are minimal in this area, and introduce simplifications into some of the expressions, especially in the limit of cracks of very small aspect ratios.

D.1 Previous Works on the Theoretical Modelling of Velocity Anisotropy:

D.1.1 Eshelby's Interaction Energy:

The most direct way to calculate the effects of velocity anisotropy due to an oriented crack is by the Eshelby interaction energy method. From equation (2-15), we have the effective stiffness tensor of a material with an ellip-

soidal inclusion of fractional concentration ϕ given by

$$C^{*}_{ijkl} e^{A}_{ij} e^{A}_{kl} = C_{ijkl} e^{A}_{ij} e^{A}_{kl} - \phi p^{A}_{ij} e^{T}_{kl} \qquad \text{(D-1)}$$

where p^{A}_{ij} is the applied stress field and is given by

$$p^{A}_{ij} = C_{ijkl} e^{A}_{kl} \qquad \text{(D-2)}$$

and e^{T}_{ij} is the "stress-free" strain associated with the inclusion, and is related to the applied strain e^{A}_{ij} by equations (2-5) to (2-9). In particular, the shear components are given by

$$e^{T}_{ij} = \frac{\mu-\mu'}{2(\mu'-\mu)S_{ijij} + \mu} e^{A}_{ij} \qquad \begin{matrix} i \neq j \\ \text{no summation} \end{matrix} \qquad \text{(D-3)}$$

The dilatational parts are given by eq. (2-9).

In Chapter 2, we were dealing only with materials that are macrohomogeneous and macroisotropic, hence the stiffness tensors were reduced to each containing two independent constants only. For a material having axial symmetry, the number of independent constants in the stiffness tensor is 5 (Love, 1927). These correspond to $C_{1111} = C_{2222}$, C_{3333}, $C_{1313} = C_{2323}$, C_{1133} and $C_{1212} = (C_{1111} - C_{1122})/2$ in the case where the axis of symmetry in the three axis.

Up to this day equation (D-1) remains the most used equation in the calculation of velocity anisotropy. The rest of this appendix will deal with different attempts to simplify equation (D-1) in the case of oblate spheroidal inclusions.

D.1.2 Previous Numerical Studies:

Nur (1971) was the first to make use of the Eshelby interaction energy to calculate the velocity anisotropy in a real rock (Barre granite). Unfortunately, instead of substituting for the stress-free strain e^T_{ij} in eq.(D-1), he substituted the total strain $e_{ij} = T_{ijkl}\, e^A_{kl}$. This substitution is only valid for empty inclusions where $K' = \mu' = 0$. This point was not made clear in the text.

Another criticism of Nur's approach is that he used simplified expressions for T_{ijkl}, ignoring all terms that do not have a factor of $1/\alpha$, besides the constant term. This is debatable since there are terms in which an addition or subtraction of the T's are involved and higher order terms may be significant. A better practice is to simplify the expressions after a full algebraic form is obtained, as is shown in a later section of this chapter.

Despite the above criticisms, Nur made an important contribution to the study of velocity anisotropy by introducing expressions for the opening and closing of preferentially oriented cracks under an uniaxial stress, using the Walsh formulation of crack closing. He was able to use this theory to fit his own data on Barre granite, but recently there are questions about his results. This will be discussed in a later section.

Anderson et al. (1974) were the first ones to use equation (D-1) in its proper form for a fluid filled inclusion. They solved the system of equations numerically. They showed that the inclusion of fluids in the cracks reduce the anisotropy of the compressional waves but have little or no effects on the velocity anisotropy of the shear waves. This result is very much as expected from comparisons with isotropic cases.

D.2 Simplification of Eshelby's Equations:

D.2.1 Analytic Solution of Eshelby's Equations:

If we reindex the strain tensors from e_{11}, e_{22}, e_{33}, e_{23}, e_{13} and e_{12} to e_i, i = 1, ... , 6, then equation (D-1) can be rewritten as the following:

$$C^*_{ij} e^A_i e^A_j = C_{ij} e^A_i e^A_j - \phi p^A_i e^A_j \qquad \text{(D-4)}$$

The relationship between the "stress-free" strain e^T_i and the applied strain e^A_i (eq. 2-9, D-3) can be written as

$$e^T_i = A_{ij} e^A_j \qquad \text{(D-5)}$$

The shear components of eq (D-5) are given by eq. (D-3). Combining (D-2), (D-4) and (D-5) we obtain the following system of equations:

$$C^*_{ij} e^A_i e^A_j = (C_{ij} - \phi C_{ki} A^A_{kj}) e^A_i e^A_j \qquad \text{(D-6)}$$

As mentioned above, for a two-phase medium with axial symmetry in the three direction, there are five independent constants in C^*_{ij}, these are:

$$C^*_{11} = C_{11} - \phi(C_{11}A_{11} + C_{21}A_{21} + C_{31}A_{31})$$

$$C^*_{33} = C_{33} - \phi(C_{13}A_{13} + C_{23}A_{23} + C_{33}A_{33})$$

$$C^*_{13} = \frac{1}{2}[C_{13} + C_{31} - \phi(C_{11}A_{13} + C_{21}A_{23} + C_{31}A_{33} + C_{13}A_{11} + C_{23}A_{21} + C_{33}A_{31})]$$

$$C^*_{44} = C_{44} - \phi C_{44}A_{44}$$

$$C^*_{66} = C_{66} - \phi C_{66}A_{66} \qquad \text{(D-7)}$$

The C_{ij}'s are of course given by

$$C_{11} = C_{22} = C_{33} = \lambda + 2\mu$$

$$C_{44} = C_{55} = C_{66} = \mu$$

$$C_{12} = C_{13} = C_{23} = C_{32} = C_{31} = C_{21} = \lambda$$

all other components are zero.

In order to get analytic expressions for eq. (D-7), we will have to solve for A_{ij}. The solution of the two shear components are immediate, and are given by equation (D-3). Substituting for A_{44} and A_{66} into equation (D-7), we obtain

$$C^*_{44} = \mu[1 - \frac{\phi(\mu-\mu')}{\mu + 2(\mu'-\mu)S_{2323}}] \qquad \text{(D-8)}$$

and

$$C^*_{66} = \mu[1 - \frac{\phi(\mu-\mu')}{\mu + 2(\mu'-\mu)S_{1212}}] \qquad \text{(D-9)}$$

Because of the symmetry of the problem, the following equalities hold true: $A_{44} = A_{55}$, $A_{11} = A_{22}$, $A_{12} = A_{21}$, $A_{31} = A_{31}$ and $A_{13} = A_{23}$.
What remains to be solved for are the dilatational parts of A, i.e. A_{ij}, i, j = 1,2,3.

Equation (2-9) can be rewritten into the following form:

$$B_{ij}e^T_j = L_{ij}e^A_j \qquad i,j = 1,2,3 \qquad \text{(D-10)}$$

So the matrix A_{ij}, i, j = 1,2,3, can be written as

$$A_{ij} = B^{-1}_{ik}L_{kj} \qquad \text{(D-11)}$$

where

$$B_{ij} = GS_j + 2HS_{ij} + \lambda + 2\mu\delta_{ij} \tag{D-12}$$

$$L_{ij} = - G - 2H\delta_{ij} \tag{D-13}$$

$H = (\mu'-\mu)$, $G = (\lambda'-\lambda)$

$S_{13} = S_{1133}$, etc., and $S_j = \sum_i S_{ij}$

The L matrix is, of course, nothing but the linear Hookean operator of the contrast in the moduli of the matrix and inclusion materials. As a result, it is easier to solve for $A^{-1} = L^{-1}B$ and then invert the A matrix. L^{-1}, the inverse Hookean operator, is given by

$$L^{-1}_{ij} = - \frac{\Delta\sigma}{\Delta E} + \frac{1+\Delta\sigma}{\Delta E}\delta_{ij} \tag{D-14}$$

where $\Delta\sigma = \sigma' - \sigma$ and $\Delta E = E' - E$.

It can also be written as

$$L^{-1}_{ij} = \frac{1}{2H(3G+2H)}[G - (3G+2H)\delta_{ij}] \tag{D-15}$$

and

$$A^{-1}_{ij} = L^{-1}_{ik}B_{kj}$$

$$= \frac{1}{2H(3G+2H)}[GB_j - (3G+2H)B_{ij}] \tag{D-16}$$

where

$$B_j = \sum_j B_{ij}$$

$$= (3G+2H)S_j + 3\lambda + 2\mu$$

Simplifying,

$$A^{-1}_{ij} = \frac{1}{2H(3G+2H)}\{G[(3G+2H)S_j + 3\lambda + 2\mu]$$

$$- (3G+2H)[GS_j + 2HS_{ij} + \lambda + 2\mu\delta_{ij}]\}$$

$$= \frac{1}{2H(3G+2H)}[G(3\lambda+2\mu)-(3G+2H)(2HS_{ij}+\lambda+2\mu\delta_{ij})]$$

$$= - S_{ij} - \frac{\mu}{H}\delta_{ij} + D \qquad \text{(D-18)}$$

where

$$D = \frac{1}{2H(3G+2H)}[G(3\lambda+2\mu) - (3G+2H)\lambda]$$

$$= \frac{1}{3}\left(\frac{\mu}{\mu'-\mu} - \frac{K}{K'-K}\right) \qquad \text{(D-19)}$$

which is a constant independent of i and j. Let $F = A^{-1}$, then by Cramer's rule,

$$A_{11} = (F_{11}F_{33} - F_{13}F_{31})/\det F$$

$$A_{12} = -(F_{21}F_{33} - F_{13}F_{31})/\det F$$

$$A_{13} = -F_{13}(F_{11} - F_{21})/\det F$$

$$A_{21} = A_{12}$$

$$A_{22} = A_{11}$$

$$A_{23} = A_{13}$$

$$A_{31} = -F_{31}(F_{11} - F_{21})/\det F$$

$$A_{32} = A_{31}$$

$$A_{33} = (F_{11}^2 - F_{21}^2)/\det F \qquad \text{(D-20)}$$

where

$$\det F = (F_{11}-F_{21})[F_{33}(F_{11}+F_{21})-2F_{31}F_{13}] \qquad \text{(D-21)}$$

Substituting (D-20) and (D-18) into (D-7), we get

$$C^*_{11} = \lambda + 2\mu - \phi[\lambda(S_{31}-S_{33}-\tfrac{\mu}{H})(S_{21}-S_{11}-\tfrac{\mu}{H})$$

$$+ 2\mu(S_{33}S_{11}-S_{31}S_{13}+\tfrac{\mu}{H}(S_{33}+S_{11}-2D+\tfrac{\mu}{H})$$

$$+ D(S_{31}+S_{13}-S_{11}-S_{33}))]/\det F \qquad \text{(D-22)}$$

$$C^*_{33} = \lambda + 2\mu - \phi(S_{21}-S_{11}-\tfrac{\mu}{H})[(\lambda+2\mu)(-S_{21}-S_{11}-\tfrac{\mu}{H})$$

$$+ 2\lambda S_{13} + 4\mu D]/\det F \qquad \text{(D-23)}$$

$$C^*_{13} = C^*_{31} = \lambda - \phi(S_{21}-S_{11}-\tfrac{\mu}{H})[(\lambda+2\mu)(S_{13}+S_{31})$$

$$- 4\mu D + \lambda(S_{13}-S_{21}-S_{11}-S_{33}-\tfrac{2\mu}{H})]/2\det F \qquad \text{(D-24)}$$

and

$$\det F = (S_{21}-S_{11}-\tfrac{\mu}{H})[S_{33}S_{11}+S_{33}S_{21}-2S_{31}S_{13}$$

$$+ \tfrac{\mu}{H}(S_{11}+S_{21}+S_{33}+\tfrac{\mu}{H}-3D)$$

$$- D(S_{11}+S_{21}+2S_{33}-2S_{13}-2_{31})] \qquad \text{(D-25)}$$

D.2.2 The Limiting Case of a Small Aspect Ratio Crack:

The expressions for the effective elastic moduli of a solid with oblate spheroidal inclusion given by equations (D-8), (D-9), (D-22), (D-23), (D-24) and (D-25) are exact, with the Eshelby S tensor given in Appendix A. In most rocks, however, the cracks that cause the velocity anisotropy are usually very thin and of very small aspect ratios. Hence it would be useful to simplify the expressions we obtained above by expanding the S tensor in terms of the aspect ratio α and keeping only terms to the first order in α. By doing so, we obtain the following expressions for the S tensor (see also Walsh, 1969):

$$S_{11} = S_{22} = \pi\alpha(9-5R)/16$$

$$S_{33} = 1 - \pi\alpha R/2$$

$$S_{12} = S_{21} = \pi\alpha(3-7R)/16$$

$$S_{13} = S_{23} = - \pi\alpha R/4$$

$$S_{31} = S_{32} = 1 - 2R - \pi\alpha(3-5R)/4$$

$$S_{1313} = S_{2323} = \frac{1}{2} - \pi\alpha(3-2R)/8$$

$$S_{1212} = \pi\alpha(3+R)/16$$

where
$$R = \frac{1-2\sigma}{2(1-\sigma)} = \frac{3\mu}{3K+4\mu} = \frac{\mu}{\lambda+2\mu} \qquad \text{(D-26)}$$

Substituting these approximations into equations (D-8), (D-9), (D-22), (D-23), (D-24) and (D-25), we obtain the simplified expressions for the effective elastic moduli for an axially anisotropic material:

$$\begin{aligned} C^*_{11} = \lambda + 2\mu - \phi[&\lambda(\tfrac{\mu}{H}(2R+\tfrac{\mu}{H}) + \tfrac{\pi\alpha}{8}(6R+2R^2+\tfrac{\mu}{H}(9-13R))) \\ &+ 2\mu(\tfrac{\mu}{H}(1-2D+\tfrac{\mu}{H})-2DR + \tfrac{\pi\alpha}{16}(9-R-8R^2 \\ &+ \tfrac{\mu}{H}(9-13R)-D(21-29R)))]/ \\ &(-\tfrac{\pi\alpha}{8}(3+R) - \tfrac{\mu}{H})[\tfrac{\mu}{H}(1+\tfrac{\mu}{H}-3D)-4DR \\ &+ \tfrac{\pi\alpha}{4}(3-R-4R^2+\tfrac{\mu}{H}(3-5R)-3D(3-5R))] \end{aligned} \qquad \text{(D-27)}$$

$$\begin{aligned} C^*_{33} = \lambda + 2\mu - \phi[&(\lambda+2\mu)(-\tfrac{\mu}{H} - \tfrac{3\pi\alpha}{4}(1-R)) \\ &- 2\lambda(\tfrac{\pi\alpha R}{4}) + 4\mu D]/[\tfrac{\mu}{H}(1+\tfrac{\mu}{H}+3D) \\ &- 4DR + \tfrac{\pi\alpha}{4}(3-R-4R^2+\tfrac{\mu}{H}(3-5R)-3D(3-5R))] \end{aligned} \qquad \text{(D-28)}$$

$$C_{13}^{*} = \lambda - \phi[(\lambda+2\mu)(1-2R-\frac{\pi\alpha}{4}(3-4R))$$

$$- 4\mu D - \lambda(1+\frac{2\mu}{H}) - \lambda\frac{\pi\alpha}{4}(3-4R)]/2[\frac{\mu}{H}(1+\frac{\mu}{H}-3D)$$

$$- 4DR + \frac{\pi\alpha}{4}(3-R-4R^2+\frac{\mu}{H}(3-5R)-3D(3-5R))] \qquad (D-29)$$

$$C_{44}^{*} = \mu(1 + \phi/[\frac{\mu}{H} + 1 - \frac{\pi\alpha}{4}(3-2R)]) \qquad (D-30)$$

$$C_{66}^{*} = \mu(1 + \phi/[\frac{\mu}{H} + \frac{\pi\alpha}{8}(3+R)]) \qquad (D-31)$$

As in the case for isotropy materials the interative procedure (or numerical integration) can be applied here to take care of the effects of crack interaction.

D.3 Velocities Of An Axially Anisotropic Material:

For an axially anisotropic, or equivalently, transversely isotropic material with the three axis the axis of symmetry, the strain energy function W is given by (Love, 1927):

$$2W = C_{11}(e_{11}^2 + e_{22}^2) + C_{33}e_{33}^2$$

$$+ 2C_{13}(e_{11} + e_{22})e_{33} + 2(C_{11} - 2C_{66})e_{11}e_{22}$$

$$+ C_{44}(e_{23}^2 + e_{31}^2) + C_{66}e_{12}^2 \qquad (D-32)$$

The stresses are given by (Stoneley, 1949)

$$\sigma_{11} = C_{11}e_{11} + (C_{11} - 2C_{66})e_{22} + C_{13}e_{33}$$

$$\sigma_{22} = (C_{11} - 2C_{66})e_{11} + C_{11}e_{22} + C_{13}e_{33}$$

$$\sigma_{33} = C_{13}(e_{11} + e_{22}) + C_{33}e_{33}$$

$$\sigma_{12} = \sigma_{21} = C_{66}e_{12}$$

$$\sigma_{23} = \sigma_{32} = C_{44}e_{23}$$

$$\sigma_{13} = \sigma_{31} = C_{44}e_{31} \qquad \text{(D-33)}$$

The equations of motion are (Stoneley, 1949)

$$\rho\frac{\partial^2 u}{\partial t^2} = \frac{\partial}{\partial x_1}[C_{11}e_{11} + (C_{11} - 2C_{66})e_{22} + C_{13}e_{33}]$$

$$+ \frac{\partial}{\partial x_2}(C_{66}e_{12}) + \frac{\partial}{\partial x_3}(C_{44}e_{31})$$

$$\rho\frac{\partial^2 v}{\partial t^2} = \frac{\partial}{\partial x_1}(C_{66}e_{12}) + \frac{\partial}{\partial x_2}[(C_{11} - 2C_{66})e_{11} + C_{11}e_{22}$$

$$+ C_{13}e_{33}] + \frac{\partial}{\partial x_3}(C_{44}e_{23})$$

$$\rho\frac{\partial^2 w}{\partial t^2} = \frac{\partial}{\partial x_1}(C_{44}e_{31}) + \frac{\partial}{\partial x_2}(C_{44}e_{23}) + \frac{\partial}{\partial x_3}[C_{13}(e_{11} + e_{22}) + C_{13}e_{33}] \qquad \text{(D-34)}$$

For solutions analogous to P and SV waves travelling in a plane containing the three axis, we set $v = 0$ and $\partial/\partial x_2 = 0$ and look for solutions of u and w that are proportional to $\exp\{ik(x_1\sin\theta + x_3\cos\theta \pm ct)\}$ where c is the velocity of propagation, k the wavenumber, and θ the angle between the direction of propagation and the three axis. Substituting into (D-34), we obtain (Stoneley, 1949)

$$2\rho c^2 = C_{11}\sin^2\theta + C_{33}\cos^2\theta + C_{44} \pm \{[(C_{11}-C_{44})\sin^2\theta - (C_{33}-C_{44})\cos^2\theta]^2 + 4\sin^2\theta\cos^2\theta(C_{13}+C_{44})^2\}^2 \qquad \text{(D-35)}$$

The + sign corresponds to the P wave in an isotropic medium and the - sign the SV-wave. Similarly, for the analog to the SH-wave, we set $u = w = 0$, $\frac{\partial}{\partial x_1} = \frac{\partial}{\partial x_3} = 0$ and take v to be proportional to $\exp\{ik(x_1\sin\theta + x_3\cos\theta - ct)\}$

and substitute into equation (D-34). We obtained (Stoneley, 1949):

$$\rho c^2 = \sin^2\theta C_{66} + \cos^2\theta C_{44} \qquad \text{(D-36)}$$

Unlike the isotropic case, the two shear waves in an axially anisotropy material travel with different velocities. The two shear wave velocities are equal only when $\theta = 0$, i.e., when the direction of propagation coincides with the axis of symmetry.

Finally, Rudzki (1911) and Potsma (1955) has obtained some bounds on the moduli of a general transversely isotropic material. These are

$$C_{11} > C_{66} \geq C_{44} > 0 \qquad \text{(D-37)}$$

and in the case where the inclusion is "softer" than the matrix, i.e. $K' < K$ and $\mu' < \mu$,

$$C_{11} > C_{33} \qquad \text{(D-38)}$$

D.4 Effects of Saturation and Pore Shape on Velocity Anisotropy:

In this section we do a brief numerical study of the effects of saturation and pore shapes on the velocity anisotropy of a two-phase material, similar to that done in section 3.1. Figure (D-1) shows a plot of the p-wave velocity and the two s-wave velocities of a theoretical rock with matrix moduli K = 0.65 Mb, μ = 0.39 Mb and a pore concentration of 0.02 and aspect ratio of 0.05, as a function of θ, the angle from the axis of symmetry, and saturation. For V_p, both the dry and the wet rock show significant amounts of anisotropy, with the dry rock having the larger amount. The anisotropy is about 20 percent for the wet rock and over 30 percent for the dry rock. The horizontally polarized s-wave ($s_\perp$) shows no effects of saturation, as can be expected since the cross terms of the Eshelby S tensor are not functions of the fluid bulk modulus. The velocity anisotropy for this s-wave is less than the p-wave, about 15 percent. The vertically polarized s-wave ($s_\parallel$, parallel to the axis of symmetry) does not have any anisotropy at 0 and 90 degrees, as can be expected from the previous section (see also Anderson et al., 1974). The wet and dry velocities do differ at the intermediate angles in this case. This is because at these angles, the velocities are functions of the compressional moduli (C_{11}, C_{33} and C_{13}) as well as the shear moduli (C_{44} and C_{66}). This fact is well

understood from the solutions to the wave equation (see equation D-35).

Figure (D-2) shows the effects of pore shape on the velocity anisotropy. The p- and s-wave velocities along the axis of symmetry (the "slow" axis in this case) are plotted as a function of percent concentration for three different aspect ratio cracks (α = 0.1, 0.05 and 0.01). In the case of p-waves, the velocities are also plotted for both dry and wet rocks (their s-wave velocities are identical). The matrix moduli are taken to be K = 0.65 Mb and μ = 0.39 Mb.

As can be seem from figure (D-2), the effect of pore shape is even more pronounced than the isotropic case (figure 3-1), especially for the dry rock. For the s-wave, at the same concentration, the decrease in velocity almost goes as $1/\alpha$. The same is true for the p-wave velocities of the dry rock. The dependence of aspect ratio for p-wave velocities in wet rock is more complicated, the decrease in velocity being slower than $1/\alpha$.

FIGURE CAPTIONS

Figure D-1: Theoretical P- and S-wave velocities of a dry and water-saturated rock with anisotropy caused by an oblate ellipsoidal crack (fractional porosity 0.02 and aspect ratio 0.05) as a function of θ, the angle from the axis of symmetry. The matrix moduli are K = 0.65 Mb and μ = 0.39 Mb. The subscripts d and w represent the dry and water-saturated rock respectively. $S_{\perp}$ is the horizontally polarized S-wave (perpendicular to the axis of symmetry). $S_{\parallel}$ is the vertically polarized S-wave (parallel to the axis of symmetry).

Figure D-2: Theoretical P and $S_{\parallel}$ at $\theta = 0$ as a function of saturation, fractional porosity and aspect ratio of the oblate ellipsoidal inclusion. The matrix parameters are the same as those in figure (D-1).

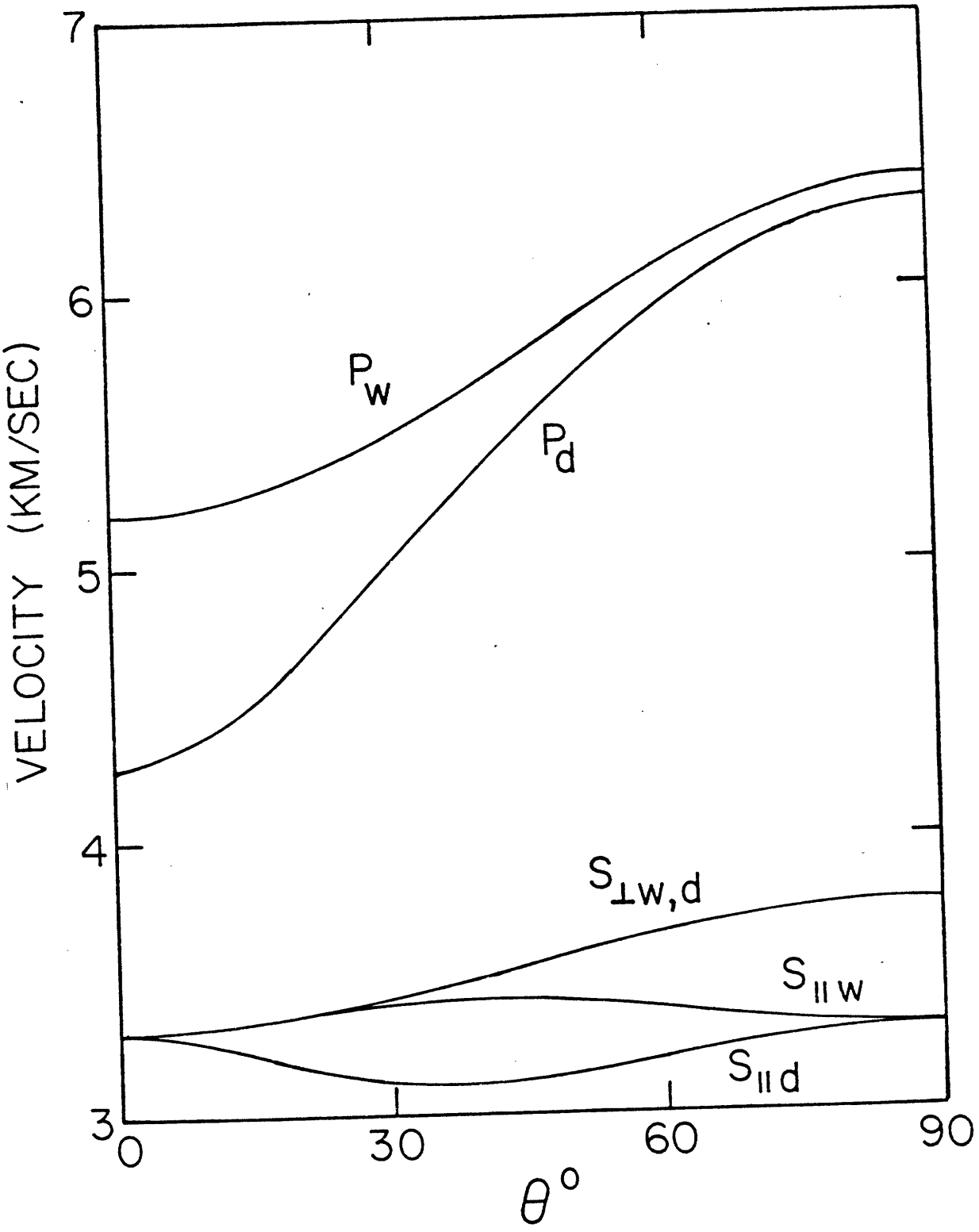
7
6
5
4
3
VELOCITY (KM/SEC)
P_w
P_d
$S_{\perp w,d}$
$S_{\parallel w}$
$S_{\parallel d}$
0
30
60
90
θ°

Figure D-1

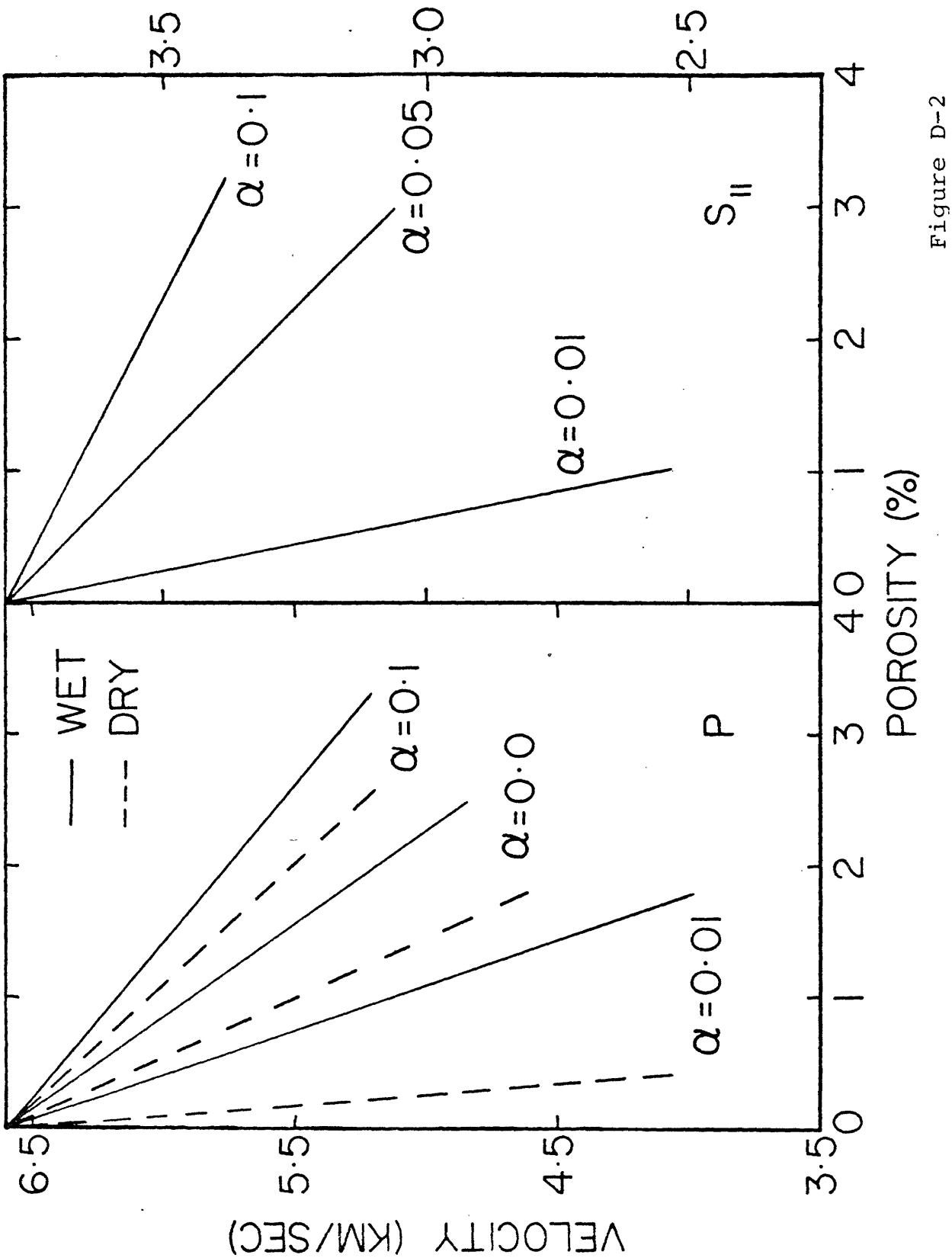
VELOCITY (KM/SEC)
6·5
5·5
4·5
3·5
P
WET
DRY
α=0·1
α=0·0
α=0·01
S_II
α=0·1
α=0·05
α=0·01
3·5
3·0
2·5
0
1
2
3
4
POROSITY (%)

Figure D-2

BIOGRAPHY

The author was born on October 4, 1950, in Happy Valley, Hong Kong (where, according to Doonesbury's Uncle Duke, old China hands go and sit around in shabby, linen suits, drinking gin and filing dispatches to stodgy London journals). As a youth, he was the perennial winner of the Bugs Bunny look alike contest until his reign was rudely terminated by the wires of an orthodontist. After graduating from high school, he ventured east to the land of opportunities and double knit leisure suits. He attended Cornell University, from where he graduated with a baccalaureate in Engineering Physics in 1973. From high above Cayuga's waters he heard the cries of "M-I-T-P-H-D, M-O-N-E-Y" which lured him to the great tool factory on the north bank of the muddy Charles. Forseeing the oncoming energy crisis and the windfall profits of the Seven Sisters, he majored in geophysics. At M.I.T., he founded, with his officemates, the Institute of Applied Theoretical Geophysics which awards annually to a deserving seismology student the M. Nafi Toksöz Award for spending the most time away from M.I.T. without a formal leave of absence. Besides this thesis, the author was also known for his theory on how the Earth and the Moon tugs on one another until each develops hiccups ("Scientists Say the Earth Gives Moon Hiccups" -- Boston Globe, 4/15/76; "Quakes Linked to Moon's Pull" -- Boston Globe, 4/24/78). For the future,

the author plans to follow the traditions of his homeland -- sit around in shabby, linen suits, drinking gin and submitting papers to stodgy American journals. Previous dispatches include:

Toksöz, M. N., C. H. Cheng and A. Timur, 1976, Velocities of Seismic Waves in Porous Rocks, Geophysics, v.41, p.621-645.

Toksöz, M. N., N. R. Goins and C. H. Cheng, 1977, Moonquakes: Mechanisms and Relation to Tidal Stresses, Science, v.196, p.979-981.

Cheng, C. H. and M. N. Toksöz, 1978, Tidal Stresses in the Moon, J. Geophys. Res., v.83, p.845-853.